D.V. Radziuk

FORMATION OF NANOPARTICLES OF NONSTEROIDAL ANTI-INFLAMMATORY DRUGS WITH METALLOGRAPHENE STRUCTURE AND IMPROVED ELECTROKINETIC PROPERTIES

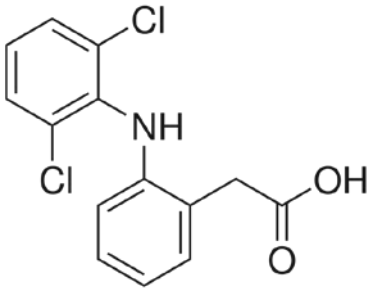

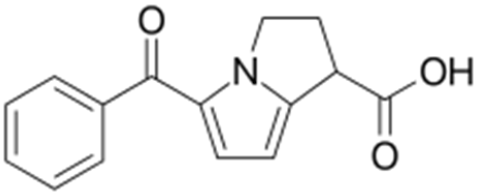

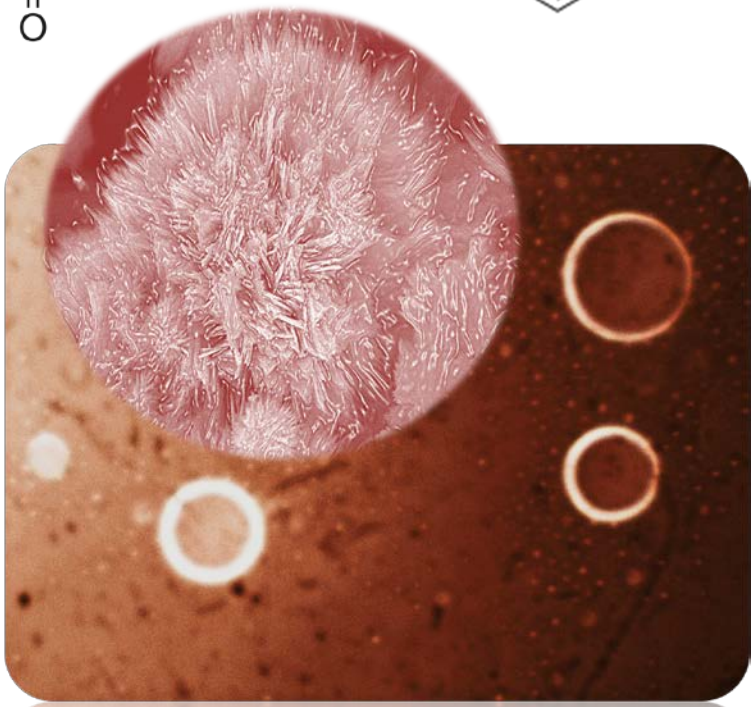

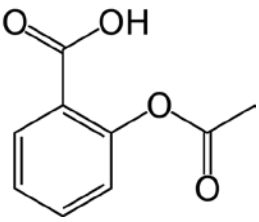

To the people I love.

ANNOTATION

This monograph is a comprehensive guide to creating advanced functional nanomaterials based on oxidized graphene and copper, iron, copper/iron and zinc oxides complexed with some nonsteroidal anti-inflammatory drugs (ketorolac, diclofenac, acetylsalicylic and salicylic acids) by ultrasound (20 kHz). It is written with the aim to introduce a new concept of ultrasonic functionalization of pristine NSAIDs at the contact with metallographene nanoplatform to ameliorate the electronic molecular structure and electrokinetic properties of drugs as potential pharmaceutical NSAID-metallographene nanoparticles. The text includes the defined principles of formation and stability of final nanomaterials in aqueous solutions adjusted to pH=1, 5 and 8. Moreover, it shows the defined conditions of improved *in vitro* bacteriostatic and anticancer efficiency of formed NSAID-metallographene nanoparticles, e.g. with E.coli M-17 bacteria, and three cancer cell lines: HeLa (cervix), HepG2 (liver) and HT29 (colon) supported by the electro-Fenton cyclic voltammetry experiments of OH radical formation and inhibition. The reader can also find the discovered *in vitro* molecular switch in apoptosis of colon cancer cells HT29 by Fe_3O_4-rGO-SA nanoparticles in the addition of ascorbic acid in the frame of theoretically modeled H^+ production on the surface of nanoparticles and their electromagnetic field distribution profile.

This monograph is dedicated to the readears of the broad and multidisciplinary scientific community comprising of physicists and biophysicists, chemists and microbiologists working in the fields of nanoelectronics, nanomedicine and nanomaterials.

TABLE OF CONTENTS

INTRODUCTION

NSAIDs and their functions

Nonsteroidal anti-inflammatory drugs (NSAIDs) are widely used to reduce inflammation, pain, fever, and to treat diseases such as Alzheimer's, type 2 diabetes, rheumatism and many types of malignancies [1]. NSAIDs have been used in one form or another for centuries as extracts and preparations from plants, e.g. willow tree, *Salix alba*, for relief from pain and fever. These plants contain derivatives of salicylic acid, which commercial production began by 1874, and first reports of salicylate (5–6 g per day) for the treatment of rheumatic disorders were first published in 1876. Since then research has been dedicated to the synthesis of NSAIDs, resulting in the production of one of the first well-known acetylsalicylic acid (ASA) being synthesized by Felix Hoffmann in 1897 and later marketed by Bayer as Aspirin [2]. The opinion of the scientist K.D. Rainsford from the Biomedical Research Centre at the Sheffield Hallam University (United Kingdom) about the aspirin, its history and development of the pharmacology and biochemistry of salicylates and related drugs is an example of the classical approach to the study of many NSAIDs [3]. Most of NSAIDs have common features in their chemical structure such as hydrophilic (carboxylic acid or enolic) and lipophilic (aromatic ring, halogen atoms) groups and ehxhibit high affinity in binding with plasma proteins, DNA and RNA. The NSAIDs can be classified according to their chemical structures into several main groups [4] (Table 1)

Table 1

Classification of NSAIDs according to their chemical structure

Class	NSAID
1 Salicylic acid derivatives	Acetylsalicylic acid, salicylic acid, diflunisal
2 Aniline and *p*-aminophenol derivatives	Paracetamol
3 Arylalkanoic acid derivatives	Diclofenac, indomethacin, tolmetin, sulindac
4 Arylpropionic acid derivatives (profens)	Ibuprofen, naproxen, ketoprofen, suprofen, fenoprofen
5 N-Arylanthranilic(fenamic) acid	Mefenamic, flufenamic, tolfenamic, meclofenamic, anthranilic acids
6 Oxicams	Piroxicam, meloxicam, tenoxicam, lornoxicam
7 Sulfonamide	Nimesulide

In 1971 the scientist J.R. Vane was the first who proposed the mechanism of action of NSAIDs, which is based on inhibition of prostaglandin biosynthesis [5]. Since then, there has

been intense interest in the interactions between this diverse group of inhibitors and the enzyme known as cyclooxygenase (COX or PGH2 synthase), which exists in two isoforms COX-1 and COX-2. In 1994 the study of the X-ray crystal structure of the membrane protein prostaglandin H2 synthase-1 by scientists D. Picot and his colleagues allowed to determine the three-dimensional structure of COX-1, thereby providing a new understanding for the actions of COX inhibitors [6]. Later it has been proven that most NSAIDs non-selectively inhibit both COX-1 and COX-2 [7] and also lipoxygenase (LOX) [8]. As a consequence, it has been shown beyond doubt that the anti-inflammatory actions of NSAIDs arise from the inhibition of COX-2 because COX-2 is induced by inflammatory stimuli and by cytokines in migratory and other cells, while the ulcerogenic side effects (irritation of the stomach lining and toxic effects on the kidney) arise from inhibition of the constitutive enzyme, COX-1 [9]. Among NSAIDs aspirin, indomethacin and ibuprofen are much less active against COX-2 than against COX-1 and cause the most damage to the stomach [10]. In contrast, meloxicam is a new potent NSAID with the best activity relatively to the COX-2:COX-1 ratio as 1:5 and a minimal damaging effects on the gastrointestinal tract in comparison to aspirin with a ratio 1:150 [11]. Therefore, the identification of selective inhibitors of COX-1 and COX-2 will not only provide an opportunity to test the hypothesis that the anti-inflammatory (therapeutic) effects of NSAIDs are attributed to inhibition of COX-2, but also lead to advances in the therapy of inflammation. In this way, the selective inhibition of COX-2 is a promising drug target in the cancer treatment because the isoform of this protein is overexpressed in many human tumors cells [12], but not the surrounding healthy cells [13].

Besides the COX-dependent mechanism, it has been reported that some NSAIDs participate in calcium-mediated intracellular response, suppression of free radicals and superoxide, downregulation of the production of IL-1, and inhibition of chemotaxis [14]. For example, inhibition of superoxide production by NSAIDs was reported in the study of infection caused by bacteria. In this way, the authors C. Gunaydin and S.S. Bilge from the University School of Medicine (Turkey) proposed to look for more innovative molecular methods for solving the problems of cellular pathways modulation and interaction of NSAIDs with multiple targets to learn more about their COX-independent mechanisms [15]. In particular, NSAIDs can exert activation of mitochondrial oxidative stress (MOS) through the electron leakage via partial reduction of molecular oxygen to form the membrane impermeable superoxide, $O_2^{\cdot -}$, and its immediate conversion to H_2O_2 by the mitochondrial superoxide dismutase (SOD) as a protective response against oxidative stress (Figure 1) [16].The membrane permeable H_2O_2 escapes the mitochondria before subsequent neutralization and causes oxidative damage to cellular macromolecules including DNA, protein, lipids and carbohydrates, rendering them functionally inactive. While inside mitochondria, $O_2^{\cdot -}$ damages various Fe-S cluster proteins including

aconitase and cytochrome c, leading to Fe^{2+} release which in turn reacts with H_2O_2 via Fenton reaction to produce hydroxyl radical ($^{\cdot}OH$), the most damaging ROS [17]. All these events perturb the cellular redox homeostasis leading to the activation of intrinsic pathway of apoptosis. Therefore the major target of NSAIDs is mitochondrial electron transport chain (ETC) complex I. Among NSAIDs diclofenac has been found to be most potent in inhibition of ETC complex I activity, thereby leading to electron leakage from the respiratory chain. Other cytotoxic actions of NSAIDs also include arrested cell proliferation, activation of multiple death pathways including extrinsic apoptosis, increase of the sensitivity of cancer cells to apoptosis while overcoming chemo and radioresistance along with inhibiting tumor-associated angiogenesis.

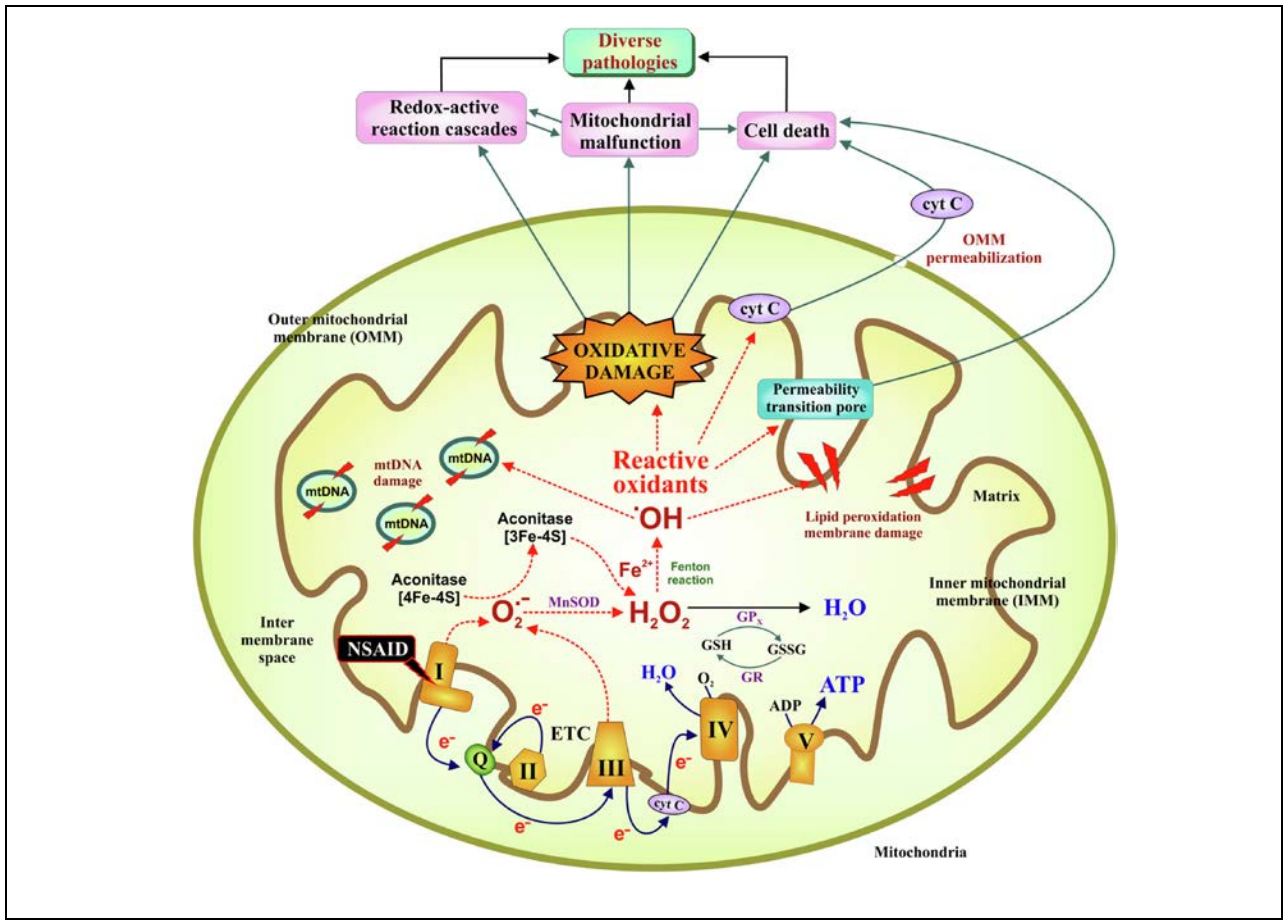

Figure 1. – The illustrated scheme showing an overview of NSAID-induced mitochondrial reactive oxidants production leading to cellular pathology, adapted from ref. [16].

Besides reported COX-dependent NSAID cytotoxicity in the gastric mucosa, the pathophysiology of NSAID-induced mucosal injury in stomach and small intestine can be

explained by the ‘ion trapping symmetry’ [18]. According to this theory it is proposed that the acidic pH of the gastric lumen facilitates passive cellular diffusion of the non-ionized, lipid soluble NSAIDs followed by re-conversion into ionized and lipophobic form within the neutral cytosolic pH of the gastric mucosal cell where they are assumed to induce subsequent toxicity. This theory has not been questioned for many years, but recent research has shown that suppression of gastric acid secretion and neutralization of luminal acidity can cause severe complications and alter intestinal microbiome composition [19,20]. On the other hand, the suppressive, protective and anti-inflammatory effects of NSAIDs as drugs against cancer and neurodegenerative diseases can be ascribed to their antioxidant properties via neutralization of the destructive free hydroxyl radicals and radical mediated neurotoxicity. In particular, it has been shown that the scavenging of hydroxyl radicals by aspirin, ibuprofen and naproxen can delay the onset and slow the progression of Alzheimer's disease [21].

Molecular approaches may further enhance our understanding of the pathological pathways, improve the identification of risks, and aid in the design of novel treatment strategies. In this way, one of the successful strategies is related to the addition of metal ions to NSAIDs in order to modulate the bioavailability of these drugs to various biomolecules in cells. Most NSAIDs are anionic at physiological pH, and metal ion complexation can change the electronic molecular structure of NSAIDs to be able to interfere with the biological pathways of the cell, thereby causing either the enhancement or inhibition of their growth.

Properties of metallo-NSAIDs complexes

It has been established that the modification of NSAIDs with metal ions significantly improves the effectiveness of NSAIDs due to an energetically more favorable change in their electronic molecular structure. Metals have been used in medicine for many years, and drugs based on them have successfully passed clinical trials and some of them are now approved by the ministries of health in many countries [22]. With a fundamental understanding of how organometallic drugs interact with cellular targets at the atomic level, it is a growing need to identify factors that affect their action and efficacy [23]. Nowadays, the effectiveness of organometallic drugs is explained by the variety of molecular structures of the ligand, coordinated around the central metal ion through complexation. Such organometallic drug complexes manifest their action by modifying or replacing the ligand, which leads to a change in their thermodynamics and kinetics of interaction with biomolecules [24]. The acceleration of thermodynamic and kinetic biological processes with the participation of organometallic drug complexes is determined by the physicochemical characteristics of the metal complex and the oxidation states of the metal, which promotes interaction with biomolecules through controlled redox reactions. However, often in such reactions, the lack of bioavailability of organometallic

drug complexes and their low selectivity for different proteins leads to systemic toxicity and serious side effects caused by metal ions.

Many NSAID metal complexes can mimic the action of the superoxide dismutase (SOD) enzyme, which accelerates the disproportionation of the superoxide radical into ordinary molecular oxygen (O_2) and hydrogen peroxide (H_2O_2) in various inflammation processes. It has been established that the binary metal complex of NSAIDS (e.g. naproxen) exhibits improved catalytic properties in the oxidation of catechols to quinones due to a more efficient imitation of the SOD of the enzyme due to its low molecular weight relative to the enzyme itself.

A great contribution to the development of NSAID metal complexes with improved antioxidant and anticancer properties was made by prof. N. Davies (University of Alberta, Canada) [25-27]. He and his colleagues extensively studied the cytotoxicity effects of many NSAIDs and defined the conditions of the gastrointestinal toxicity, anti-inflammatory activity, and SOD activity of their complexes with copper and zinc [28]. In his research, prof. Davies posed the question about the origins of ani-inflammatory and gastric-sparing actions of Cu-NSAIDs, which still remain uncertain. According to the opinion of this researcher, the ability of Cu-NSAIDs to influence cellular copper metabolism belongs to the category of controversial statements because relatively little is known about how these metallodrugs ultimately regulate the inflammatory process and/or immune system. Furthermore, little knowledge exists about their pharmacokinetic and biodistribution profile in both humans and animals, stability in biological media and pharmaceutical formulations, or the relative potency/efficacy of the Cu(II) monomeric versus Cu(II) dimeric complexes. As a consequence, no Cu(II) anti-inflammatory drug is currently available for oral human use, although an ethanolic gel-base of Cu-salicylate (Alcusal) is available for topical temporal relief of pain, and inflammation in humans and a Cu(II) dimer of indomethacin with low toxicity is commercially available in Australasia [29], South East Asia and South Africa [30] in a variety of oral pharmaceutical dosage forms for veterinary use.

Significant contribution to determining the antioxidant and anticancer properties of metallo-NSAID complexes has been made by a group of prof. S.K. Hadjikakou (University of Ioannina, Greece). In particular, his research group developed numerous methods of NSAID-Cu, Zn or Ag complexes and revealed binding effects of aspirin-Cu complex [31], enhanced anticancer effects of nimesulide-silver ligands against human breast cancer [32], and efficient wound healing activity of salicylic acid-silver complexes [33] amongst many others. Cu cations are of special choice because they serve as a catalytic component in many enzymes-metalloproteins such as oxidases or hydroxylases, which exhibit oxidative reductase activity, and lysyl oxidase (required for connective tissue) and cytochrome oxidase (electron transport protein) [34]. In inflammation, Cu has been recognized for its role as a co-factor in metabolic

processes involving articular/connective tissue and the immune system and its effect on COX synthesis [35]. The research work of prof. Hadjikakou relied on the findings of prof. Sorenson, being proven by prof. Schubert, who proposed the hypothesis in 1966 that salicylates may deliver Cu to target cells in the body [36]. They also suggested that both monomer and dimer Cu-NSAID complexes may occur for a given NSAID, depending upon the electronic properties of the added solvent. In 1995 Sorenson highlighted the modes of Cu-NSAID complexes including gastric-sparing activities caused by down-regulation (inhibition) of SOD activity. In this way, the stability of Cu-NSAID complexes has been shown to be a critical determinant of their activity and toxicity. Other proposed modes of amelioarated anti-inflammatory function of Cu-NSAID complexes include scavenging of free radicals, the activation of lysyl oxidases (collagen cross-linking enzymes) and NO release [37]. However, whilst NO synthase has been recognized as a mediator of mucosal blood flow, mucus release, repair of mucosal injury, and an inhibitor of neutrophil activation, no significant difference has been reported between the NO synthase activities stimulated by pristine NSAIDs and Cu-NSAIDs, e.g. in case of indomethacin [38].

Another significant contribution in this field of research has been made by prof. D.P. Kessissoglou (Aristotle University of Thessaloniki, Greece) through the development of synthetic models of drug ligands to improve enzymatic activity and determining the relationship between NSAID drug and metal ions to study the processes of antagonism in the body. In particular, Zn-flufenamic acid complexes with enhanced antioxidant activity [39] and Cu-diclofenac complexes with high binding constants to calf-thymus DNA and increased cytotoxicity against HL-60 cells have been developed [40]. Overall, one can deduce that the synthesized Zn-flufenamic acid and Cu-diclofenac complexes exhibit better pharmacological activity than that of free NSAIDs due to possible contributions: 1) an intrinsic high activity of the complex itself, 2) a protection from the enzymatic degradation of the drug once it is firmly linked to a metal center, 3) the modulated hydrophobicity/hydrophilicity of final compound in a manner allowing a better solubility of drug in the biological fluids and 4) changed transport process through the cell membranes, which we can not distinguish at present. As metal ions are connected in several ways with inflammatory diseases, Zn(II) (at 80-200 μmol/L) has been found to inhibit Scl-70/Topoisomerase DNA unwinding enzyme essential for gene transcription and for selective activation of gene clusters required for the coding of dermal collagene [41]. Complexation of metal ions with NSAIDs of carboxylic acid family can be related to hydrophobic neutral molecules, thereby facilitating passage of the complex molecule through the membrane. It is proposed that the weakly apically bound ligands of most of the Cu(II) complexes can easily dissociate and the $O_2^{\cdot -}$ radicals can interact with the metal via the free sites: in this way the SOD-like activity can be rationalized.

The described work highlights the need to develop methods enabling to predict the bioavailability of metal-NSAIDs and ameliorate their selectivity towards cellular targets besides COX-2 enzymes to reduce the systemic toxicity and side effects of pristine NSAIDs. Although metal-NSAID complexes exhibit better cytotoxicity than the parent drugs or cisplatin, their central mechanism of action on the immune and central nervous systems has not been determined yet. In this way, the investigation of the decay of the metal-NSAID complexes and the analysis of the interactions between the metal-contaning fragments and the biomolecules require new approaches to assess the COX-independent antioxidant mechanisms. These opened questions require the research efforts to perform *in vitro* studies of metal-NSAID complexes on biomolecules and cell lines with multiple tests for activity, toxicity and ˙OH radical scavenging modulation to define those mechanisms. Of course, studies in this field of research mandate a high level of interdisciplinary effort, but there is ample opportunity for even small research groups oriented toward nanomedicine through the development of new advanced functional nanomaterials with precisely defined orthogonal bioavailability and selectivity to biomolecules.

Strategies to improve the bioavailability and selectivity of organometallic drugs

The required properties of bioavailability and selectivity of organometallic drug complexes can be qualitatively improved by objects on the nanoscale. One of these nano-objects is oxygen-containing graphene, which is used in the processes of absorption, transfer and targeted drug delivery due to its large effective surface area and variety of functional groups. The most important advantages of graphene oxide (GO, the highest oxidation state of graphene) are its biocompatibility and degradation properties, when interacting with peroxidase, which indicates its potential application in pharmacology. To date, the cytotoxicity and activity of oxygen-containing graphene in initiating inflammatory biochemical processes has been well studied depending on its size, morphology, surface composition, and colloidal stability. However, little knowledge has been acquired about metal-NSAID complexes of oxygen-containing graphene.

Unlike many methods of engineering nanoparticles based on metal oxides and graphene used in nanomedicine (e.g. hydrolysis, precipitation, thermal synthesis, self-assembly, etc.), the high-tech ultrasound method makes it possible to form functional nanomaterials with improved properties at a much lower cost, related to the amount of substance, time and process of synthesis. It is about the possibility of applying a new ultrasonic technique being based on the formation of free radicals and their products involved in redox reactions when interacting with gas bubbles formed in acoustic cavitation. In this case, unique conditions are formed for the synthesis of both organic and inorganic materials (metals, their oxides and various composites), as well as for the controlled modification of a substance on the nanoscale. The main advantage of ultrasonic technology is the creation of exceptional conditions for the production of functional

nanomaterials with improved properties based on the modification of existing components, which significantly reduces expenses and the cost of the final product. In general, the acoustic cavitation technology is highly efficient, easy and affordable to maintain an ultrasonic device (does not require high temperatures and pressure, specially trained personnel).

Although metal-NSAID complexes exhibit better cytotoxicity than the parent NSAIDs or cisplatin, their central mechanism of action on the immune and central nervous systems has not been determined yet. The hypothesis of the tight relation of antioxidant properties of metal-NSAID complexes and their anticancer activities (apoptosis, ROS modulation, inhibition of cellular proliferation, mitochondrial functions, etc.) through the mimickry of the enzymatic activity and their regulation processes has not been proven yet. The proposed hypothesis of metal ion activation of pristine NSAIDs resulting in precisely defined electron molecular structure of final metal-NSAID complexes with ameliorated functions modulated by ultrasound requires new knowledge and multidisciplinary research efforts. Moreover, the work highlights the need for new approaches to solve the problems of controlled hydrophilicity/hydrophobicity and bioavailability through the formation metal-NSAID complexes at the contact with inorganic allotropic forms of carbon at the atomic and molecular level in the aquatic environment. Therefore, the problems of the relationship between the parameters of acoustic cavitation and the properties of metal graphene nanomaterials with the original NSAID drugs remain open for research. In this regard, the hypothesis of ultrasonic formation of such nanomaterials has not been presented and the role of oxygen-containing graphene in them upon contact with metals has not been determined yet.

The current state of affairs in the fields of research of NSAIDs and their metal ion complexes, ultrasound and nanomaterials based on GO prompted the authors to write an in-depth monographic study on the topic of formation of nonsteroidal anti-inflammatory drugs with metallographene structure and improved electrokinetic properties. High state standards of scientific activity in these research fields confirm the relevance of the topic chosen by the authors. The present work highlights the need to develop new approaches for rationalized functionalization of NSAIDs *per se* at the contact with oxidized metallographene structure through the metal ion complexation in the sonochemical redox reactions. In this context, we would like a reader to gain a deeper insight into the main principles of Cu-, Fe or Zn-based GO nanoplatform formation and ultrasonic complexation with some pristine NSAIDs such as ketorolac, diclofenac, acetylsalicylic and salicylic acids. As a result, we hope that a reader will obtain useful knowledge about interesting properties and functions of these potential pharmaceutical nanomaterials bearing the metal oxide-GO-NSAID structure.

CHAPTER 1 FORMATION OF PHOTOLUMINESCENT $CuS/Cu_2O/CuO$-GRAPHENE OXIDE NANOPLATFORMS

Biocompatible and biodegradable photoluminescent nanomaterials are highly required in nanomedicine, cell imaging and in chemo/biosensing applications especially in cancer diagnostics, imaging and treatment [1]. Among them SiO_2 has been successfully employed as nanoscale carriers and biomolecular transport agents due to its monodispersity, higher specific surface area, controllable pore size and diameter, and versatile functionalization [2]. Incorporation of metals, metal or non-metal oxides, polymers, etc. into the SiO_2 network results in new hybrid nanomaterials with highly reproducible and advanced photocatalytic properties.

The combination of SiO_2 with GO paves the way for hybrid properties of both substances such as improved interfacial contact, advanced conducting pathways and suppression of charge recombination [3]. GO especially stands out because of its dispersibility in aqueous medium due to the sp^3-hybridized carbons enriched with hydroxyl and epoxy/carboxyl functional groups arranged on the top and bottom of its surface. Hydrogen bonds may appear between the GO layers due to the presence of sp^2-hybridized carbons with carbonyl and carboxyl functional groups in the sheet and on the edges. However, pristine GO is a poor light emitter as its functional groups usually induce the nonradiative recombination by the transfer of their electrons to the holes present in sp^2 clusters producing localized electron−hole (e-h) pairs. Ultrasonic technique, which is based on acoustic cavitation [4], can be used for oxygen removal and cause reduction of GO leading to the recovery of its electrical conductivity, thereby improving its photoluminescent efficiency. Therefore, novel hybrid nanomaterials based on rGO/CuS, rGO/Cu_2O and CuO can significantly improve photocatalytic [5] and catalytic [6], selective sensing [7] and optoelectronic [8] properties, which make them useful in electronics, imaging and drug delivery applications [9].

1.1 Properties of synthesized graphene oxide

We synthesized water soluble GO nanoparticles using the improved Hummers method proposed by Tour [10] by applying a horn-type ultrasonic dispergator N.4-20 (Cavitation Inc., Belarus) after calibration performed according to the method of calorimetry [11] (Figure 1a). The formation of GO was confirmed by the appearance of an absorption peak at 237 nm with a shoulder near 295 nm, indicating the π–π^* transition of aromatic C=C bonds and the n–π^* transition of C=O bonds, in agreement with literature [12] (Figure 1b). Synthesized GO consists of carbon with 37.2 at.% lower amount than the bulk graphite material, but with increased on 35.9 at.% concentration of oxygen due to carbon oxidation (Tables 1,2, Figure 2).

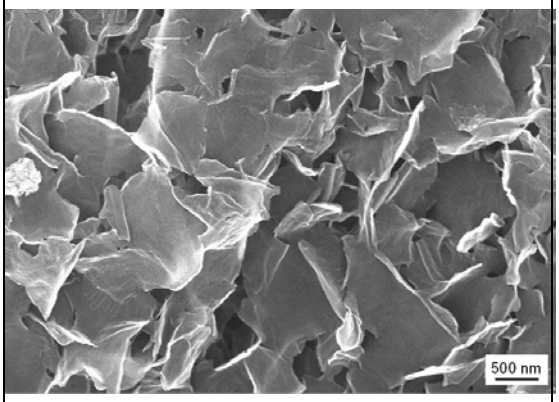

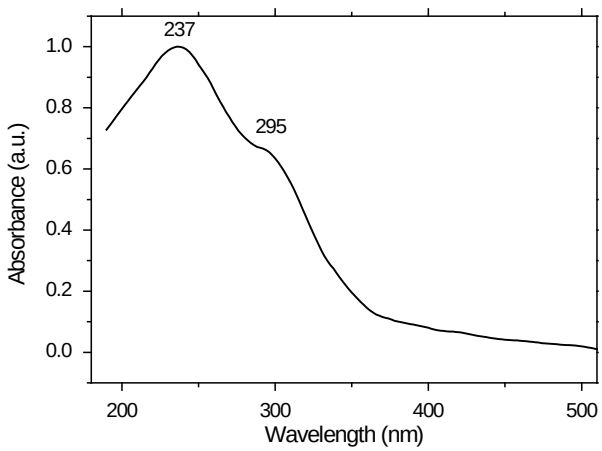

a b

a – prepared pristine GO powder; b – aqueous colloidal solution of synthesized GO

Figure 1. – Representative SEM image and UV-Vis absorption spectrum of synthesized pristine GO

Table 1

Elemental composition of original bulk graphite material obtained from the EDX spectra

Element	**Atomic number**	**Atom. C, at.%**
C	6	95.9±10.0
O	8	3.7±0.8

The bulk graphite material also contains some impurities such as Ca, Ti and Mn at <1 at.%.

Table 2

Elemental composition of synthesized GO nanosheets obtained from the EDX spectra

Element	**Atomic number**	**Atom. C, at.%**
C	6	58.7±5.6
O	8	39.6±5.2
S	16	1.3±0.1

The synthesized GO has some impurities such as P, Cl, K, Ca and Mn at <1 at.%.

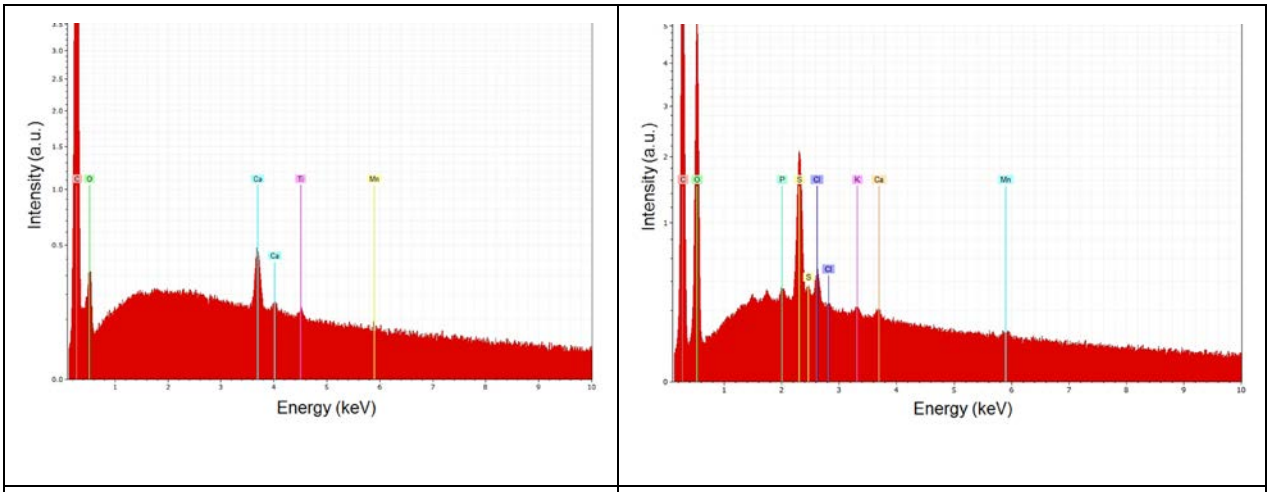

a	b

a – original bulk graphite material; b – synthesized GO

Figure 2. – Energy dispersive X-ray (EDX) fluorescent spectra of original bulk graphite material and synthesized GO nanosheets measured on Si wafers

Surface molecular structure of synthesized GO

Raman scattering spectra of graphite material and synthesized GO are shown in Figure 3. In general, Raman scattering is a process related to photo-excited electron–hole pairs, phonon scattering by electrons or holes, and electron–hole recombination, which determine the band structure of a material. Analysis of Raman spectrum of graphite reveals the characteristic D band at ~1331 cm^{-1}, indicating the significant fraction of the diamond phase with the sp^3-hybridization with T_{2g} zone center mode [13], G band at ~1576 cm^{-1} due to highly ordered graphite with small crystal sizes [14] and a secondary order peak 2D at ~2660 cm^{-1} (Figure 3a). The peaks of D and G bands in the Raman spectrum of GO are upshifted on ~31 cm^{-1} and ~23 cm^{-1} because isolated double bonds resonate at higher frequencies than in graphite [15] (Figure 3b). The G mode has E_{2g} symmetry with an eigenvector involving the in-plane bond-stretching motion of pairs of C atoms with the sp^2 hybridization. This mode does not require the presence of hexagonal aromatic rings and occurs at all C atom sites with sp^2 hybridization. The peak position of G mode is sensitive to external perturbations such as defects, doping, strain, and temperature [16]. Therefore the upshifted G peak position at ~1599 cm^{-1} is indicative of the phonon quantum confinement effect induced by the small domain size in GO. This G mode can be ascribed to the symmetric doping of physically adsorbed solvent molecules on the GO surface with no net electric field between the oxygenated graphene layers. The D mode has K-point phonons of A_{1g} symmetry and is forbidden in perfect graphite, but becomes active in the presence of disorder,

which makes it dispersive upon variation of photon excitation energy. In contrast to G band, the intensity of D band is strictly connected to the presence of hexagonal aromatic rings and is increased in nanocrystalline graphite containing small aromatic clusters. The intensity ratio of D to G bands I(D)/I(G) of graphite (~0.273) is lower than of GO (~0.975), demonstrating the decreasing amorphization of final GO product and increasing number and clustering of aromatic rings. In contrast to graphite, the development of D band in GO is caused by disordering of graphite fraction and ordering of the amorphous carbon content. As a result the stronger and broader D band of GO together with higher I(D)/I(G) ratio confirm the GO's lattice distortions and a large amount of sp^3-like defects caused by the oxidation process.

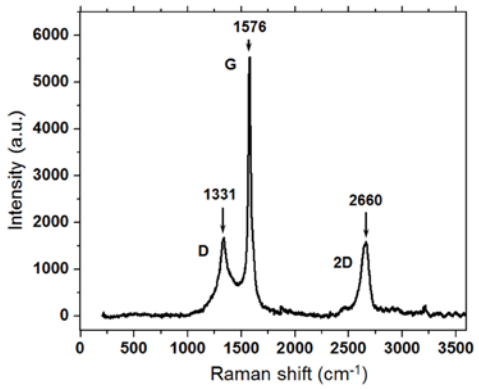

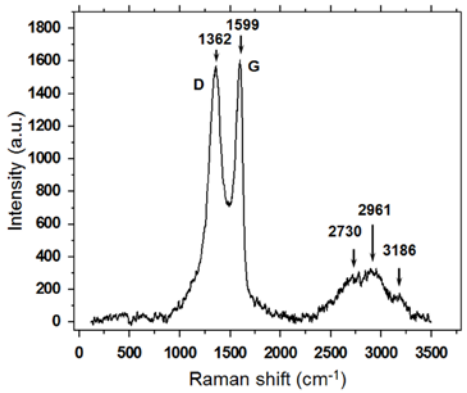

a | b

a –graphite after 4 h of grinding by balls with 3 mm diameter; b – synthesized GO

Figure 3. – Raman spectra of grinded graphite and synthesized GO powders (λ_{exc}=633 nm, 40x objective, 60 s accumulation)

The secondary order 2D peaks of graphite and GO (~2730 cm^{-1}) arise from the overtone of TO phonons around the K point being activated by triple resonance Raman scattering (TRRS). This band is more dispersive in GO than in graphite, indicating stronger effects of a Kohn anomaly at the K point [17] sensitive to the defect formation. In contrast to graphite, the {D+G} band of GO at ~2961 cm^{-1} arises from the overtone of LO phonons around the G point, which is also activated by TRRS due to defect formation because of the broken translational symmetry. The defect formation can be caused by chemical doping resulting in either surface transfer doping (doesn't destroy the chemical bonds of graphene) or substitutional doping (heteroatoms such as N, B, S replace the carbon atoms in the skeleton and break the structure of graphene).

The defects induced by doping are generally the active centers in graphene for the surface chemical reaction involving adsorbed OH molecules. Adsorbed water vapor on the GO's surface can induce the p-type doping.

The crystalline structure of synthesized GO

The crystalline structure of synthesized GO was studied by the X-ray powder diffraction method in comparison with the oxidized graphite obtained without pretreatment of precursor compounds (Figure 4, Table 3). The XRD diffractogram of oxidized graphite shows a strong peak at 2θ=30.63° ($\lambda K_{\alpha 1}$ (Co) = 1,79 Å) and two smaller peaks at 2θ=22.34° and 41.59° (Figure 4a) with calculated interplanar spacing values listed in Table 3.

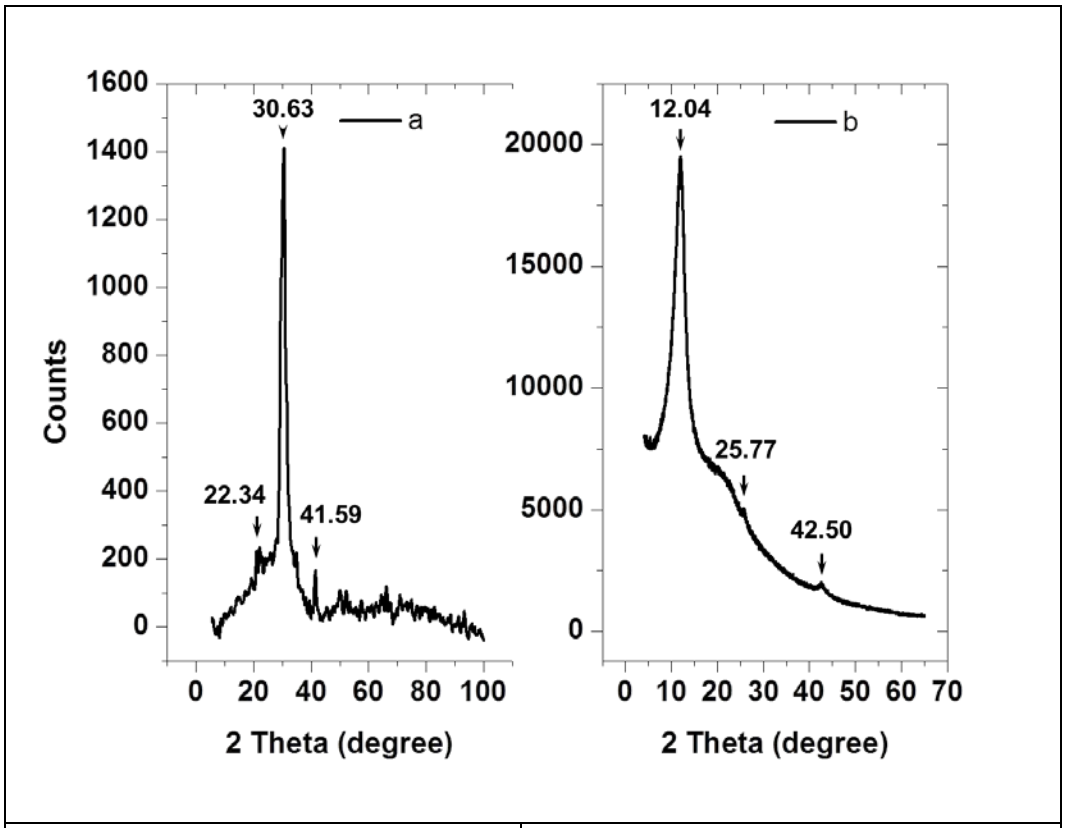

a	b

a – oxidized graphite without pretreatment of precursor compounds; b – synthesized GO

Figure 4. – X-ray powder diffraction patterns of synthesized oxidized graphite ($\lambda K_{\alpha 1}$ (Co) = 1,79 Å) and GO ($\lambda K_{\alpha 1}$ (Cu) = 1,54 Å)

During oxidation hydroxyl, carbonyl, epoxy, and peroxy groups can be bonded to the edges of basal planes of the graphite structure, resulting in carbon hydrolyzation and the change from sp^2 to sp^3 bonds. At the same time, H_2O, NO_3^-, or SO_4^{2-} ions can be inserted into the

graphene layer causing an increase in the interlayer spacing of the graphite structure. The calculated interplanar spacing values of oxidized graphite material can be assigned to oxidized graphite with the exfoliated structure (Table 3) and are indicative for reduced GO structure [18].

In contrast, the XRD pattern of synthesized GO reveals the underlying amorphous halo with a strong sharp peak at 2θ=12.04° ($\lambda K_{\alpha 1}$ (Cu) = 1,54 Å) and two little peaks at 2θ=25.77° and 42.50°, which are indicative of the full oxidation of exfoliated graphite (Figure 4b). The interplanar spacing value of the reflex at 25.77° is 3.453Å is comparable to the (002) reflex with d-spacing of a single graphene layer (~0.34 nm) [19]. The broadening of the interplanar d-spacing can be caused by the formation of oxygen-containing functional groups attached on both sides of the graphene sheet and the atomic scale roughness arising from structural defects involving carbon atoms with sp^3 hybridization. Therefore individual graphene oxide sheets can be expected to be thicker than individual pristine graphene sheets. Besides, different molecules can be inserted into the graphite layers during oxidation, which can also expand the intergraphene spacing as indicated by the (201) reflex of graphite with the d-spacing ~2.11Å [20,21]. The interplanar spacing of the reflex at 2θ=12.04° is 7.342Å, which corresponds to the GO, in agreement with literature [22].

Table 3

X-ray powder diffraction analysis of synthesized GO and oxidized graphite

Material	**2θ, °**	**Intensity, a.u.**	**(hkl)**	**d, nm**	**Assignment**
Oxidized graphite	22.34	40	(001)	4.620	Diamond [20]
	30.63	100	(002)	3.389	Graphite [23]
	41.59	45	(020)	2.521	Graphite [23]
GO	12.04	100	-	7.342	GO [22]
	25.77	26	(002)	3.453	Graphene [19]
	42.50	10	(201)	2.125	Graphene [20,21]

The electronic molecular structure of synthesized GO

The optical absorption of GO is dominated by the π-π^* plasmon peaks ~219 nm (5.66 eV), ~240 nm (5.17 eV), ~244 nm (5.08 eV), ~263 nm (4.72 eV) and n-π^* transition at ~283 nm (4.38 eV). Intense peaks at ~219 nm and ~263 nm can be ascribed to the absorption bands of individual conjugated olefins $(\text{-HC=CH-})_2$ and $(\text{-HC=CH-})_3$ of GO (Figure 5).

The decreased intensity of the UV-Vis absorption spectra of synthesized GO can be caused by the conjugative effect of chromophore aggregation [24]. At increased reduction state

of GO the absorption peaks tend to shift to the longer wavelength region. The absorption bands with low intensity are relatively broad because each electronic energy level has multiple vibrational and rotational energy levels associated with it. The elevated underlying continuum of GO' absorption band appears because of the overlap of a large number of the electronic transitions with the close energy spacing of the vibrational levels and rotational sublevels. The intensity distribution is related to the probability of the transition to a given vibrational sublevel, which can be determined using the Franck–Condon principle. At increased rotational and vibrational energies of molecules more absorption bands are added to a single band, thereby leading to the broadening of the absorption peak. However, their contributions to the band broadening are much smaller in comparison to the electronic excitation energy.

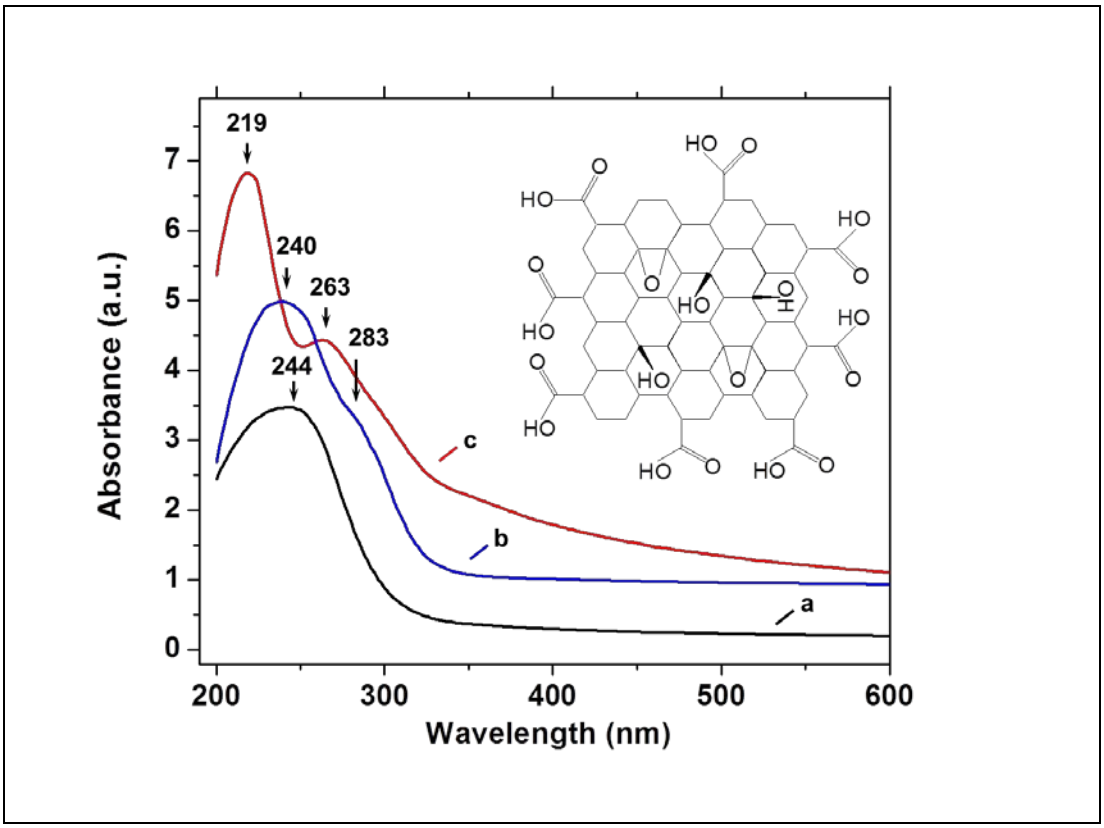

a – synthesized GO at C/O=6.22; b – at C/O=1.83 and c at C/O=1.22.

Figure 5. – UV-Visible absorbance spectra of aqueous colloidal solutions of GO

The π-π^* transition in C=C bonds of GO undergoes a bathochromic shift at ~240 nm and ~244 nm as a result of the reduced structure of GO if compared with the UV-Vis absorption spectrum of graphene with its band at ~270 nm [21]. In addition, the n-π^* transition in epoxide (C-O-C) and peroxide (R-O-O-R) bonds acting as auxochromes of GO at ~283 nm undergoes a

hypsochromic shift, which can be caused by the reduction of the electronic conjugation increasing the HOMO and LUMO away in unshared (nonbonding) electron pairs such as OH, in agreement with the formation of reduced GO structure. The *n* electrons in a GO molecule are highly affected by hydrogen bond formation. The energy levels of *n* electrons decrease significantly in a solvent that has the ability to form hydrogen bonds. The result is an increase in the energy difference between the *n* orbital and the π orbital. This causes a hypsochromic shift in the absorption maximum of an n-π^* transition by as much as 25–50 nm. It can be assumed that the decrease in the energy of *n* electrons is almost equal to the energy of the formed H-bond.

The molecular structure of GO

Analysis of FTIR transmittance spectrum of synthesized GO allowed to assess the molecular structure of final product (Figure 6 and Table 4).

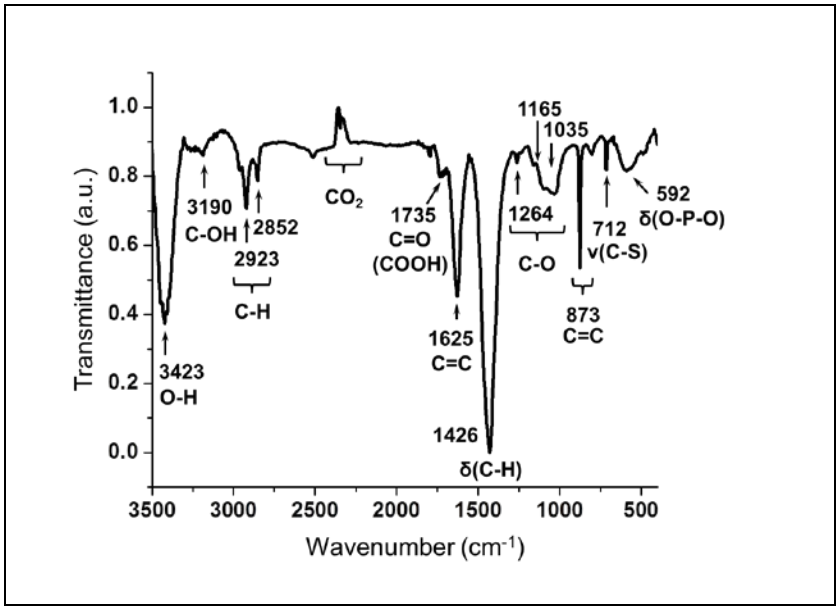

Figure 6. FTIR transmittance spectrum of synthesized GO at C/O=1.22

The synthesized GO is composed of abundant of oxygen functional groups including epoxide, carboxyl and hydroxyl, which are conjugated to the graphitic domains with adsorbed water molecules. The GO structure contains intercalated S and P atoms as revealed by the appearance of weak peaks at ~712 cm^{-1} due to $_{\nu}$(C-S) and at ~873 cm^{-1} due to O displacement by P in C-O bonds.

Table 4

FTIR transmittance spectrum analysis of synthesized GO at C/O=1.22

Wavenumber, cm^{-1}	**Assignment**
712	$_{v}$(C-S)[25]
873	O displacement (mode 4) in C-O [26]
1021-1220	C-O stretching and C-O-C of epoxide group [27]
1426	$_{v}(COO^{-})$ symmetric of carboxyl groups [28]
1625	C=C skeletal vibration of oxidized graphitic domains [29,30]
1735	$(C=O)_{carboxy}$ stretching of carboxyl groups [31]
2852	C-H [27]
2923	C-H [27]
3190	C-OH [27]
3423	O-H stretching [27,29,30]

In summary, the GO material can be synthesized by using the improved Hummers method allowing to control the transformation of bulk graphite phase to nanocrystalline oxidized graphene sheets with the electronic molecular structure determined by varying the atomic C/O ratio during ultrasonic treatment.

1.2 Properties of $CuS/Cu_2O/CuO$-GO nanoplatform ultrasonically synthesized at the air/water interface

Morphology and surface molecular structure of $CuS/Cu_2O/CuO$-GO

Analysis of the synthesized material by SEM revealed rough morphology of GO sheets containing nanostructures (Figure 7a,b). The surface molecular structure of synthesized nanoplatform at the conditions of twofold and fivefold increased concentration of copper precursor was assessed by Raman scattering spectroscopy method (Figure 7c). The successful formation of covellite CuS (p-type semiconductor) in the GO structure was confirmed by the appearance of a sharp Raman peak at ~262 cm^{-1} [7]. Raman spectra also revealed the presence of cuprite Cu_2O (~412 cm^{-1}), which is a Bloch p-type semiconductor [6], and the successful formation of Cu bis-μ-oxo dimer [32] in GO nanocomposites due to the appearance of a sharp feature at ~608 cm^{-1}. The formation of $Cu(OH)_2$/Cu is less probable because of the absence of characteristic Raman bands at 298/347/591 cm^{-1} or at 297/344/629 cm^{-1} and 490/523/623 cm^{-1} [33]. Therefore the structure of prepared nanoplatform is presumably composed of $CuS/Cu_2O/CuO$-GO. The observed bands of copper compounds appeared with higher intensity in

nanoplatforms prepared at fivefold higher concentration of copper precursor, demonstrating the pronounced effect of copper ion at the contact with preformed GO structure.

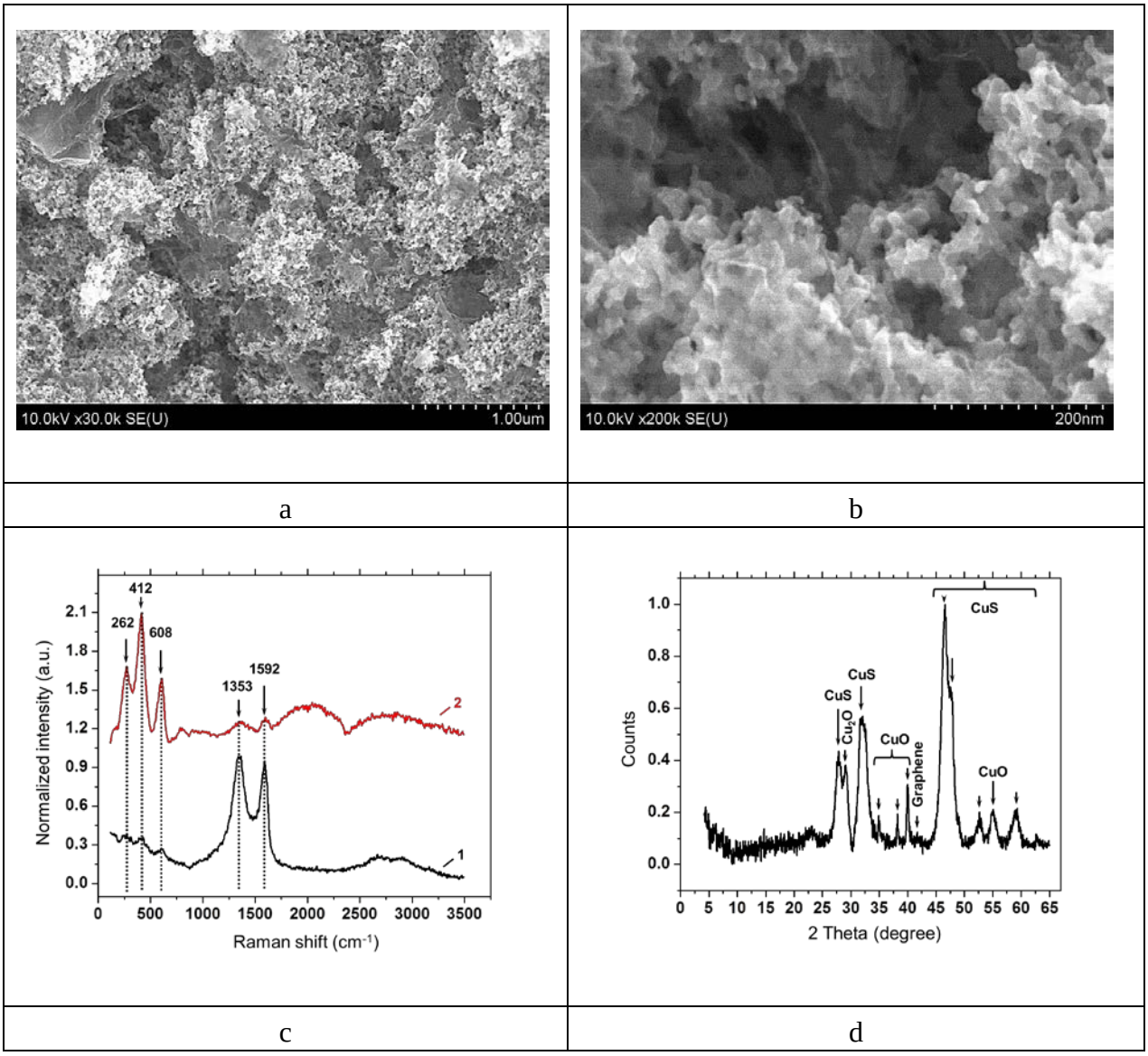

a,b – SEM images of synthesized $CuS/Cu_2O/CuO$-GO nanoplatform (scale bar 1 μm, 200 nm); c – its Raman scattering spectra at twofold (spectrum 1) and fivefold (spectrum 2) increased concentration of copper precursor (λ_{exc}=633 nm); d – X-ray powder diffraction pattern of $CuS/Cu_2O/CuO$-GO nanoplatform at fivefold increased concentration of copper precursor ($\lambda K_{\alpha 1}$ (Cu) = 1,54 Å).

Figure 7. Characterization of morphology, surface molecular structure and phase composition of synthesized $CuS/Cu_2O/CuO$-GO nanoplatform

In addition to these bands, two strong peaks at ~1353 cm^{-1} and ~1592 cm^{-1} appeared in Raman spectra of synthesized nanoplatform, indicating the characteristic D- and G-bands of GO in conjugation with the ultrasonically formed copper compounds. The intensity of these two bands decreases at a fivefold increased concentration of copper precursor, demonstrating that copper compounds in CuS/Cu_2O/CuO-GO selectively act as activation centers in nanoplatform.

Crystalline structure of CuS/Cu_2O/CuO-GO

In Figure 7d the XRD pattern of prepared nanoplatform reveals multiple peaks of tenorite CuO with reflections (002), (111), (200) and (020) (databases amcsd № 0018812 and JCPDS card № 80-1917), of cuprite Cu_2O with (110) plane (database amcsd № 0007351 and JCPDF № 78-2076), of covellite CuS with (101), (103), (110), (107), (108) and (116) planes (database amcsd № 0000065 and JCPDS card № 78-0876), but only small peak from graphene (100), while the reflection (100) of GO disappears, indicating the formation of complexes between carbon and copper without intercalation of water molecules.

The presence of three phases (CuS, Cu_2O and CuO) in individual GO nanoparticles demonstrates the efficiency of the developed ultrasonic method in the preparation of p-type doped semiconductor nanoplatform with advanced charge carrier properties. For example, CuS can provide a significant density of valence-band delocalized holes without the need for intervening metal vacancies in the lattice. However, CuS is reluctant to incorporate cation vacancies due to the high activation energy required for their formation and the slow diffusion coefficient of cations within the lattice [34]. Cu_2O is known to produce water splitting into H_2 and O_2 under the action of visible light [35]. In addition, Cu_2O is intrinsically copper-deficient due to formation of copper vacancies that act as a shallow and efficient hole producers. The defect structure calculations of Cu_2O revealed that hydrogen can form a strongly bound complex with a copper vacancy. This hydrogen prefers not to occupy the center of the vacancy, but to move away from the center closer to one of the two oxygen anions. Small fraction of Cu_2O can be formed by reduction of CuO at fusion temperature of 773 K. Cu_2O is a classic exciton active semiconductor and CuO is known to act as a charge-transfer gap insulator. In this way, the Cu_2O/CuO heterojunction can facilitate the electron-hole separation and significantly improve photo-to-chemical energy conversion efficiency. The enhanced photocatalytic activity can be increased due to the efficient electron transfer in Cu_2O-rGO-CuO via GO as a new and effective electron mediator providing large specific surface area.

The electronic molecular structure of CuS/Cu_2O/CuO-GO

Analysis of UV-Vis absorbance spectra of CuS/Cu_2O/CuO-GO revealed the characteristic π-π^* transition of C=C bonds in aromatic ring of GO at ~230 nm (5.39 eV) at 1.5 times stronger intensity and a hypsochromic shift of a plasmon peak in comparison with GO (~237 nm, 5.23 eV) (Figure 8a). The Zeta potential (ZP) of prepared CuS/Cu_2O/CuO-GO is

slightly lower (-18±9 mV) than the ZP value of synthesized GO nanosheets (-21±7 mV) (Figure 8b). In general, the π-π* plasmon peak depends on two conjugative effects related to the chromophore aggregation: i) nanometer-scale sp^2 clusters and ii) linking chromophore units such as C=C, C=O and C–O bonds. On one side, the change of the UV-Vis absorbance intensity can be explained by a conjugative effect related to chromophore aggregation: higher intensity indicates a few-layer (1-3) of GO and a smaller one – multilayer (4-10) of GO [36,37]. This can indicate that our nanocomposite has a few-layer structure with the thickness of GO sheets increased by the presence of CuS/Cu_2O/CuO-GO, in agreement with the XRD analysis (Figure 7d). On the other side, the hypsochromic shift of the plasmon peak of CuS/Cu_2O/CuO-GO can be explained by the closer conjugation of copper compounds and GO nanosheets resulting in rapid electron transfer and increased transition energy. In addition, a hypsochromic shift can be also caused by introducing Cu vacancies into the CuS lattice resulting in generation of hole carriers. Ideally, a few-layer of GO should exhibit a single strong plasmon peak, but prepared CuS/Cu_2O/CuO-GO has a weak shoulder at ~340 nm (3.64 eV), which is smaller and has a bathochromic shift at 45 nm than a plasmon band of the synthesized GO. This bathochromic shift can be caused by the electronic conjugation within CuS/Cu_2O/CuO-GO nanosheets during the ultrasonic synthesis.

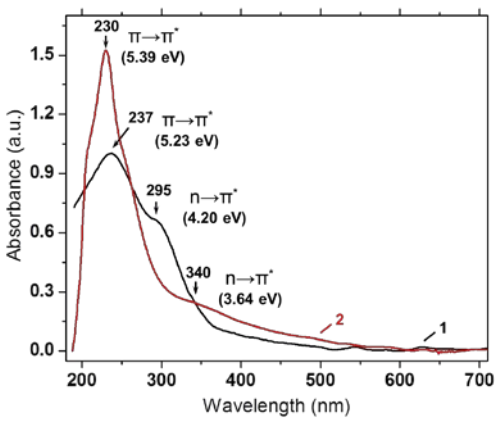

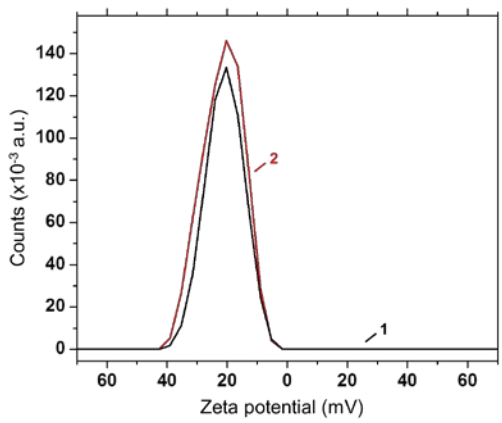

a b

a – UV-Vis absorbance spectra of synthesized GO (1) and CuS/Cu_2O/CuO-GO at fivefold concentration of copper precursor (2); b – Zeta potential plots of these nanomaterials (1 and 2)

Figure 8. Optical absorbance spectra and surface charge of synthesized GO and CuS/Cu_2O/CuO-GO nanoplatform

In general, the electronic absorption spectrum of the $Cu(II)_2$ side-on peroxo-bridged species (*i.e.* Cu bis-μ-oxo) shows intense charge transfer band at 28000 cm^{-1} (3.47 eV), which is assigned as O_2^{2-} π_σ* Cu(II) d_{xy} transition involving transfer of e^- density [36,37]. This charge transfer is indicative of a high degree of Cu-O covalency. A weak plasmon shoulder of our $CuS/Cu_2O/CuO$-GO is related to the charge transfer with the energy of 3.64 eV, indicating an energy increase on 0.17 eV involving O-Cu-O on the surface of GO nanosheets. If one compares plasmon peaks from GO (5.23 eV) and our $CuS/Cu_2O/CuO$-GO nanoplatform (5.39 eV), one can find an increase of the energy on 0.16 eV, which can be explained by the presence of O-Cu-O or sulfide nanostructures on the GO surface.

1.3 Properties of $CuS/Cu_2O/CuO$-GO nanoplatform ultrasonically synthesized at the oil-SiO_2/water interface

Ultrasonic emulsification was performed of a biphasic mixture containing $CuS/Cu_2O/CuO$-GO at the SiO_2:oil interface. Control experiments were carried out by applying ultrasound to the mixture of $CuS/Cu_2O/CuO$-GO and SiO_2 or oil (Figure 9).

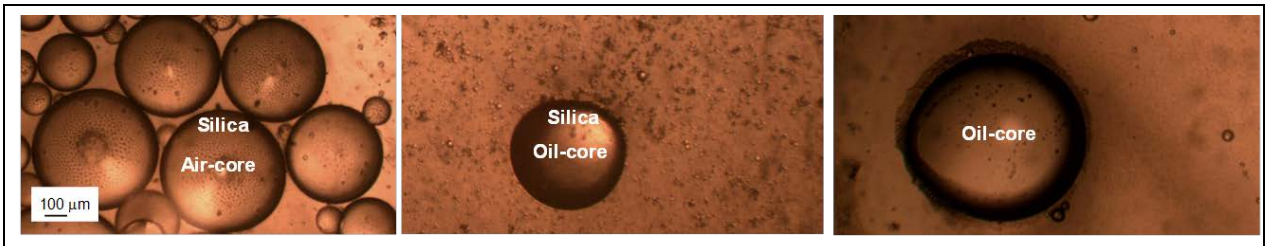

a	b	c

a – microspheres with an air-core and a SiO_2-$CuS/Cu_2O/CuO$-GO-shell structure; b – microspheres with an oil-core and SiO_2-$CuS/Cu_2O/CuO$-GO-shell; c – microspheres with an oil-core and $CuS/Cu_2O/CuO$-GO-shell

Figure 9. Representative optical phase contrast microscopy images of ultrasonically synthesized (20 kHz, 27 W/cm^2 intensity, 3 min of treatment) microspheres with a $CuS/Cu_2O/CuO$-GO-shell and a core (air, oil) prepared at a volume ratio of SiO_2:oil as 1:1 and 5 wt.% polyvinyl alcohol as the aqueous phase

Those microspheres, which were formed by emulsification with SiO_2 (without oil) consisted of encapsulated air and changed their shape upon evaporation under ambient air (Figure 9a). However, they retain their morphology at 100°C and after additional 30 min of ultrasonic treatment at 18 W/cm^2 in water. Most of the sonochemically prepared microspheres were stable colloidal solutions if consisted of encapsulated oil (Figure 9b,c). These oil-filled

microspheres did not change their morphology and avoided coalescence or damage against repeated washing with isopropanol and centrifugation at 3.287xg for 30 min, pointing out that the outer shell may be rigid by its composition.

Air-filled silica@CuS/Cu_2O/CuO-GO microspheres

The mechanism of colloidal stability of CuS/Cu_2O/CuO-GO in microspheres was determined by extending the synthesis at acidic (pH=2) or alkaline (pH=12) conditions of aqueous phase. Analysis of colloids by optical phase contrast microscopy revealed that at low pH of aqueous phase no microspheres were formed and at alkaline conditions they appeared to be larger than those at pH=5.5, but were destroyed during separation from the mother liquor solution. After incubation in aqueous solution at pH=2 or at pH=12 most of preformed microspheres shrinked. Although microspheres were very stable during 7 days before separation from the mother liquor solution, they also shrinked after incubation in deionized water (DI) at pH=5.5. Analysis of the morphology of these microspheres allowed determining small particles of different phase contrast. TEOS undergoes hydrolysis and can condensate in the form of small silica particles acting as nucleation centers during ultrasonic emulsification. The appearance of these small silica nuclei was previously reported in the frame of the proposed ultrasonic clustering model [38]. When microspheres were dispensed on a glass cover slip under ambient air some of them were entrapped in partially crystallized silica on top of them and retained their morphology during evaporation process. Addition of small amount of isopropanol resulted in separation of dried microspheres from the pieces of crystallized silica, but led to the microsphere collapse. When isopropanol was replaced by a drop of DI water (pH=5.5), similar effects were observed. However, when a drop of SiO_2 was added, no visible changes of microspheres were noticed: no separation from crystallized silica, no shrinking and no collapse. The evaporation of the SiO_2 drop resulted in the formation of a microsphere shell with enhanced phase contrast and a transparent core, in agreement with the ultrasonic clustering model. However, this shell developed visible defects, was ruptured and collapsed during evaporation under air.

Oil-filled silica@CuS/Cu_2O/CuO-GO microspheres

The stability of microspheres was significantly improved when oil and polyvinyl alcohol (PVA) were added into the biphasic SiO_2:water mixture containing CuS/Cu_2O/CuO-GO nanoplatform. In the aqueous phase PVA acted as surface active material resulting in the formation of a precursor emulsion system, which consisted of the hydrophobic part pointing towards the core and leaving outer OH^- groups in the bulk aqueous solution. PVA is known to contribute to the formation and stability of colloidal suspension by lowering the interfacial tension, increasing the surface elasticity (viscosity) and electric double layer repulsion, enhancing the tighter packing of hydrophobic groups at the oil/water interface.

The presence of oil in the SiO_2:water mixture or in water was essential for the enhanced stability of these microspheres, in agreement with the previous findings of dodecane or soya bean oil [39,40]. Indeed, without oil (with SiO_2) most microspheres quickly dried and collapsed during evaporation independently on the presence of PVA. In contrast, our sonochemically formed oil-filled microspheres were stable upon drying under ambient air and after 2 h of heating at 100°C, retained their shape and could be dispersed in water without collapse or shrinking. No defects of the microsphere morphology or its damage after heating at 100°C were noticed because the oil-core of microspheres was protected by the densely formed silica@CuS/Cu_2O/CuO-GO composite shell. In addition, no damage of these microspheres was revealed after repeated centrifugation cycles, mechanical shaking and stirring.

Surface molecular composition of microspheres

The surface molecular composition of ultrasonically prepared microspheres was studied by Raman scattering spectroscopy method (Figure 10).

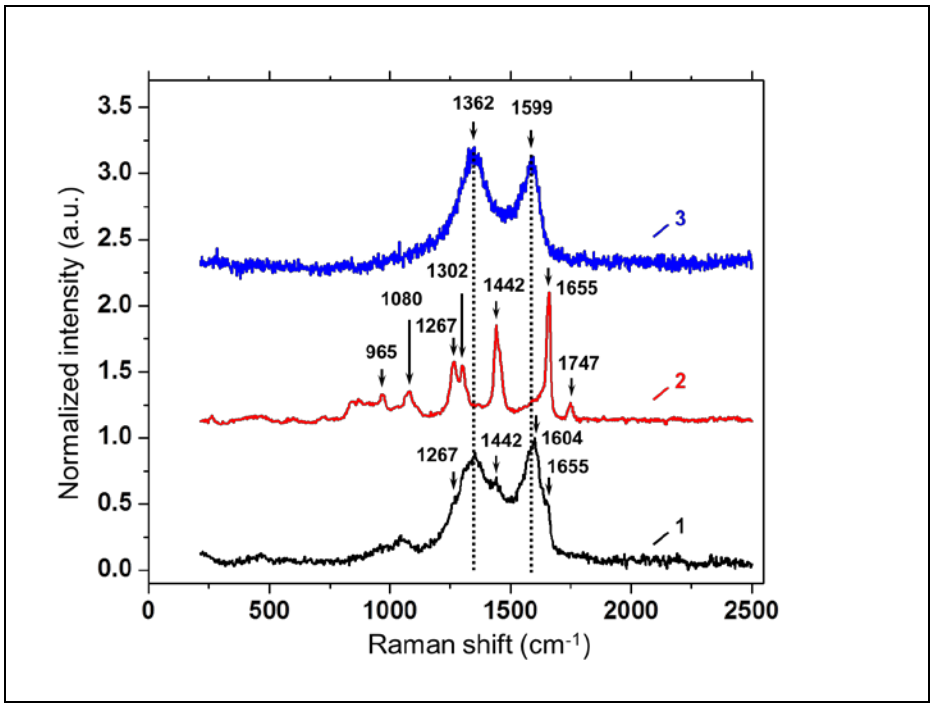

Figure 10. Raman spectra of microspheres with the following composition: 1) oil-SiO_2-CuS/Cu_2O/CuO-GO, 2) oil-SiO_2 and 3) CuS/Cu_2O/CuO-GO acquired at $2x10^{-3}$ W of laser power, λ_{exc}=473 nm, averaged over 5 measurements of each for 1 s of integration time

Raman spectra of oil-filled microspheres containing SiO_2 and CuS/Cu_2O/CuO-GO showed the presence of D band at ~1362 cm^{-1} and a shifted G at ~1604 cm^{-1}, indicating the

presence of GO (Figure 10, spectrum 1). Both peaks appeared with lower intensity than in CuS/Cu_2O/CuO-GO (Figure 10, spectrum 3) and became broader with small peaks nearby at ~1267 cm^{-1} due to oil phase δ(=C-H) and 1442 cm^{-1} due to the presence of liquid $(SiOC_2H_5)_4$, indicating that CuS/Cu_2O/CuO-GO is indeed incorporated into the silica matrix [41]. This silica-CuS/Cu_2O/CuO-GO matrix is in close contact with the oil phase due to the appearance of a weak shoulder at 1655 cm^{-1} arising from the cis double bond stretching of ν(C=C) [42]. For comparison, Raman spectrum of oil-SiO_2 microspheres shows characteristic bands of liquid phases $(SiOC_2H_5)_4$ at ~965 cm^{-1}, 1080 cm^{-1} and 1442 cm^{-1} and oil at 1267 cm^{-1}, 1302 cm^{-1} (=C-H), 1655 cm^{-1} and 1747 cm^{-1} ν(C=O).

Photoluminescence of CuS/Cu_2O/CuO-GO microspheres

Analysis of morphology of ultrasonically synthesized oil-PVA-CuS/Cu_2O/CuO-GO microspheres by optical phase contrast microscopy revealed the color change in their shell from intense green through yellow to red (Figure 11).

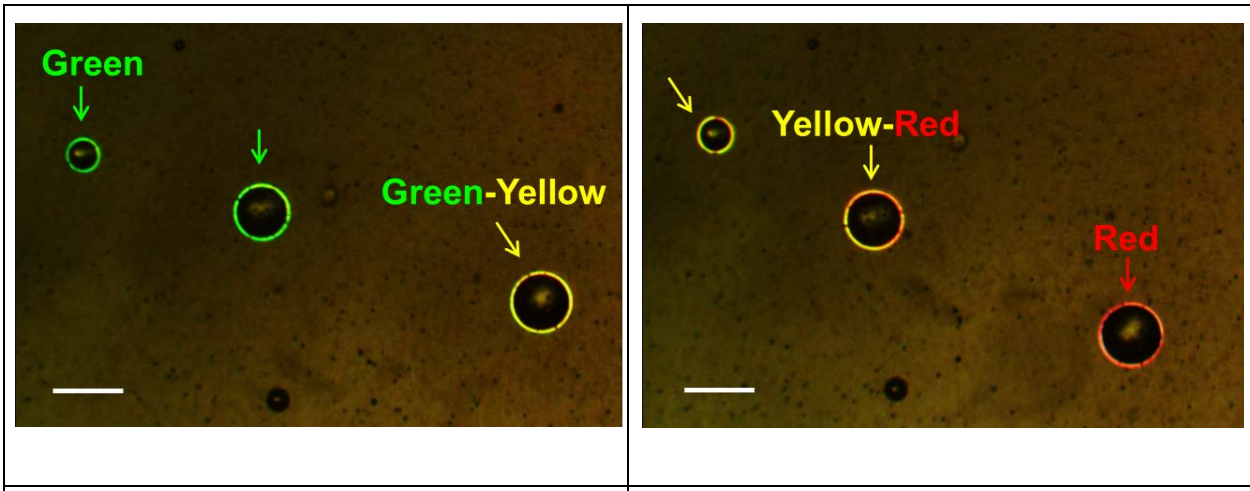

a b

a – green and green-yellow photoluminescent microspheres with an oil-core and a PVA coated CuS/Cu_2O/CuO-GO-shell; b – yellow-red and red photoluminescent microspheres with oil-PVA-CuS/Cu_2O/CuO-GO structure

Figure 11. Representative optical phase contrast microscopy images of ultrasonically synthesized photoluminescent oil-PVA-CuS/Cu_2O/CuO-GO microspheres (scale bar 50 μm)

Not all of microspheres appeared to be highly photoluminescent and we found this optical property to be dependent on pH, the presence of SiO_2 and PVA. At higher pH (5.5 or 12) and without SiO_2 only few oil-PVA/CuS/Cu_2O/CuO-GO microspheres were photoluminescent. No photoluminescence was detected from microspheres at acidic conditions without SiO_2. We

suggest that the hydrophilicity of CuS/Cu_2O/CuO-GO and their interaction with PVA may play a role in the mechanism of photoluminescence. At pH=5.5 CuS/Cu_2O/CuO-GO is amphiphilic and at higher pH it becomes more hydrophilic, facilitating interaction with PVA in the aqueous phase during sonication. In addition, at higher pH photoluminescence can arise due to the electronically excited carboxylate ion of GO [43,44]. However, at low pH CuS/Cu_2O/CuO-GO is more hydrophobic, facilitating the interaction with the oil phase, which may lead to the quenching of photoluminescence.

Very intense photoluminescence appeared from oil-SiO_2-PVA/CuS/Cu_2O/CuO-GO microspheres after 2 h of drying at ~100°C. These microspheres exhibited intense pale yellow color independently on pH. Presumably SiO_2 may lead to the decrease of the oil phase viscosity and facilitate the hydrolysis with CuS/Cu_2O/CuO-GO and PVA during sonication. In this case the hydrophilicity of CuS/Cu_2O/CuO-GO becomes less significant. Thermal treatment of these microspheres may lead to the removal of excess of water from the microsphere's shell containing SiO_2 network, PVA and CuS/Cu_2O/CuO-GO and induce the radiative processes.

However, the highest detectable photoluminescence was observed from oil-PVA/CuS/Cu_2O/CuO-GO microspheres without SiO_2. The most intense colors of their shells were green, yellow and red, while their core remained black during exposure to the visible light. To explain this effect, the role of electrostatic interactions in the formation mechanism of microspheres can be excluded because the surface charge of cavitation bubbles, PVA precursor emulsion and CuS/Cu_2O/CuO-GO nanoplatform is negative. Interaction of PVA with CuS/Cu_2O/CuO-GO may occur via the formation of hydrogen bridges. It was reported that hydrogen bonds can be formed between the hydroxyl groups of PVA and GO due to the supramolecular organization of GO-PVA complex, which is facilitated in acidic medium (pH=4) during prolonged sonication (~2 h) [43]. This PVA-GO hybrid is highly photoluminescent and exhibits intense green light because of passivation by hydrogen bonding. Our ultrasonic synthesis was carried out in aqueous solution at pH=12 and sonication lasted for only 3 min in order to prepare green-light emitting PVA-CuS/Cu_2O/CuO-GO microspheres. In a basic medium CuS/Cu_2O/CuO-GO become more hydrophilic and their interaction with the –OH groups of PVA can be easier during sonication and may lead to the formation of a joint photoluminescent complex at the oil/water interface.

On the other hand, it was reported that Cu_2O exhibits yellowish-red color as a result of light absorption before thermal oxidation under air [35]. However, after thermal oxidation it changes its color to black, indicating the formation of CuO. This color change is reversible as a result of a bilayer structure that is composed of an inner Cu_2O layer and an outer CuO layer with a possible Cu_2O/CuO heterojunction between the two layers. In our PVA-CuS/Cu_2O/CuO-GO microspheres the color of the emitted light reversibly changes from green to yellow and to red

and back to green in each photoluminescent microsphere during exposure to the visible light for several min under air. Therefore the shell of highly photoluminescent microspheres may consist of sonochemically formed PVA-CuS/Cu_2O/CuO-GO complex via H-bonding and the color change is due to the light absorption by Cu_2O avoiding reactive oxidation species (ROS) formation with the CuO acting as a charge transfer insulator.

In this way, the electronic molecular structure of ultrasonically synthesized CuS/Cu_2O/CuO-GO can be used as an versatile nanoplatform for encapsulation and complexation of different NSAID and their interaction with the outer medium can be accurately controlled by oil and PVA phases in analogy with dye molecules as model compounds [45]. Moreover, the CuS/Cu_2O/CuO-GO nanoplatform can be applied as an efficient photoluminescent biosensor enabling controlled targeted delivery of NSAIDs *in vitro* and *in vivo*.

*****

The presented results allow us to draw the following conclusions:

1. The compostion of GO synthesized by the improved Hummers method proposed by Tour can be precisely controlled by the C/O ratio from 6.22 to 1.22 during ultrasonic treatment through the transformation of bulk graphite phase to nanocrystalline oxidized graphene.
2. Ultrasonically formed CuS/Cu_2O/CuO-GO nanoplatforms at the air/water interface are composed of two p-types semiconductors and Cu bis-μ-oxo dimer in nanometer scale sp^2 clusters of GO and linking chromophore units such as C=C, C=O and C-O bonds within electronically conjugated nanosheets.
3. Photoluminescence was discovered from ultrasonically formed oil-PVA-CuS/Cu_2O/CuO-GO microspheres in aqueous medium.
4. The ultrasonic synthesis of highly photoluminescent oil-PVA-CuS/Cu_2O/CuO-GO microspheres requires the basic condition of a reaction aqueous phase solution facilitating interaction of CuS/Cu_2O/CuO-GO with PVA and electronic excitation of carboxylate ions of GO.
5. The reversible color change of oil-PVA-CuS/Cu_2O/CuO-GO microspheres from green through yellow to red can be attributed to the passivation of PVA-GO by hydrogen bonding, light absorption by Cu_2O avoiding reactive oxidation species (ROS) formation and charge transfer insulation by CuO.

CHAPTER 2 FORMATION OF KETOROLAC-COPPER/IRON-GRAPHENE OXIDE NANOPARTICLES

In the last few decades much efforts have been invested into developing of inorganic nanostructures based on GO with controlled morphology, size, crystallinity and functionality. Among them the most studied nanomaterials have been based on the crystal structure of Cu [1], Cu_2O [2] and Fe_3O_4 [3] because they exhibit improved electronic, optical and electrochemical properties. The methodology of chemical functionalization of GO is based on *in situ* crystallization of metals or metal oxides on the surface of GO. One of main advantages of this methodology is the controlled formation of a uniform nanocrystalline coating on the surface of GO through the directed growth of nucleation centers located nearby during the process.

Functionalization of GO can be assessed by applying the chemical reduction methods when exposed to 1) microwave irradiation, 2) electrochemical deposition, 3) electrostatic interaction with aminopropyltrimethoxysilane, 4) hydrolysis of tetraethyl orthosilicate or 5) $FeCl_3$ and 6) redox chemical reactions in aqueous solution of Fe^{2+} and Fe^{3+} with NaOH [4]. Distinctive features of the 1st method are the relative simplicity of the process and material production scalability lacking of accurate uniform nanostructure formation and its distribution on the GO surface. The advantage of the 2nd method is the direct formation of uniform nanostructure on GO, the possibility of applying a nanostructured template on GO and appropriate combination with the sol-gel technology. However, the electrochemical potential of inorganic material limits its application. In 4th-6th methods the synthesis of nanomaterial is versatile being based on redox reactions or hydrolysis followed by crystallization of metal oxide structure on GO.

In these methods sonochemistry especially stands out as one of the efficient tools to construct multifarious molecular GO nanostructures for drug modification, functionalization, delivery and release [5]. Sonochemistry derives from acoustic cavitation, which is the formation, growth and implosive collapse of gaseous bubbles formed by ultrasound, acting as highly energetic hot spots. These hot spots can reach 5000 K and ~10^3 bar in a bulk aqueous solution producing sonolysis of water [6]. Sonolysis of water generates OH· and H· radicals and the primary products such as H_2, H_2O_2 and HO_2· in redox reactions [7]. Sonochemistry is involved in the molecular assembly and encapsulation processes through the cross-linking mechanisms in proteins [8] that retain their biological function. In many cases superoxide (HO_2·) is the principal cross-linking agent [7,9]. To date, this sonochemical pathway has been very successful in the encapsulation of antibiotic nanoparticles in GO [10] that is immaculate or modified with Ag [11], Fe_3O_4 [12], Au [13] and their bimetallic compounds [14]. Nowadays little is known about the sonochemical formation mechanism of copper/iron GO nanostructures and much less about their complexation with NSAIDs.

2.1 Strategies to improve the efficiency of ketorolac

Ketorolac is a synthetic pyrrolizine carboxylic acid derivative with anti-inflammatory, analgesic, and antipyretic activities with efficacy comparable to opioids [15]. Ketorolac's pyrrolizidine carboxylic acid derivative is structurally related to indomethacin acting as cyclooxygenase-2 (COX-2) inhibitor and is involved in the progression of several types of cancer [16]. The anticancer activity of ketorolac can be associated with its free binding energy being closer to DDX3 inhibitors, its capability to form strong hydrogen bonds similar to crystallized DDX3 protein and to inhibit the ATP hydrolysis decreasing the number of neoplastic lesions. Ketorolac also suppresses early breast cancer relapse and improves its postoperative oncological outcome [17]. Ketorolac's anticancer effects and its aptitude to deactivate inflammatory pathways can be particularly useful in retardation of tumor growth [18]. However, in its most frequent form, i.e. the oral tablet, the drug is delivered to the human body through the gastro-intestinal system, which undergoes bleeding and develops gastritis after repeated doses over prolonged administration [19]. In addition, its ability to selectively inhibit COX2 has important cardiovascular side-effects that include increased risk for myocardial infarction, stroke, heart failure and hypertension [20]. Therefore for human health benefits one has to consider appropriate approaches for the administration of ketorolac at a lower dose over shorter period of the systemic exposure while maintaining its therapeutic efficacy.

The anti-inflammatory activity of ketorolac can be enhanced through the metal ion complexation [21] with the carboxylate group operating as a bridging ligand involving Cu-O and Cu-Cu bonds in the complexes undertaking the enzyme superoxide dismutase (SOD) [22]. These neutral binuclear molecules with a high peripheral hydrophobicity can exert a SOD-like activity once the apical positions on Cu(II) are made free, which can be useful in the understanding of the drug-metal and drug-enzyme interactions [23]. Importantly, the copper carboxylates drugs constitute an important element of anti-inflammatory and anticancer agents, some of which are a part of several commercially available drugs [24].

The complexation of many NSAIDs with other metals such as Cd (II), Pt (II), Fe (II), Ni (II) or Zn (II) [21,25] leads to the scavenging of free radicals (incl. oxygen) and results in enhanced gastric protection [26]. This improved pharmacological activity of metal complexes of active drugs as ligands can derive from the synergistic effects of the ligand and the coordination residue upon the decomposition of the molecular metal-NSAID complex or an intrinsic high activity of the complex itself, the neutralization of overall negative charges on the drug molecule upon the complex formation, superior transport process through the cell membranes due to the changes of the hydrophobicity/hydrophilicity ratio. The anti-inflammatory, anti-pyretic and analgesic activity of NSAIDs can be improved through the formation of the Fe(III)-peptide complex yielding the ligand moieties containing oxamide functionality [27]. Other studies show

the antibacterial efficiency of some Fe(III)-NSAID complexes against *Escherichia coli* [28] and *Staphylococcus aureus* due to the ability of the complex to cross a cell membrane and inactivate the pathogens secreting various enzymes, which are involved in the breakdown of activities [29]. Importantly, the Fe(III)-complex can facilitate the ion diffusion through the lipid layer of the spore membrane to the site of action and ultimately kill them by combining with the OH, SO_2 and C=N groups of certain cell enzymes. On the other hand, the metal complex of Fe(II) can be very active against breast cancer cell line (MCF7) with inhibition ratio values between 74-86 %.

Other approaches in minimizing dosage can be based on NSAID encapsulation, which utilize a nanoscale carrier that transports the active drug ingredient and facilitates controlled release at the therapeutic target site [30-32]. This strategy can overcome issues with drug solubility, prevent degradation in the gastrointestinal system, improve bioavailability at the therapeutic site, and reduce systemic exposure. Still a major obstacle of the encapsulation approach is the uptake of nanoscale carriers by macrophages and clearance of the drug [33,34].

One of the successful approaches is to use GO as a nanoscale carrier for ketorolac due to its high surface area, biocompatibility and a very rich surface chemistry offering a wide choice for the smart design of effective delivery nanoplatform [35-39]. GO can remain for a long time in a body and have good biocompatibility, but size, shape, agglomeration state and toxicity (presence of contaminants) can cause undesired inflammation [33, 40]. GO biodegradation can be modulated by dispersion and digestion by peroxidases naturally present in cells. Appropriate GO purification and modification can increase the efficacy of drug loading in GO and optimize adsorption/desorption kinetics at minimal toxicity [41-44]. The rich GO surface chemistry facilitates functionalization with diverse molecular compounds: dyes [45], inorganic[46-48] and organic (DNA [49], ssRNA [50], gene [51]) substances, polymers [52-54], luminescent or fluorescent particles [55,56] enabling synergistic effect of drug delivery and bioimaging [57-60] of a carrier platform. Immobilization with drug molecules can regulate GO dispersal in water or in the cell culture media, reduce its cell/tissue toxicity and induce accumulation to the target cells and tissues [10, 61-63]. Drug release from GO can be activated by the pH gradient naturally present in the cells/tissues through the distortion of the interactions between the drug and GO nanocomposite [53].

2.2 Formation of copper/iron-GO nanoplatform

The successful GO formation was confirmed through the characterization of its physico-chemical properties by using SEM and UV-Vis absorption spectroscopy (Figure 1), Energy dispersive X-ray fluorescence (Figure 2, Tables 1,2), Raman scattering spectroscopy (Figure 3), X-ray powder diffraction (Figure 4, Table 3) and FTIR transmittance spectroscopy (Figure 6, Table 4). Synthesized GO has a broad size distribution of ~ 500 nm (r.s.d. ≈25%) (Figure 1a).

The thermal stability of GO

The thermal stability of synthesized GO was examined during thermal treatment at 600°C at a rate 10°/min under O_2 or N_2 atmosphere via monitoring a substance mass loss as a function of temperature and was compared to the bulk graphite material. Thermogravimetric analysis (TGA) of synthesized GO was conducted to understand the transformation mechanism and phase processes of GO including decarboxylation, oxidation and reduction (Figure 1b).

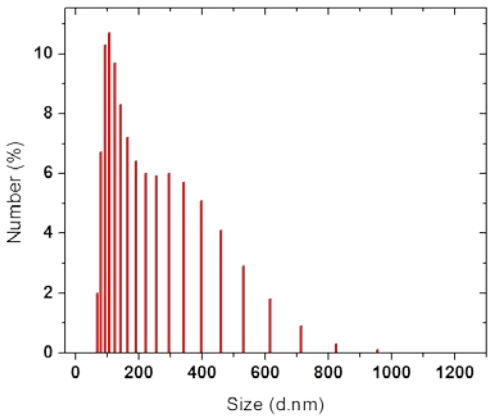

a

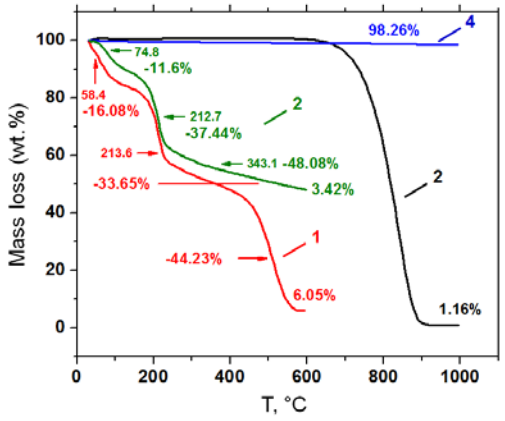

b

a – Size distribution diagram of synthesized GO; b – Thermogravimetric plot of GO and graphite in O_2 or N_2 atmosphere (the color coding presents TGA curves of GO after thermal treatment under O_2 (red line, 1) and N_2 (green line, 3) atmosphere; TGA curves of original bulk graphite after thermal treatment under O_2 (black line, 2) and N_2 (blue line, 4) atmosphere)

Figure 1. Size of synthesized GO and its phase composition during decarboxylation, oxidation and reduction

The mass loss, which was studied under O_2, is attributed to the combustion processes, and under N_2 – to the thermal decomposition of material. Synthesized GO undergoes combustion via a three stage process at ~58.4°C, ~213.6°C and ~599.1°C with the corresponding mass loss of ~16.08%, ~33.65% and ~44.23% leaving 6.05% of the residual mass. In contrast, the TGA curve of bulk graphite material does not exhibit any peak and its residual mass is 1.16%, demonstrating that the bulk graphite is of high quality. The residual mass of GO after combustion is about six times higher than of graphite because of the presence of small impurities such as P (≤0.07±0.01 at.%), S (≤1.31±0.10 at.%), Cl (≤0.18±0.01 at.%), K (≤0.04±0.01 at.%), Ca (≤0.05±0.01 at.%) and Mn (≤0.04 ± 0.01 at.%). At a temperature below ~70°C the structure of GO is retained and this temperature is often used to obtain a dried powder of GO. At ~58.4°C

GO loses ~16.08% of its mass because of the removal of the adsorbed H_2O molecules. A strong vaporization of adsorbed H_2O molecules and a partial exfoliation of GO take place in the higher temperature range from ~140°C to ~180°C. Much larger loss of the GO mass (~33.65% and ~44.23%) occurs below 350°C due to the thermal removal and partial decomposition of oxygen-containing functional groups such as carboxyl, OH, epoxy and carbonyl, [64] and also CO, CO_2 and O_2 release [65]. The critical dissociation temperature of OH groups is about ~650°C and their full removal from the GO plane can occur only above this value, while epoxy groups remain even at ~700°C. In contrast, carboxyl groups tend to be slowly reduced at ~100-150°C, while carbonyl groups are much more stable, and their removal requires much higher temperature (i.e. > 600°C).

The sudden mass loss of GO due to the thermal decomposition can be attributed to the removal of labile oxygen functional groups on plane surface, and ~48.08% of the mass loss at ~343.1°C can designate the CO release under the N_2 atmosphere. At ~400°C carboxyl groups are removed at the edge plane of GO but the carbonyls remain stable. At ~600°C the carbon skeleton undergoes combustion with the release of CO_2 and CO under the O_2 atmosphere. Overall, the following effects are observed: reduction of oxygen concentration and introduction of defects in reduced GO structure. Under N_2 at ~600°C significant mass loss of the synthesized GO may signify the extent of defects in GO, which is mostly associated with the departure of the rest of carbonyl groups, resulting in GO of smaller size with wrinkled morphology [66]. This can be explained by the fact, that the decomposition of oxygen-containing groups also removes carbon atoms from the carbon plane, which splits the graphene sheets into small pieces and causes the distortion of the carbon plane. The thermal exfoliation may cause the structural damage of graphene sheets because of the release of CO_2.

Sonochemical functionalization of GO with Cu(II) and Fe(III)

The main principle of GO functionalization with Cu^{2+} and Fe^{3+} precursor compounds by ultrasound and its subsequent complexation with pristine ketorolac is demonstrated in Figure 2. As a result, Cu/Fe-GO nanoplatform was synthesized at first step and ketorolac-Cu/Fe-GO nanomaterial – at the second step (Appendix 2). The ultrasonic synthesis was extended to the ketorolac-Cu-GO and ketorolac-Fe-GO formation following the proposed principle of nanostructure growth and NSAID complexation.

Figure 3 shows representative SEM images of morphology of the synthesized GO, Cu/Fe-GO, Cu-GO and Fe-GO nanostructures (Figure 3). SEM analysis of nanomaterials revealed the change of GO nanosheets (Figure 3a) into elongated Cu-Fe-GO nanostructure in the shape of smaller grain rice of ~460 nm (r.s.d. ≈3%) (Figure 3b). The GO surface was decorated by spherical nanostructures in Cu-GO nanoplatforms (Figure 3c) and elongated rice-like morphology of ~580 nm (r.s.d. ≈16%) in Fe-GO (Figure 3d).

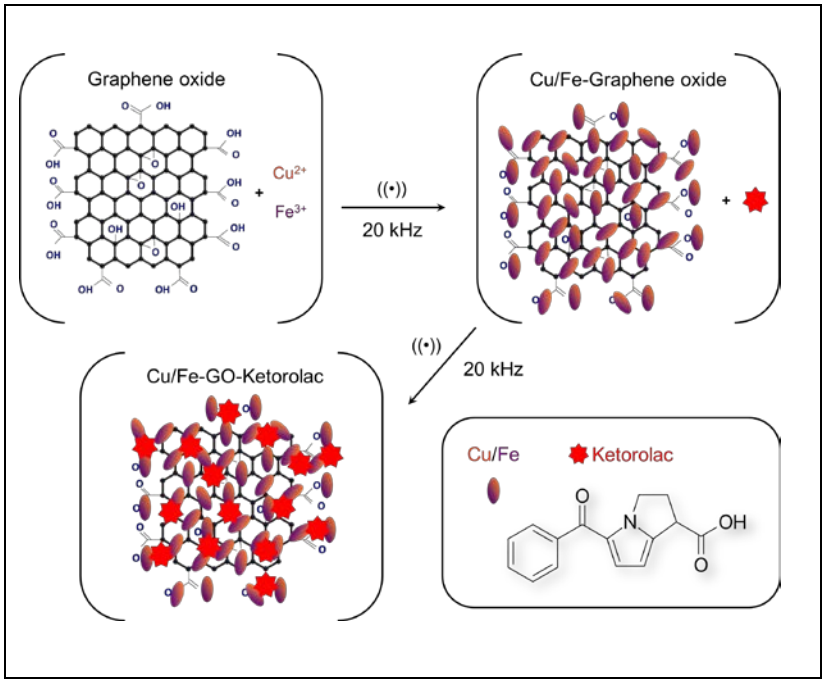

Figure 2. Schematic illustration of the principle of ultrasonic functionalization of synthesized graphene oxide (GO) in aqueous solution containing Cu^{2+} and Fe^{3+} precursor compounds followed by complexation with pristine ketorolac (20 kHz, 18 W/cm^2, 3 min)

These sonochemically formed morphologies are clearly distinct from nanoparticles that were ultrasonically grown on the external walls of sonicated multi-walled carbon nanotubes functionalized with the carboxylic acid groups from our previous studies [67]. In contrast to GO, those erbium carboxioxide nanoparticles appeared with the nonuniform geometry and a broad diameter distribution from 50 nm to 200 nm, the size being comparable to the highly fluorescent polymeric nanoparticles that exhibit the 4.5-fold increase in the quantum efficiency, when compared with the free dye molecules in water [68].

Importantly, the presence of GO leads to the growth of nanoparticles with a more pronounced morphology that has a spherical or elongated rice-like shape than carbon nanotubes being used as template material. On the other hand, ultrasonic treatment with the carbon nanotubes yields smaller nanoparticles than those with GO. Presumably GO provides a larger surface area enriched with higher amount of oxygen containing chemical groups than carbon nanotubes resulting in enhanced nanoparticle's growth with a more defined morphology.

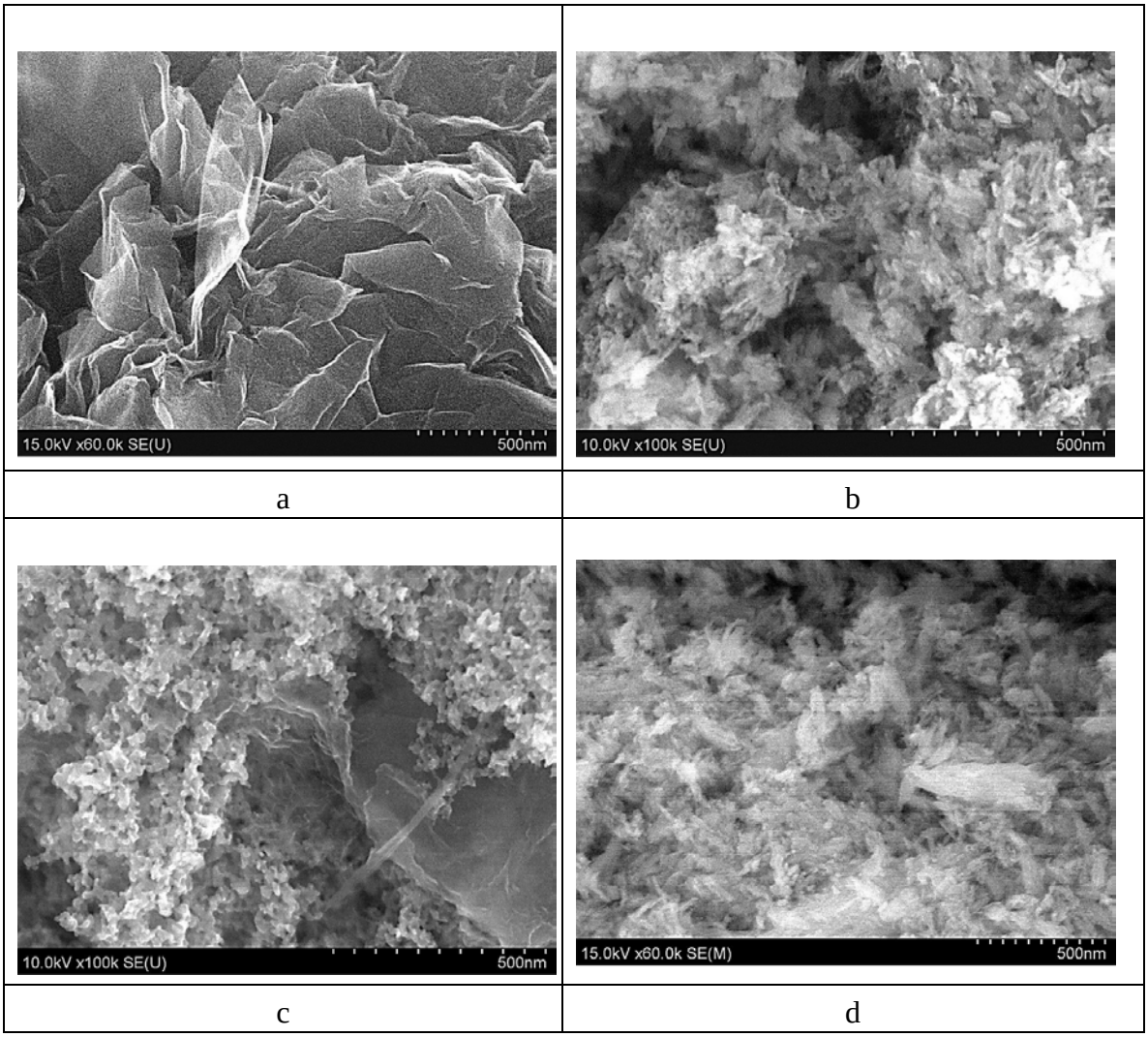

a – synthesized GO; b – Cu/Fe-GO; c – Cu-GO; d – Fe-GO nanostructures

Figure 3. Representative SEM images of GO and ultrasonically synthesized Cu/Fe-GO, Cu-GO and Fe-GO nanoplatforms (20 kHz, 18 W/cm^2 intensity, 3 min of treatment)

The crystalline structure of Cu/Fe-GO nanoplatform

The phase composition of crystalline structure of Cu/Fe-GO nanoplatform was characterized by X-ray powder diffraction in comparison with pristine GO, Fe-GO and Cu-GO (Figure 4). XRD pattern shows the GO phase due to the presence of a characteristic peak at $2\theta=11.9°$ arising from (001) plane, demonstrating that GO has a layered structure and its calculated interplanar spacing is ~0.61 nm (Figure 4a). This strong diffraction peak is relatively broad as a result of very short range atomic coherence. Small XRD peaks of graphene at

2θ=25.8° from (002) plane and 2θ=42.7° from (100) plane infer a loss of coherence between graphene-like layers [ref. 45 Chapter 1].

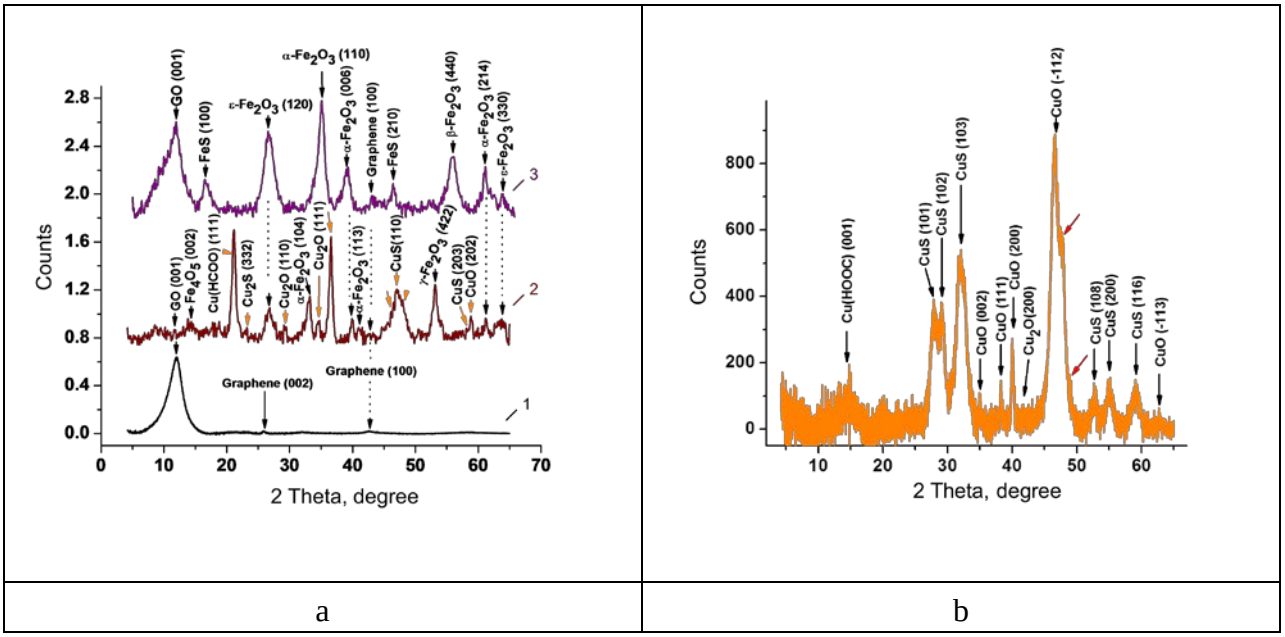

a | b

a – XRD patterns of synthesized GO (1), Cu/Fe-GO (2) and Fe-GO (3) nanoplatforms; b – XRD pattern of Cu-GO nanoplatform

Figure 4. X-ray powder diffraction patterns of GO, Cu/Fe-GO, Cu-GO and Fe-GO nanoplatforms ($\lambda K_{\alpha 1}$ (Cu) = 1,54 Å)

The phase composition of Cu/Fe-GO is complex and consists of characteristic reflections (110) and (111) of cuprite Cu_2O; (202) of tenorite CuO; (104), (110), (006), (113) and (214) of hematite α-Fe_2O_3; (422) of maghemite γ-Fe_2O_3; (120) of ε-Fe_2O_3; (002) of recently discovered Fe_4O_5[69]; (203) and (110) of covellite CuS; (332), (046) and (12 4 2) of Cu_2S and (001) of GO (XRD pattern 2) (Figure 4a). In this nanoplatform the XRD (001) plane of GO is very weak, indicating large range atomic coherence. The relatively larger d-spacing of GO may also indicate the formation of oxygen-containing functional groups in metal oxides in the sonochemically modified GO [70]. Most prominent reflexes appear from (111) Cu(HCOO), (111) Cu_2O, (110) CuS, (104) α-Fe_2O_3 and (422) γ-Fe_2O_3, indicating that synthesized nanoplatform indeed contains copper and iron oxides as well as copper sulfide.

Analysis of EDX spectra reveals that Cu/Fe-GO is composed of C ~35.6 at.%, O ~44.5 at.%, Cu ~1.7 at.%, Fe ~13.8 at.% and S ~2.6 at.% (Figure 5a, Table 1), in agreement with the XRD analysis (Figure 4a). For comparison, GO contains only higher amount of C

~58.7 at.%, but lower concentration of O ~39.5 at.% with the amount of sulfur being twice less than in Cu/Fe-GO.

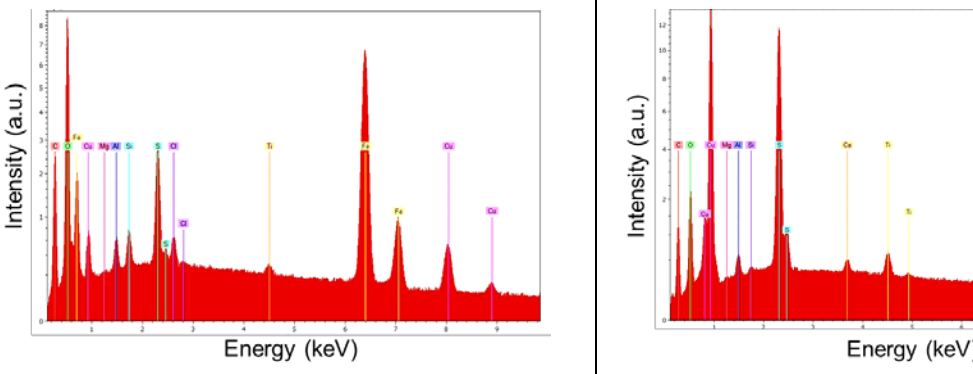

a

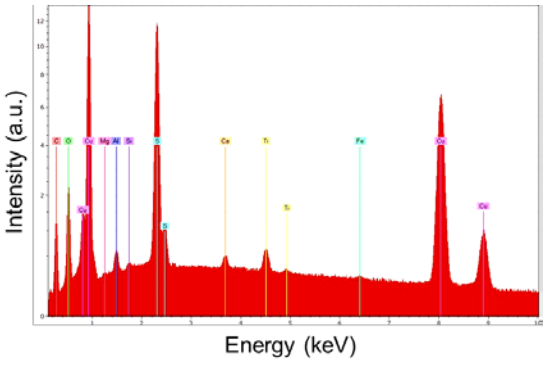

b

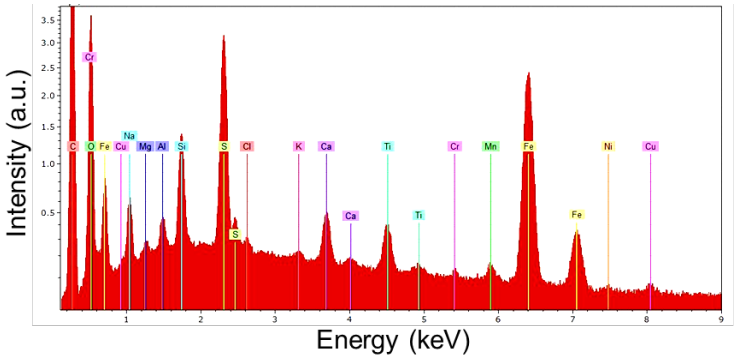

c

a – synthesized Cu/Fe-GO (at U=20.3 kV); b – Cu-GO (at U=20.0 kV); c – Fe-GO (at U=20.0 kV) nanoplatforms

Figure 5. Energy dispersive X-ray fluorescence spectra of Cu/Fe-GO, Cu-GO and Fe-GO

These changes in the elemental composition can be attributed to the ultrasonic defect formation and intercalation of S in the carbon lattice of GO, the sonochemical redox reactions between copper, iron, sulfur and radical species, i.e. hydrogen acting as reductant, hydrogen peroxide, hydroxyl and oxygen acting as oxidants [5-8]. The dominant (111) XRD peak of Cu_2O is relatively sharp, demonstrating the presence of a material larger than 5 nm in Cu/Fe-GO (Figure 4a). Very small (110) peak of Cu_2O may result from nanocrystal partial reduction post synthesis involving diffusion of atoms and lattice expansion process, which may be limited to atom rearrangement and lattice/unit cell reconstruction yielding rich Cu_2O phase (i.e. copper in

oxidized state). We assume that complete transformation of Cu_2O to crystalline CuO does not occur because of the following possible reasons: i) sonochemical reactions involving reductants such as Na_2S and radicals (i.e. $H_2\cdot$) and oxidants (i.e. $OH\cdot$, $H_2O_2\cdot$, $HO_2\cdot$); ii) there is a considerable energetic difference between the *Pn3* group of Cu_2O and monoclinic *C2/c* group of CuO structure; iii) Cu_2O has the high-symmetry cubic and CuO has a low-symmetry monoclinic structure; iv) possible stabilization of the (I) oxidation state by the carbon network of GO and the present Fe^{3+} ions may take place. This carbon network of GO can be ultrasonically doped by S^{2-} due the presence of Na_2S resulting in the formation of reduced S-GO nanostructure, and later CuS synthesis through the sonochemical reduction of Cu(II). Indeed, XRD reveals CuS, Cu_2O and CuO phases in Cu-GO nanoplatform, indicating that Cu(I) phase may be stabilized by the carbon lattice network of GO containing intercalated sulfur as a result of interaction with the sonochemically produced radicals, Cu^{2+} and S^{2-} ions (Figure 4b).

Table 1

Elemental composition of synthesized Cu/Fe-GO, Fe-GO and Cu-GO nanosheets

Sample	**C, at.%**	**O, at.%**	**Cu, at.%**	**Fe, at.%**	**S, at.%**
GO	58.7±5.6	39.5±5.2	-	-	1.3±0.1
Cu/Fe-GO	35.6±2.2	44.5±3.4	1.7±0.2	13.8±0.9	2.6±0.2
Fe-GO	58.5±4.5	29.9±3.1	-	5.6±0.5	2.3±0.2
Cu-GO	33.5±1.6	18.2±1.1	28.2±0.5	-	17.9±0.6

The synthesized GO contains P, Cl, K, Ca and Mn at <1 at.%; Cu/Fe-GO has Mg, Cl and Ti at <1 at.% (Al 0.69 at.% and Si 0.58 at.% arise from the substrate on which the powder of nanoplatforms was placed); Fe-GO has Mg, Cl, K, Ca, Ti, Cr, Mn, Ni and Cu at <1 at.% (Al 0.25 at.% and Si 0.90 at.% arise from the substrate); Cu-GO has Mg, Ca, Ti and Fe at <1 at.% Al 0.91 at.% and Si 0.14 at.% arise from the substrate).

Three crystal structures of Fe_2O_3: γ-ε-α as well as rare Fe_4O_5 phase were revealed in Cu/Fe-GO nanoplatform, showing that the phase transformation may take place depending on the particle size, temperature or pressure during the sonochemical synthesis [71-73]. Most of these XRD peaks are relatively small, but not significantly broadened, denoting the formation of nanoparticles smaller than submicron size, in agreement with the SEM in Figure 3b. The XRD pattern reveals α-Fe_2O_3 (≈80%) as the main phase along with γ-Fe_2O_3 (≈10%), ε-Fe_2O_3 (≈7%) and Fe_4O_5 (≈3%). In this iron oxide polymorph structure the most thermodynamically stable form is α-Fe_2O_3. Other metastable polymorphs can be stabilized during the decrease of the iron oxide crystallite size.

Another parameter is the reaction temperature: at 530°C all these polymorphs can be formed, while heating to 650°C may lead to the disappearance of γ-Fe_2O_3 and ε-Fe_2O_3 phases, and leaving α-Fe_2O_3 at 700°C. Such high temperatures can arise during the acoustic cavitation, which forms highly energetic hot spots upon the bubble collapse (T ≈5000 K and P ≈10^3 atm) in the bulk solution [6]. The existence of these conditions is confirmed by the presence of a high-pressure and high-temperature polymorph of iron oxide Fe_4O_5, which is stable from 5 to at least 30 GPa [69]. Fe_4O_5 can be readily synthesized at 10 and 20 GPa upon heating at 1500-2200 K. This recently discovered phase can result from the breakdown of magnetite into Fe_4O_5 and Fe_2O_3. The magnetite can be also formed as a result of transformation of γ-Fe_2O_3 under 600 K [74] and due to the sonochemical reduction of Fe^{3+} [75]. There is no β-Fe_2O_3 in Cu/Fe-GO, which can be a result of longer thermal treatment during sonication, indicating the existence of independent transition chain γ-Fe_2O_3 → ε-Fe_2O_3 → α-Fe_2O_3. Other factors such as increase of the α-Fe_2O_3 particle size may contribute to the formation of the β polymorph [76].

XRD discloses (001) plane of GO and the following phases (110), (006) and (214) α-Fe_2O_3; (120) and (330) ε-Fe_2O_3; (440) β-Fe_2O_3, (100) and (210) FeS along with (100) graphene in Fe-GO nanoplatform (Figure 4a). In contrast to Cu/Fe-GO, in XRD pattern of Fe-GO the (100) plane of GO disappears and (001) plane of GO appears as intense and broad reflection, indicating the layered structure of nanomaterial with a very short range atomic coherence. Strong XRD (001) peak is characteristic of GO because it shows oxygen containing functional groups on carbon sheets. To note, the γ-Fe_2O_3 phase was not revealed in XRD pattern. The presence of polymorph metastable ε-Fe_2O_3 and β-Fe_2O_3 phases, which exhibit relative intensity comparable to that of the α-Fe_2O_3 phase may result from high heating/cooling rates (i.e. >10^7 K/s) during acoustic cavitation, which can lead to the partial or complete amorphization or recrystallization of material [77]. The layered structure of GO doped by Fe^{3+} ions may act as a buffer against transition to the α-Fe_2O_3 phase in aqueous solution. The existence of the transition chain ε-Fe_2O_3 → α-Fe_2O_3 without γ-Fe_2O_3 shows effects of high temperature during the sonochemical synthesis. Typically ε-Fe_2O_3 is an intermediate polymorph between γ-Fe_2O_3 and α-Fe_2O_3. The formation of the γ-Fe_2O_3 phase requires the presence of Fe_3O_4 at 300°C, but XRD does not reveal this phase in material [78] because of the absence of Fe_4O_5 [69]. On the other hand, there is a FeS phase, which is a very stable crystalline phase even at 800°C and under pressure of up to several GPa. Presumably FeS may be formed according to the mechanism similar to copper sulfide, in agreement with our recent work. In this way, the difference in the composition between copper- and iron-modified-GO may be attributed to the characteristic electrochemical potential of Cu (0.153 J/mol) and Fe (-0.037 J/mol), implying that more energy may be required for the reduction of Fe^{3+}.

In Figure 4b the crystalline phases in Cu-GO nanoplatform are indicated by black arrows as following (001) of Cu(HOOC) at 2θ=14.5; (101) of CuS at 27.6, (102) at 29.2, (103) at 31.9; (002) of CuO at 34.9, (111) at 38.4, (200) at 40.0; (200) of Cu_2O (at 42.1), (108) at 52.8(200) at 55.1; and (116) of CuS at 59.0; and (-113) of CuO at 62.7 according to the database listed in the Table 2. Red arrows indicate strong peak at 2θ=46.4 being assigned to the (-112) plane of CuO considering its shift from 2θ=48.8.

Table 2

X-ray powder diffraction data of crystalline phases obtained from American Mineralogist Crystal Structure database

Crystalline phase	**Database**
Cuprite Cu_2O	amcsd № 0007351 and JCPDF № 78-2076
Tenorite CuO	amcsd № 0018812 and JCPDS № 80-1917
Covellite CuS	amcsd № 0000065 and JCPDS № 79-2321
Chalcocite Cu_2S	amcsd № 0019203
Cu(HOOC)	amcsd № 0012979
Cu	amcsd № 0011145

The surface chemical composition and bonding in Cu/Fe-GO nanoplatform

The surface chemical composition and bonding of synthesized GO, Cu-GO, Cu/Fe-GO and Fe-GO nanoplatforms was studied by X-ray photoelectron spectroscopy (Figure 6). Analysis of XPS spectra revealed that GO is mainly composed of carbon and oxygen containing surface groups at atomic ratio C/O=1.7 (Table 3) and a small amount of S (~0.6 at.%) (Figure 6a). The identified surface groups can be assigned to carbonyl (R-C=O-R'), epoxide (R-C-O-C-R') and carboxyl (C(=O)OH) [79].

As the C/S ratio is relatively high ~105, presumably the carbon lattice is not intercalated by S and sulfur undergoes oxidation during ultrasonic dispersion of GO in the aqueous solution. Sulfur has several oxidation states and tends to stabilize into SO_4 (O/S ratio ~62). The lower energy C1s line at ~284.5 eV (C-C bond in each nanomaterial) is assumed to be rather generic aliphatic than graphitic carbon (~284.0 eV) [80]. Another C1s component at ~286.7 eV (in each nanomaterial) is attributed to the π-π* shake-up bands of the highly aromatic 18π electron system and can be assigned to the C-O bond. The OH group may also present in the GO structure because its C1s binding energy is similar to the epoxide group (C-O-C) [81].

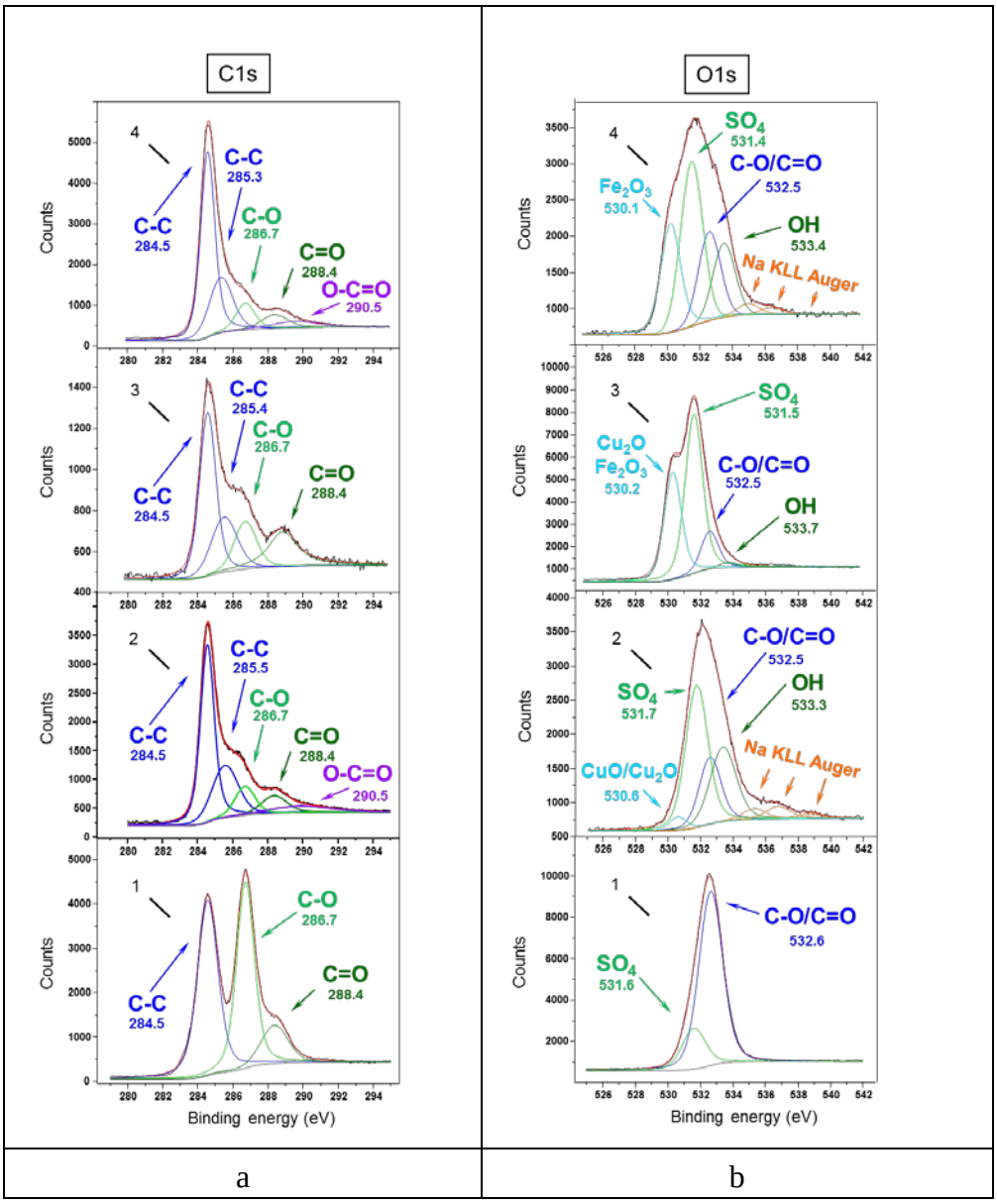

a b

a – XPS C1s spectra of synthesized GO (1), Cu-GO (2), Cu/Fe-GO (3) and Fe-GO (4); b – XPS O1s spectra of these nanomaterials, respectively. The curve fitting of the C1s and O1s XPS spectra was performed using a Gaussian-Lorentzian peak shape after performing a Shirley background correction. The color coding represents raw spectra (black) and their fits (red), and fitted peak components are shown in other colors.

Figure 6. X-ray photoelectron spectra of synthesized GO, Cu-GO, Cu/Fe-GO and Fe-GO nanoplatforms

The lower energy C1s line is indicative for the carbon atoms with sp^2-hybridization in graphite consisting of the hexagonal network of parallel carbon layers with covalent C-C bonds.

The C1s component at ~ 288.4 eV (present in each nanomaterial) is indicative for the oxidized surface containing higher amount of oxygen (Figure 6a). The higher energy C1s component is attributed to the carbon atoms with sp^3-hybridization in a typical diamond structure. Overall, the ratio of all samples is higher with the sp^3 hybridized carbon chemical state that is related to a diamond structure with a C-C bond length ~0.15 nm.

Table 3

Atomic concentration (at.%) estimated from peak areas corrected by the sensitivity factor for the chemical bonds derived from the XPS spectral lines of synthesized GO, Cu-GO, Cu/Fe-GO and Fe-GO nanoplatforms

C, at.%	**C**	**O**	**Fe**	**Cu**	**S**	**Na**
GO	62.8	36.7	-	-	0.6	-
Cu-GO	61.3	29.2	-	3.8	3.8	1.4
Cu/Fe-GO	15.7	55.2	24.2	1.2	3.1	-
Fe-GO	65.2	27.1	4.9	-	0.9	1.6

The lower C/O atomic ratio ~0.3 of Cu/Fe-GO indicates the excess of oxygen and oxygen-containing compounds involving both copper and iron, and a much lower amount of carbon (Table 3). In Fe-GO and Cu-GO the amount of carbon is twice higher than oxygen (C/O ~2.4 and 2.1), but their surface enrichment with copper or iron oxides is comparable (O/Cu ~8 and O/Fe ~6). The increasing loss of oxygen from Cu-GO to Fe-GO could be associated with the oxygen-deficient regions (*i.e.* vacancies) [82,83] and the S ion doping effect. In contrast to GO, the binding energy of the C-C band in each type of nanomaterials shows another component at higher values ~285 eV (aromatic carbon), indicating that the separation between C and other atoms decreases. The binding energy of this second C-C component is systematically shifted by ~0.1 eV to the lower values being at ~285.5 eV (in Cu-GO), ~285.4 eV (in Cu/Fe-GO) and ~285.3 eV (in Fe-GO). In general the peak at 285 eV corresponds to the C-O or C-S suggesting that S ion can be intercalated into the carbon lattice. To note, in Cu-GO and Fe-GO a small broad C1s component peak at ~290.5 eV discloses copper or iron carbonaceous compounds or their sulfides bound to the carbonyl groups of GO [84]. It will be proven later in the text that this peak cannot be assigned to the presence of $CuCO_3$, $FeCO_3$ or iron-hydroxyl carbonate $Fe(OH)_2CO_3$.

In Figure 6b the XPS O1s line in GO is introduced by two components: main peak at ~532.6 eV (C-O/C=O) and minor peak at ~531.6 eV (SO_4). In Cu/Fe-GO the O1s line is composed of four components being assigned to Fe_2O_3 and Cu_2O (~530.2 eV), SO_4 (~531.5 eV), C-O/C=O (~532.5 eV) and OH (~533.7 eV). We assume that the surface of Cu/Fe-GO is more

enriched with oxygen (C/O ~0.3) and sulfur (C/S ~5) than in Cu-GO or Fe-GO, in contrast to GO (Table 3). Cu/Fe-GO nanoplatform contains more iron than copper (Fe/Cu ~20), which is bound to sulfur (S/Fe ~0.1) and oxygen (O/Fe ~2), implying the presence of FeS (*i.e.* $Fe^{2+}S^{2-}$) and FeOOH compounds. Cu/Fe-GO may also contain $Cu^{+}Fe^{3+}S_2$ and $Cu^{+}Fe^{2+}Fe^{3+}S_3$ because S/Cu ~2.6 and also Cu-CO(O) and CuO because O/Cu ~46 and C/Cu ~13 (Table 3). For comparison, Cu-GO can contain CuS (S/Cu ~1) and CuO (O/Cu ~8). The carbon lattice can be intercalated with a greater amount of sulfur in Cu-GO than in Fe-GO because C/S ~16 and ~72, respectively.

It can be ascertained that in Fe-GO iron hydroxides and oxides such as $Fe^{3+}O^{2-}(OH)^{-}$, $Fe^{2+}(OH)_2^{-}$, $Fe^{3+}(OH)_3^{-}$, Fe_2O_3 and $Fe^{2+}O^{2-}$ may be also present. In Cu-GO and Fe-GO XPS spectra confess the appearance of Na KLL Auger lines at 534-541 eV that overlap with O1s, suggesting the presence of NaOH and Na_2SO_4. In Fe-GO FeS with Fe^{2+} and S^{2-} oxidation states and SO_4 can be formed. We expect that the presence of negligible amount of sodium compounds in both Cu-GO and Fe-GO may be also contributed by the acoustic cavitation impact on the glass walls of a reaction vessel due to diffusion processes [85,86], in addition to the sonochemical reactions involving Na_2S and radical species. The XPS Cu2p lines reveal main component peaks for the Cu^{+} (designated as Cu (I)) in Cu-GO and Cu/Fe-GO, proving the formation of $Cu^{+}S^{-}$, $Cu_2^{+}S^{2-}$ and $Cu_2^{+}O^{2-}$ (Figure 7a).

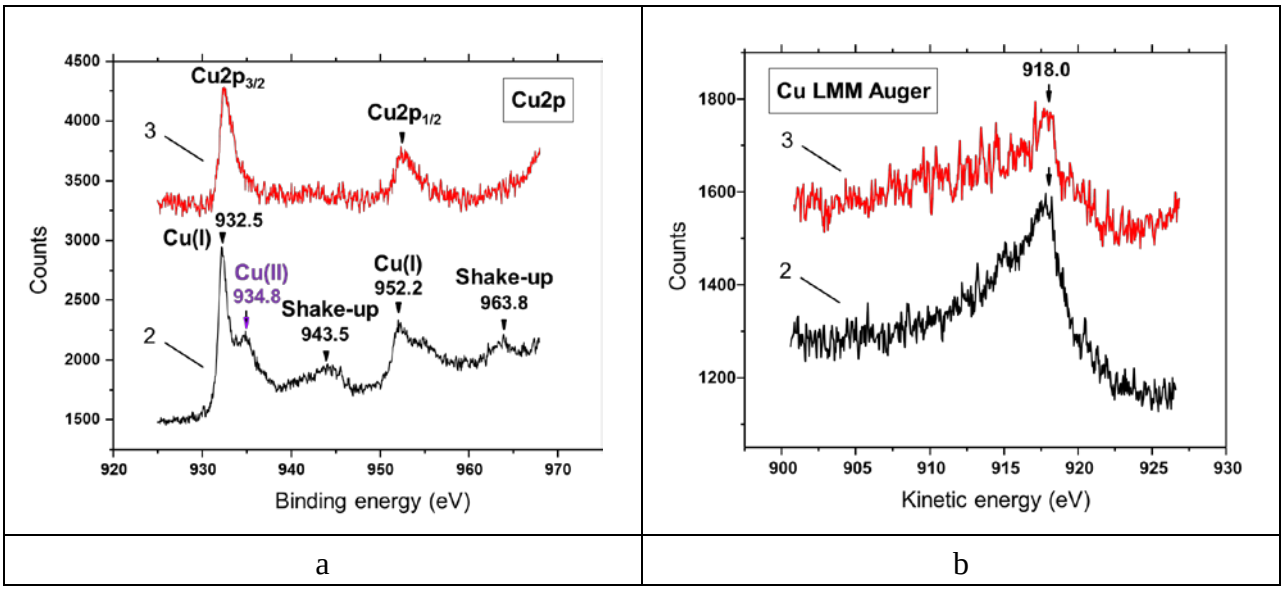

a – XPS Cu2p spectra of synthesized Cu-GO (2) and Cu/Fe-GO (3); b – XPS Cu LMM Auger spectra of these nanoplatforms

Figure 7. X-ray photoelectron spectra of copper in synthesized Cu-GO and Cu/Fe-GO

The existence of the Cu^{+} state in Cu-GO and Cu/Fe-GO was also confirmed by the Cu LMM Auger line at ~918 eV (Figure 7b). The possible formation of metallic copper cannot be excluded because its binding energy values are at ~933 eV and ~952.75 eV [87]. It is suggested that no $CuCO_3$ or $Cu(OH)_2$ are produced because their binding energies for the Cu2p3/2 and Cu2p1/2 lie at higher values, i.e. ~935 eV and ~955 eV in Cu-GO, and ~937 eV and ~957 eV in Cu/Fe-GO. The appearance of $CuCO_3$ is associated with the C1s peak at ~287.5 eV and O1s at ~533.9 eV, which are not observed in either Cu-GO or Cu/Fe-GO. In addition, the formation of $CuSO_4$ and $Cu_3(SO_4)(OH)_4$ can be excluded because the XPS Cu2p also have higher binding energy values (~935.2 eV and ~955.0 eV) [84]. Small broad peak at ~934.8 eV and shake-up components at ~943.5 eV and ~963.8 eV appear only in Cu-GO, disclosing the Cu^{2+} state [84, 87, 88], which can be attributed to the formation of $Cu^{2+}S^{2}$ and $Cu^{2+}O^{2-}$ [89-92]. High temperature (~ 800°C) may lead to the appearance of Cu_2O preventing CuO formation [93]. On the other hand, the reduction of CuO to Cu_2O may be expected from the decomposition to Cu_2O at >1073°C [94], *i.e.* conditions of hot spots during acoustic cavitation [95].

The XPS Fe2p line reveals a doublet at ~711.6 eV and ~725.6 eV in Cu/Fe-GO and Fe-GO, denoting hydrated iron oxide [96] or ferric oxidation products [97] (Figure 8).

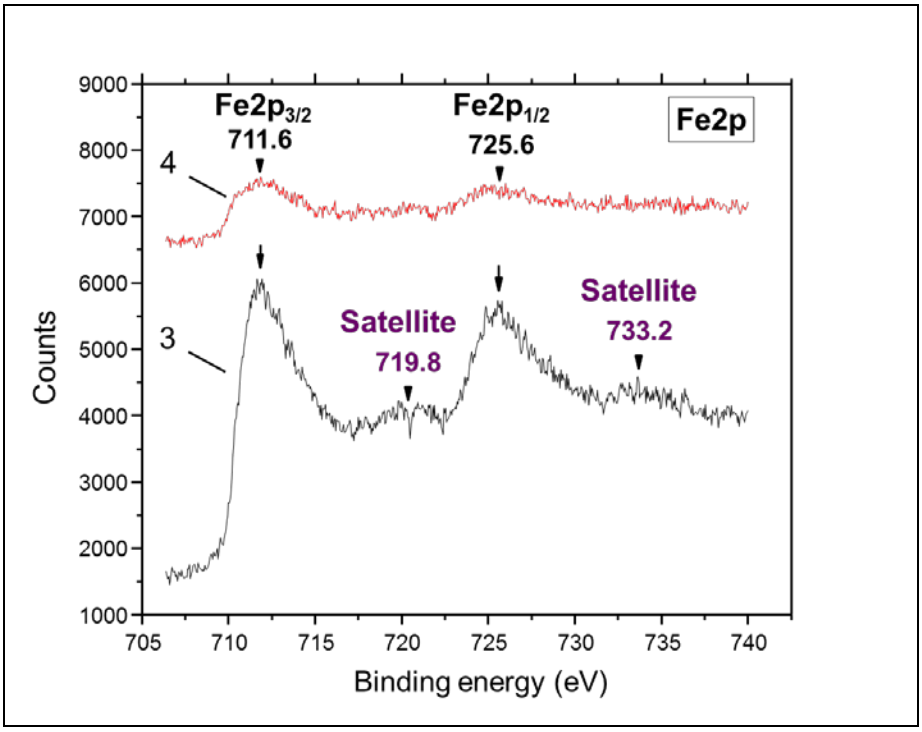

Figure 8. X-ray photoelectron spectra of iron in Cu/Fe-GO (3) and Fe-GO (4)

This doublet may be indicative for $Fe^{2+}O^{2-}$, hematite α-Fe_2O_3 (~711.4 eV), γ-Fe_2O_3 (~711.8 eV), hydroxyl-oxide FeO(OH) that may have an intermediate composition between goethite α-FeOOH (711.8 eV) and α-Fe_2O_3 [98]. Small satellite peaks (at ~719.8 eV and ~733.2 eV) appear only in Cu/Fe-GO, designating for Fe^{3+} in FeO(OH) and Fe_2O_3. The magnetite phase is not detected on the surface of neither Cu/Fe-GO nor Fe-GO, in agreement with the XRD data (Figure 4a). Usually the formation of magnetite requires low temperature (<100°C) and reducing conditions, meaning low or no-oxygen environment. The presence of the sulfate ion may lead first to the formation of iron oxyhydroxysalts followed by transformation into goethite [99], which is a product of pyrite oxidation [100]. Pyrite oxidizes to produce S and SO_4, and the formation of S is restricted to the order of a monolayer in basic aqueous solution. Products of pyrite dissolution in alkaline medium are hematite α-Fe_2O_3 and ferrihydrite. Cu/Fe-GO and Fe-GO contain hematite, whilst ferrihydrite can be produced only in Fe-GO because of the higher O/Fe ratio ~6 in Fe-GO and ~2 in Cu/Fe-GO. Reduction of iron hydroxide in the presence of S leads to the formation of iron sulfide. Iron hydroxide can be formed on the pyrite surface in Fe-GO because of stronger OH peak relatively to O.

Formation mechanism of Cu/Fe-GO nanoplatform

The synthesis of Cu/Fe-GO is conducted in three successive steps: 1) ultrasonic treatment of the synthesized GO with Na_2S acting as a strong reductant; 2) sonication of pretreated GO in aqueous solution of Cu^{2+} and Fe^{3+} ion precursors; 3) sonication of Cu/Fe-GO with Na_2S.

In the first step water undergoes sonolysis, producing free H· and OH· radicals and their recombination products such as molecular hydrogen (H_2) and hydrogen peroxide (H_2O_2). In an oxygenated aqueous solution, additional H_2O_2 may be formed by a route involving hydroperoxyl (HO_2) radical. These radical species are not scavenged as no additives were added during the synthesis. Treatment of GO with Na_2S leads to the reduction of GO and intercalation of S ions into the carbon lattice, yielding S-rGO with a C-S bond acting as a mild oxidizer. S is most probably intercalated in the carbon lattice of GO by substitution with oxygen and this reaction is enhanced by acoustic cavitation (jets, shock waves, capillary waves) [85]. Oxidation of unreacted S forms SO_3 followed by SO_4 through the nucleophilic reaction between the surface OH and epoxy groups of GO.

In the second step Cu^{2+} and Fe^{3+} can react with the S-rGO, sulfate ions (adsorbed on GO) and sonochemically formed radical species. Metal ions can react with sonochemically produced H· (reductant) and a number of oxidizers such as OH·, H_2O_2 and O_2· and lead to the oxidation of copper and iron in the form of oxides or hydroxides. According to the oxidation potentials of Cu and Fe [89], Cu^{2+} can remain in its oxidation state as Cu^{+} is not stable in the presence of Fe^{3+}. According to the standard chemical potentials of Cu and Fe [90], Cu^{2+} and Fe^{3+} can react with S and undergo oxidation, yielding copper and iron oxides/sulfides and iron hydroxides. The

structure of CuS can be introduced by trigonal Cu ion bridge Cu_3S-CuS_3 with the disulfide layer (S-S). Oxidation of CuS produces sulfates. Pyrite oxidation in alkaline medium (our solutions have pH=10) causes reduction of Fe^{2+} and formation of SO_4 [96]. Product of pyrite oxidation is Fe^{3+} oxyhydroxide, i.e. goethite α-FeOOH [100]. In addition, ultrasound also causes dissolution and hydrolysis of chemical substances [101], whilst oxidation and dissolution reactions are not well-distinguished processes.

In the third step sonochemical reactions proceed with the excess amount of a strong reductant (Na_2S/Me molar ratio is ~100) meaning that the dominant process will be reduction. Faster and easier reduction will proceed at higher values of the standard chemical potential of metals, *i.e.* the reduction from ferric Fe^{3+} to ferrous Fe^{2+} will be faster and more favorable than from Cu^{2+} to Cu^{+}, while formation of metallic compounds (*i.e.* Fe^0 and Cu^0) will proceed very slowly. Sonochemical reduction may also lead to the formation of binary compounds such as $Cu^{+}Fe^{3+}S_2$ (chalcopyrite) and $Cu^{+}Fe^{2+}Fe^{3+}S_3$ (cubanite), taking into account similar system with Ag [101]. Strong reducing conditions will lead to the formation of iron hydroxide, which may have an intermediate composition between α-FeOOH and α-Fe_2O_3 (at pH=10). Outer hydrous FeOOH may act as a matrix for the Fe^{3+}/Fe^{2+} reactions. In this case possible reaction products could be Fe_2O_3, $Fe(OH)_2$, Cu_2S and Cu_2O.

2.3 Ultrasonic complexation of ketorolac with Cu/Fe-GO nanoplatform

Raman scattering spectroscopy was applied to examine the formation of ketorolac-Cu/Fe-GO nanoparticles (Figure 9). Raman spectrum 4 of ketorolac-Cu/Fe-GO is compared with pristine GO (spectrum 1), ketorolac-GO (spectrum 2) and ketorolac-Fe-GO (spectrum 5). All these Raman spectra except of GO show characteristic peaks of ketorolac as indicated by green arrows, but with different intensities depending on the type of nanoplatform. In particular, the most prominent Raman bands of ketorolac appeared at ~1002 cm^{-1} of $_{\beta}$HCC bending (in 2-4); shifted at ~1278 cm^{-1} of {$_{\gamma}$CC+$_{\beta}$HCC} stretching and bending (3) and ~1258 cm^{-1} of {$_{\tau}$HCCC+$_{\beta}$HCC} (4); ~1328 cm^{-1} of {$_{\gamma}$CC+$_{\beta}$HCC} stretching and bending (2-5); shifted at ~1423 cm^{-1} (2) and ~1432 cm^{-1} (3-5) of {$_{\beta}$HCH+$_{\gamma}$NC+$_{\gamma}$CC}; shifted at ~1459 cm^{-1} (2) and ~1472 cm^{-1} (3) and 1469 cm^{-1} (4); ~1524 cm^{-1} (2-4) of $_{\beta}$HCC bending; shifted ~1555 cm^{-1} of $_{\gamma}$CC stretching (2-4) and shifted at ~1622 cm^{-1} (2-5) of {$_{\gamma}$CC+$_{\beta}$HCC} stretching and bending, in agreement with literature [102, 103]. Most of these peaks became broader and less defined in ketorolac-Fe-GO. The prominent Raman peaks from the ketorolac at 1328 cm^{-1} and 1622 cm^{-1} appear as strong bands in all nanomaterials. The band of ketorolac at 1328 cm^{-1} develops closer to the D band of GO, and its stronger delocalization illustrates the significant contribution by carboxylate groups. Another band of ketorolac at 1622 cm^{-1} is shifted towards the G band of the GO and appears as a shoulder in all samples, perturbing the G peak, indicating particular binding or complexation mechanisms, which we cannot distinguish at the moment.

Next, we were interested in understanding why explicit Raman peaks of ketorolac appear as multiple bands in ketorolac-Cu/Fe-GO than in ketorolac-Cu-GO or ketorolac-Fe-GO nanomaterials. Heretofore the functioning mechanism of ketorolac (like many other NSAIDs) is not completely understood, but may be related to prostaglandin synthesis inhibition.

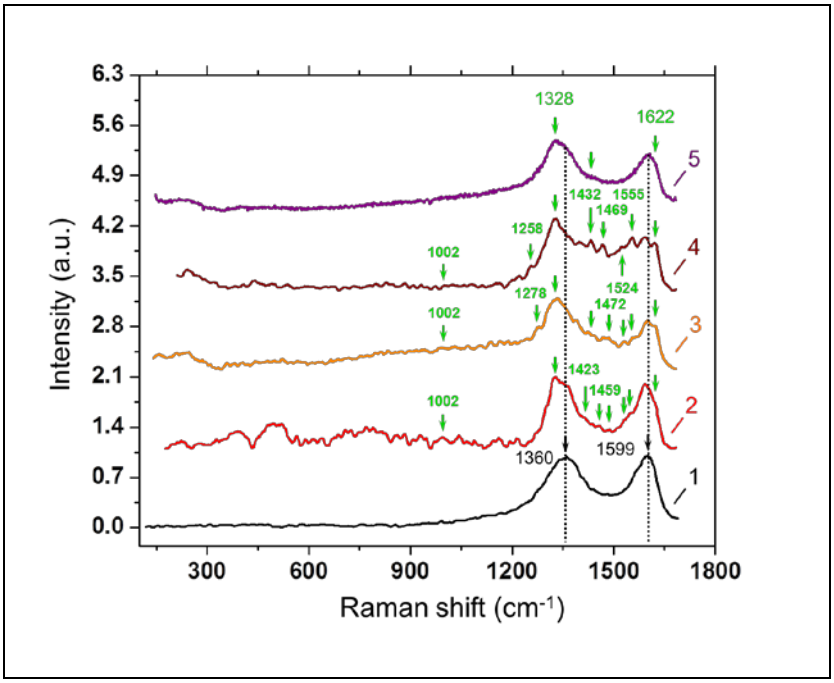

Figure 9. Raman scattering spectra of synthesized GO (1), ketorolac-GO (2), ketorolac-Cu-GO (3), ketorolac-Cu/Fe-GO (4) and ketorolac-Fe-GO (5) (At least five Raman spectra were collected with 10 s of integration time for an individual spectrum acquisition at $6x10^{-3}$ W laser power, λ_{exc}=633 nm)

It is accepted that the biological activity of ketorolac tromethamine is associated with the S-form having analgesic activity. We found a model dye, S-containing methylene blue (MB) that is Raman active and has a similar chemical structure to the ketorolac that can be used for the sonochemical complexation with Cu-GO, Cu/Fe-GO or Fe-GO nanoplatforms to reveal the binding mechanism of this drug under acoustic field. In contrast to ketorolac, Raman spectra show multiple characteristic peaks of MB after sonochemical intercalation into Cu-GO, Cu/Fe-GO and Fe-GO nanoplatforms (Figure 10). Intense Raman peak at ~447 cm^{-1} is attributed to the $_{\delta}$(C-N-C) skeletal bending band of MB, indicating that the dye molecules were adsorbed on the surface of GO nanoplatforms [104]. The shifted small Raman peak (~600 cm^{-1}) designates $_{\delta}$(C-S-C) vibration, suggesting that sonochemical intercalation of MB into nanoplatforms may access

via the linkage with S and the carbon lattice or via the complexation with CuS or FeS sites including interaction with the sulfate groups. Negligible Raman peaks positioned at 677 cm^{-1} and ~1039 cm^{-1} may signify the out-of-plane bending $_{\gamma}$(C-H) and $_{\beta}$(C-H), and at ~1183 cm^{-1} may specify the stretching $_{\nu}$(C-N) bond of MB, suggesting the in-plane intercalation of MB into the GO carbon network structure.

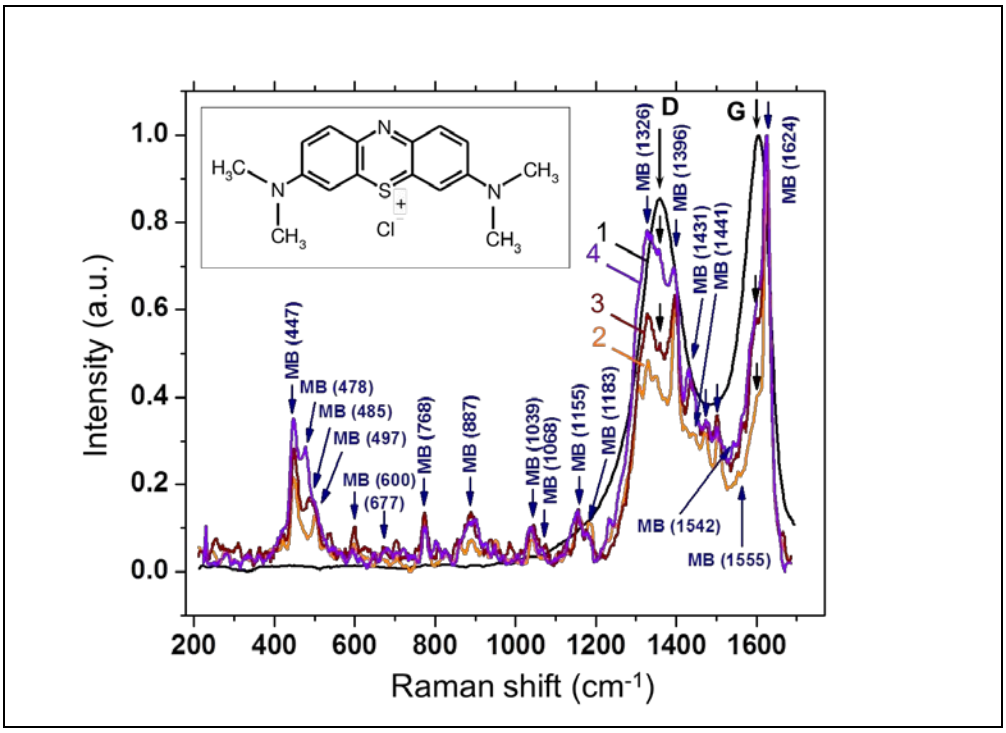

Figure 10. Averaged Raman scattering spectra of synthesized GO (1) and methylene blue (MB) after ultrasonic complexation with Cu-GO (2), Cu/Fe-GO (3) and Fe-GO (4) (10 s of integration time, $6x10^{-3}$ W, λ_{exc}=633 nm). The inset shows the chemical structure of MB.

In these spectra strong Raman bands of MB appear at ~1326 cm^{-1} and ~1396 cm^{-1} being assigned to $_{\alpha}$(C-H) in-plane ring deformation, at ~1431 cm^{-1} and ~1441 cm^{-1} designating ν_{asym}(C-N) and at ~1624 cm^{-1} demonstrating ν(C-C) ring vibration. These Raman bands develop shoulders at ~1360 cm^{-1} and ~1606 cm^{-1} corresponding to the characteristic Raman D and G bands of GO, evidencing successful intercalation of MB into all three types of nanoplatforms.

2.4 Stability of ketorolac-Cu/Fe-GO nanoparticles

The stability of ketorolac-Cu/Fe-GO nanoparticles was examined through the changes of the characteristic Raman band of ketorolac (~1328 cm^{-1}) before and after incubation in aqueous solutions adjusted to one of the following pH values 1, 5 and 8 (Figure 11). These pH values were chosen in accordance with the pH values of human gastric juice in stomach (~1.5-3.7)

[105], lysosomes (~4.3-5.3) [106], urine (~5.9-6.7) [107], duodenum (~6.0-8.0) [108] and pancreas or insulin secretion (~5.0-10.5) [109].

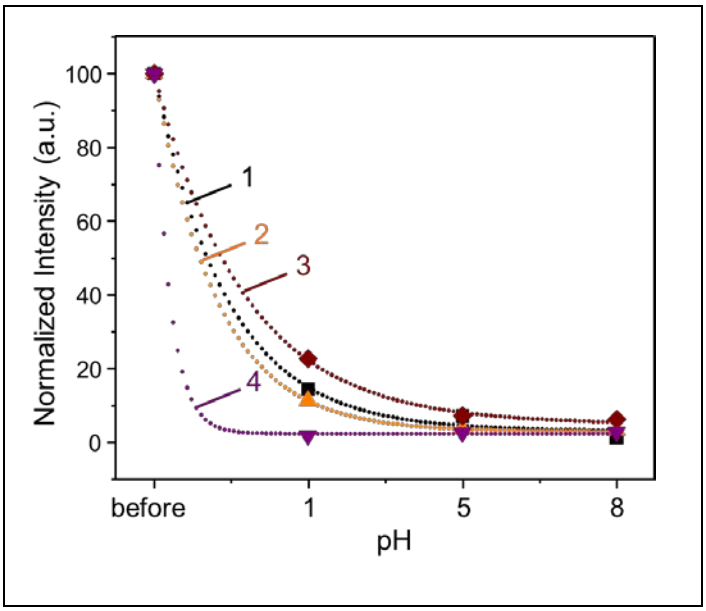

Figure 11. Plot of normalized intensity of prominent Raman peak of ketorolac (~1328 cm^{-1}) complexed with GO (1), Cu-GO (2), Cu/Fe-GO (3) or Fe-GO (4) before and after incubation in aqueous solution adjusted to one of the following pH values: 1, 5 and 8. Experimental data (dots of different shapes and color coding) are fitted with the exponential decay curves according to the mathematical equations $y_1=3+794e^{(-x/0.5)}$, $y_2=3+1132e^{(-x/0.4)}$, $y_3=5+521e^{(-x/0.6)}$ and $y_4=2+1.6e^{(-x/0.1)}$, where the calculated decay constants are 0.6 (ketorolac-Cu/Fe-GO), 0.5 (ketorolac-GO), 0.4 (ketorolac-Cu-GO) and 0.1 (ketorolac-Fe-GO).

Release of ketorolac from GO-based nanoplatforms was compared to the pristine GO with the aim to find out the usefulness of Cu, Cu/Fe or Fe compounds in the binding to ketorolac. Overall the Raman intensity of ketorolac in each GO material monotonically decreases following the exponential decay curve if the pH of aqueous solutions was increased from 1 to 8. From the values of the peak intensity at maximum conditions of the precipitant one can estimate the peak intensity decay values from the drops of supernatant at the studied pH values in terms of the approximate amount of the unreacted ketorolac (in mg) after incubation (Table 4). The rate of Raman intensity decay of ketorolac depends on the type of GO nanoplatform over the selected pH range. In particular, the decay constant of Cu/Fe-GO is higher (~0.6) than of Fe-GO (~0.1), suggesting the faster release of ketorolac from Fe-GO amongst all types of GO nanoplatforms

starting from low pH values. In contrast, ketorolac is still entrapped in Cu/Fe-GO carrier at acidic conditions and slowly disintegrates at pH values increased to 8.

Table 4

Values of the residual mass of the unreacted ketorolac in the aqueous solution of ketorolac-GO (m_1), ketorolac-Cu-GO (m_2), ketorolac-Cu/Fe-GO (m_3) and ketorolac-Fe-GO (m_4) nanoparticles after the incubation at one of the pH values 1, 5 or 8, estimated by using Raman peak intensity 1328 cm^{-1}

pH	**m_1, mg**	**m_2, mg**	**m_3, mg**	**m_4, mg**
1	0.43	0.34	0.68	0.08
5	0.21	0.11	0.22	0.07
8	0.04	0.09	0.19	0.05

The disintegration of ketorolac from pristine GO and Cu-GO is comparable with a decay constant being 0.5 and 0.4, suggesting that the complexation of ketorolac with Cu in the carbon structure of GO enriched with oxygen compounds is important for drug retaining. This action is strengthened by the presence of both Cu and Fe compounds in Cu/Fe-GO. In addition, at pH=5 and 8 the surface of GO is enriched with COO^- groups and GO becomes more hydrophilic, while the drug is hydrophobic, meaning that the trapped ketorolac in the GO will stay in the fluid flow for extended period of time. This finding suggests that ketorolac intercalated into the Cu/Fe-GO nanoparticles may survive aggressive gastric medium avoiding harmful action on stomach cells and most probably stay in the flow of aqueous medium for the targeted delivery.

*****

The presented results allow us to draw the following conclusions:

1. Ultrasonic functionalization of preformed GO with Cu^{2+} and Fe^{3+} cations results in formation of Cu/Fe-GO nanoplatform with improved semiconductor properties due to a complex crystalline structure being composed of CuS, Cu_2O and CuO with α-, γ-Fe_2O_3 and Fe_4O_5 phases.
2. We proposed an approach of microspheres with a core-shell structure to study the charge transfer process of an organic substance complexed with the Cu/Fe-GO nanolatform.
3. Ketorolac that is ultrasonically complexed with Cu/Fe-GO nanoplatform disintegrates at the slowest rate in aqueous medium at pH=8 in contrast to that from Cu-GO or Fe-GO nanoplatforms.

CHAPTER 3 FUNCTIONALIZATION OF DICLOFENAC THROUGH ULTRASONIC COMPLEXATION WITH GRAPHENE OXIDE COATED COPPER OXIDE NANOPARTICLES

Based on analysis of NSAIDs, it was postulated that an effective antirheumatic agent should have the following characteristics: acidity constant between 4 and 5, a partition coefficient of approximately 10, and two aromatic rings twisted in relation to each other [1]. For example, sodium diclofenac inhibits cyclooxygenase COX-2 enzyme with greater potency and retains antidepressant and anxiolytic response in patients with pain. Such enhanced efficiency of this drug amongst other NSAIDs is ascribed to the chemical structure that is introduced by a phenylacetic acid group, a secondary amino group, and a phenyl ring containing chlorine atoms, which cause maximum twisting of the ring (Figure 1). The chlorine atoms cause maximal twisting of the phenyl rings acting as chief points of biotransformation of diclofenac with the corresponding hydroxy derivatives being found as metabolites.

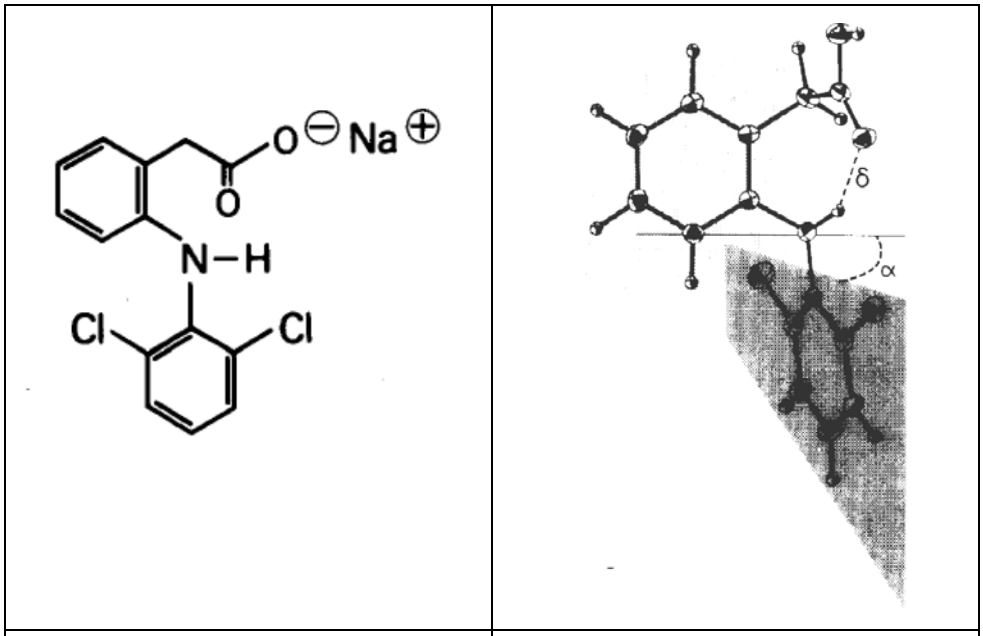

a – the structural elements of sodium diclofenac *per se*; b – the crystalline structure of diclofenac molecule with the phenyl rings being twisted at an angle of torsion α=69°and the intramolecular hydrogen bond δ between the carboxyl oxygen and the amino hydrogen adapted from ref. [1].

Figure 1. The electronic-molecular structure of pristine sodium diclofenac

3.1 The properties of Cu-complexes of diclofenac

The pharmaceutical effects of diclofenac are frequently associated with the formation of H-bonds between its carboxyl group and several side chains of the COX enzymes [2]. Prolonged administration of diclofenac causes severe dose-dependent gastrointestinal injury [3,4] and leads to serious cardiovascular and renal side effects [5]. The modulation of the n-π* interaction and its interrelation with the H-bonding can improve the biological activity of diclofenac. Such modulation has been realized in liquid-filled soft gel capsules [6] or submicron particles in a tablet to treat osteoarthritis, rheumatoid arthritis, and cancer-related pain [7,8]. In consequence, modified diclofenac caused fewer digestive and central nervous system-associated side effects.

It has been shown that the anti-inflammatory activity of many NSAIDs can be significantly improved through their metal complexes. Metal complexes and metallodrugs are in the existent clinical use to treat inflammation ailment, diabetes, bacterial infections and many types of cancer [9-12]. Among them copper (II) complexes with NSAIDs exhibit excellent ability to cleave the pathogenic DNA and participate in the formation of H-bonds at the DNA surface [13]. Nowadays both *in vitro* and *in vivo* studies confirm the enhanced anticancer and anti-inflammatory effects of Cu(II)-NSAIDs complexes [14]. The Cu(II) complexes of diclofenac exhibit good antitumor and antimicrobial activity [15]. For example, tetranuclear copper(II) complexes containing multiple diclofenac and Schiff base moieties exhibit cytotoxic effect on cancer stem and bulk breast cancer cells by elevating intracellular reactive oxygen species (ROS) levels and inhibiting COX-2 expression [16].

Diclofenac is bonded to the central Cu atom through the carboxyl groups and can constitute an important element of commercially available anti-inflammatory drugs since 2001 [17]. However, most of the existing Cu(II)-NSAID complexes have weakly bound carboxylic acid ligands and can easily dissociate favoring the interaction of $O_2\cdot$ radicals with the free sites of copper. Therefore, it is necessary to understand the electronic molecular surface structure of Cu(II)-NSAID complexes and define their ionization form in aqueous solution at different pH values. The solubility, bioavailability, absorption and cell penetration of drug to the site of action are strongly correlated with the H-bond formation and depend on the ionization form of the pharmaceutical compound [18]. Nonionized species of the drug compound are major forms in the stomach and in the upper small intestine [19]. Drug molecular compounds undergo ionization to different extents in various parts of the body and this process is pH-dependent. About 85% of marketed drugs contain functional groups that are ionized to some extent at physiological pH (1.5-8). However, if the compound forms many hydrogen or ionic bonds with water, the desolvation becomes compelling. An oral drug should follow the Lipinski “rule of five” to be

able to remain unimpaired at acidic conditions within the stomach (pH=1-3), undergo absorption through the intestine and be soluble in a blood before it reaches the required area [20].

3.2 The role of CuO and GO for functionalization of diclofenac

In nanomedicine, nanoscale carriers can significantly enhance the bioavailability of drug and decrease the dose of administration by utilizing safer methods for modification of NSAIDs with metals and carbon-based substances [21,22]. Among nanoscale carriers GO is biocompatible [23], bactericidal [24] and can provide high surface area enriched with carboxyl, carbonyl, hydroxyl and lactone groups useful for the complexation with copper [25]. The operation of CuO nanoparticles lie beyond their antibacterial effects [26] because of specific optical [27], electrical [28], and magnetic [29] morphology-dependent properties that can be beneficial for pharmaceutical purposes. The mergence of CuO and GO into a single nanoplatform significantly improves antibacterial activity [30], enhanced anticancer catalytic sensing [31] and specific binding ability of drugs [32]. The improved antibacterial effects of such a nanoplatform arise from Cu ions release from the CuO surface and enhanced formation of reactive oxygen species (ROS) at the contact with GO (*e.g.* H_2O_2, $OH\cdot$, O_2^-) resulting in deformation of cellular biomolecules such as proteins, fats, DNA and RNA and, as a consequence, destruction of cellular membrane in bacteria and microbes [33].

The size, morphology and crystallinity of CuO nanostructures are equally important to control their properties of light absorption and catalytic activity [34]. Different synthetic methods were developed to control the properties of CuO nanoparticles such as sonochemical [35], sol-gel [36], electrochemical [37], laser ablation [38] and chemical precipitation [39]. The size of CuO nanoparticles can be precisely controlled from 4 nm to 10 nm by using the methods of electrochemical, chemical precipitation or sol-gel synthesis, and from 20 nm to 30 nm by applying the sonochemical technique. Electrochemical method is based on reactions taking place between the electrode and electrolyte. Therefore the final product is formed in a small amount at the surface of electrode. Despite this drawback the electrochemical method allows a very precise control over the size and morphology of CuO nanoparticles by adjusting reaction temperature, synthesis duration, current density and voltage. Sol-gel method is the most widespread thanks to the simplicity of operation and speed of obtaining of final product with the required size and morphology. The advantage of this method is the possibility of formation of stable nanoparticles with the desired morphology in the absence of additional chemical substances to control the colloidal stabilization.

The optical properties of CuO nanoparticles can be predicted in the use of thermal treatment, *e.g.* at T=400±1°C [40], and through the control over size and morphology [41]. The electrical conductivity of CuO nanoparticles increases if their diameter is increased up to 95 nm, also at higher temperature and concentration of colloids. Mechanical strength and capacity of

CuO nanoparticles can be ameliorated via mergence with graphene [42]. Overall the improved properties of CuO-graphene based nanoplatform depend on the morphology design, at which CuO nanoparticles are coated by a thin layer of graphene acting as elastic buffer. Oxidized graphene at the contact with CuO exhibit improved catalytic activity in hydrogenation reactions of nitrogen-containing aromatic compounds [43]. In particular, CuO-GO exhibits high efficiency of reduction of 4-nitrobenzine and conversion of 4-aminobenzine. Enhanced catalytic property of CuO-GO is explained by a synergetic effect between CuO and GO [44]. CuO-GO can be used as efficient and environmentally friendly catalyst of a one-step reaction of a new compound based on flavanone and its complexation with triazole [45]. Compounds of flavanone exhibit a wide range of biological and pharmaceutical properties such as antiviral, anticancer, anti-inflammatory, antioxidant and antiallergic as triazole molecules do. Up to date, CuO-GO has never been used as nanoplatform for direct functionalization of NSAID, *e.g.* diclofenac, and their interaction remains unexamined.

Among many techniques a sonochemical method especially stands out because of unique physico-chemical effects produced by ultrasound in aqueous solution during acoustic cavitation [46,47]. The synergetic effects of sonochemical reactions and high energy gradients in hot spots have been successfully applied for the synthesis of various nanomaterials with enhanced antibacterial functions [48,49]. One can find much information about the CuO nanoparticle formation and its interaction with carbon dots and textile material or polymers by using the fundamental principles and mechanisms of sonochemistry. At present, this knowledge is restricted to CuO-GO formation, and the interaction of this new nanomaterial with diclofenac is not revealed.

3.3 Formation of CuO-GO nanoplatform

As the interface dominates the structure and function of the material, GO has been chosen because it provides the extended surface area at the nanoscale that is rich with oxygen containing functional groups such as carboxyl and carbonyl on the edges, and hydroxyl, epoxide groups on the basal plane. GO has amphiphilic properties and its surface is suitable for chemical modification with molecular substances. For this reason the synthesized GO was used for the coating of CuO nanoparticles and ultrasonic (20 kHz) functionalization with diclofenac *per se*. The ultrasonically formed CuO-GO nanoplatform has a flower-like morphology consisting of twisted thin sheets with a specific orientation as a result of the growth in a perpendicular direction to the surface of the initial nucleation units, i.e. $[Cu(OH)_4]^{2-}$ (Figure 2a).

The DLS histogram exhibits a unimodal size distribution of CuO-GO with a single peak at ~342±160 nm (Figure 2b). The surface charge has a positive ζ-potential of 2.57±1.13 mV, that is in agreement with CuO nanoparticles at pH=7-9 and is indicative of the isoelectric point of CuO nanoparticles in aqueous solution at pH=5.42 [51] (Figure 2c).

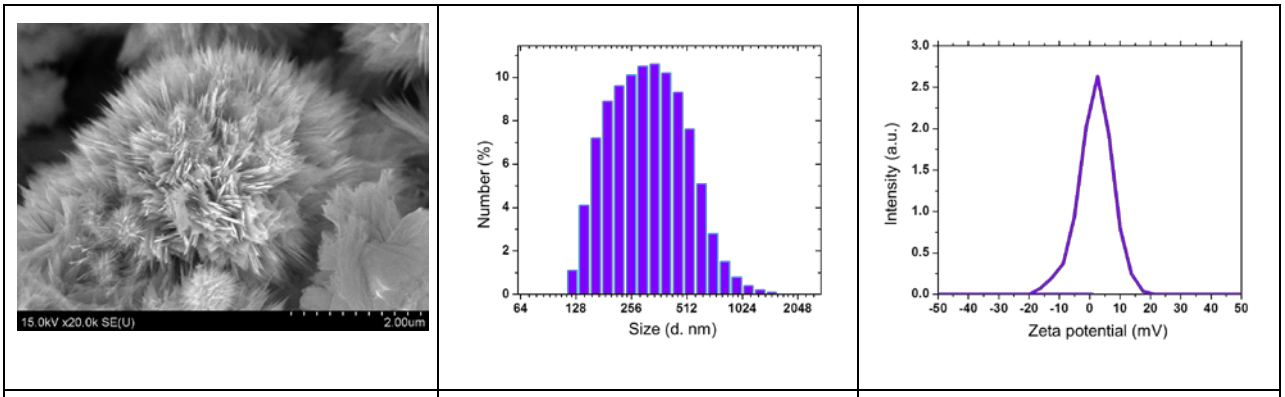

a	b	c

a – representative SEM image of synthesized CuO-GO (scale bar is 2 μm); b – DLS histogram of size distribution of CuO-GO; c – Zeta potential plot of CuO-GO.

Figure 2. The morphology, average size and surface charge of synthesized CuO-GO

As next, the electronic molecular structure of CuO-GO was examined in comparison with GO and CuO colloids by using the UV-Vis absorption spectra (Figure 3).

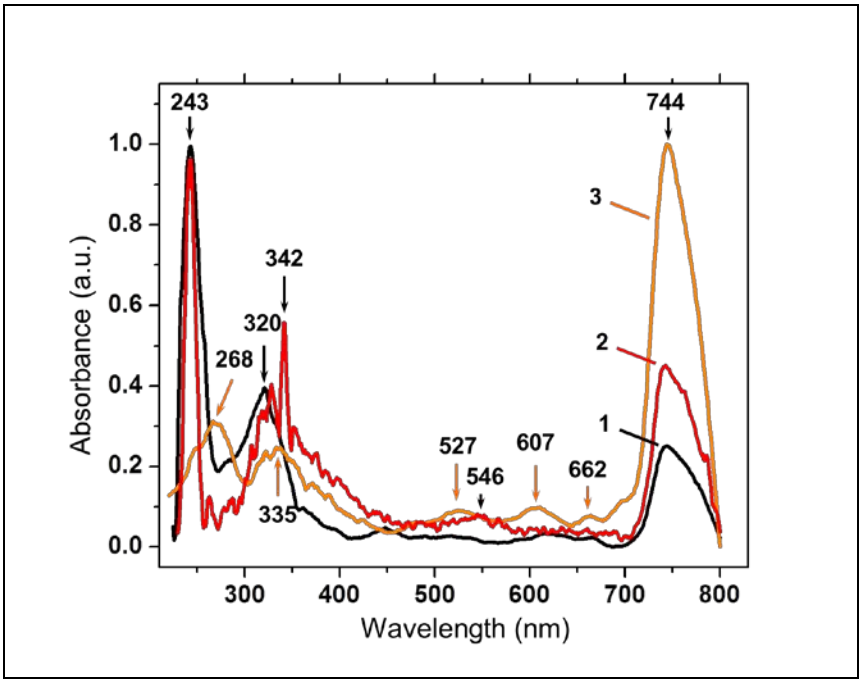

Figure 3. The UV-Visible absorption spectra of aqueous solutions of GO (1), CuO (2) and CuO-GO (3)

GO exhibits a strong narrow absorption band at ~243 nm (5.10 eV) due to the $\pi_{C=C} \rightarrow \pi_{C=C}^*$ transition in aromatic rings and a smaller broader peak at ~320 nm (3.88 eV) as a result of the $n_{C=O} \rightarrow \pi_{C=O}^*$ transition.

In contrast to GO, the absorption spectrum of CuO-GO nanoplatform is more complex and exhibits multiple peaks with most prominent maxima at ~268 nm (4.63 eV), ~335 nm (3.70 eV) and a very strong band at ~744 nm (1.67 eV). The first two absorption peaks are red shifted in comparison to the common absorption band of GO (220-230 nm and a shoulder near 300-303 nm), indicating a restored electronic conjugation within the graphene sheets [52]. An absorption band near ~744 nm is attributed to the electronic excitation of solvent molecules [53].

The first absorption peak in the CuO-GO nanoplatform is red shifted, indicating a reduction of GO. The second absorption peak and other small bands at ~527 nm (2.35 eV), ~607 nm (2.04 eV) and ~662 nm (1.87 eV) can be assigned to the band-to-band transition in a flower-like morphology of GO-coated CuO nanoparticles based on the observation of similar n–π* transitions in CuO nanoparticles with a sisal-like morphology due to a quantum confinement in radial direction of nanoneedle structures [53].

The crystalline structure of CuO-GO nanoplatform

The phase compositions of GO and CuO-GO nanoplatform were defined by the X-ray powder diffraction technique (Figure 4). The XRD pattern of GO shows an intense strong peak at 2θ=12.66° that corresponds to the interplanar spacing d=5.83 Å (Table 1, Figure 4).

Table 1

The X-ray powder diffraction data (2θ, °) and interplanar spacing ($d_{(hkl)}$, Å) of GO

2θ, °	**Int., a.u.**	**(hkl)**	**$d_{(hkl)}$, Å**
12.66	100	(001)	5.83
22.84	27	(002)	3.96
35.06	15	(111)	2.53
38.30	19	(020)	2.60
40.05	33	(021)	2.49
42.87	24	(201)	2.33

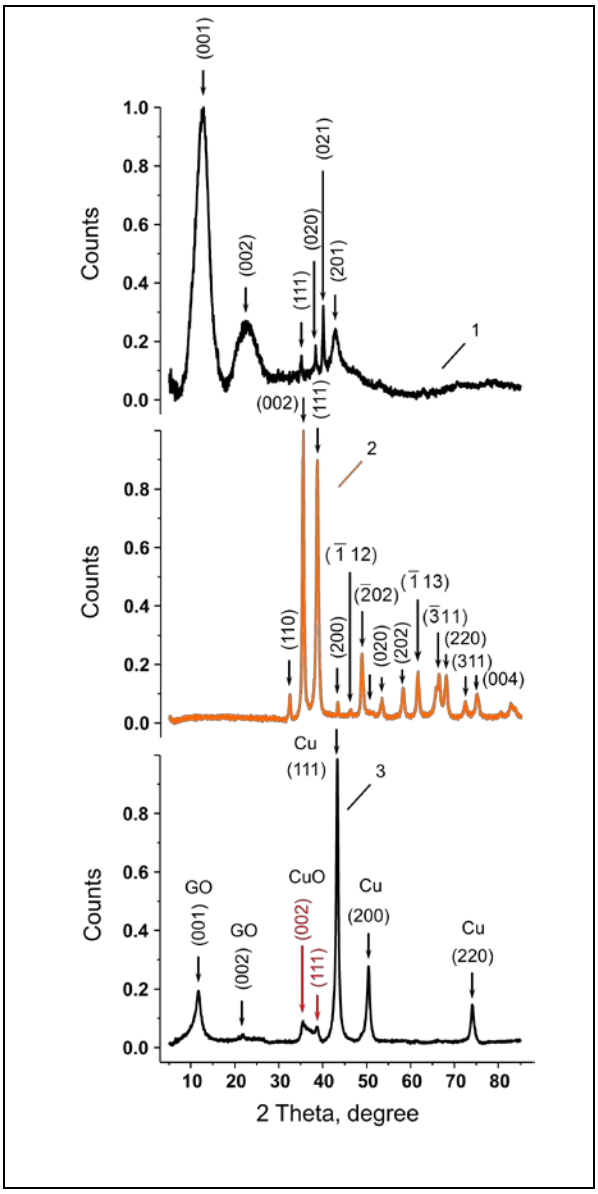

Figure 4. The X-Ray powder diffraction patterns of GO (1), synthesized CuO-GO nanoplatform (2) and ultrasonically formed {CuO+GO} colloidal mixture (20 kHz, 18 W·cm^{-2}, 15 min) (3)

This d value is on ~1.44 Å larger than of a (001) reflex in diamond (amcsd 0013983). Another XRD peak of GO is broad and has a lower intensity with a maximum at 2θ=22.84° corresponding to d=3.96 Å that is closer to the d value of (002) reflex in graphite (amcsd 0000049) at 2θ=26.63° (d=3.34 Å). Other four narrow sharp peaks of GO appear on the amorphous halo at 2θ=35.06°, 38.30°, 40.05° and 42.87° with d=2.53 Å, 2.60 Å, 2.49 Å and 2.33 Å that are larger than of (111), (020), (021) and (201) reflexes in diamond. These changes

of XRD reflexes point out to the thinning of graphite sheets and a disordered stacking of graphene layers enriched with oxygen functional groups. The mechanical shock waves and shear forces, arising in cavitation hot spots, can cause exfoliation and deformation of GO leading to its amorphization [55].

The XRD pattern of synthesized CuO-GO nanoplatform shows characteristic reflexes of CuO crystalline phase (amcsd 0018812) (Figure 4). However, the calculated d values of CuO-GO with (110), (111), (020) and (202) planes are on ~0.1 Å larger than in CuO (Table 2). In addition, the (112) reflex of CuO in CuO-GO has a d=1.81 Å being larger than in CuO (1.77 Å). The overall broadening of reflexes is indicative for the presence of oxidized graphene and formation of oxygen-containing functional groups in CuO-GO, in agreement with the proposed sonochemical formation mechanism [56]. However, small (200) reflex of CuO-GO at 2θ=43.28° has a d=2.07 Å that is on ~0.24 Å smaller than in CuO nanoparticles, pointing out to the coating of CuO with GO occurs through the binding with C-O or C=O bearing functional groups.

In a control experiment the mixture of preformed CuO nanoparticles and GO was ultrasonically treated (20 kHz, 18 $W \cdot cm^{-2}$) for 15 min. The XRD pattern of this {CuO+GO} mixture reveals (001) and (002) planes of GO, (002) and (111) planes of CuO, and strong (111), (200) and (220) planes of Cu (Figure 4). Among them the dominant XRD reflexes arise from GO and Cu, demonstrating the copper in a zerovalent state in GO as a result of sonochemical redox reactions involving electron transfer from copper cations to carbon and oxygen through the interaction with -OH and -COOH groups during acoustic cavitation [57].

Table 2

The X-ray powder diffraction data (2θ, °) and interplanar spacing ($d_{(hkl)}$, Å) of CuO-GO

2θ, °	**Int., a.u.**	**$d_{(hkl)}$, Å**	**(hkl)**
32.43	9	2.76	(110)
35.46	100	2.53	(002)
38.66	90	2.33	(111)
43.28	7	2.07	(200)
46.21	5	1.96	(-112)
48.78	24	1.87	(-202)
50.47	4	1.81	(112)
53.36	9	1.72	(020)
58.10	12	1.59	(202)
61.50	18	1.51	(-113)
65.72	13	1.42	(022)
66.35	17	1.41	(-311)
67.89	17	1.38	(220)
72.27	8	1.30	(311)
75.04	10	1.27	(004)

The structure of {CuO+GO} colloidal mixture is completely different from CuO-GO nanoplatform being entirely composed of a pure CuO phase and a carbonaceous network of graphene oxide. Analysis of the elemental composition of CuO-GO was performed in comparison with the {CuO+GO} colloidal mixture and GO (Table 3, Figure 5).

Table 3

Elemental composition of synthesized GO, CuO-GO and {CuO+GO} colloidal mixture

Sample	**C, at.%**	**O, at.%**	**Cu, at.%**
GO	59.2±5.7	39.7±5.3	-
CuO-GO	51.2±2.4	36.8±1.6	12.0±0.5
{CuO+GO} mixture	59.6±4.5	30.8±3.2	8.6±1.0

The carbon concentration in CuO-GO is on 0.8 at.% lower than in GO and {CuO+GO} mixture, which is indicative for the bonding between CuO and GO in nanoplatform.

The oxygen concentration in CuO-GO nanoplatform is on 2.8 at.% lower than in GO, which can be caused by the partial removal of carbon oxide or dioxide during the CuO phase formation at the contact with GO.

The concentration of O and Cu in the {CuO+GO} mixture is on 6.0 at.% and 1.4 at.% lower than in CuO-GO nanoplatform, demonstrating less amount of CuO phase in the mixture, which is in agreement with the XRD results (Figure 4).

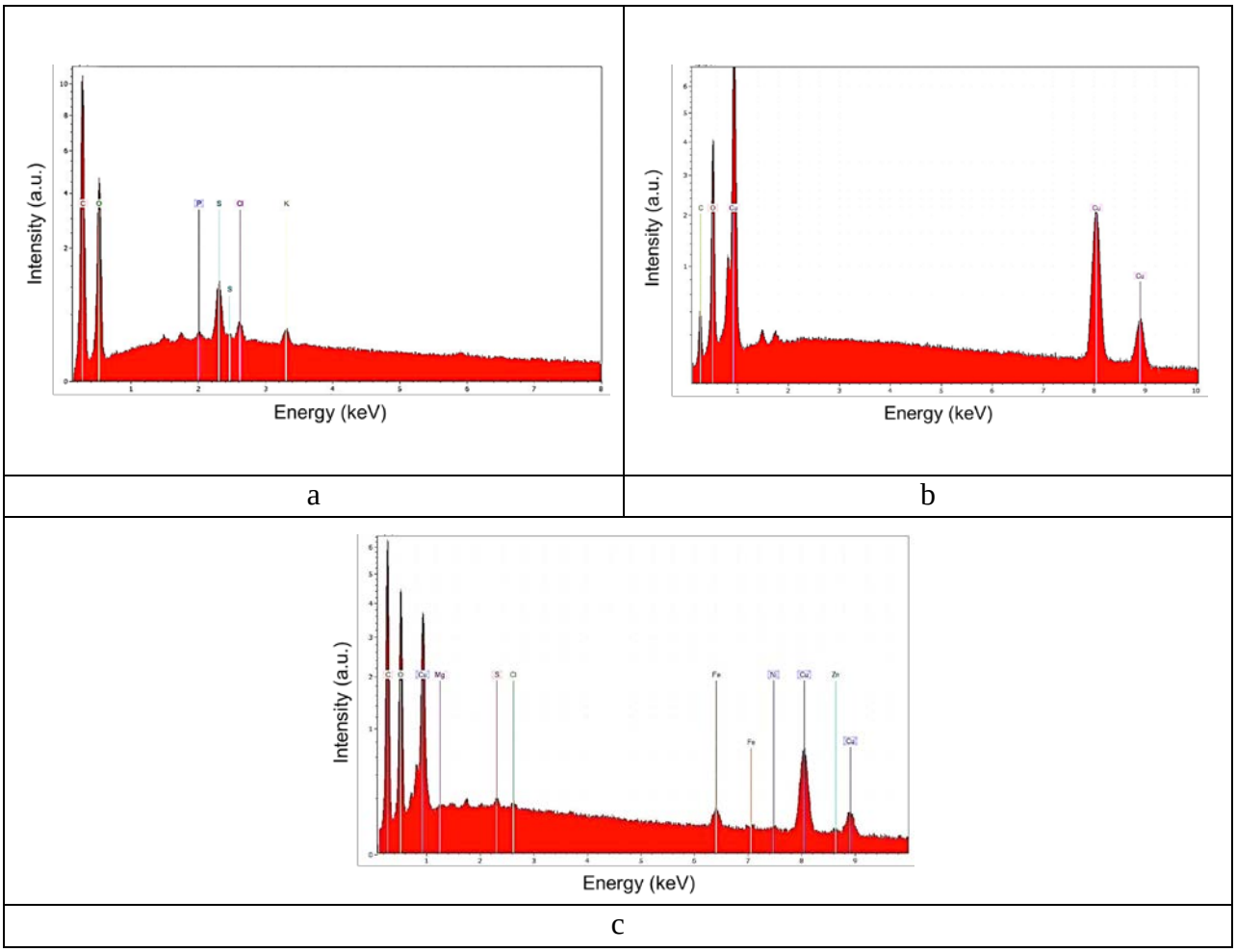

a – synthesized GO (at U=20.0 kV); b – Cu-GO nanoplatform (at U=15.0 kV); c – {CuO+GO} colloidal mixture (at U=15.0 kV)

Figure 5. Energy dispersive X-ray fluorescence spectra of GO, CuO-GO nanoplatform and {CuO+GO} colloidal mixture

3.4 Functionalization of diclofenac with CuO-GO nanoplatform

The molecular chemical structure and complexation of diclofenac with CuO-GO nanoplatform was defined by the FTIR transmittance spectroscopy and compared to pristine drug (Figure 6, Table 4).

The ultrasonic binding of diclofenac to CuO-GO nanoplatform can occur involving interaction with the Cu-O and C-H benzene ring (~664-853 cm^{-1} and 1025 cm^{-1}) as indicated by their strong bands, but also through the C=C-OH bonding and interaction with –C=O carboxylic groups (~900 cm^{-1} and 1160 cm^{-1}), and C-Cl (to a much lesser degree) (Figure 6a).

The complexation of diclofenac can also involve its interaction with the –C=O carboxylic moiety through the formation of the internal H-bonding: band at 1638 cm^{-1} in diclofenac-CuO-GO. The presence of H-bonding is identified by the appearance of a broad band at ~3435 cm^{-1} in diclofenac-CuO-GO nanoparticles (Figure 6b).

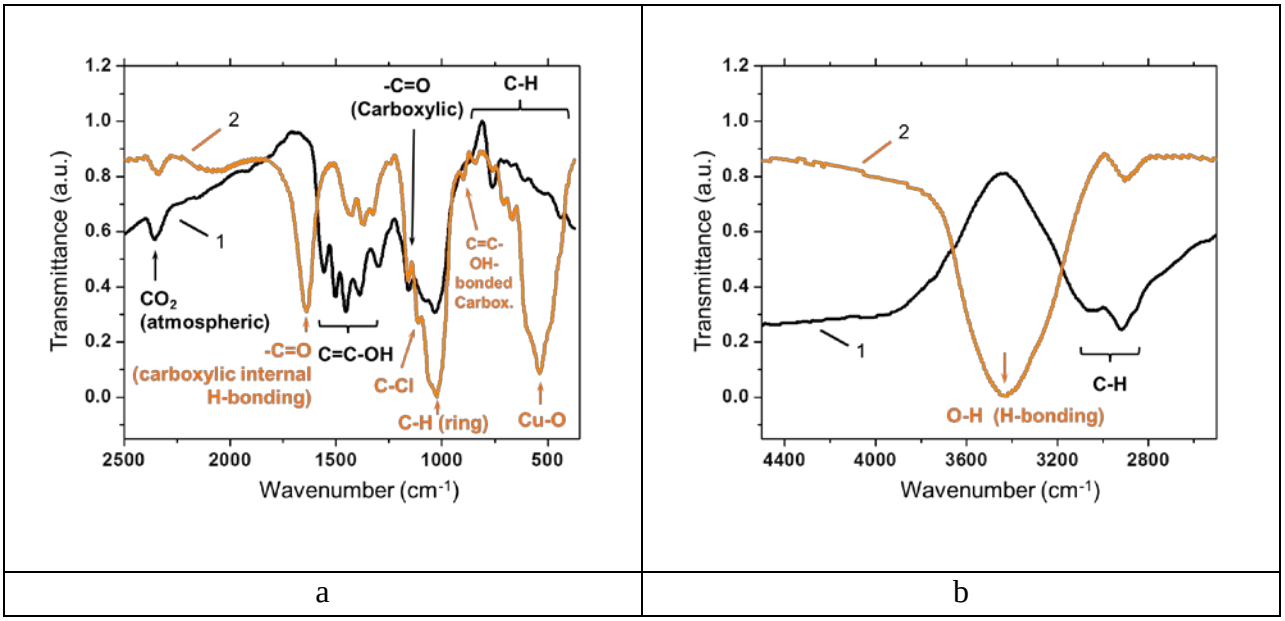

a b

a – FTIR transmittance spectra of diclofenac *per se* (spectrum 1) and diclofenac-CuO-GO (spectrum 2) in 450-2500 cm^{-1}; b – in 2500-4500 cm^{-1}

Figure 6. The molecular chemical structure of diclofenac *per se* and diclofenac-CuO-GO obtained from FTIR transmittance spectroscopy analysis

Table 4

Analysis of FTIR transmittance spectra of diclofenac-CuO-GO in comparison with pristine diclofenac in the powder form

Diclofenac-CuO-GO nanoparticle		**Pristine diclofenac**	
ν, cm^{-1}	**Assignment**	**ν, cm^{-1}**	**Assignment**
537	Cu-O	437-875	C-H
664-853	C-H	1033	C-H[d]
900	C=C-OH[a]	1080	C-Cl
1025	C-H (ring)	1156	-C=O (carboxylic group)
1112	C-Cl	1296-1500	C=C-OH
1160	-C=O (carboxylic group)	1556	-C=O[b]
1240-1440	C=C-OH	2357	CO_2*
1638	-C=O[b]	2920, 3055	C-H
2340	CO_2*		
2905	C-H		
3435	O-H[c]		

[a]C=C-OH bonded to the carboxylic group, [b]-C=O of the carboxylic group with the internal H-bonding, CO_2* - atmospheric carbon dioxide, [c]O-H in the H-bonding, [d]C-H benzene ring vibration

The next question to answer was, whether CuO and GO can prevent the drug from undesirable surface defects or damage caused by ultrasound. To find it out, pristine sodium diclofenac (in a powder form) was treated by ultrasound (20 kHz, 18 $W \cdot cm^{-2}$) in DI water (pH=5.5) for 1, 3, 5, 10, 15 or 30 min. To note, sonication of diclofenac (powder) in aqueous solution for 30 min did not result in its entire dissolution enabling us to collect the sediment and use it for the study by FTIR spectroscopy. Overall, FTIR spectra of pristine diclofenac after 1-15 min of ultrasonic treatment in aqueous solution are similar to those of untreated powder, demonstrating that ultrasound did not changed the chemical structure of this drug (Figure 7).

However, considerable changes in spectra were observed in diclofenac after 30 min of ultrasonic treatment. In particular, multiple peaks were replaced by two small C-H bands of diclofenac (440 cm^{-1} and 675 cm^{-1}) and C-Cl vibration (1108 cm^{-1}) disappeared (Table 5). In addition, the C-H vibration in the far infrared region splitted into two peaks at 2853 cm^{-1} and 2917 cm^{-1} and the disappearance of the N-H stretching (3245 cm^{-1}) was accompanied by the appearance of a strong broad OH band (3463 cm^{-1}), indicating the H-bond formation between the disrupted benzene rings of diclofenac.

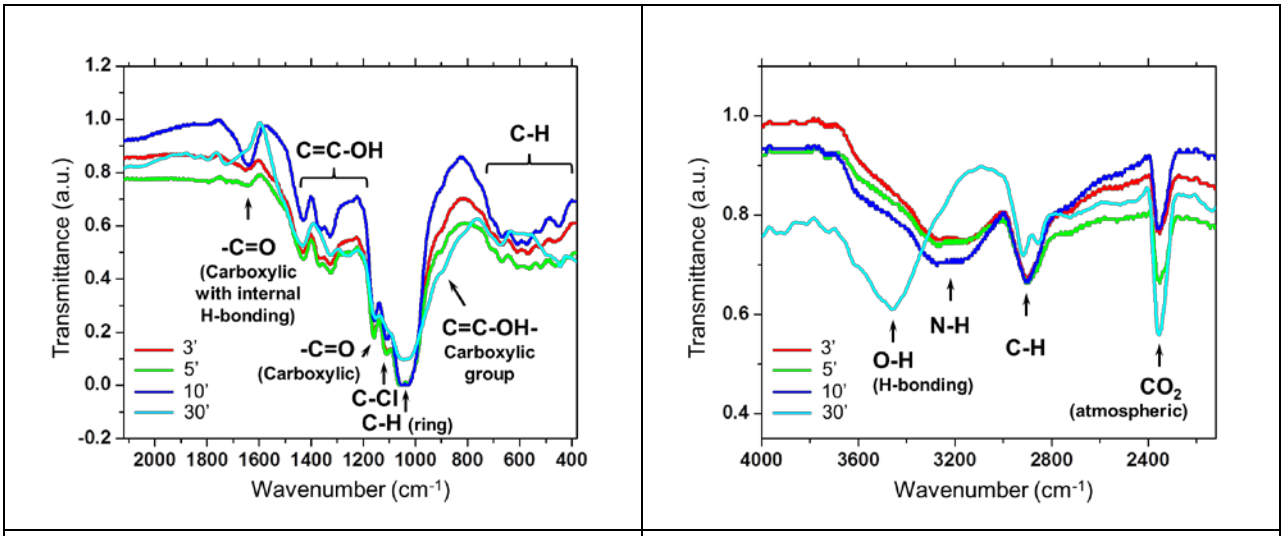

a b

a – FTIR transmittance spectra of diclofenac *per se* powder after 30 min of ultrasonic treatment in aqueous solution in 400-2200 cm^{-1}; b – in 2200-4000 cm^{-1}

Figure 7. The molecular chemical structure of diclofenac *per se* and diclofenac-CuO-GO fter 30 min of ultrasonic treatment obtained from FTIR transmittance spectroscopy analysis

It is important to note, that the C=C-OH vibration of the carboxylic acid group in diclofenac remained unchanged at 900 cm^{-1}, but disappeared at 1367 cm^{-1}, while the –C=O band of this group was blue shifted at 1153 cm^{-1} and disappeared at 1640 cm^{-1} after 30 min of sonication, indicating the loss of the internal H-bonding involving the C=O carboxylic acid groups. However, three small C=O bands of carbonyl group in diclofenac appeared at 1725 cm^{-1}, 1796 cm^{-1} and 1845 cm^{-1} after 30 min of sonication demonstrating that H-bonding mostly involves the C-H vibrational bands of one of the benzene rings and carbonyl groups instead of the C-Cl and carboxylic acid moieties. In general, ultrasound caused the scissoring of two benzene rings and a significant loss of the carboxylic acid groups and C-Cl moiety in pristine diclofenac, but preserved C=O carbonyl groups that were interconnected by H-bonds. Therefore ultrasound can cause binding of diclofenac through the Cu-O bond formation with the C-H benzene ring and –C=O carboxylic acid moieties with the internal H-bonding in CuO-GO nanoparticles.

Table 5

Analysis of FTIR transmittance spectra of pristine diclofenac after ultrasonic treatment at 20 kHz (18 W/cm^2) in the aqueous solution at pH=5.5 in the open air.

1 min	**3 min**	**5 min**	**10 min**	**30 min**	**Assignment**
400-712	400-712	400-712	400-712	440-675	C-H
900	900	900	900	900	C=C-OH[a]
1040	1040	1040	1040	1040	C-H[b]
1108	1108	1108	1108	-	C-Cl
1160	1160	1160	1160	1153	-C=O[c]
1325	1325	1325	1325	1325	C=C-OH
1367	1367	1367	1367	-	
1428	1428	1428	1428	1428	
1640	1640	1640	1640	-	-C=O[d]
-	-	-	-	1725	C=O (carbonyl group)
-	-	-	-	1796	
-	-	-	-	1845	
2355	2355	2355	2355	2355	CO_2 (atmospheric)
-				2853	C-H
2903				2917	
3245				-	N-H stretching
-				3463	O-H[e]

[a]C=C-OH bonded to the carboxylic group, [b]C-H of the benzene ring, [c]-C=O of the carboxylic group, [d]-C=O of the carboxylic group with the internal H-bonding, [e]O-H (H-bonding)

3.5 Stability of diclofenac-CuO-GO nanoparticles

The stability of diclofenac-CuO-GO nanoparticles was explored by the UV-Vis absorption spectroscopy in aqueous solutions adjusted to pH=1, 5 or 8 (Figure 8).

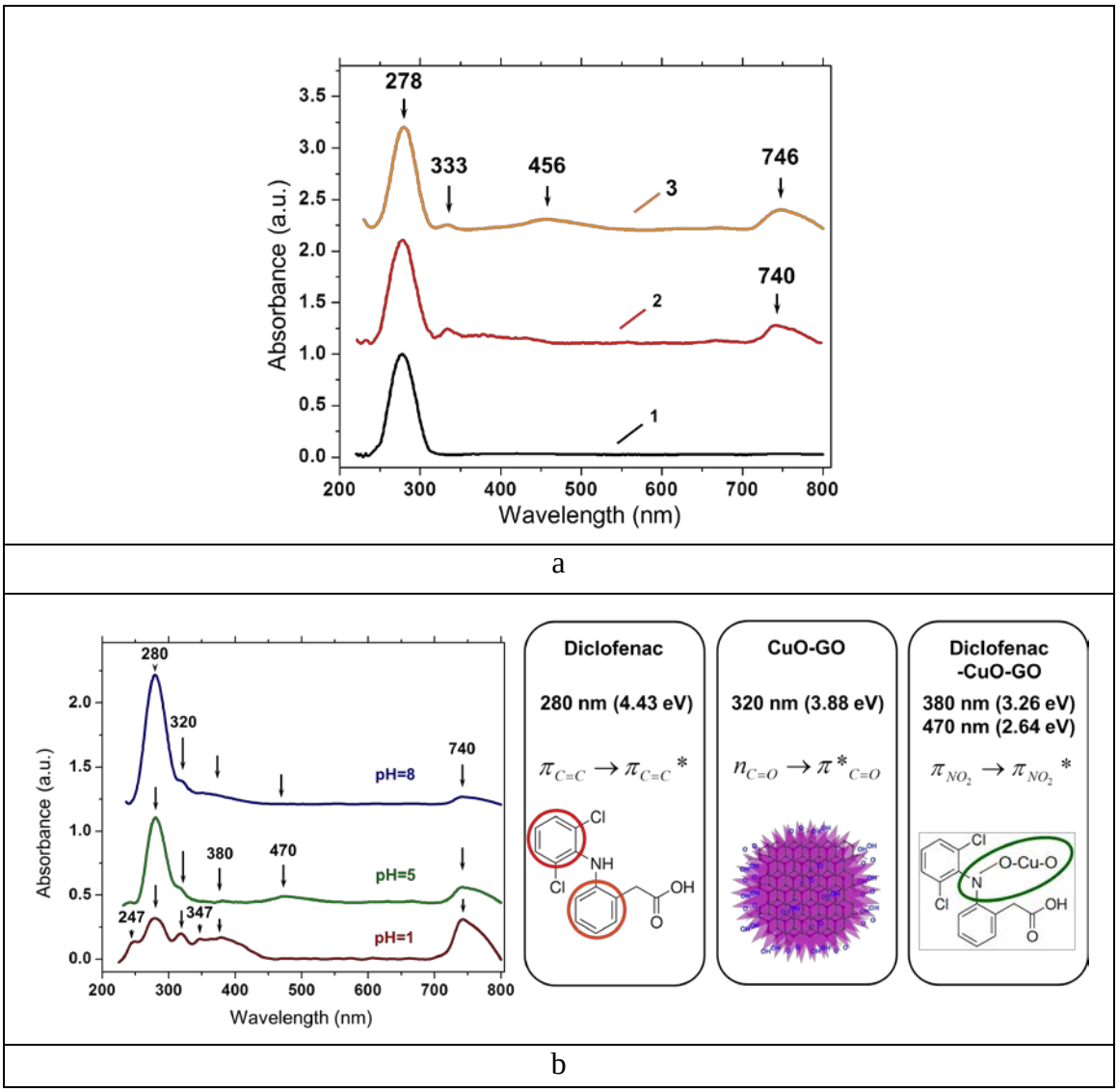

a – UV-Vis absorption spectra of aqueous solutions of pristine diclofenac (spectrum 1), diclofenac-GO (spectrum 2) and diclofenac-CuO-GO (spectrum 3) prepared by ultrasound (20 kHz, 18 W/cm^2); b – UV-Vis absorption spectra of aqueous solutions of diclofenac-CuO-GO adjusted to pH=1, 5 or 8

Figure 8. The electronic structure of diclofenac *per se*, diclofenac-GO and diclofenac-CuO-GO (after incubation at pH=1, 5 or 8)

In general, pristine diclofenac absorbs light at 278 nm (4.46 eV) as a result of π–π* transition in aromatic C=C bonds, and the position of this band cannot be influenced by the binding of diclofenac to GO or CuO-GO nanoplatform (Figure 8a). Diclofenac-GO and diclofenac-CuO-GO nanoparticles exhibit a small peak at ~333 nm (3.72 eV) showing the band-to-band transition in GO. Another two broad weak peaks near ~432 nm and ~456 nm can be assigned to diclofenac with the structure comparable to the O-nitro aniline depending on its oxidation state [58-60].

The absorption spectra of diclofenac-CuO-GO nanoparticles in aqueous solution adjusted to pH=1, 5 or 8 are shown in Figure 8b. It is established that diclofenac undergoes the intramolecular cyclization in acidic medium leading to inactivation of this drug. In contrast, at pH=1, diclofenac-GO-coated CuO nanoparticles exhibit a complicated UV-Vis absorption spectrum that shows multiple peaks with a maximum at 247 nm (5.02 eV) due to the interaction with GO. In this absorption spectrum a broad peak at 280 nm (4.43 eV) that is assigned to diclofenac appears with a lower intensity because the drug loses Na^+ and becomes less soluble as only Na^+ favors its dissolution in H_2O. The presence of a smaller band at 320 nm points out to the binding of diclofenac to the CuO-GO surface. Another important feature is a broad band with distinct maxima near 347 nm and 380 nm that are located in the absorption region of n–π* transition in CuO-GO nanoplatform and π–π* transition in NO_2 group of aniline's phenyl ring of diclofenac.

At pH=5, all these peaks became weaker except of the main absorption band of diclofenac (280 nm) and a very small peak appeared near 470 nm pointing out to the formation of Cu-8-quinolinate in H_2O [61]. At pH=8 the characteristic absorption peak of diclofenac became more pronounced but without any spectral shift. Other bands appeared at ~320 nm, 347 nm and 740 nm with a decreased intensity, while the band near ~380 nm disappeared, demonstrating a lower amount of diclofenac molecules in CuO-GO nanoparticles in basic medium.

In our experiments, CuO-GO nanoplatform has a relatively large average size (342±160 nm) and a well-defined flower-like morphology, CuO crystalline phase and amphiphilic GO coating in the complex with diclofenac that would be beneficial for intracellular studies because of the following reasons. This large size and well-defined spherical morphology of CuO would induce less toxicity to mammalian cells. The possible cytotoxicity caused by ROS production and copper ion leaching of CuO-GO could be controlled by the specific interaction with diclofenac and functional groups of GO. The bioavailability of diclofenac together with GO would also contribute to the reduction of possible toxic effects in mammalian cells, and can profitably enhance antibacterial action in bacteria. We suggest that for more reliable *in vivo* studies the size of diclofenac-CuO-GO nanoparticles should be decreased to 100 nm or lower.

*****

The presented results allow us to draw the following conclusions:

1. Ultrasound-assisted synthesis of CuO-GO nanoplatform leads to the coating of pure CuO phase with GO through the binding with C-O or C=O bearing functional groups, in contrast to the ultrasonically treated mixture of preformed GO and CuO particles.
2. The ultrasonic binding of diclofenac to CuO-GO nanoplatform can occur involving interaction with the Cu-O bond and C-H benzene ring, the C=C-OH and –C=O carboxylic groups bonding.
3. The ultrasonic complexation of diclofenac can also involve its interaction with the –C=O carboxylic moiety through the formation of the internal H-bonding with CuO-GO nanoplatform.
4. Ultrasound acts differently on the structure of pristine free and complexed diclofenac molecules: 15 min of treatment of free drug did not change its structure, but after 30 min leads to H-bond formation and disruption of benzene rings of diclofenac, in contrast to complexed diclofenac.
5. We defiend the conditions of stability of diclofenac-CuO-GO nanoparticles: at pH=1 diclofenac is strongly bonded to CuO-GO and becomes less soluble, at pH=5 and pH=8 diclofenac retains its structure as Cu-8-quinolinate in H_2O, but becomes more soluble at higher pH.

CHAPTER 4 FUNCTIONALIZATION OF ACETYLSALICYLIC ACID THROUGH ULTRASONIC COMPLEXATION WITH GRAPHENE OXIDE COATED COPPER OXIDE NANOPARTICLES

After more than a century, acetylsalicylic acid (ASA, aspirin) remains one of the most commonly used drugs for its anti-thrombotic, anti-pyretic, and analgesic properties [1]. Aspirin is an O-acetyl derivative of salicylic acid and its dominant mechanism of action is believed to be through the transfer of this acetyl group to (−OH) and amino ($-NH_2$) functionalities present in biological macromolecules. The acyl ester group is unstable under basic conditions, and its hydrolysis to acetate can proceed by a general base-assisted mechanism. Computational studies reveal the existence of an $n \rightarrow \pi^*$ interaction between the aromatic carboxylic acid and the carbonyl carbon of the acetate group in ASA [2]. The chemistry of ASA explains that the negatively charged a nucleophilic hydroxide anion generated by water can attack the carbonyl carbon of the acetate group resulting in hydrolysis of ASA into salicylate and acetate (general base catalysis) (Figure 1) [3,4]. It was suggested that a mixed anhydride can be formed through a hemiorthoester anion intermediate, but the detailed mechanism of hydrolysis remains unexplored.

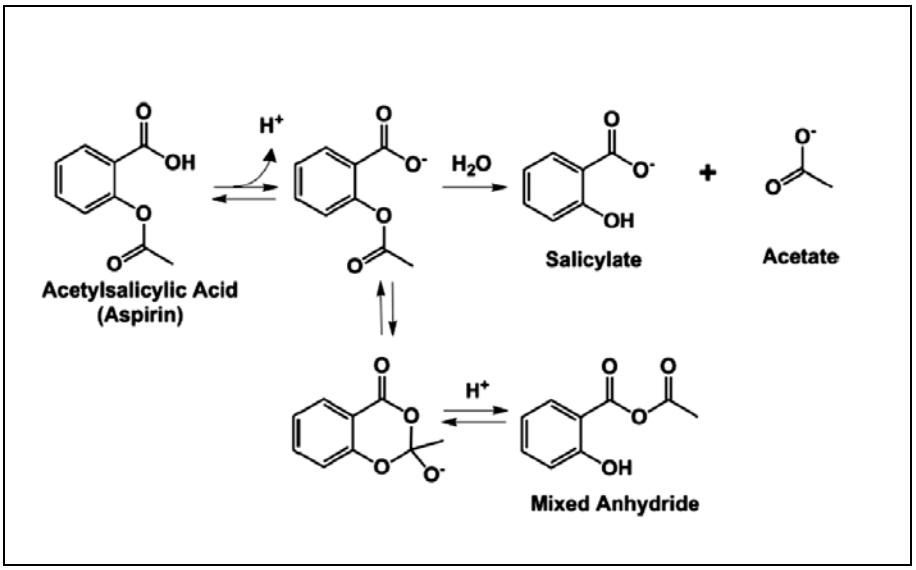

Figure 1. Scheme explaining the basic chemistry of acetylsalicylic acid under basic conditions adapted from reference [2]

ASA inhibits COX-1 and COX-2 via the covalent modification of active site serine residues, resulting in irreversible inhibition through steric blockade of the active site. The site-selective acetylation of COX-1 and COX-2 can occur through molecular recognition of the

benzoic acid functionality of ASA, while the non-specific acetylation function of ASA depends on the chemical environment and its pH. For example, in the acidic medium of the gastric mucosa (pH=2-3) the carboxylic acid (pK_{α}=3.5) is in the protonated state, thereby reducing the hydrolysis rate of ASA. In contrast, in the basic medium of the gastroduodenum (pH=7-8) the carboxylate group is deprotonated, thereby increasing the rate of hydrolysis and transacetylation. In addition to pH of the chemical environment, the aromatic ring and carboxylic acid play important roles in aspirin's reactivity and stability through π-π stacking interactions or hydrogen bonding of the carboxylic acid and/or the free hydroxyl.

Overall the absorption rate and extent of ASA and salicylate in the gastrointestinal lumen can be modulated by their pH-dependent molecular electronic structure. The gastric metabolism of ASA, in which the acetyl moiety binds covalently to proteins and other biomolecules in the stomach wall, is consistent with its gastric toxicity, and its analgesic activity increases with the raised availability of the intact drug [5]. Only recently the effects of ASA on the platelet functions are better understood so that new methods based on metal ion complexation can be developed to lessen in extent of harmful gastrointestinal damage [6].

For example, the copper-ASA complexes can exhibit improved potent anti-inflammatory and anti-thrombotic activity than free drug resulting in a fewer side effects in rats or mice [7,8]. Such advanced pharmacological activity of this compound is related to its final crystal structure, the specific coordination to water molecules via H-bonding and the improved COX-1/COX-2 selectivity. In many compounds ASA is bonded to the central Cu atom through the carboxyl groups. However, most of the existing Cu(II)-ASA complexes have weakly bound carboxylic acid ligands and can easily dissociate favoring the interaction of $O_2\cdot$ radicals with the free sites of copper. Therefore, it is necessary to understand the electronic molecular surface structure of Cu(II)-ASA complexes in aqueous solution at different pH values in order to improve their functions.

Important functions like the selective bioavailability and biodegradability of drug and increase of its surface active area can be modulated by conjugation with GO as a nanoscale carrier [9,10,11]. The joint CuO-GO structure can significantly improve selectivity towards catalytic oxidation of cyclohexane [12], anticancer sensing [13], antimicrobial and antioxidant activities [14], while aspirin-loaded GO-based nanomaterials can constitute anti-inflammatory biomaterials with enhanced bioactivity [15,16]. Up to present the physico-chemical properties of complexed ASA with CuO-GO are not yet defined.

4.1 Functionalization of pristine acetylsalicylic acid with CuO-GO nanoplatform

We use preformed CuO-GO nanoplatform, which was characterized in details in Chapter 3, for the ultrasonic complexation of pristine ASA to synthesize ASA-CuO-GO nanoparticles.

The molecular chemical structure and complexation of ASA with CuO-GO was defined by the FTIR transmittance spectroscopy and compared to pristine ASA (Figure 2).

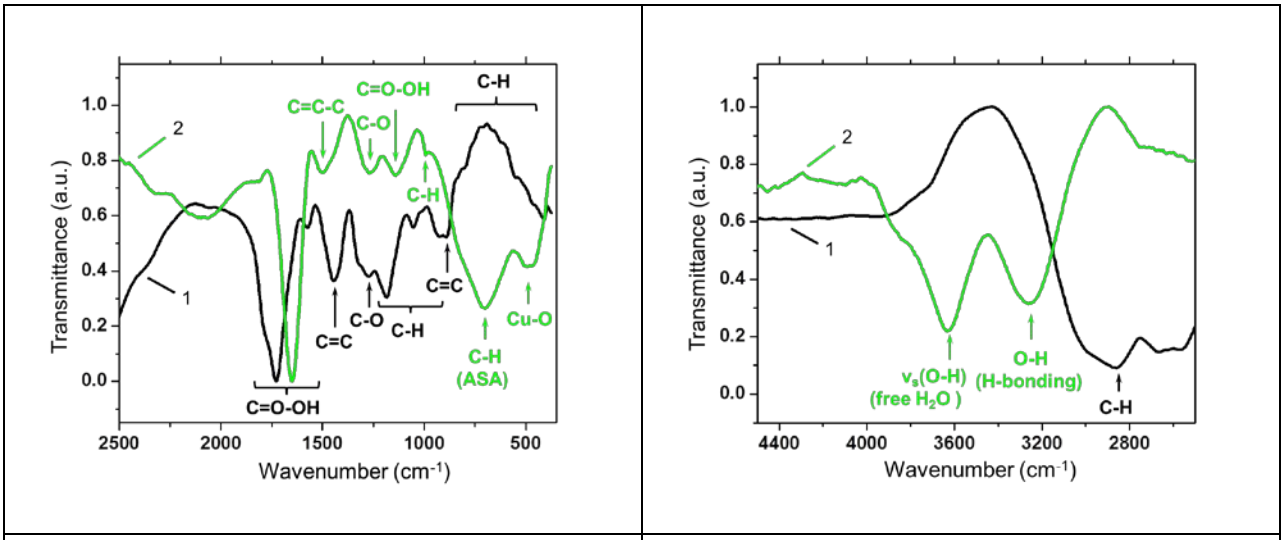

a b

a – FTIR transmittance spectra of acetylsalicylic acid (ASA) *per se* (spectrum 1) and ASA-CuO-GO (spectrum 2) in 450-2500 cm^{-1}; b – in 2500-4500 cm^{-1}

Figure 2. The molecular chemical structure of pristine ASA and ASA-CuO-GO obtained from FTIR transmittance spectroscopy analysis

FTIR spectra of ASA-CuO-GO nanoparticles show characteristic peaks of Cu-O vibration [17-20] at ~485 cm^{-1} and at ~537 cm^{-1} (Table 1). These observations point out to the binding mechanism of ASA to CuO-GO that is different from diclofenac because of changes in the electronic configuration of the neighboring functional groups. The closest bands to the Cu-O vibration are the C-H out of plane ring bending of ASA (~702 cm^{-1}), C-H vibration of the methyl group and the C=O-OH stretching of the carboxylic group due to the interaction with the Cu-O-H in ASA-CuO-GO nanoparticles (Figure 2a). The binding of ASA can involve its interaction with the –C=O carboxylic moiety through the formation of the internal H-bonding due to the appearance of a band at ~1650 cm^{-1} in ASA-CuO-GO. The presence of H-bonding is identified by the appearance of a broad OH band at ~3260 cm^{-1} in ASA-CuO-GO (Figure 2b). In contrast to diclofenac, the O-H stretching of free water molecules at ~3632 cm^{-1} in ASA-CuO-GO can be associated to CuO [21,22]. To note, sonication of pristine ASA (20 kHz, 18 $W \cdot cm^{-2}$) in DI water (pH=5.5) for 1, 3, 5, 10 or 15 min did not change the chemical structure of this drug (Figure 3).

Table 1

Analysis of FTIR transmittance spectra of pristine ASA and ASA-CuO-GO

ASA-CuO-GO nanoparticle		**Pristine acetylsalicylic acid**	
ν, cm^{-1}	**Assignment**	**ν, cm^{-1}**	**Assignment**
485	Cu-O	410-875	C-H
702	C-H (ASA)	890	C=C
993	C-H	925	C-H (CH_3)
1140	C=O-OH/Cu-O-H	1053	C-H (ASA)
1267	C-O	1184	C-H (ASA)
1500	C=C-C	1272	C-O
1650	C=O-OH	1445	C=C (ASA)
1815	-C=O (Carbonyl)	1513	C=C-C
2320	CO_2 (atmospheric)	1727	C=O-OH
3260	O-H (H-bonding)	2860	C-H
3632	O-H (free H_2O)		

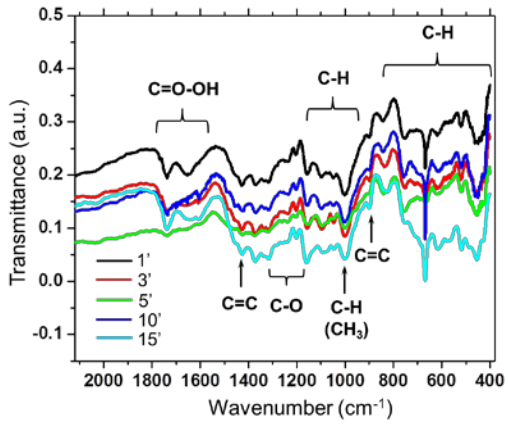

a

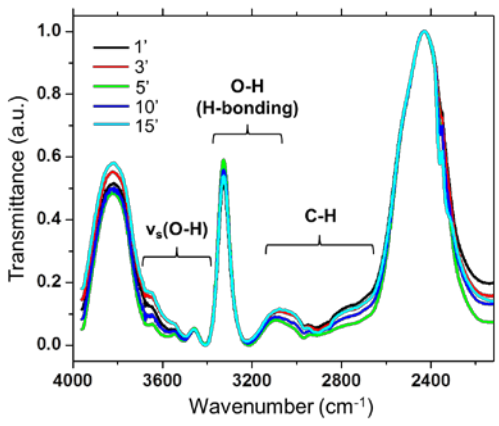

b

a – FTIR transmittance spectra of acetylsalicylic acid (ASA) *per se* after 15 min of ultrasonic treatment in aqueous solution (20 kHz, 18 W/cm^2) in 380-2120 cm^{-1}; b – in 2120-4000 cm^{-1}

Figure 3. The molecular chemical structure of pristine ASA and ASA-CuO-GO after 15 min of ultrasonic treatment obtained from FTIR transmittance spectroscopy analysis

4.2 Stability of ASA-CuO-GO nanoparticles

The stability of ASA-CuO-GO was examined in solutions at pH=1, 5 or 8 (Figure 4).

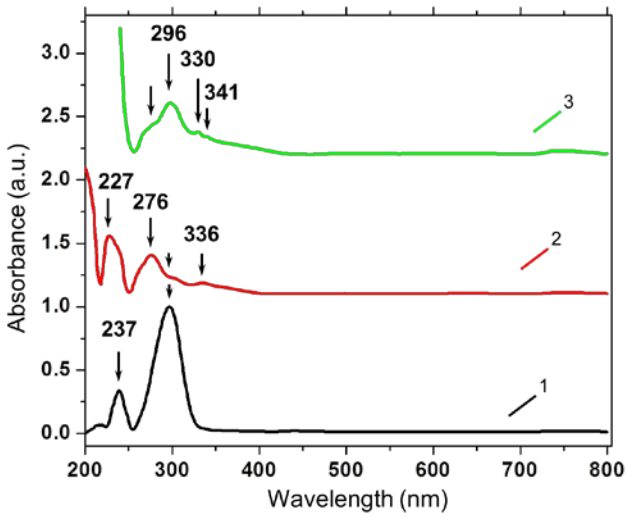

a

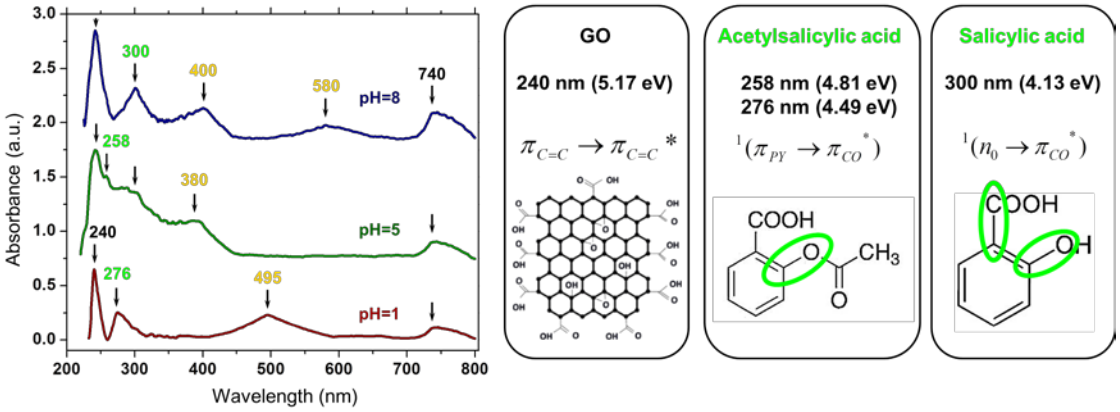

b

a – UV-Vis absorption spectra of aqueous solutions of pristine ASA (spectrum 1), ASA-GO (spectrum 2) and ASA-CuO-GO prepared by ultrasound (20 kHz, 18 W/cm^2); b – UV-Vis absorption spectra of aqueous solutions of ASA-CuO-GO adjusted to pH=1, 5 or 8

Figure 4. The electronic structure of ASA *per se*, ASA-GO and ASA-CuO-GO (after incubation at pH=1, 5 or 8)

The UV-Vis absorption spectrum of pristine ASA aqueous solution shows two absorption maxima at ~237 nm and ~296 nm (Figure 4a). The first absorption peak (5.23 eV) can be assigned to the singlet transition in the π (bonding) molecular orbital from the phenyl ring involving –C=C- or C=O bonds to its π* (anti-bonding) orbital and is designated as $^1(\pi_{py}\text{-}\pi_{co}^*)$ of ASA [21-23]. The π-π* transition typically occurs in a molecule that possesses a chromophore with an unsaturated bond such as C=C or C=O in the carboxylic acid. The second absorption peak (4.19 eV) results from the singlet transition in electronically excited oxygen lone pair of the *n* (non-bonding) atomic orbital of the -C-OH bond to the *π** (anti-bonding) orbital and is designated as $^1(n_o\text{-}\pi_{co}^*)$ of the salicylic acid [23].

The binding of ASA to GO transformed the peak at 237 nm into a shoulder of an intense absorption band at ~227 nm of GO due to the π–π* transition in aromatic C=C bonds as confirmed by the calculated triplet electronic transition, demonstrating the conjugation of this drug with GO. The absorption peak of salicylic acid at ~296 nm appeared as a broad peak with a maximum at ~276 nm that is a characteristic band of ASA. These changes in the absorption spectra were followed by the appearance of a small peak near ~336 nm (3.69 eV) due to the C=O band-to-band $n_o\text{-}\pi_{co}^*$ transition in GO. In contrast to GO, the binding of ASA to GO-CuO occurs via the n-π* transition in the C=O band of GO. Its closer junction to CuO (330 nm) takes place through the singlet electronic transition of the acetyl-carbonyl group (341 nm) involving interaction with the salicylic acid moiety of the second derivative (296 nm) component. These observations are in agreement with the FTIR analysis (Figure 2, Table 1).

It is important to note, that the electronic molecular structure of ASA-CuO-GO nanoparticles changed at pH=1, 5 or 8 (Figure 4b). UV-Vis absorption spectra of ASA-CuO-GO exhibited an intense peak of GO at 240 nm at any pH. At pH=1 a single absorption peak of ASA at 276 nm reveals that the drug (~99%) is in its nonionized form. Therefore ASA-CuO-GO can be potentially able of diffusing through the lipid membrane in the stomach acidic medium. Another very broad absorption band (~495 nm) appeared at pH=1, pointing out to the closer junction of ASA to the sisal-like CuO nanoparticle with a typical band closer to GO (~2.27 eV). At pH=5, the main absorption peak of ASA (~276 nm) appeared as a broad band with small maxima at ~258 nm (~4.81 eV) and ~400 nm (~3.1 eV). These changes demonstrate the gradual ionization of ASA in contact with the carboxylic and salicylic acid groups and CuO with a nanoplatelet morphology, which has a characteristic absorption band at 400 nm (indicated by an orange color in Figure 4b). At pH=8, three broad absorption maxima (~300 nm, ~400 nm and ~580 nm) appeared in addition to the previously mentioned GO peak at ~240 nm. These peaks point out to the dissolution of ASA from CuO-GO in basic medium, leaving the salicylic acid moiety as the hydrolysis product in the closer junction with the CuO-GO surface.

Overall, the results show that ultrasound binds free ASA to CuO-GO nanoplatform through the complexation with Cu-O, C-H of the benzene ring and carboxylic acid moiety that are linked with H-bonds, as determined by the UV-Vis absorption and FTIR spectroscopy methods. ASA-CuO-GO nanoparticles are linked with H-bonds within the CuO-GO complex. As the aqueous medium becomes more basic, ASA undergoes hydrolysis and its active component (salicylic acid) is retained in CuO-GO within the H-bonded network. This knowledge improves our understanding about the electronic molecular structure of ASA and salicylic acid and their ionization states during interaction with CuO nanoparticles and oxidized graphene that can be expanded to many other drugs. The obtained results can be of use for the fundamental studies of the intracellular drug-enzyme functions especially in *in vivo* application.

*****

The presented results allow us to draw the following conclusions:

1. Ultrasound-assisted synthesis of CuO-GO nanoplatform leads to the binding of ASA to GO-CuO via the n-π^* transition in the C=O band of GO.
2. The closer junction of ASA to CuO takes place through the singlet electronic transition of the acetyl-carbonyl group involving interaction with the salicylic acid moiety of the second derivative component.
3. The electronic molecular structure of ASA-CuO-GO nanoparticles undergoes changes in aqueous medium at pH=1, 5 and 8.
4. At pH=1 ASA is in its nonionized form, meaning that ASA-CuO-GO nanoparticles can be potentially able of diffusing through the lipid membrane in the stomach acidic medium.
5. At pH=5 ASA undergoes the gradual ionization in contact with the carboxylic and salicylic acid groups and CuO with a nanoplatelet morphology.
6. At pH=8, ASA dissolves from nanoparticles, leaving the salicylic acid moiety as the hydrolysis product in the closer junction with the CuO-GO surface.

CHAPTER 5 FORMATION OF ACETYLSALICYLIC ACID-ZnO-GRAPHENE OXIDE NANOPARTICLES WITH ENHANCED ANTIBACTERIAL FUNCTION

Acetylsalicylic acid, the common household drug, is extensively used as cardioprotective and antithrombotic agent. Numerous clinical observations and laboratory studies show that regular use of ASA enhances the chemopreventive and chemotherapeutic effects, resulting in reduced risk for cancer: colorectal, oesophageal, breast, lung, prostate, liver and skin via COX-dependent or independent mechanisms [1]. Overall, studies have revealed that inhibition activity of ASA on proteins can be enhanced through the increased binding affinity for either steric blocking of enzymatic transformations, or the covalent acetylation of nucleophilic functional groups (Figure 1).

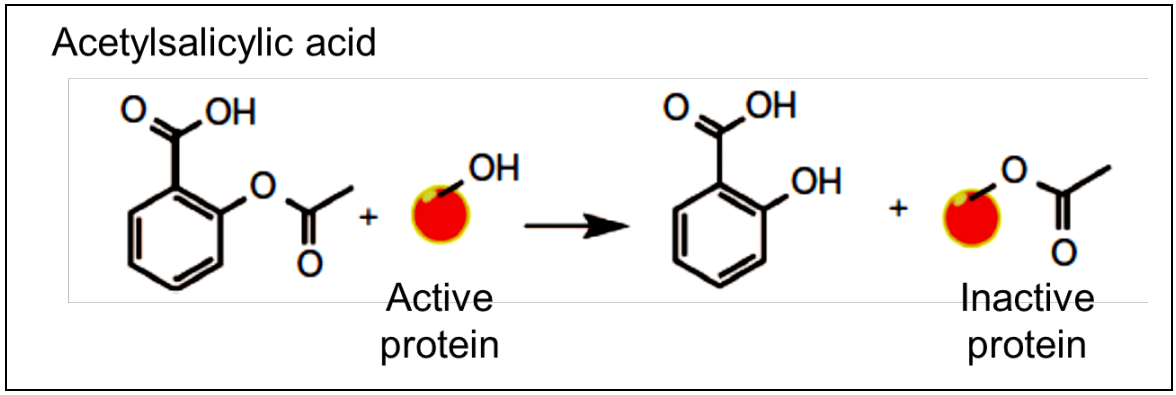

Figure 1. Schematic illustration of protein inhibition activity of ASA in reaction with serine hydroxyl groups in the active site of proteins, in which the acetylation renders the target protein inactive, adapted from ref. [1]

ASA can also affect mitochondrial functions. It increases the mitochondrial membrane permeability, causing the release of cytochrome c, resulting in the activation of caspases followed by cell apoptosis in several cell lines. Another mechanism includes the inhibition of mitochondrial calcium uptake by salicylic acid leading to anti-proliferative effects. Overall, targets of ASA may directly or indirectly modulate the activity of transcription factors, cell signaling proteins, metabolic enzymes and mitochondrial proteins. The acetyl group of ASA can acetylate several proteins other than COX: human serum albumin and fibrinogen *in vitro* and *in vivo*, haemoglobin, DNA, RNA, histones, transglutaminase, hormones and enzymes, glycoproteins and lipids of the stomach, kidney, liver and bone marrow [2-5]. However, ASA is

not currently prescribed for cancer prophylaxis owing to its adverse effects such as the risk of bleeding.

5.1 Antibacterial properties of ASA

Among many NSAIDs, ASA has been applied in co-treatment of bacterial infections showing significant inhibition of bacterial clinical isolates. Studies show that the mixture of ASA and vancomycin results in reduction of *E. faecalis* and methicillin-resistant *S. aureus endocarditis* [6]. ASA with ibuprofen and interferon-gamma exhibit antibacterial activity in the spleen, liver, and main organs infected with Listeria monocytogenes [7]. The growth of Gram-negative and Gram-positive bacteria can be significantly inhibited by ASA in combination with lidocaine hydrochloride [8]. Functionalization of ASA with a D-alanine-D-alanine dipeptide moiety through its attachment to the carbonyl carbon leads to the significant reduction of *Escherichia coli* bacterial growth and colony-forming units (CFU) in contrast to pristine ampilicin [9]. The pronounced antibacterial effect of dipeptide functionalized ASA can be attributed to a larger value of molecular size, indicated by greater values for molar volume, parachor, and molar refractivity.

At therapeutic plasma levels ASA can inhibit the growth of Gram-negative microaerophilic bacteria *Campylobacter pylori*; Gram-negative, microaerophilic and spiral bacteria *Helicobacter pylori*; Gram-negative, non-motile, encapsulated, lactose-fermenting, facultative anaerobic, rod-shaped bacteria *Klebsiella pneumoniae*; filamentous fungus *Epidermophyton floccosum*; *Microsporum spp.* and *Trichophyton spp*. [10-12]. Salicylic acid (SA) can reduce fibronectin binding in *S. aureus* and the adherence of *E. coli* to silastic catheters [13,14] and overall the biofilm production in many types of bacteria [15]. In addition to the modulation of genes by SA, ASA can reduce the production of hemolysin, elastase, protease, and pyocyanin, urease and vacuolating cytotoxin activities. ASA can increase the antimicrobial susceptibility of many pathogens and induce β-lactamase activity through the modulation in the permeability of the outer membrane porin protein (OMP) to antibiotics. The exposure of *E. Coli* to ASA can result in an increase in the relative expression level for *grpE* and *recA* whereas no significant change has been observed for *katG* and *fabA* genes [16]. Up regulation of *grpE* gene upon exposure to ASA can be caused by protein damage because ASA can activate heat shock transcription factor 1 (HSF1), resulting in increased expression of heat shock genes involving in protein misfolding repair pathway. In bacteria ASA can inhibit quorum sensing, reduce virulence and toxins, and protect human melanocytes against H_2O_2-induced oxidative stress [17].

5.2 Effects of Zn-based graphene oxide nanomaterials on bacteria

Contact-dependent growth inhibition is one of competitive mechanisms, which have been identified in probiotic *E. coli* bacteria [18]. The probiotic *E. coli*-mediated growth inhibition involves a Zn^{2+}-dependent enzymatic process, resulting in degradation of the target-cell genomic

DNA. Zinc supplementation can be used in prophylaxis to reduce diarrhea morbidity or as a treatment to shorten the duration of symptoms, and ZnO can protect the cultured human enterocytes from the damage by inhibiting the adhesion of pathogenic bacteria.

It was reported that small ZnO nanoparticles (< 100 nm) exhibit shape-dependent biomimetic inhibition of enzyme and antibacterial activity [19], and have been used in the treatment for oral biofilms [20] and bacterial infections. Overall, ZnO is considered biocompatible and biosafe as approved by U.S. Food and Drug Administration (FDA) [21]. Although the modes of antibacterial action of ZnO nanoparticles are not entirely understood, it has been observed that the bacterial growth inhibition can be increased if smaller NPs are used (6.8 nm size -~ 99.8 %) and their concentration is <100 μg/mL. Three possible mechanisms have been proposed explaining the bacterial growth inhibition by ZnO nanoparticles: 1) bacterial membrane disruption caused by the active surface area of nanoparticles and their concentration; 2) generation of oxidative stress by the formation of reactive oxygen species (ROS), and 3) toxicity caused by the release of free Zn^{2+} ions.

The active surface area and stability of nanoparticles can be modulated by the deposition, precipitation or adsorption of ZnO on GO [22]. GO is biocompatible and its interaction with *E. coli* can be controlled by the oxidation degree (*i.e.* amount of oxygen functional groups), C radical density, and orientation of nanosheets [23]. In addition, the extended 2D surface of GO can serve as a storage for concentration-dependent released Zn^{2+} ions. Deposition of ZnO nanoparticles on GO significantly can lead to the reduction of the minimum inhibitory concentration (MIC) of *E. coli* (~7 μg/mL) as GO cuts the bacterial membrane. Moreover, ZnO-GO nanoparticles can enable a long-term antibacterial activity. At higher concentration these nanoparticles can form complexes with pathogens, leading to either inhibition or enhancement of bacterial growth in a surface potential-dependent manner.

Many methods such as hydrothermal [24], solvothermal [25], spray pyrolysis [26], microwave-assisted [27] and sonochemical [28] have been introduced to produce ZnO nanoparticles with various carbon containing structures (*e.g.* carbon dot-ZnO, GO-Zn or spindle-like ZnO-GO) for various biological applications [29]. In particular, ZnO nanoparticles have been used for encapsulation of antibacterial therapeutics 9-aminoacridine hydrochloride hydrate [30] and plant flavonols such as quercetin [32], propolis extracts [33]. Only few studies have been performed on integration of pharmaceutical compounds such as gentamicin [34] or doxorubicin [35] onto ZnO-GO nanocarriers. Nanocarriers that have a mesoporous ZnO scaffolds showed controlled drug loading efficiency and its faster *in vitro* release kinetics, while GO facilitated enhanced bioactivity of nanomaterial at the contact with live cells.

5.3 Ultrasonic formation of ZnO-GO nanoplatform

Results of analysis of size and morphology of synthesized ZnO-GO nanoplatform is shown in Figure 2.

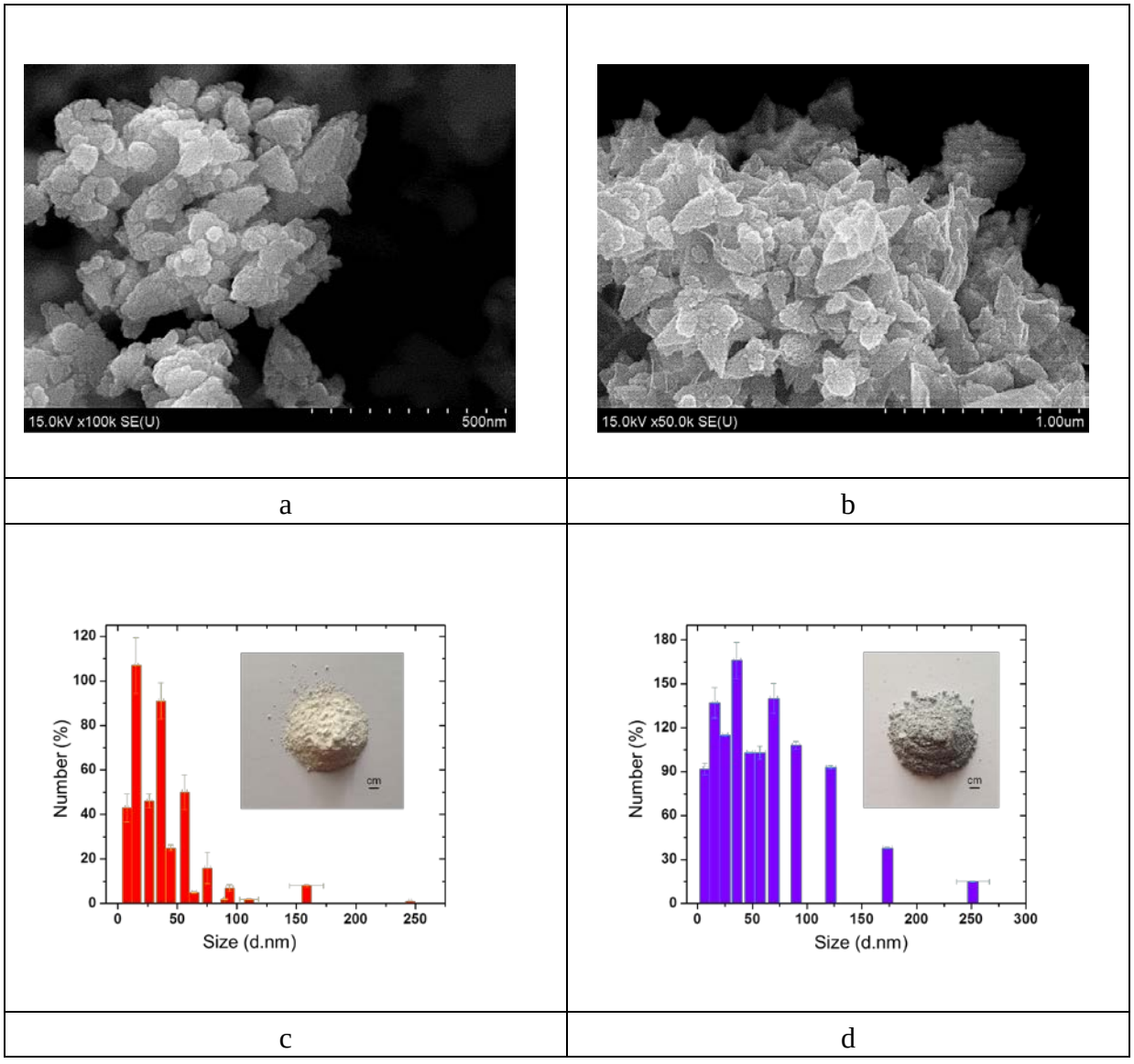

a b

c d

a – SEM images of ZnO nanoparticles (scale bar 500 nm); b – of ZnO-GO nanoplatform (scale bar 1 μm); c – histogram of size distribution of ZnO nanoparticles; d – of ZnO-GO.

Figure 2. The morphology and average size distribution of synthesized ZnO and ZnO-GO nanomaterials

ZnO-GO nanoplatform was synthesized by applying the ultrasound-assisted hydrothermal method based on the mechanism of dissolution–precipitation of ZnO from a system of Zn^{2+} and OH^- [36]. Control experiments were performed without GO (Appendix 4). Analysis of

morphology and size of synthesized nanomaterials revealed irregular shape consisting of small aggregated crystallites with a nonuniform size distribution. Most of ZnO nanoparticles have a spherical shape and are grown into larger nanoparticles with random orientation (Figure 2a). In contrast, formed ZnO-GO nanoplatform has a cone-shaped morphology being composed of small crystallites (Figure 2b). The powders of synthesized nanomaterials have different colors: white ZnO (Figure 2c) and grey ZnO-GO (Figure 2d), which are indicative for white bulk ZnO and GO at the contact with ZnO. The size distribution histograms of ZnO (Figure 2c) and ZnO-GO (Figure 2d) were obtained by estimating the number of nanoparticles per surface area versus the size d (nm) being calculated by using the standard statistical method in electron microscopy [37]. The majority of ZnO nanoparticles have the average size 15.33±1.84 nm (~26.55% of the total number N of collods) and 36.28±1.80 nm (N ~22.50%) [38]. In contrast, most of ZnO-GO nanoplatforms have the average size of 35.95±3.03 nm (N ~14.95%), 69.51±3.41 nm (N~12.61%) and 15.55±2.28 nm (N ~12.34%), 25.01±2.28 nm (N ~10.36%).

Formation mechanism of synthesized ZnO-GO nanoplatform

The final morphology and size of synthesized nanoplatform depend on the molar ratio of precursors and the sequence of addition of aqueous solution of $ZnSO_4$ and NaOH during the thermal treatment at T<100°C [36]. At OH^-:Zn^{2+} molar ratio 2.5, smaller rounder particles with ZnO wurtzite crystal structure are produced, indicating that the larger excess of OH^- ions leads to a complete chemical reaction. When NaOH aqueous solution is added to the $ZnSO_4$ solution in a single addition (as in our experiments), the amount of hydroxide passes the stoichiometric ratio very rapidly and Zn-OH species are formed, followed by decomplexation and fast production of ZnO. The number of nucleation sites is more than sufficient, leading to the particle growth of small (<100 nm) round nanoparticles. When $ZnSO_4$ aqueous solution is added to the NaOH solution in a single addition, the reaction rapidly proceeds from soluble zinc complex to formation of ZnO nuclei. Fewer nuclei are formed, leading to the production of larger cone-shaped nanoparticles.

Nanoparticles are synthesized through the formation of Zn-OH species, followed by their subsequent decomplexation via solubility and precipitation of ZnO. The solubility of zinc hydroxide species depends on the type of anions. In the case of ZnO-GO, OH^- and COO^- anions are formed at pH=5.5. At this pH value both solid $Zn(OH)_2$ and ZnO can be produced. In general, the decomposition of solid $Zn(OH)_2$ to ZnO and water is an endothermic process at room temperature, but is increasingly favorable if larger energy is provided through higher temperature and ultrasonic treatment. Acoustic cavitation and sonochemistry accelerate the decomplexation of $Zn(OH)_2$ via reactions with ultrasonically formed radical species ($\cdot OH$, $\cdot O_2^-$, H_2O_2, etc.) and promote the dissociation of zinc complexes, leading to a controlled supersaturation of free metal ions at the contact with GO.

The crystal growth of cone-shaped ZnO-GO nanoplatform is determined by the thermodynamically less stable polar faces with surface dipoles, which undergo rearrangement to minimize their surface energy. The final morphology is determined via two competing processes, which are based on equilibrium (minimum in the surface energy) or kinetic growth. In ZnO-GO the kinetic growth is additionally supplied by the deposition of ZnO due to the decomplexation of $Zn(OH)_2$ and volatility of zinc carboxylates during acoustic cavitation.

There is an indirect evidence from work involving etching of ZnO single crystals that indicates that carboxylates inhibit the rates of dissolution by 100-fold and tend to aid aging and growth of crystallites [39]. This may cause the arrested growth of cone-shaped ZnO-GO nanoplatform, which acquires the final average size <100 nm.

5.4 Crystalline structure of ZnO-GO nanoplatform

The X-Ray powder diffraction analysis reveals the characteristic reflexes of hexagonal ZnO phase with the wurtzite structure (JCPDS 36-1451) of ZnO and ZnO-GO (Figure 3a). The calculated interplanar spacing d values are listed in Table 1.

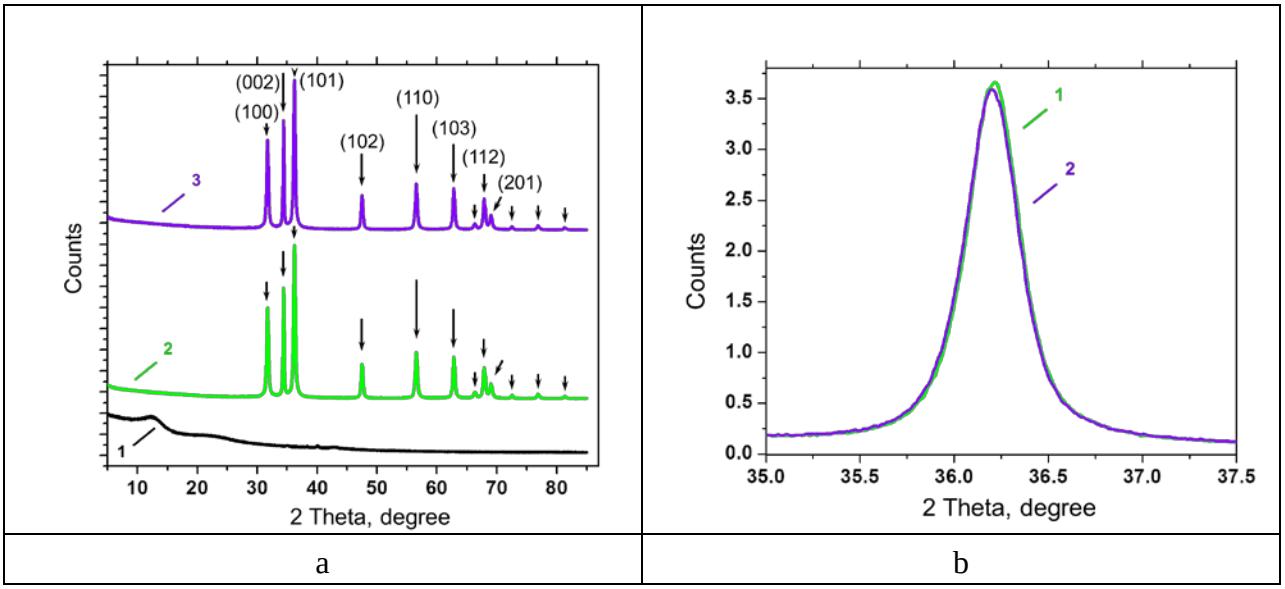

a b

a – X-ray powder diffraction patterns of synthesized GO (1), ZnO (2) and ZnO-GO (3) (Cu Kα=1.54 Å); b – XRD reflex at $2\theta_B$=36.22° for ZnO (1) and $2\theta_B$=36.18° for ZnO-GO (2) to calculate the crystallite size values.

Figure 3. The crystalline structure of synthesized GO, ZnO and ZnO-GO nanomaterials

No diffraction peaks of synthesized GO (shown for comparison), $Zn(OH)_2$ (JCPDS 48-1066), graphite (amcsd 0000049) and diamond (amcsd 0013983) were observed, demonstrating that both ZnO and ZnO-GO are composed of a pure ZnO crystalline phase.

Table 1

Analysis of XRD patterns of synthesized ZnO nanoparticles and ZnO-GO nanoplatform with the calculated interplanar spacing d_{hkl} values

ZnO				**ZnO-GO**			
2θ (°)	**Int. (a.u.)**	**(hkl)**	**d_{hkl} (Å)**	**2θ (°)**	**Int. (a.u.)**	**d_{hkl} (Å)**	**(hkl)**
31.68	59	(100)	2.82	31.70	60	2.82	(100)
34.39	72	(002)	2.61	34.39	73	2.60	(002)
36.22	100	(101)	2.48	36.20	100	2.48	(101)
47.46	21	(102)	1.91	47.48	73	1.91	(102)
56.55	29	(110)	1.63	56.51	81	1.63	(110)
62.76	26	(103)	1.48	62.82	26	1.48	(103)
66.29	3	(200)	1.41	66.30	3	1.41	(200)
67.90	19	(112)	1.38	67.90	20	1.38	(112)
68.97	8	(201)	1.36	69.00	8	1.36	(201)
72.53	2	(004)	1.30	72.49	1	1.30	(004)
76.86	2	(202)	1.24	76.90	2	1.24	(202)
81.32	1	(104)	1.18	81.30	1	1.18	(104)

The size *t* of crystallites was calculated by using the Scherrer's formula with the estimated values of $\Delta\theta_B$ (ZnO)=0.326 and $\Delta\theta_B$ (ZnO-GO)=0.368, β (ZnO) ≈0.005 and β (ZnO-GO) ≈0.006 (Figure 3b). The size *t* of ZnO crystallites is ~25.37 nm and of ZnO-GO is ~22.45 nm, indicating that nanoplatform with the cone-shaped morphology has a smaller width than nonuniform nanoparticles with random orientation.

The Zeta potential of ZnO-GO (-3.6±2.3 mV) is comparable with ZnO (-4.7±2.7 mV), but not with GO (-19.9±5.4 mV) (Figure 4).

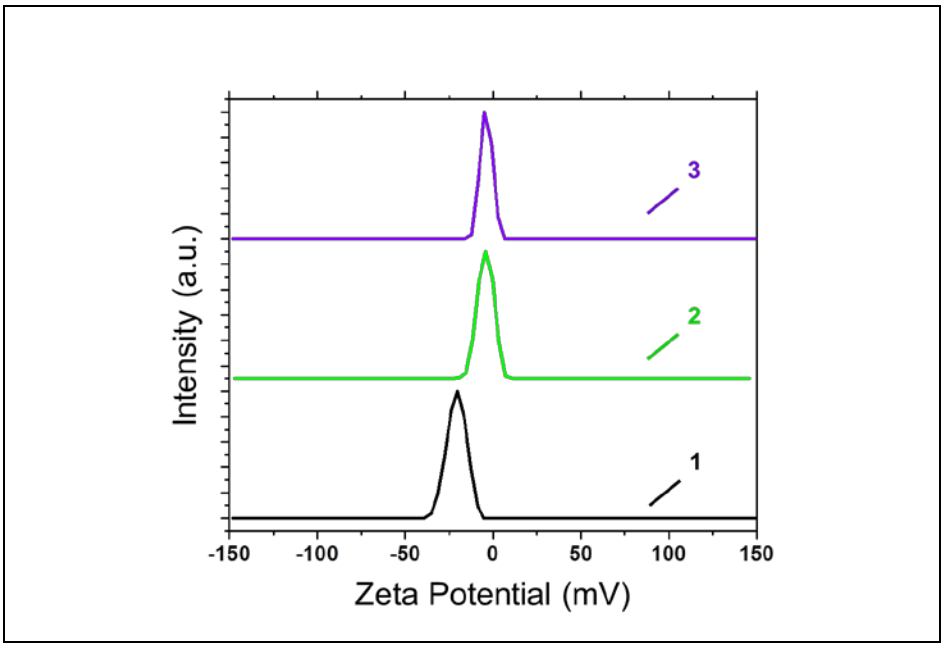

Figure 4. Zeta potential plots of synthesized GO (1), ZnO (2) and ZnO-GO (3)

Analysis of EDX spectra revealed that ZnO-GO is composed of Zn (33.5±2.1) at.%, O (33.9±1.9) at.% and C (32.6±1.7) at.% (Figure 5).

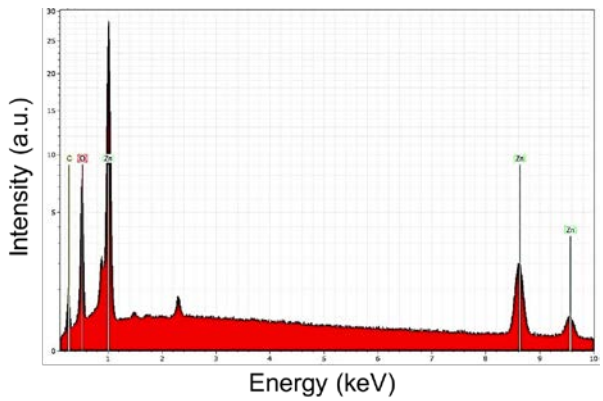

a

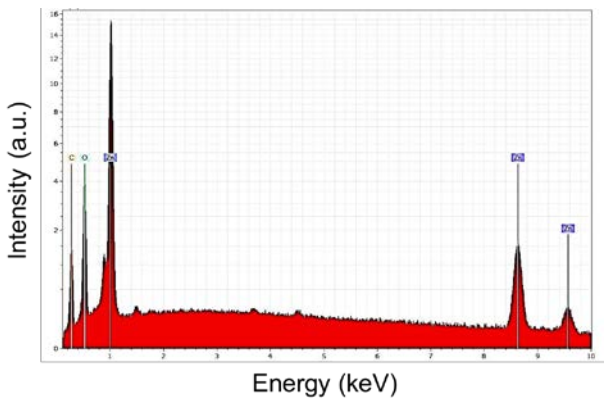

b

a – synthesized ZnO nanoparticles (at U=15 kV); b – ZnO-GO nanoplatform (at U=15 kV).

Figure 5. Energy dispersive X-ray fluorescence spectra of ZnO and ZnO-GO nanomaterials

For comparison, ZnO nanoparticles contain Zn (42.7±2.3) at.%, O (41.2±1.9) at.% and C (32.6±1.7) at.%, and have the atomic ratio of Zn:O as ~1.04 comparable with ZnO-GO (~0.99) (Table 2).

Table 2

Elemental composition of synthesized ZnO and ZnO-GO obtained from the EDX spectra

Sample	**Zn, at.%**	**O, at.%**	**C, at.%**
ZnO	42.7±2.3	41.2±1.9	16.1±0.7
ZnO-GO	33.5±2.1	33.9±1.9	32.6±1.7

5.5 The electronic molecular structure of ZnO-GO nanoplatform

The electronic molecular structure of ZnO-GO was examined by the UV-Visible absorption and SERS spectroscopy methods, aiming at understanding the interaction between ZnO and GO and determining the impact of ultrasound on the formation of nanoplatform. The UV-Visible absorption and SERS spectra of GO, ZnO and ZnO-GO nanoparticles are shown in Figure 6. The UV-Visible spectrum of GO exhibits a strong absorption band with two peaks at ~219 nm (~5.66 eV) and at ~264 nm (~4.70 eV) due to the $\pi_{c=c}$–$\pi_{c=c}$* transitions in neighboring carbon atoms with sp^2 hybridization and those, which are bonded with oxygen in the form of carboxyl and carbonyl groups located at the edges of the graphene sheets [40] (Figure 6a). The red shift of the second absorption peak (~264 nm) demonstrates the reduction of the electronic structure in GO due to a decreased concentration of oxygen containing functional groups [41], in agreement with the Zeta potential data (Figure 4). The absorption spectrum of ZnO nanoparticles shows two distinct bands at ~210 nm (5.90 eV) and ~369 nm (3.36 eV) on an elevated continuum, in agreement with the characteristic electronic transitions of II-VI-semiconductor clusters [42]. The band at ~210 nm can be assigned to the charge transfer between ZnO clusters and the solvent band of OH^- in water [43]. The peak at ~369 nm is the intrinsic band-gap absorption of ZnO due to the electron transitions from the valence to the conduction band ($O_{2p} \rightarrow Zn_{3d}$). This peak is indicative for ZnO nanoparticles (<100 nm size) being formed by the Ostwald growth mechanism.

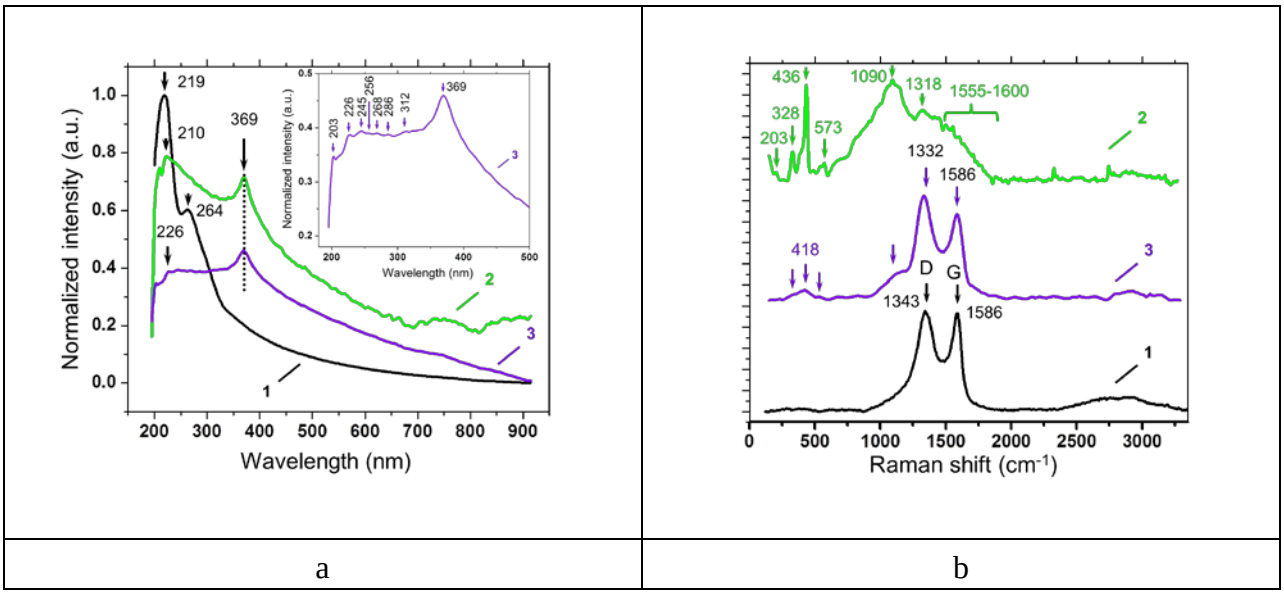

a b

a – UV-Visible absorption spectra of aqueous solutions of synthesized GO (1), ZnO (2) and ZnO-GO (3) (inset Figure shows absorption spectrum 3 at higher magnification); b – SERS spectra of GO (1), ZnO (2) and ZnO-GO (3) (at λ_{exc}=633 nm, grating 600 gr/mm blazed at 600 nm).

Figure 6. The electronic molecular structure of synthesized GO, ZnO and ZnO-GO nanomaterials

The UV-Visible absorption spectrum of ZnO-GO nanoplatform shows several small bands in the wavelength region from 226 nm to 312 nm and a distinct peak at ~369 nm (Figure 6a and inset spectrum 3). The appearance of manifold electronic transitions in the first region points out to the charge transfer in the close junction between ZnO and GO, which is inversely proportional to the adsorption strength of the anion [44]. The appearance of a distinct peak in the longer wavelength region (~369 nm) occurs due to decreasing quantum confinement with increasing particle growth parameters such as 2D surface area and thickness. As this shift is related to the quantum size effect, the equation considering the effective mass model of the particle radius as a function of peak absorbance wavelength was applied for the estimation of ZnO nucleation centers in ZnO-GO [45]. The estimated mean radius of nucleation centers is ~2.66 nm, considering the effective mass for electrons m_e=0.26 and holes m_h=0.59 in ZnO.

SERS spectroscopy was applied to examine the surface structure of synthesized ZnO-GO in comparison with ZnO and GO (Figure 6b, Table 3).

Table 3

Analysis of SERS spectra of synthesized ZnO and ZnO-GO (λ_{exc}=633 nm) (*fundamental optical mode of wurtzite-type ZnO crystals; sh. - shoulder)

ZnO, cm^{-1}	**Assignment**	**ZnO-GO, cm^{-1}**	**Assignment**
203	$2E_2^{low}$ 2^{nd*}[48] and 2TA**	-	-
328	(E_2^{high}-E_2^{low})[48]	-	-
436	E_2^{high},[48] (oxygen vibration)[47]	377 sh.	A_1 (TO***)[48]
489	2nd A_1 symmetry[47]	418	E_1 (TO)[48]
540	2nd A_1 symmetry[47]	-	-
573	A_1 (LO)[49]	-	-
1090	TO and LO****[47]	1124	A_1 (LO)^{2nd},[50]
1318	(TA + LO)^{2nd},[50]	1332	(TA + LO),^{2nd},[50] D (GO)
1555	(LA + TO)^{2nd},[50]	1585	(LA + TO),^{2nd},[50] G (GO)
1601	(LA + TO)^{2nd},[50]	-	-
2326	2A_1(LO), E_1(LO), 2LO^{2nd},[50]	2324	2A_1(LO), E_1(LO), 2LO^{2nd},[50]
2745	$_{\nu}$OH[51]	2795	$_{\nu}$OH[51]

GO exhibits characteristic Raman bands at ~1343 cm^{-1} due to the K-point phonons of A_{1g} D breathing mode and ~1586 cm^{-1} due to the zone center phonons of E_{2g} G mode with the IntD/IntG ratio of ~1.03, indicating that GO is composed of the hexagonal carbon structure with sp^2 hybridization [46]. SERS spectrum of ZnO nanoparticles exhibits fundamental optical modes of wurtzite-type ZnO crystals [47]. The most prominent Raman bands appearing as E_2 modes at ~328 cm^{-1} (E_2^{high}-E_2^{low}) and ~436 cm^{-1} E_2^{high} are assigned to the oxygen vibration in the ZnO crystal lattice (Table 3).

A broad intensive Raman peak at ~1090 cm^{-1} can be assigned to the transverse and longitudinal optical components (TO and LO) in ZnO with random orientation. In contrast, SERS spectrum of ZnO-GO nanoplatform shows a broad polar band at ~418 cm^{-1} and can be assigned to E_1 TO mode with a shoulder at ~377 cm^{-1} (A_1 TO). The decreased intensity,

broadening and a blue shift of this Raman peak indicates that the mechanical action of ultrasound on ZnO with GO doesn't lead to the crystal lattice disorders [47], in agreement with the XRD analysis (Figure 3). SERS spectrum of ZnO-GO shows strong Raman bands of GO with a blue shifted D mode at ~1332 cm^{-1} and a non-shifted G mode, which appears without a significant broadening. The IntD/IntG ratio is ~1.2, demonstrating the increased disorder in GO nanosheets, which can be caused by the formation of ZnO-GO with a cone-shaped morphology [36]. In this spectrum prominent Raman bands of ZnO don't appear in the 1090–1601 cm^{-1} frequency region, but develop a small shoulder, indicating the presence of ZnO without second order optical components. Both the increased disorder in GO and a small peak from ZnO demonstrate that ZnO-GO formation with the cone-shaped morphology can occur without the replacement of carbon atoms in the skeleton avoiding the breakage of the graphene nanostructure.

5.6 Surface chemical composition of ZnO-GO nanoplatform

The surface chemical composition and bonding of ZnO-GO nanoplatform was studied by the X-Ray photoelectron spectroscopy (XPS) and compared with GO and ZnO (Figure 7). The XPS survey scans of GO (1), ZnO (2) and ZnO-GO (3) are shown in the range from 1200 eV-0 eV identifying the photoelectron lines of C 1s, O 1s and Auger O KLL of GO and elements of C, O and Zn in ZnO and ZnO-GO [52]. The XPS survey scans of ZnO and ZnO-GO show Zn 2s, Zn $2p_{1/2}$, Zn $2p_{3/2}$, Auger Zn LMM, Zn 3s, Zn 3p and Zn 3d, revealing the characteristic doublet splitting of Zn 2p lines into $2p_{1/2}$ and $2p_{3/2}$. The presence of a small In 3d peak in a spectrum of GO is caused by the contribution of In foil which was used as a substrate for the measurement.

Next, the binding energy of C 1s lines was examined in order to understand the change in oxidation state and chemical environment of GO and ZnO-GO (Figure 8). The XPS C 1s line of GO shows a peak, which is fitted to three components at ~284.5 eV, ~286.7 eV and ~288.6 eV being assigned to carbon with sp^2 and sp^3 hybridization in aromatic C-C bonds [53], carbon in C-O bond [54], and O-C=O bond of the carboxyl group [55,56]. In addition, the peak at ~286.7 eV can be indicative for the C-OH hydroxide type of carbon with the hydrogen-bridge oxide structure, in which H atom can be symmetrically placed between two oxygen atoms.

In contrast, the XPS C 1s spectrum of ZnO-GO exhibits a peak, which is fitted to five components at ~283.8 eV, ~284.5 eV, ~284.8 eV, ~286.2 eV and ~288.8 eV, revealing the presence of Zn-C [57], carbon with sp^2 and sp^3 hybridization and adventitious carbon in C-C bond [55], carbon in C-O bonds in hydroxyl group [58-61] and O-C=O bond of carboxyl group [53,55,58-61]. The component at ~283.8 eV is observed at higher binding energy values than of Zn-C being examined in literature (*e.g.* ~282.2 eV), and this chemical shift of 1.6 eV can be caused by the interaction with the carbon and oxygen atoms resulting in the changed electron density, which is transferred from zinc to oxygen atom and then to the carbon atom.

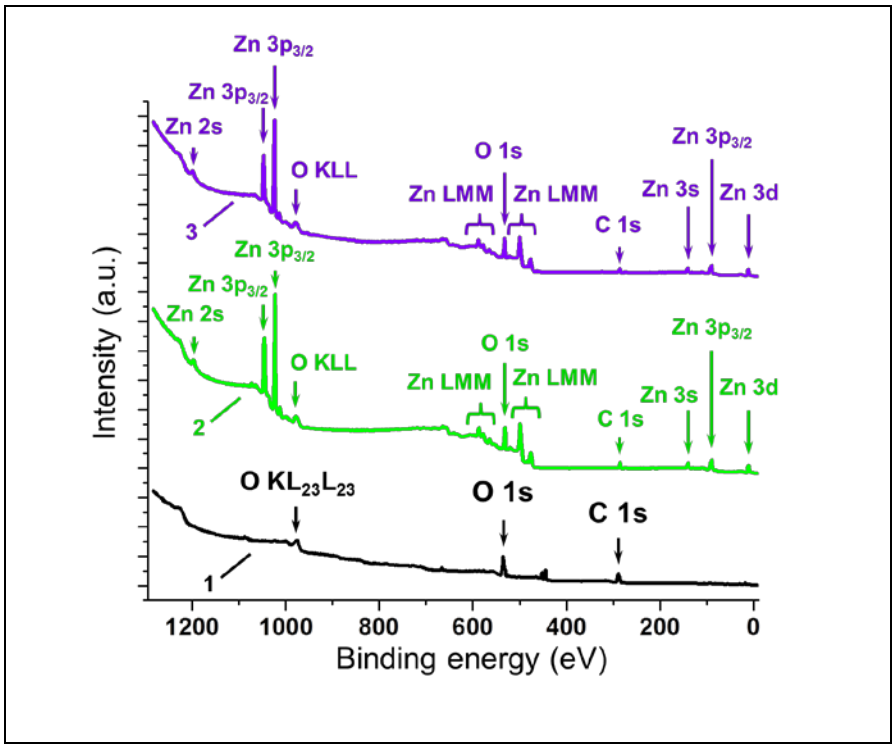

Figure 7. Representative XPS survey scans of GO (1), ZnO (2) and ZnO-GO (3) in the range from 1200 eV-0 eV

For comparison, the XPS C 1s spectrum of ZnO [61] (Figure 8 bottom A) was fitted by adventitious carbon at ~284.8 eV, adsorbed hydroxyl groups at ~285.9 eV [58-61] and CO_x at ~289.2 eV due to contribution of carbonate-type species or to adsorption of molecular water [62]. The XPS O 1s line in GO is introduced by two components at ~530.9 eV (O-C=O bonds) and ~532.6 eV (C-OH bond) [55] (Figure 8). In contrast to GO, both XPS O 1s lines in ZnO-GO and ZnO (Figure 9) are composed of three components: ~530.3 eV, ~531.3 eV and ~532.6 eV, indicating Zn-O bonding in ZnO (*i.e.* the O_2^- ions on the wurtzite structure of the hexagonal Zn^{2+} ion array, which are surrounded by zinc atoms in the close proximity to nearest-neighbor O_2^- ions), O_2^- ions that are in oxygen-deficient regions within the ZnO structure, and chemisorbed OH species on the ZnO surface including CO_x [42,63].

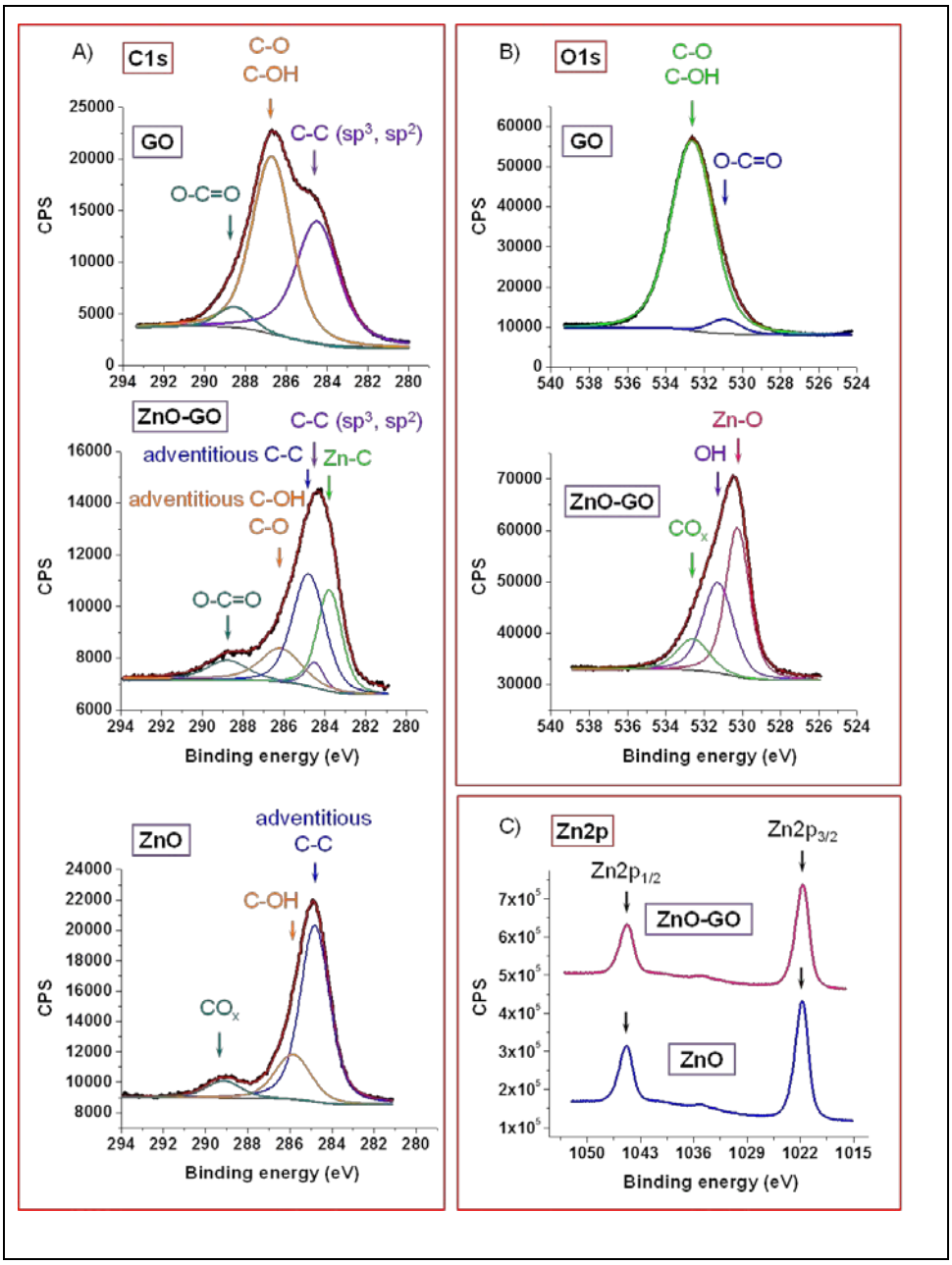

Figure 8. Representative XPS spectra of GO, ZnO and ZnO-GO NPs showing lines of C 1s (A), O 1s (B) and Zn 2p (C) (CPS: counts per second). The curve fitting of the C 1s, O 1s and Zn 2p spectra was completed using a Gaussian-Lorentzian peak shape after performing a Shirley background correction. The color coding in (A) and (B) represents raw spectra (black) and their fits (red), and fitted peak components are presented in other colors. The raw XPS Zn 2p spectra of ZnO and ZnO-GO are shown in blue and pink colors.

Both XPS Zn 2p lines of ZnO and ZnO-GO show Zn $2p_{3/2}$ peaks at ~1021.8 eV and Zn $2p_{1/2}$ at ~1044.9 eV, revealing Zn^{2+} bound to oxygen in the ZnO structure [52], which was confirmed by the Zn LMM Auger lines at ~498.2 eV (kinetic energy ~988.5 eV) and a shoulder at ~495 eV (kinetic energy ~990 eV) [64] (Figure 9). The formation of metallic Zn is excluded because no shift to higher kinetic energy ~992 eV was observed in Zn LMM spectra.

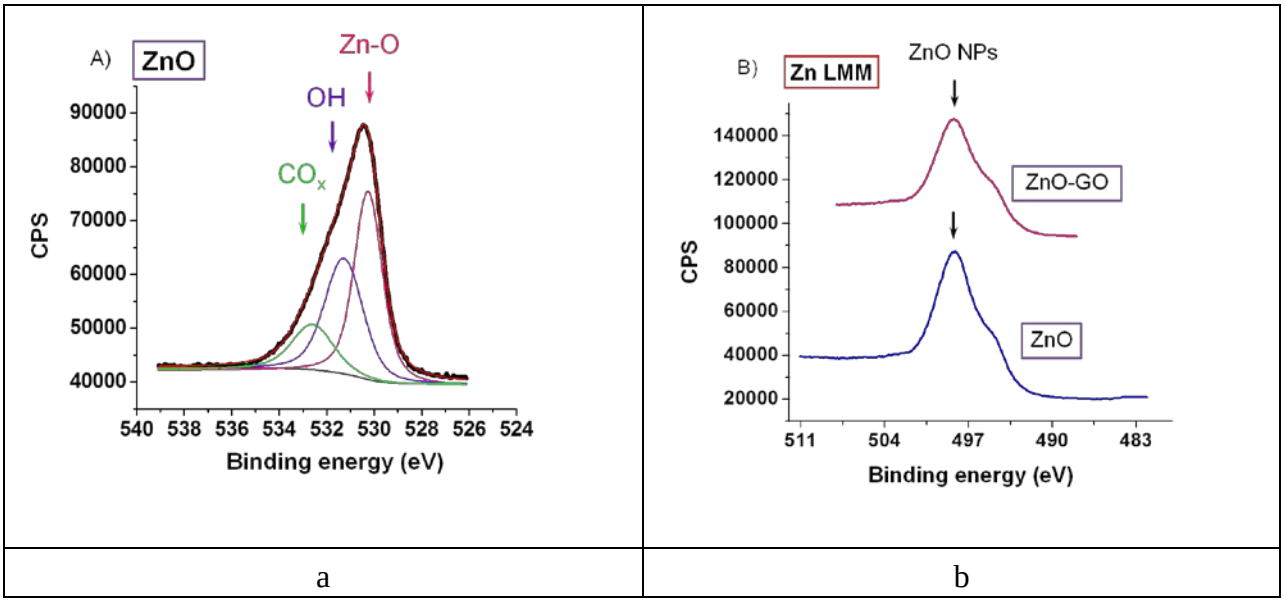

a – Representative XPS O 1s spectrum of ZnO nanoparticles; b – XPS Zn LMM spectra of ZnO and ZnO-GO nanomaterials.

Figure 9. Surface composition of ZnO and ZnO-GO nanomaterials studied by XPS

Overall, ZnO and ZnO-GO were formed by using the ultrasound-assisted hydrothermal reaction of $ZnSO_4$ and NaOH [36]. In this reaction mechanism an excess of hydroxide is required in order to transform the intermediate phase of $Zn(OH)_2$ into ZnO NPs via the dissolution-precipitation process, in which the surface composition and morphology of the final product is controlled by the $H_2O/Zn^{2+}/OH^-$ stoichiometric mole ratio [63]. We may assume that in ZnO-GO the surface carboxyl (-O-C=O) groups of GO together with OH can contribute to the catalytic hydroxylation effect, which is also accelerated by ultrasound; on the transformation of $Zn(OH)_2$ to ZnO in such a way that carbon atoms are not intercalated into the ZnO wurtzite crystalline structure, which is free of impurities.

5.7 Ultrasonic complexation of ASA with ZnO-GO

Figure 10a shows the Zeta potential values of pristine ASA (-0.48±3.73) mV, ASA-ZnO (-0.90±2.59) mV and ASA-ZnO-GO (-1.51±2.36) mV are changed towards more neutral values,

indicating the complexation of ASA with ZnO and ZnO-GO as compared with the data of synthesized ZnO (-4.7±2.7) mV and ZnO-GO (-3.6±2.3) mV (Figure 4).

The UV-Visible absorption spectra of pristine ASA show two distinct peaks at ~242 nm and ~278 nm (Figure 10b), which can be assigned to salicylic acid (SA) and ASA with the C1 point group structure, in agreement with the computed sum of electronic transitions of SA [64]. Aqueous solutions of ASA-ZnO and ASA-ZnO-GO exhibit a broad absorption maximum in the region 200-300 nm with a peak at ~370 nm, which is indicative of the acetyl group with the complexed starch [65]. Other absorption bands, which appear in the wavelength region 700-1100 nm, reveal the excitation of solvent molecules that are in a close proximity with the surface of ASA and nanomaterials. The Beer-Lambert law and the calculated optical density (OD) absorption values of ASA-ZnO and ASA-ZnO-GO are 0.79 and 0.58 allowed for estimating the concentration of pharmaceutical substances in ASA-ZnO (~283.5 μg/mL) and in ASA-ZnO-GO (~208.1 μg/mL).

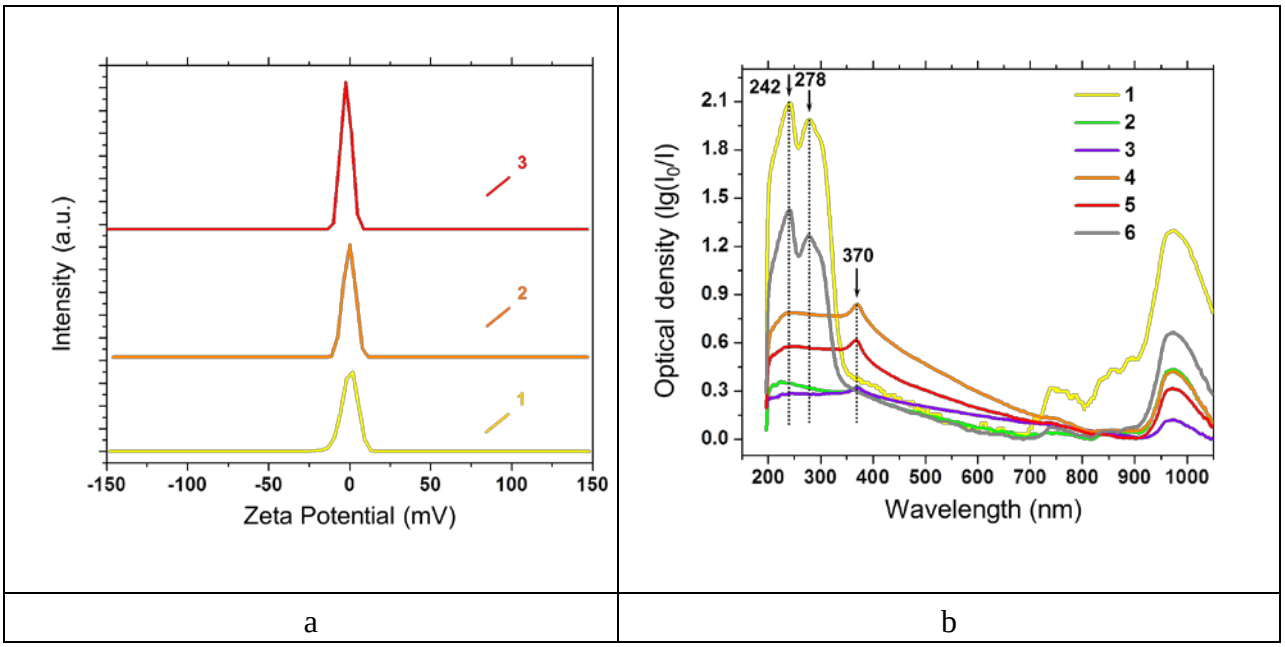

a b

a – Zeta potential plots of pristine ASA (1), ultrasonically complexed ASA-ZnO (2) and ASA-ZnO-GO (3) nanoparticles; b – the UV-Visible absorption spectra of aqueous solutions of pristine ASA (1), ZnO (2) and ZnO-GO (3), ASA-ZnO (4) and ASA-ZnO-GO (5) nanomaterials in comparison with pristine ASA after 3 min of sonication (6).

Figure 10. Surface charge and electronic molecular structure of pristine ASA before and after ultrasonic complexation with ZnO and ZnO-GO nanomaterials.

Next, the ultrasonic complexation of pristine ASA with ZnO and ZnO-GO nanomaterials was studied by Raman spectroscopy (Figure 11). Raman spectrum of pristine ASA shows its characteristic manifold vibrational modes and reveals the presence of starch (260 cm^{-1}, 319 cm^{-1}, 422 cm^{-1} and 919 cm^{-1}) in a compound [38].

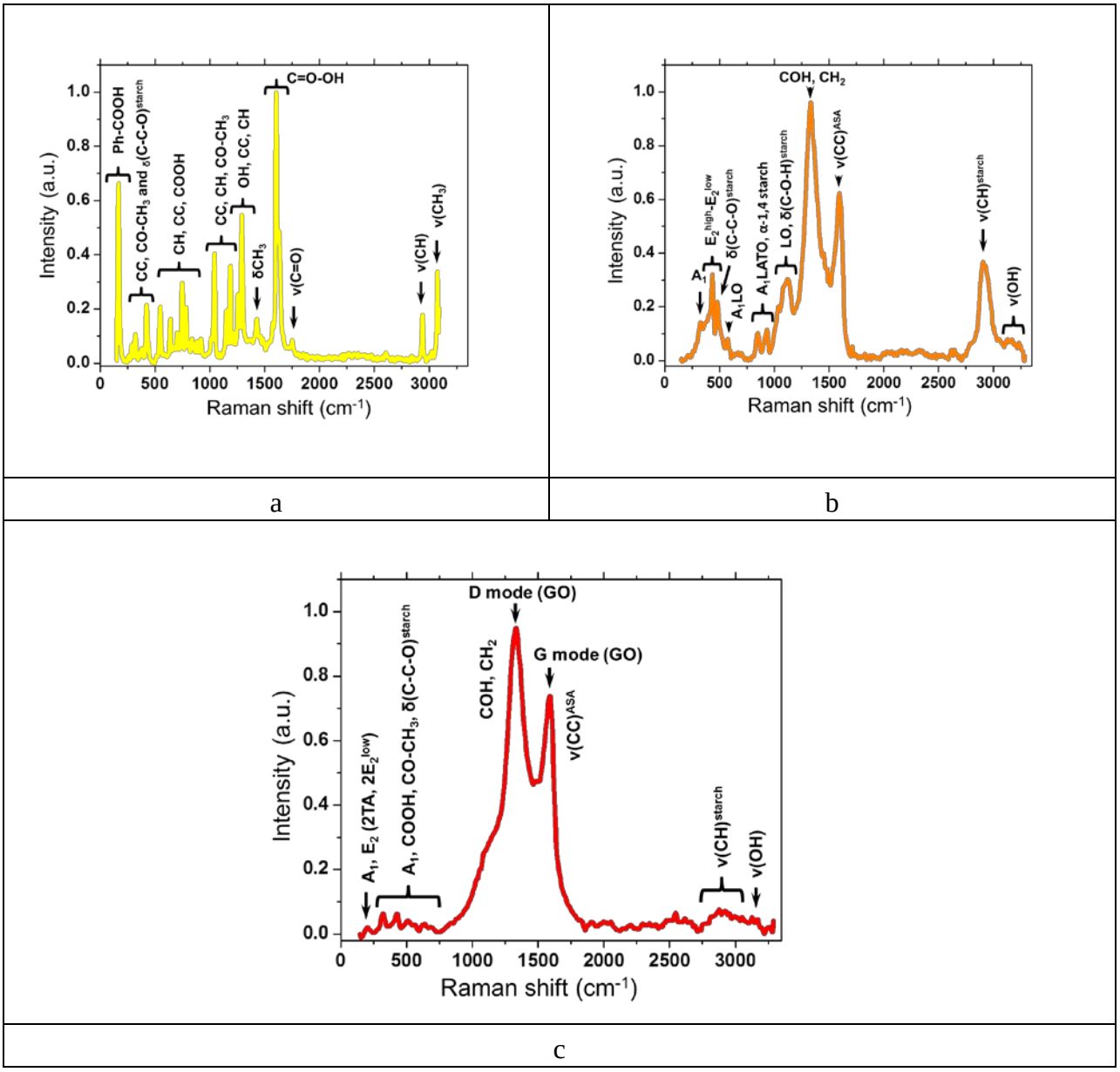

a – Raman spectrum of pristine ASA; b – of ASA-ZnO; c – of ASA-ZnO-GO nanoparticles (λ_{exc}=633 nm).

Figure 11. Surface molecular structures of pristine ASA and ultrasonically complexed ASA-ZnO and ASA-ZnO-GO nanoparticles.

Characteristic Raman bands of inactive ingredients such as talc [66], calcium stearate [67], citric acid [68] and SiO_2 [69] were not observed. The mass fraction of ASA is ~4.21 wt. % and of starch is ~0.82 wt. % in pristine ASA, as determined by the Raman intensity ratio method [70] and the calculated data are presented in Table 4.

Table 4

Concentration and mass fraction of ASA and starch in ASA-ZnO and ASA-ZnO-GO nanoparticles estimated by the Raman intensity ratio method in comparison with pristine ASA

Compound	**α**	**Concentration, μM**		**Mass fraction, wt.%**	
		ASA	**Starch**	**ASA**	**Starch**
Free ASA	18.11	167.00	43.00	4.21	0.82
ASA-ZnO	0.12	1.10	0.29	2.80×10^{-2}	5.00×10^{-3}
ASA-ZnO-GO	14.58	134.00	35.00	3.38	0.67

In contrast, the mass fractions of ASA and starch in ASA-ZnO nanoparticles are by two and three orders of magnitude lower than in ASA-ZnO-GO being comparable with the values in free ASA, i.e. ~3.38 wt.% and ~0.67 wt.%. The estimated concentration of ASA in free ASA is ~167 μmol/L, in ASA-ZnO (~1 μmol/L) and in ASA-ZnO-GO (~134 μmol/L), revealing that ASA forms a strong complex with ZnO-GO.

We suggest that the lowest concentration of ASA and starch in ASA-ZnO nanoparticles in relation to free ASA and ASA-ZnO-GO can be caused by the following effects:

1) pH-dependent swelling of starch during interaction with ZnO and the changed ionization state of carboxylic groups in aqueous solution [71];
2) sonochemical modification of starch during acoustic cavitation.

The swelling of starch in aqueous solution suggests that water can penetrate ASA-ZnO and lead to leaching of ASA. We may assume that modification of starch can be enhanced by ZnO and ultrasound, resulting in the extraction of ASA from nanoparticles and increased solubility (hydrolysis) of starch. These effects may be retarded in ASA-ZnO-GO due to the ZnO-GO structure, which forms a strong complex with ASA. It was reported that Zn^{2+} more easily interact with the hydroxyl oxygen of the starch molecular chain, leading to the hydrolysis of its glycoside bonds. As a result of it, weakening of the intermolecular hydrogen bonding and reduction of the crystalline regions of starch occur [72]. Zn^{2+} can appear as a result of dissolution of ZnO nanoparticles in aqueous solution, which typically occurs at acidic conditions. In our experiments, the pH of aqueous colloidal solutions was 5.5, meaning that dissolution of ZnO is

less probable. On the other hand, ultrasound can contribute to the dissolution of ZnO and release of Zn^{2+} [73] which can be retained to a higher degree in the ZnO-GO structure.

5.8 Enhanced antibacterial activity of ASA-ZnO-GO nanoparticles

The growth inhibition of *E. coli M-17* bacteria, as a model microorganism, was assessed by interaction with free ASA, ASA-ZnO and ASA-ZnO-GO nanoparticles (Figure 12, Appendix 4).

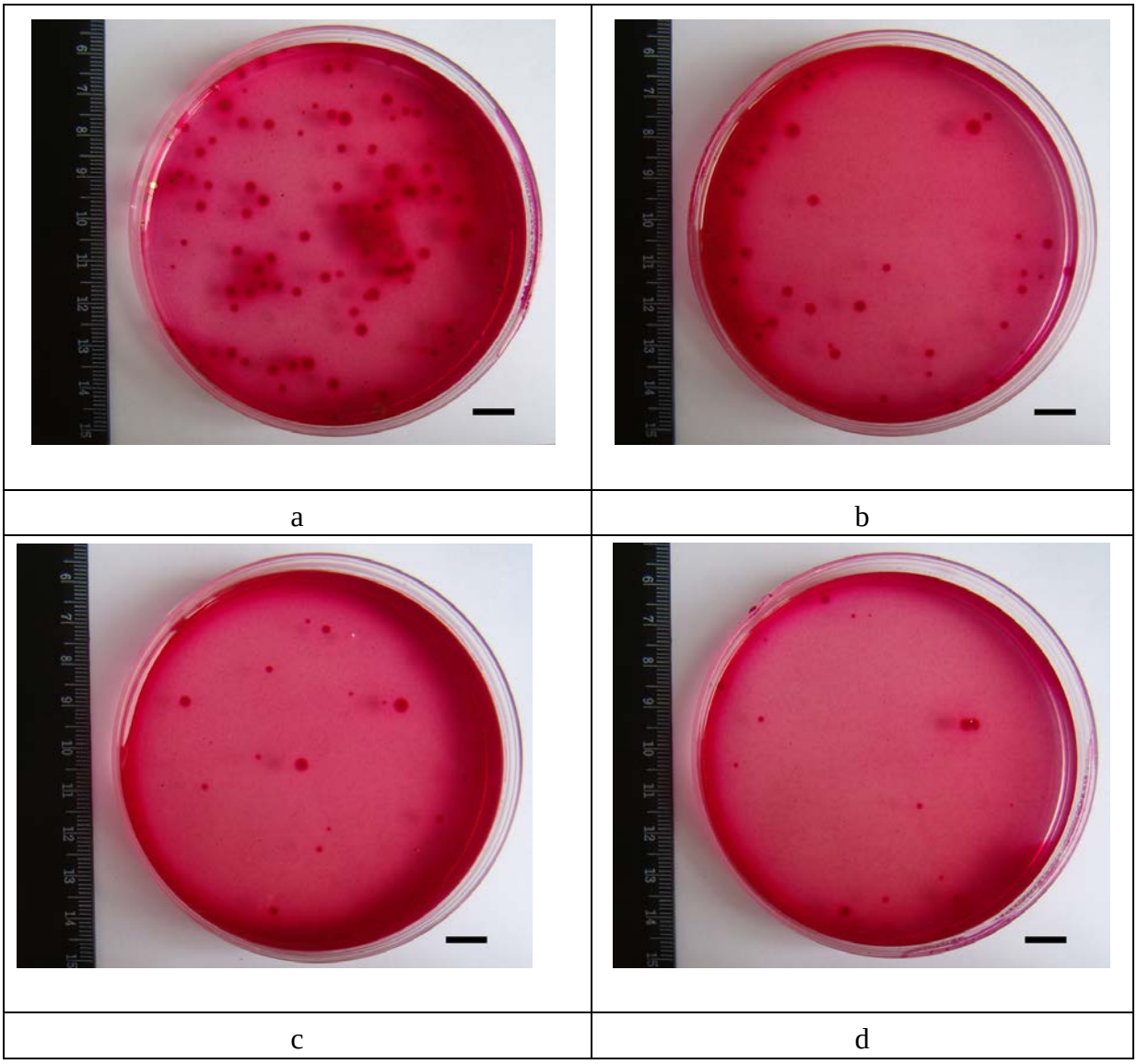

a – live free *E. coli M-17* colonies; b – *E. coli M-17* colonies after incubation with pristine ASA; c – with ASA-ZnO; d – with ASA-ZnO-GO nanoparticles (scale bars are 1 cm).

Figure 12. True color photo images of live free *E. coli M-17* colonies without any treatment and after incubation with pristine ASA (E. coli + {free ASA}), ASA-ZnO (E. coli + {ASA-ZnO}) and ASA-ZnO-GO (E. coli + {ASA-ZnO-GO})

Figure 12 shows true color photo images of *E. coli M-17* colonies grown on differential agar media in petri dishes without any treatment and after incubation with free ASA, ASA-ZnO and ASA-ZnO-GO nanoparticles. Control experiments were performed by incubating pristine differential medium alone (no bacteria) and with free ASA, ASA-ZnO and ASA-ZnO-GO at 37°C for 20 h [38].

A tendency was revealed in the decreased amount of *E. coli M-17* colonies after treatment with synthesized nanomaterials following the order from large amount of bacteria to small: E. coli M-17 + {free ASA} → E. coli M-17 + {ASA-ZnO} → E. coli M-17 + {ASA-ZnO-GO}. Details about the calculated data with their standard errors and deviation values can be found in ref. [38]. Overall, live *E. coli M-17* populations occupy ~58 % of the total surface area after 20 h of incubation, which is characteristic of a fast growing type of a bacteria family [78]. The number of bacterial colonies per surface area decreased by 2.4 times in a sample of {E. coli M-17 + free ASA}, by 5.8 times in {E. coli M-17 + ASA-ZnO} and by 7.3 times in {E. coli M-17 + ASA-ZnO-GO} (Figure 13a) and the occupied average surface area of grown treated *E. coli M-17* was ~23.9 %, ~10.0 % and ~8.0 % with respect to free E. coli M-17 (Figure 13b), demonstrating the pronounced bacteriostatic effect of ASA-ZnO and ASA-ZnO-GO in comparison with pristine ASA.

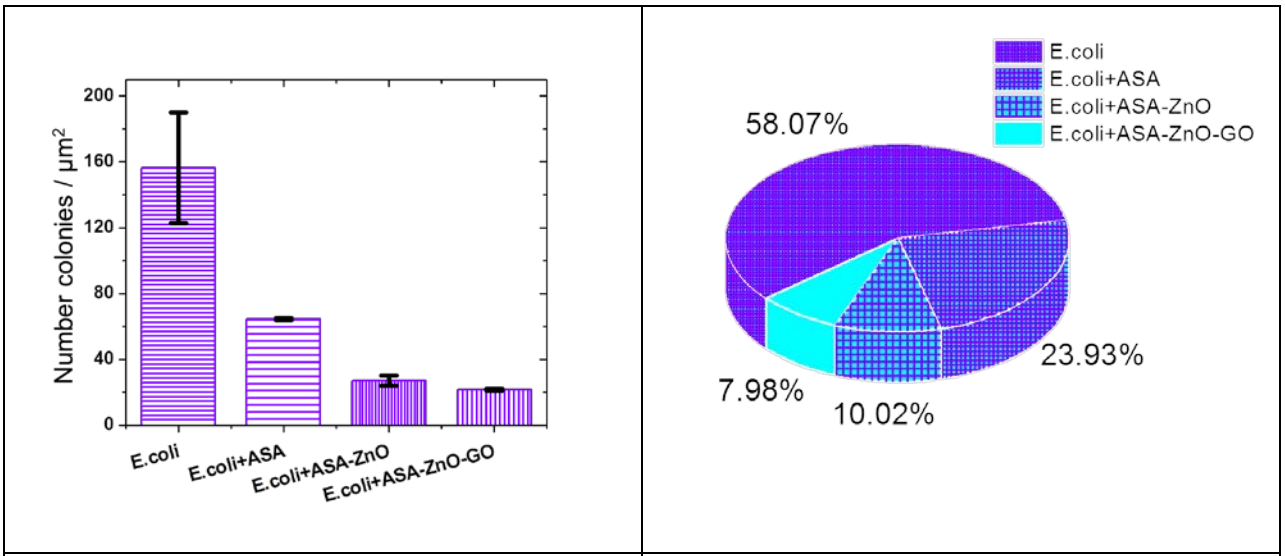

a – the calculated statistical histogram showing the number of bacterial colonies per surface area (μm^2); b – distribution diagram of a grown bacterial surface area relatively to live free *E. coli M-17* (in %). Error bars are the standard errors from 45 optical microscope images.

Figure 13. The bacteriostatic effect of ultrasonically complexed ASA-ZnO-GO nanoparticles in comparison with pristine ASA and ASA-ZnO on *E. coli M-17* bacteria

It was reported that ZnO nanoparticles exhibit bactericidal activity against *E. coli* through the formation of reactive oxygen species (ROS: O_2^-, H_2O_2, singlet oxygen $^1O_2$ and ·OH) and oxidative stress at MIC ~5 mg/mL [75]. The released Zn^{2+} ions have been reported to be toxic to bacteria too, but eluted zinc ions cannot be considered to inhibit the bacterial growth because of the low solubility of ZnO *in vivo*. It is accepted by the scientific community that ZnO nanoparticles of smaller size produce larger amount of ·OH radicals and cause bacterial suicide response, which is characterized by *E. coli* growth arrest under continuous stress conditions, while maintaining the metabolism in bacteria [76].·OH radicals can be formed as a result of reaction between O_2^- and H_2O_2, and can be catalyzed by ZnO because its surface is coated by OH. O_2^- can capture H^+ in solution, yielding the formation of hydroperoxyl radical HO_2·, which can penetrate the cellular membrane like H_2O_2 causing its damage and disorganization in the cell wall, thereby inhibiting the growth of the cells or leading to their apoptosis. It is proposed that H_2O_2 is one of the primary factors in the bacteriostatic effect caused by ZnO nanoparticles [77].

The interaction with the cellular membrane of *E. coli M-17* can be modulated with ASA-ZnO-GO nanoparticles due to the enhanced biocompatibility of GO and ZnO. It was reported that GO can cause no viability loss, at a concentration of 50 μg/mL, indicating low cytotoxicity of GO and enabling long-term antibacterial performance [78]. We may consider that GO can cut the *E. coli M-17* membrane because these effects were previously observed at low concentration of GO colloidal suspension (<6 μg/mL) [23]. Moreover, sharp edges of cone-shaped ASA-ZnO-GO nanoparticles can enable a tighter contact and complexation with the bacterial cellular membrane, thereby enhancing the bacteriostatic effects of *E. coli M-17*.

5.9 Improved antioxidant efficiency of ASA-ZnO-GO nanoparticles

Next, we performed the electrochemical Fenton reaction process with free ASA, ASA-ZnO and ASA-ZnO-GO nanoparticles to find out the scavenging efficiency of hydroxyl radicals by these potential pharmaceutical nanomaterials. The cyclic voltammograms of the relative response of current (mA) vs the applied voltage (from -0.5 V to +1.2 V) by varying the concentration of pharmaceutics in free ASA, ASA-ZnO and ASA-ZnO-GO are shown in Figure 14. Control electrochemical experiments were performed in aqueous solutions containing Fe^{2+} cations (catalyst) and sodium phosphate dibasic (phosphate-buffered solution, pH=9) before and after reaction with hydrogen peroxide under similar conditions, confirming that the Fenton process took place only after addition of hydrogen peroxide, which is accompanied by the appearance of two characteristic redox peaks at ~0.29 V (~14.57 mA) and ~0.15 V (~8.56 mA) [38], in agreement with literature considering different types of phosphate buffer solutions [79]. In addition, the electrochemical measurement of fresh aqueous solution of free ASA (pH=3) was also performed as another control experiment, demonstrating the prevailed reduction of ASA due

to the appearance of the larger peak at ~0.83 V (~33.15 mA) and a negligible one at ~0.53 V (~4.74 mA) caused by oxidation [38].

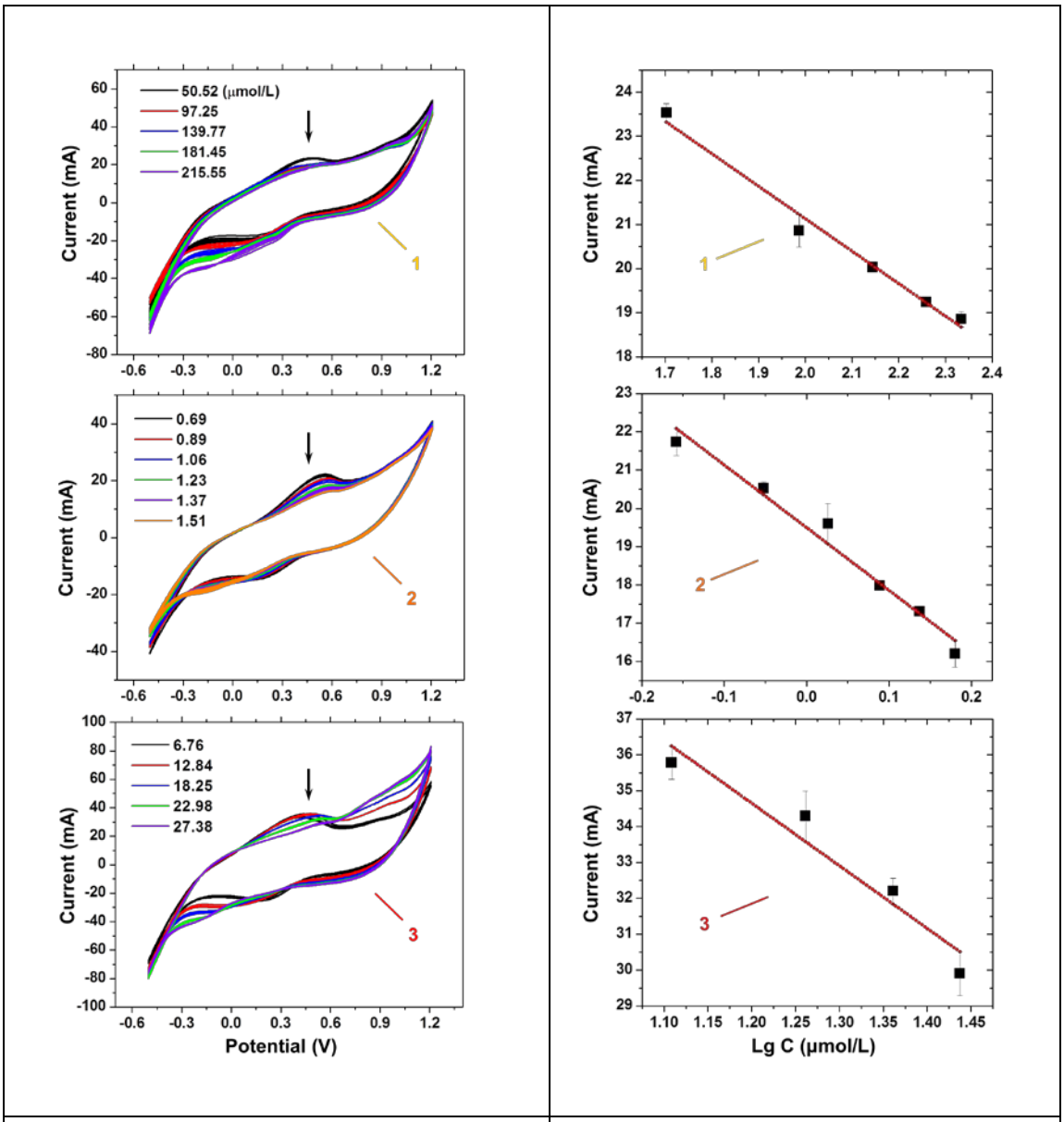

a b

a – the relative response of current (mA) in aqueous solutions of free ASA (1), ASA-ZnO (2) and ASA-ZnO-GO (3) by varying the amount of ASA in nanomaterials; b – the peak values of the measured current (mA) being plotted vs concentration of ASA (Lg C, μmol/L).

Figure 14. The electrochemical Fenton reaction process with free ASA, ASA-ZnO and ASA-ZnO-GO nanoparticles

Cyclic voltammograms of free ASA during the electro-Fenton process show a characteristic current peak of hydroxyl radicals at ~0.48 V (~23.54 mA) due to oxidation and a small broad peak at ~0.09 V (~-20.88 mA) due to reduction only at smaller concentration of ASA (~50.52 μmol/L) (Figure 14A). As the concentration of ASA increased up to ~215.55 μmol/L the oxidation peak disappeared, and two reduction peaks were developed at increased the current peak values at ~0.15 V (~-24.35 mA) and ~0.83 V (~-3.24 mA), indicating that free ASA neutralizes ·OH radicals during oxidation and enhances the reduction processes.

The decrease of current peak values of hydroxyl radicals follows the linear relationship y=35.9-7.4x at the increased concentration of ASA and its rate is ~7.4 as determined from the slope (Figure 14b). In contrast, cyclic voltammograms of ASA-ZnO nanoparticles show a pronounced current peak of ·OH radicals at ~0.55 V (~21.74 mA) due to oxidation and another peak at ~0.24 V (~-13.67 mA) due to reduction at the smallest concentration of ASA (~0.69 μmol/L), demonstrating the enhanced activity of redox reactions due to the conjugation of ASA and ZnO (Figure 14a). Both peaks are significantly decreased at increased concentration of ASA-ZnO with the oxidation peak values at ~0.59 V (~16.20 mA), while the reduction peak disappeared at the highest available amount of ASA (~1.51 μmol/L), indicating that ASA-ZnO nanoparticles diminish ·OH radicals, but also the reduction processes. This is also evidenced from the lower current peak edge values (at ~1.51 μmol/L) at ~-31.76 mA (-0.50 V) and ~38.53 mA (1.20 V) in respect to the initial edge values (at ~0.69 μmol/L) at ~-41.31 mA (-0.5 V) and ~41.38 mA (1.20 V). Similar to free ASA, the decreased current peak values of hydroxyl radicals also follows the linear relationship y=19.5-16.4x, but at a higher rate ~16.4, demonstrating that the redox reactions are accelerated by ASA-ZnO during the electro-Fenton process (Figure 14b).

Similarly to ASA, cyclic voltammograms of ASA-ZnO-GO nanoparticles show a current peak of hydroxyl radicals at ~0.47 V (~35.78 mA) due to oxidation and a small broad peak at ~0.18 V (~-25.51 mA) due to reduction only at the smallest available concentration (~6.76 μmol/L) (Figure 14a). These current peak values are larger than in free ASA, pointing out to the higher electron density of ASA-ZnO-GO. At increased concentration of ASA-ZnO-GO (~27.38 μmol/L) the oxidation peak disappeared like in free ASA, and only one reduction peak was developed at ~0.71 V (~-11.85 mA) with significantly increased current edge peak values at -75.43 mA (-0.50 V) and ~84.81 mA (1.20 V) being higher than in free ASA (-68.12 mA and 52.01 mA), demonstrating more efficient neutralization of ·OH radicals during oxidation by ASA-ZnO-GO. Similar to free ASA and ASA-ZnO, the decrease of current peak values of hydroxyl radicals follows the linear relationship y=55.6-17.4x with the increased concentration of ASA-ZnO-GO, but at a higher rate ~17.4, demonstrating the pronounced antioxidant efficiency of ASA-ZnO-GO in acceleration of redox reactions in the electro-Fenton process.

In summary, an introduced single step ultrasonic method (20 kHz) can be used for the formation of ZnO-GO nanoplatform with the average size of <70 nm. ZnO-GO are composed of the pure crystalline ZnO wurtzite phase and have a cone-shaped morphology with the Zn:O atomic ratio ~1.0. The surface structure of ZnO-GO contains hydroxyl and carboxylate groups that are particularly useful for the ultrasonic complexation with pristine ASA. Ultrasonically complexed ASA-ZnO-GO nanoparticles more effectively inhibit the growth of *E. coli M-17* bacteria as model organism than free ASA or ASA-ZnO. This improved bacteriostatic function of ASA-ZnO-GO can be attributed to the complexation of ASA and starch with ZnO-GO, biocompatibility due to GO and ZnO. Moreover, ASA-ZnO-GO more efficiently neutralize ·OH radicals during the electro-Fenton process than free ASA or ASA-ZnO at the concentration of ~28 μmol/L, which is lower than 100 μmol/L and can be considered as biosafe and nontoxic to eukaryotic cells according to FDA rules. The acquired knowledge substantially enriches our understanding about the improvement of pharmaceutical function of ASA, especially its antioxidant property, and discloses the important roles of ZnO and GO in contact-dependent growth modulation of *E. coli M-17* bacteria. As a result, these findings can be particularly useful for the fundamental studies of the drug-enzyme, drug-metal and drug-biological cell interactions, and can be expanded to other drugs in the treatment of gastrointestinal tract diseases, diabetes and cancer.

*****

The presented results allow us to draw the following conclusions:

1. Ultrasound-assisted synthesis of ZnO-GO nanoplatform leads to the formation of a pure ZnO crystalline phase in aqueous solution by the Ostwald growth mechanism without the replacement of carbon atoms in the skeleton avoiding the breakage of the graphene nanostructure.
2. ASA forms a strong complex with the ZnO-GO nanoplatform due to binding effects with GO, in contrast to ASA-ZnO nanoparticles.
3. ASA-ZnO-GO nanoparticles exhibit a threefold pronounced bacteriostatic effect than pristine ASA, which we suggest is due to cutting of the *E. coli M-17* membrane by GO involving sharp edges of cone-shaped morphology of together with the ameliorated anti-oxidant efficiency of nanoparticles.
4. ASA-ZnO-GO more efficiently neutralize ·OH radicals and at a tenfold higher rate than pristine ASA during the electro-Fenton process at the concentration of ~28 μmol/L, which is lower than 100 μmol/L and can be considered as biosafe and nontoxic to eukaryotic cells.

CHAPTER 6 SWITCHABLE ANTIOXIDANT FUNCTION OF ULTRASONICALLY COMPLEXED SALICYLIC ACID WITH MAGNETITE-REDUCED GRAPHENE OXIDE NANOPLATFORM

Salicylic acid (SA)-based drugs are widely used in type II diabetes, Alzheimer's disease, rheumatism and cancer [1,2]. SA exhibits beneficial antioxidant properties via direct interaction with enzymes or by controlling their *de novo* synthesis [3]. Antioxidant properties of SA are determined in the reduction of tissue damage caused by hypoxia/reoxygenation, where SA diminishes hydroxyl radicals due to specific binding to protein and modifying its function. SA can inhibit the mitochondrial damage and preserve ascorbate depletion due to ischemia/reperfusion in hearts [4]. The physiological antioxidant action of SA is observed in the decrease of flux of hydroxyl radicals through chelation, which causes a redox deactivation mechanism of iron Fenton reaction centers [5]. SA is considered a better *in vivo* hydroxyl radical scavenger than ascorbic acid (AA) in its ionized form or cysteine because of its site specific location, iron-binding ability and high reaction rate ($6\text{-}10\text{x}10^{9}$ $M^{-1}s^{-1}$) [6]. Therefore, the iron-salicylate complex does not have the thermodynamic driving force to act as an effective Fenton reagent necessary for the production of damaging oxygen-containing radicals. Such salicylate complexes act by redox deactivation of iron and may mimic a superoxide dismutation (SOD), indicating another antioxidant property of SA. It was shown that the salicylate-iron complex can inhibit the xanthine oxidase properties and stimulate the formation of H_2O_2 during the dismutation reaction [7]. In addition, the salicylate-iron can simultaneously reduce Fe(III) of the complex to Fe(II), generating hydroxyl radicals during the dismutation, which is indicative for the pro-oxidant action. SA (a metabolite of acetylsalicylic acid) causes severe side effects (stomach ulcer formation, bleeding, nausea, vomiting, etc.). Therefore, new methods are needed to control the SA structure in salicylate complexes aiming at improved antioxidant and enzymatic efficiency modulation.

Salicylate complexes with metal ions or atoms can lead to activation of the SA's structure, resulting in rich and multifaceted coordination functions of metallo-SA drugs. To date, activation of SA is accounted for complexation with silver for improved wound healing [8,9] and human breast cancer therapy [10] with iridium for potent tumor growth inhibition [11] or copper for higher antitumor efficacy by the proposed ROS mediated mitochondrial pathway [12] with respect to pristine SA. SA can increase ROS production via its action by carboxylic group as shown in the HT-29 human colorectal carcinoma cell line [13] and can sensitize these cells to H_2O_2 in apoptosis induced by TNF-K or a Fas ligating antibody [14].

So far, the complexation of SA with iron(II) or iron(III) is mainly introduced by the study of the electronic structure of iron-salicylates and identification of chemical coordination groups

of biological importance [15]. The iron(II)/iron(III) switch is essential for enzymatic functions, but also for formation of highly reactive hydroxyl radicals [16]. However, such metal complexes undergo ligand substitution reactions at inorganic centers and their structure/function properties are difficult to predict *in vivo*.

Alternatively, the specific interaction of metal-based nanoparticle drugs with biological entities can be controlled by their size, shape and structure. For example, superparamagnetic Fe_3O_4 nanoparticles (<20 nm) can be safely applied as biocompatible, biodegradable and non-toxic contrast agents in magnetic resonance imaging [17]. At present, Food and Drug Administration approved ferumoxytol drug containing iron oxide nanoparticles is used for iron deficiency treatment and tumor retardation growth [18]. Moreover, oral tablet formulation of anticancer drug celecoxib includes Fe_2O_3 nanoparticles, and nonsteroidal anti-inflammatory drug (NSAID) indomethacin with Fe_3O_4 nanoparticles. However, the interaction of these drug molecules with ferric or ferrous oxide has not been determined and the catalytic properties of iron-activated drugs as nanoparticles have not been studied yet.

Up to now, Fe_3O_4 nanoparticles have been designed with GO, providing a platform of many functional groups: carboxylic (-COOH), hydroxyl (-OH), carbonyl (-C=O) and epoxide (-C-O-C). This strategy has been successfully applied to complexation of doxorubicin [19] or folic acid [20] with enhanced intracellular uptake and targeted imaging of oncological tumors. In these studies Fe_3O_4 nanoparticles are either grown or coated with GO that is loaded with anticancer drugs. GO especially stands out here as it provides more binding sites for complexation with drugs and improves the electronic properties and stability of potential pharmaceutical compounds. As advantage, ultrasound causes efficient complexation of drug molecules so that the structure of pharmaceutical organic ligands doesn't undergo severe damage and remain stable during the synthesis. So far, the effects of ultrasound have been determined in sonofragmentation of molecular [21] and ionic [22] crystals, sonocatalysis of iron carbonyls [23], synthesis of iron colloids [24], nanosized hollow hematite [25] and functionalized graphenes [26]. In this context the sonochemical effects of complexed NSAID nanoparticles have not been defined yet.

Therefore we suggest a sonochemical method to form a complex between pristine SA molecules and a Fe_3O_4-rGO nanoplatform during *in situ* synthesis of magnetite phase and determine the conditions of enhanced antioxidant efficiency of Fe_3O_4-rGO-SA nanoparticles.

6.1 Ultrasonic complexation of SA with Fe_3O_4-rGO nanoplatform

For formation of Fe_3O_4-rGO-SA nanoparticles, at first we suggested to prepare GO by using the improved Hummers method, more details can be found in [27]. GO was synthesized with a few layer wrinkled graphene sheets of partially reduced carbon basal planes caused by the removal of functional groups and the C/O=1.44 atomic ratio. The average size of GO was

~202±40 nm. Control experiments were performed without GO, resulting in formation of Fe_3O_4-SA nanoparticles, and without SA, yielding bare Fe_3O_4 and Fe_3O_4-rGO nanoplatform.

Synthesized Fe_3O_4-rGO-SA nanoparticles have spherical morphology (Figure 1a) and a smaller average size <d> ~10.46±2.77 nm (Figure 1b) than Fe_3O_4-SA (~15.62±4.48 nm) and preformed GO (Figure 1c,d) (Appendix 5).

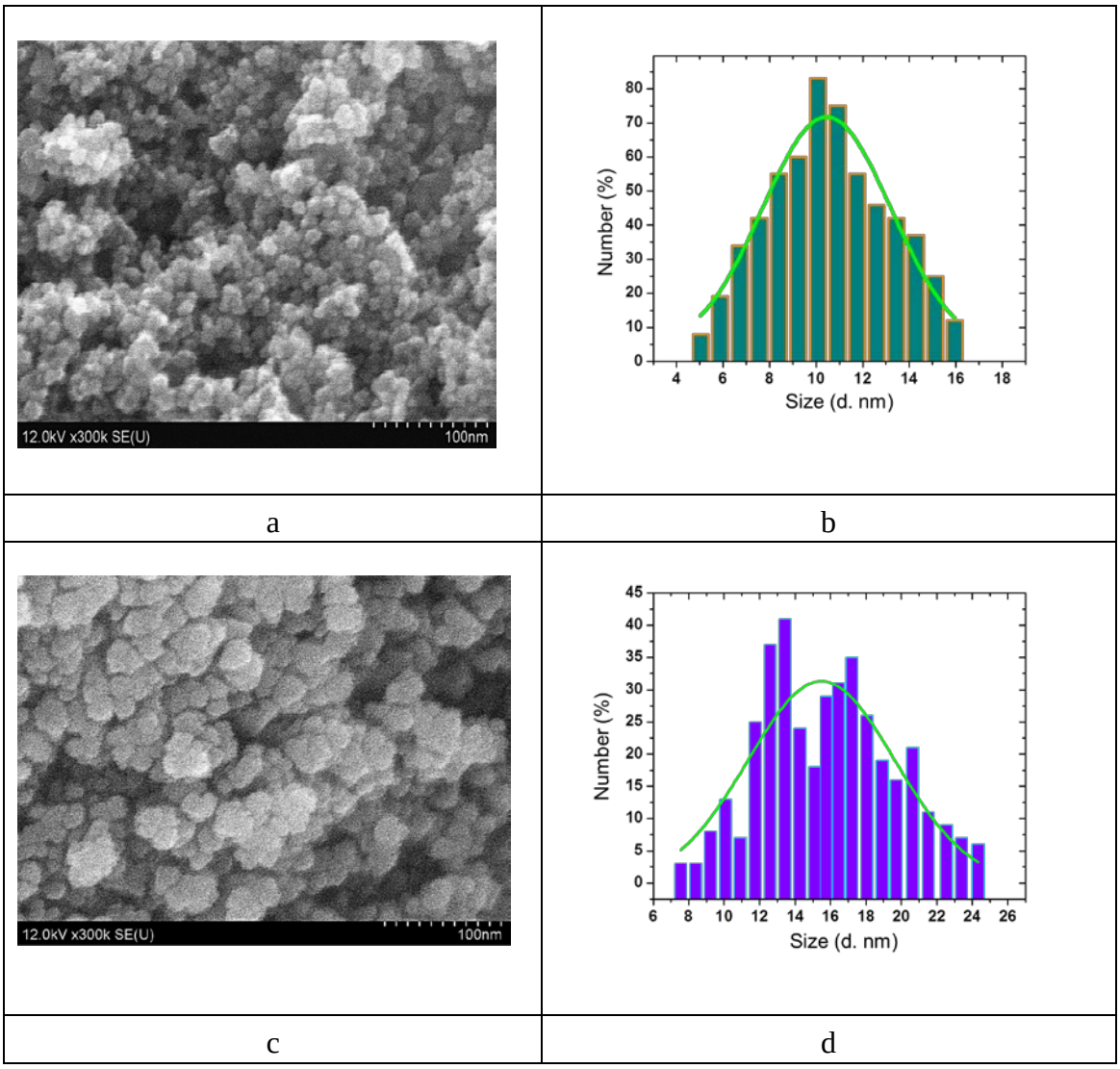

a | b

c | d

a – representative SEM image of synthesized Fe_3O_4-rGO-SA nanoparticles (scale bar is 100 nm); b – its size distribution histogram; c – SEM image of Fe_3O_4-SA nanoparticles; d – its size distribution histogram.

Figure 1. The morphology and average size of synthesized Fe_3O_4-rGO-SA and Fe_3O_4-SA nanoparticles

Analysis of X-ray diffraction patterns of Fe_3O_4-rGO-SA revealed the formation of Fe_3O_4 crystalline phase (amcsd 0007421) with calculated interplanar d spacing values comparable to Fe_3O_4 and Fe_3O_4-SA (Figure 2a and Table 1). The XRD patterns of Fe_3O_4-SA and Fe_3O_4-rGO-SA show a small (221) reflex of SA at $2\theta_B$=28.27° and 28.37° [28] indicating complexed SA.

The crystallite size *t* of all nanoparticles was estimated by using the Scherrer's formula [27] considering the (311) reflex of magnetite with a constant depending on the crystallite shape k=0.89, $2\theta_B$=35.61° of Fe_3O_4 and Fe_3O_4-SA with $\beta=7.45\times10^{-3}$ and 14.63×10^{-3}, and $2\theta_B$=35.50° of Fe_3O_4-rGO-SA nanoparticles with $\beta=14.09\times10^{-3}$ (Figure 2b). The determined size *t* of Fe_3O_4-rGO-SA ~10.20 nm is comparable with its average diameter (~10.46 nm), indicating uniform 3D space structure of synthesized nanoparticles.

In contrast, the *t* value of Fe_3O_4-SA is smaller (~9.84 nm) than the average diameter (~15.62 nm), which is presumably caused by a narrower width of these nanoparticles. Fe_3O_4-rGO-SA nanoparticles have smaller size because of two possible reasons: i) pH-size dependent amphiphilicity of rGO and ii) the relationship between the surface activity of rGO and energy of cavitation bubbles. rGO is considered as an amphiphilic molecule with a pH-dependent surface activity.

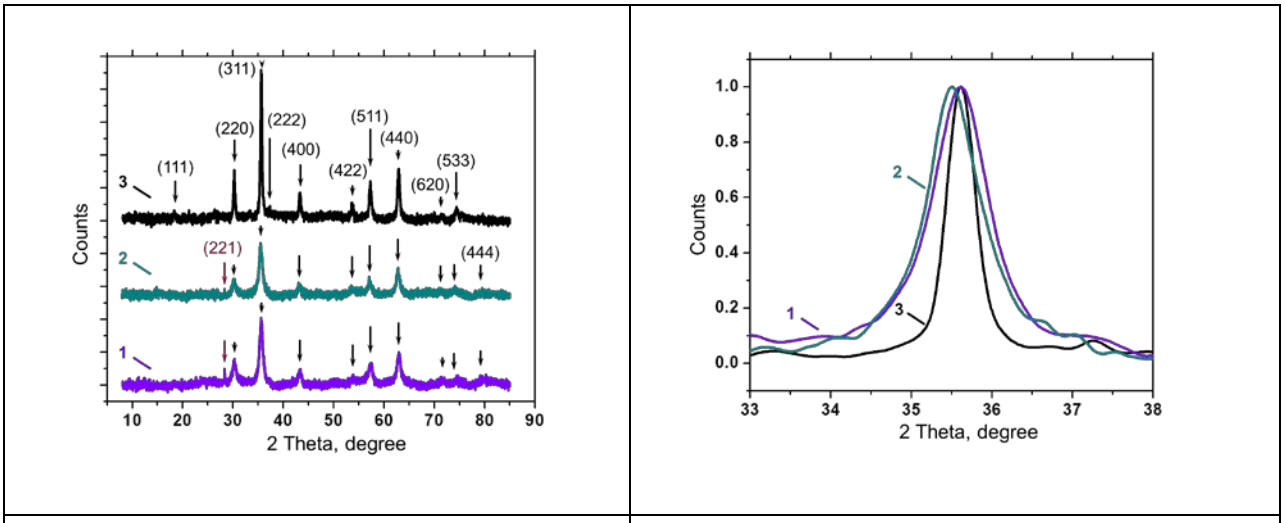

a b

a – The X-Ray powder diffraction patterns of Fe_3O_4-SA (1), Fe_3O_4-rGO-SA (2) and bare Fe_3O_4 nanoparticles (Cu K_α=1.54 Å); b – the selected XRD (311) reflex of magnetite obtained from patterns of these nanoparticles.

Figure 2. The X-Ray powder diffraction patterns of Fe_3O_4-rGO-SA nanoparticles in comparison to Fe_3O_4-SA and bare Fe_3O_4

Smaller rGO have increased the edge-to-area ratio and charge density, therefore they are more hydrophilic at higher pH values. Indeed the pH of aqueous solution of Fe_3O_4-rGO-SA nanoparticles was 5 and of Fe_3O_4-SA – 4, indicating that Fe_3O_4-rGO-SA should be more hydrophilic due to smaller size. On the other hand, rGO can enhance the effect of reduced surface tension on cavitation bubbles with adsorbed SA molecules and can lead to a decreased Laplace pressure. As a result, bubbles with larger size will be formed. Larger bubbles will release higher energy at collapse, producing high local pressure gradient and shock waves, which decrease the nanoparticles' size.

To gain deeper insight into the molecular complexation of SA with Fe_3O_4 and rGO, FTIR transmittance spectroscopy analysis of Fe_3O_4-rGO-SA was performed in comparison with Fe_3O_4-SA nanoparticles (Figure 3).

Table 1

The X-ray powder diffraction data (2θ, °) and interplanar spacing ($d_{(hkl)}$, Å) of Fe_3O_4-rGO-SA and Fe_3O_4-SA nanoparticles

Fe_3O_4-rGO-SA				**Fe_3O_4-SA**			
2θ, °	**Int., a.u.**	**(hkl)**	**d, Å**	**2θ, °**	**Int., a.u.**	**(hkl)**	**d, Å**
-	-	-	-	18.31	76	(111)	4.84
28.27	75	$(221)_{SA}$	3.15	28.37	72	$(221)_{SA}$	3.14
30.11	87	(220)	2.96	30.32	80	(220)	2.94
35.50	100	(311)	2.53	35.61	100	(311)	2.51
43.08	85	(400)	2.10	43.29	74	(400)	2.09
50.24	82	SA	1.81	50.16	69	SA	1.82
53.61	83	(422)	1.71	53.80	68	(422)	1.70
57.16	86	(511)	1.61	57.33	76	(511)	1.61
62.76	89	(440)	1.48	62.96	82	(440)	1.47
70.99	2	(620)	1.33	71.60	69	(620)	1.32
74.09	83	(533)	1.28	74.41	69	(533)	1.27
79.59	2	(444)	1.20	79.95	4	(444)	1.20

FTIR spectrum of Fe_3O_4-rGO-SA nanoparticles shows characteristic $_\nu$(Fe-O) bonds in bidentate and bridge Fe(III)-bissalicylato-diaquo complexes, and the characteristic $_\nu$(Fe-O) stretching band of Fe_3O_4 at ~574 cm^{-1} (Figure 3a) in contrast to Fe_3O_4-SA [29,30]. Another characteristic band of Fe_3O_4 at ~626 cm^{-1}, which can be assigned to the O=C-O group in-plane bending of SA, is observed as a shoulder in Fe_3O_4-rGO-SA [31]. In synthesized nanoparticles the

O-O distance in close packed anion Fe(III) arrays in the octahedral coordination of Fe_3O_4 is 0.294 nm (Fe_3O_4-SA) and 0.296 nm (Fe_3O_4-rGO-SA) (Table 1) is in a good agreement with the O-O distance of magnetite (0.29 nm) reported in literature [32].

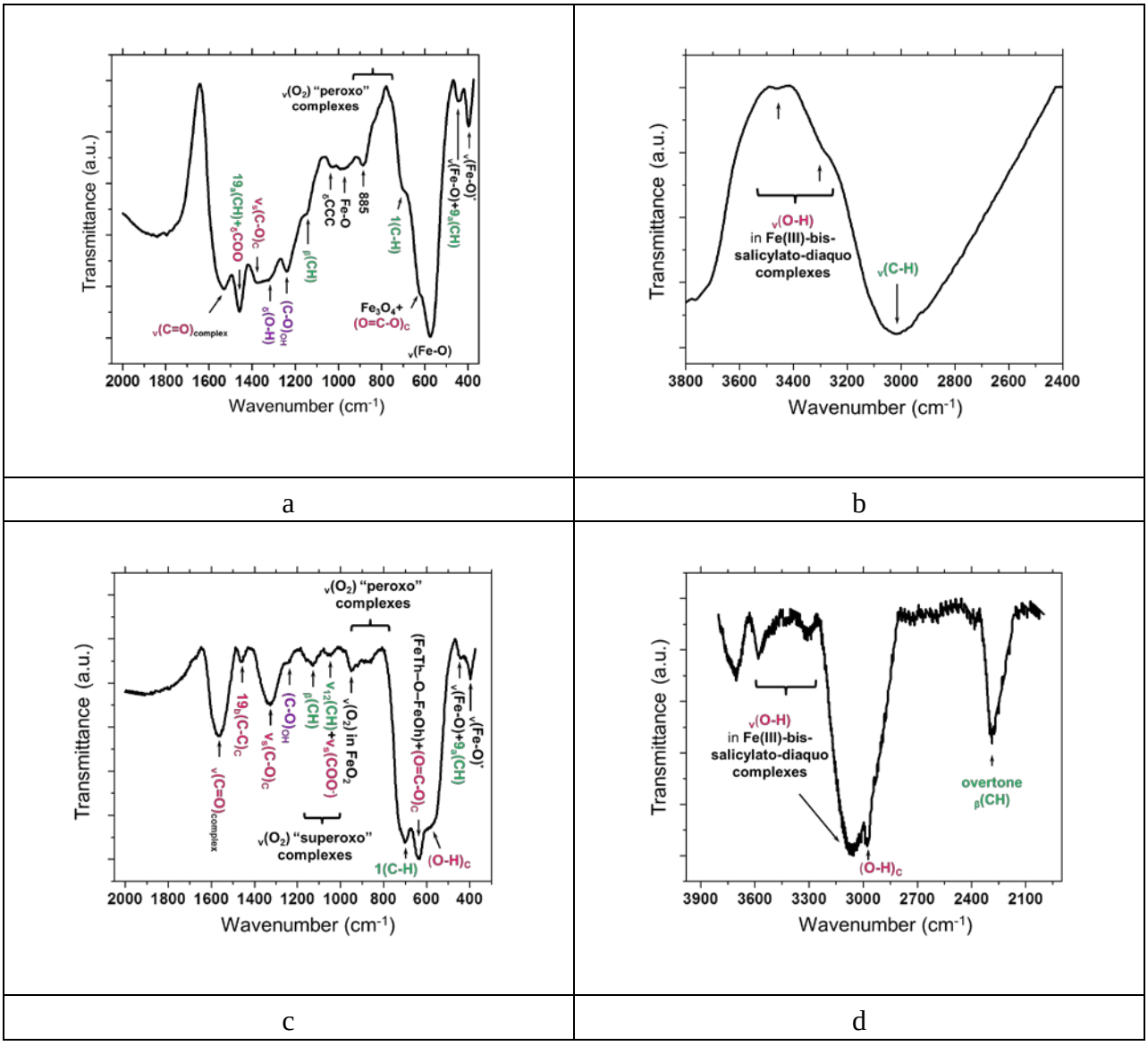

a – FTIR transmittance spectrum of Fe_3O_4-rGO-SA in 400 cm^{-1}-2000 cm^{-1}; b – in 2000 cm^{-1}-3800 cm^{-1}; c – of Fe_3O-SA in 400 cm^{-1}-2000 cm^{-1}; d – in 2000 cm^{-1}-3800 cm^{-1}.

Figure 3. The molecular chemical structure of Fe_3O_4-rGO-SA and Fe_3O-SA obtained from FTIR transmittance spectroscopy analysis

Fundamental vibrations of $_{\nu}(O_2)$ "peroxo" complexes [33] of SA and Fe-O in FeO_2 appear as weak bands in both types of nanoparticles due to ultrasonic oxidation in specific binding of SA. However, the C-O stretching coupled with the in-plane deformation of the phenolic OH group at ~1240 cm^{-1}-1244 cm^{-1}, which is indicative of the intramolecular hydrogen bonding in salicylate, is more pronounced in Fe_3O_4-rGO-SA than in Fe_3O_4-SA. These findings demonstrate the role of rGO in complexation of SA.

The symmetric $_{\nu s}$(C-O) stretching of carboxylic group of SA becomes weaker and broader in Fe_3O_4-rGO-SA at ~1317 cm^{-1}-1377 cm^{-1} involving in-plane O-H bending, which was identified in Fe_3O_4-GO by other researchers [34]. Strong band at ~1458 cm^{-1} shows the in-plane $_{\delta}$COO bending of salicylate monoanion in Fe_3O_4-rGO-SA with complexed SA through phenolic ring and hydroxyl group.

However, vibrations of Fe(III)-bis-salicylato-diaquo complexes appear stronger in Fe_3O_4-SA in contrast to the phenolic ring vibration $_{\nu}$(C-H) in Fe_3O_4-rGO-SA (Figure 3b). From these results, one can conclude that surface oxygen functional groups of rGO contribute to the specific ultrasonic reduction of Fe(II) at the contact with SA ligands and allow formation of the thermodynamically stable metallocomplex in nanoparticles. More pronounced stretching FeTh-O-FeOh vibrations, where FeTh and FeOh correspond to the iron occupying the tetrahedral and octahedral positions, and strong O=C-O out-of-plane bending of SA appears at ~636 cm^{-1} in Fe_3O_4-SA nanoparticles (Figure 3c) along with pronounced O-H bands (Figure 3d), confirming the porous structure of iron oxide nanospheres with Fe(III)/Fe(II) sites.

6.2 Surface and electronic molecular structure of Fe_3O_4-rGO-SA

Analysis of Raman spectra confirms the formation of Fe_3O_4 phase (~670 cm^{-1}) [35] and shows γ-Fe_2O_3 (~350 cm^{-1}) [36] and α-FeOOH (~492 cm^{-1}) on the surface of Fe_3O_4-rGO-SA nanoparticles caused by natural oxidation of magnetite [37] (Figure 4, Table 2).

In addition, several C-C peaks arising from vibrations of benzene ring and solid SA crystal (~707 cm^{-1}) [38], C-O stretching of carboxylic acid group (~1328 cm^{-1}) and a distinct peak at ~1600 cm^{-1} appearing from E_{2g} G mode in rGO due to amorphization of graphite with sp^2-hybridization [39] were detected in Fe_3O_4-rGO-SA. Small peak at 1153 cm^{-1} can be assigned to nanocrystalline diamond [40].

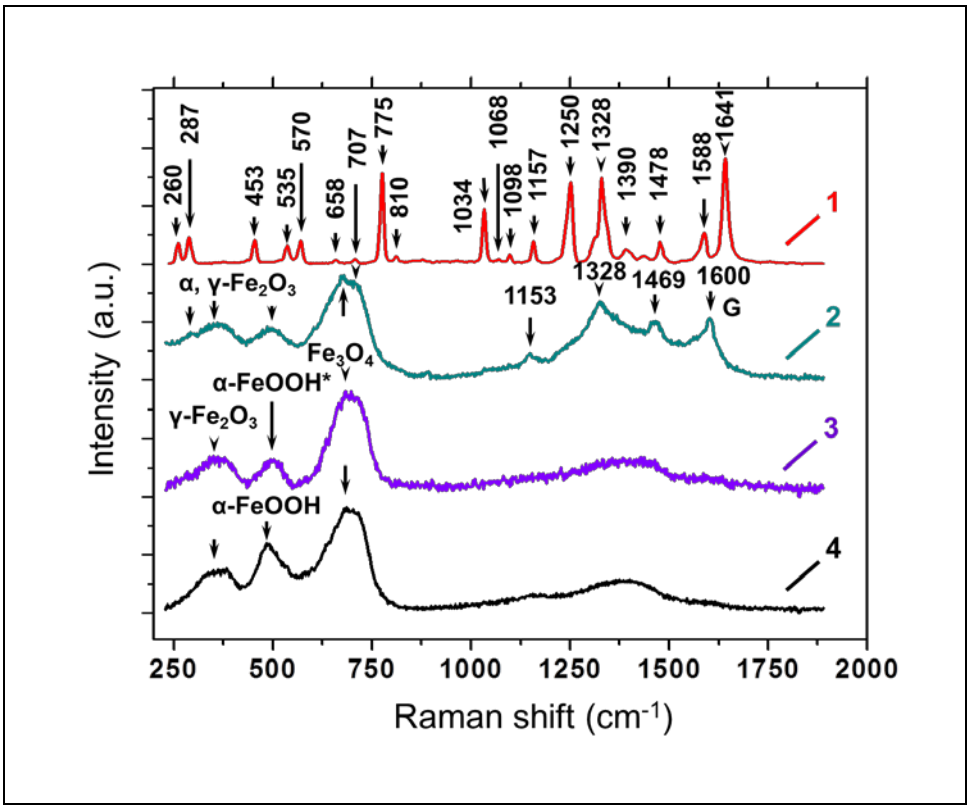

Figure 4. Raman spectra of salicylic acid *per se* (1), Fe_3O_4-rGO-SA (2), Fe_3O_4-SA (3), Fe_3O_4 (4) (λ_{exc}=633 nm, a grating 600 gr/mm blazed at 600 nm, 40x objective, 60 s accumulation)

The electronic molecular structure of Fe_3O_4-rGO-SA nanoparticles was defined by UV-Visible absorption spectroscopy (Figure 5). UV-Vis absorbance spectrum of aqueous colloidal Fe_3O_4-rGO-SA solution shows two characteristic peaks at ~231 nm and ~297 nm, which can be assigned to pristine SA [41], but are slightly shifted in comparison with observed spectra in phosphate buffer solution at pH=6.8. [42].

The first band can be related to interaction of hydroxyl groups with aromatic rings [43]. A broad small peak near ~385 nm (~3.2 eV) indicates $Fe^{3+}{}_B(e_g\downarrow) \rightarrow Fe^{3+}{}_A(e_g\downarrow, t_2\downarrow)$ interband transitions of Fe_3O_4 [44] and its shift at ~390 nm (~3.18 eV) can be caused by interaction with rGO in Fe_3O_4-rGO-SA nanoparticles.

Table 2

Analysis of Raman spectra of ultrasonically synthesized Fe_3O_4-SA and Fe_3O_4-rGO-SA in comparison with bare Fe_3O_4 nanoparticles (λ_{exc}=633 nm) (s – strong, w – weak)

Fe_3O_4 nanoparticles		**Fe_3O_4-SA**		**Fe_3O_4-rGO-SA**	
ν, cm^{-1}	**Assignment**	**ν, cm^{-1}**	**Assignment**	**ν, cm^{-1}**	**Assignment**
-	-	-	-	293	α-Fe_2O_3
350	γ-Fe_2O_3	350	γ-Fe_2O_3	350	γ-Fe_2O_3
482	α-FeOOH	496	α-FeOOH*	492	α-FeOOH*
681	α-FeOOH	670	Fe_3O_4	670	Fe_3O_4
-	-			707	21_{α}, $15_{\rho 1}$ solid crystal SA, C-C in-plane bending of the benzene ring [38]
				1153w	44_{β}, 25_{t} solid crystal SA, C-C in-plane bending of the benzene ring [38]
				1328s	$28_{\chi 1}$, $24_{\rho 2}$, C-O stretching of the carboxylic group [38]
				1469w	50_{β}, 34_{t} of SA in a solution, C-C stretching of the benzene ring [38]
				1600	G from rGO due to amorphization of graphite with sp^2-hybridization [39]

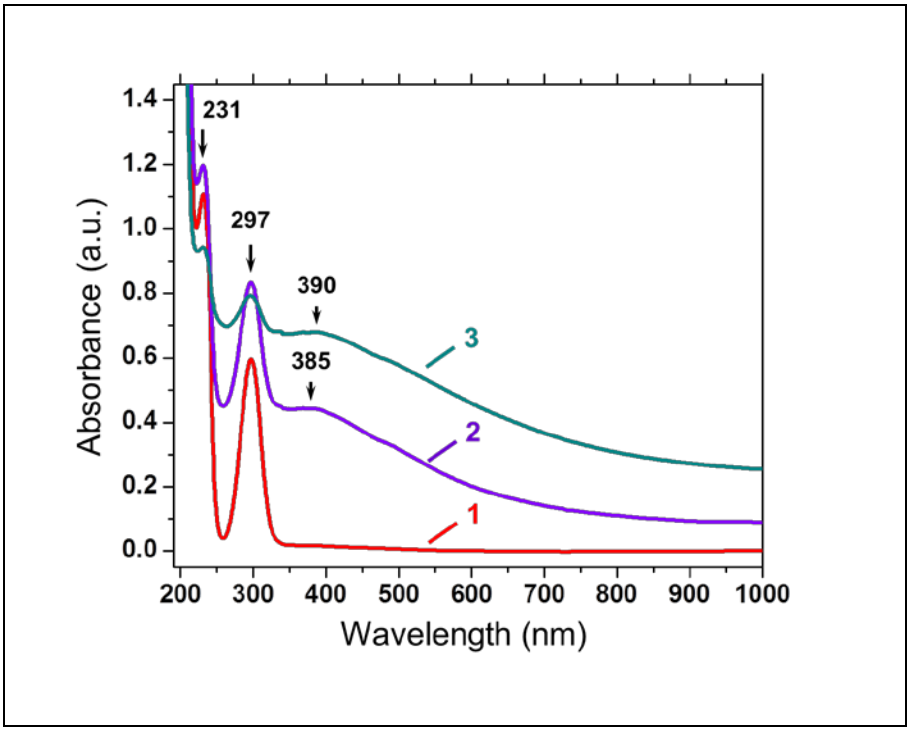

Figure 5. UV-Vis absorption spectra of aqueous solutions of pristine salicylic acid (1) and ultrasonically synthesized Fe_3O_4-SA (2) and Fe_3O_4-rGO-SA (3) nanoparticles.

The elemental composition of Fe_3O_4-rGO-SA and Fe_3O_4-SA nanoparticles was determined by Energy dispersive X-ray fluorescence spectroscopy (Figure 6).

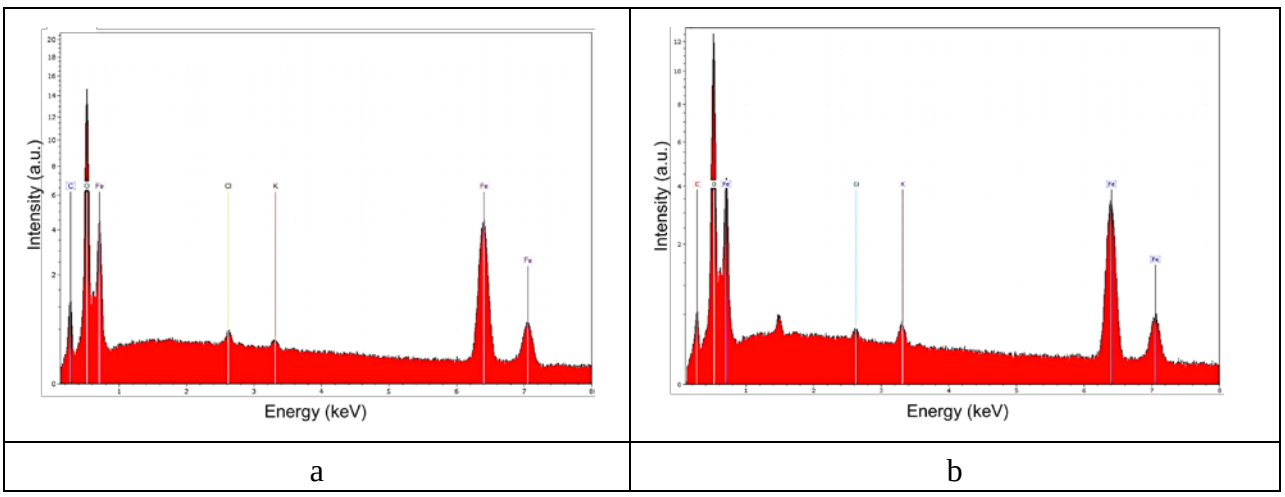

a	b

a – ultrasonically synthesized Fe_3O_4-rGO-SA; b – Fe_3O_4-SA nanoparticles.

Figure 6. Energy dispersive X-ray fluorescence spectra of Fe_3O_4-rGO-SA and Fe_3O_4-SA nanoparticles

Analysis of EDX spectra showed that Fe_3O_4-rGO-SA nanoparticles are composed of O (~59.74±3.60) at.%, Fe (~36.32±2.00) at.%, C (~2.91±0.30) at.% with negligible traces of K ~0.74±0.10 at.% and Cl ~0.28±0.00 at.% (Figure 6a) comparable to Fe_3O_4-SA (O~59.14±3.80 at.%, Fe~31.46±1.90 at.%, C~9.40±0.70 at.%) (Figure 6b). Both types of nanoparticles are mainly composed of O, Fe and C elements, but have different O/Fe atomic ratio: ~1.65 in Fe_3O_4-SA and ~1.88 in Fe_3O_4-rGO-SA than bare magnetite nanoparticles (~1.44) [45] demonstrating the excess of O caused by the complexed SA. The O/C atomic ratio of Fe_3O_4-rGO-SA (~20.53) is by factor of 3.3 larger than of Fe_3O_4-SA (~6.29), proving the complexation of SA with rGO and Fe_3O_4.

6.3 Concentration of complexed SA molecules in Fe_3O_4-rGO-SA nanoparticles

The next question to answer is how many SA molecules are complexed in nanoparticles. It is assumed that for Fe_3O_4-rGO-SA nanoparticles (~10 nm) the total average density of bulk GO is ~47.42×10^{23} L^{-1}, the volume of a single nanoparticle is ~5.23×10^{-25} m^3 with ~6.24×10^6 iron and ~8.39×10^7 oxygen atoms (Appendix 5).

The volume of single GO sheet is ~4.04×10^{-25} m^3, assuming the covalent C-C distance of graphene hexagon ~0.142×10^{-9} m, the C-H of benzene ring ~0.108×10^{-9} m and diameter ~0.426×10^{-9} m. One single GO nanoparticle consists of 6.49×10^7 oxygen and 3.21×10^5 carbon atoms, if the volume of one single carbon atom is 1.26×10^{-30} m^3. The estimated density of Fe_3O_4-rGO nanoparticles is ~5.11×10^{11} L^{-1}, taking into account the complex volume of magnetite and rGO, molecular weights of all components and the number of iron and oxygen atoms in Fe_3O_4, carbon and oxygen in rGO.

When the density of Fe_3O_4-rGO nanoplatform is divided by SA density the concentration of complexed SA molecules is 3.85×10^8. Following similar procedure of calculation the number of complexed SA molecules in Fe_3O_4-SA nanoparticles was estimated as ~7.78×10^{10} (Appendix 6). These values of SA molecules in nanoparticles are in good agreement with the concentration of complexed SA molecules obtained from the UV-Vis absorption measurements being as 186 μM Fe_3O_4-SA (~25.74 μg/mL) and 178 μM in Fe_3O_4-rGO-SA (~24.56 μg/mL) nanoparticles (Figure 7a,b).

However, the measurements of fluorescence spectra of Fe_3O_4-rGO-SA and Fe_3O_4-SA nanoparticles in ethanol (70 wt.%) at T=22±1°C and pH=5.0 revealed higher concentration of complexed SA molecules in Fe_3O_4-rGO-SA (~8.04 μM) and Fe_3O_4-SA (~3.52 μM), showing that Fe_3O_4-rGO-SA nanoparticles have larger amount of electronically active SA molecules in their complexes than Fe_3O_4-SA (Figure 7c,d).

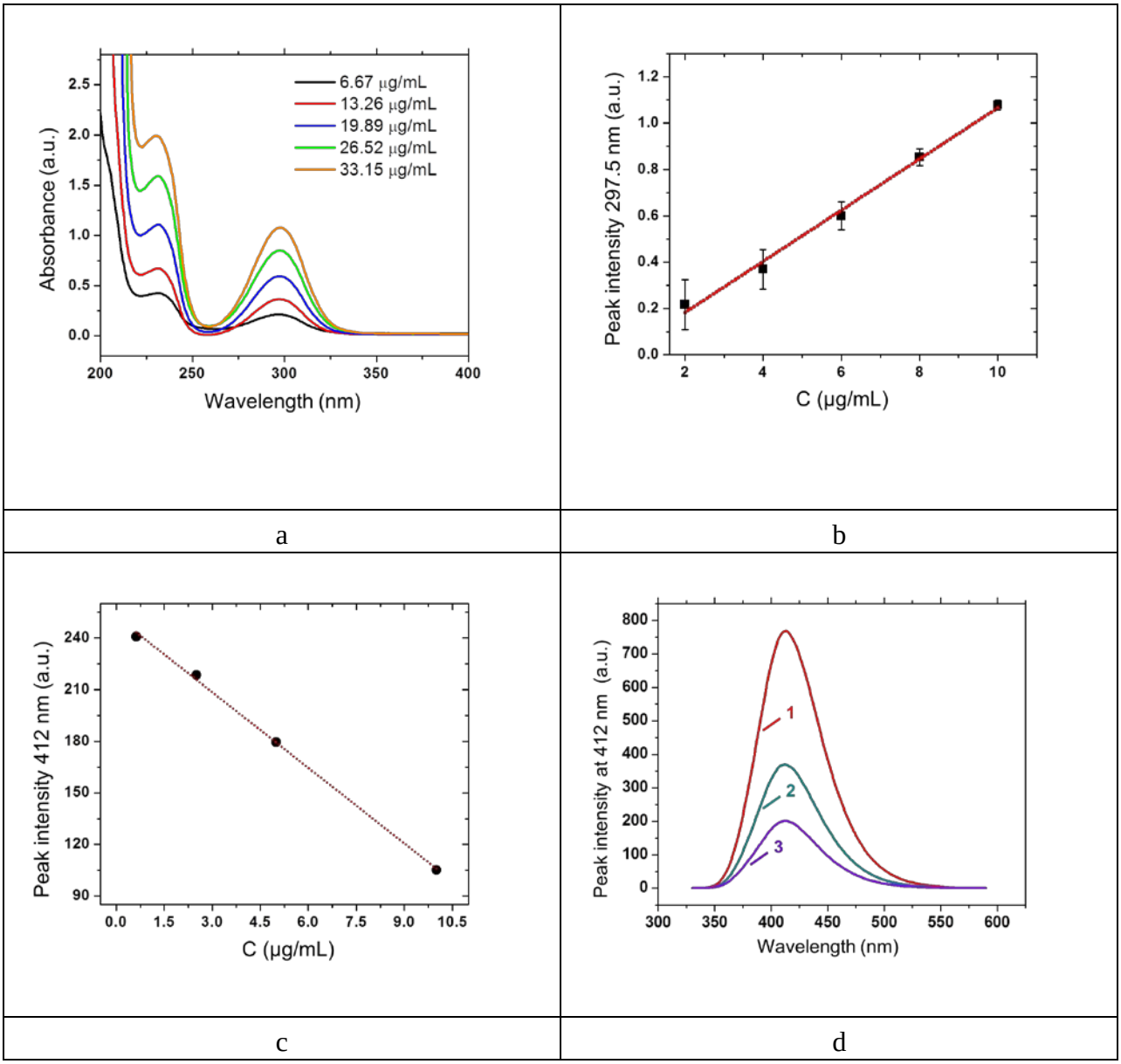

a – UV-Visible absorption spectra of salicylic acid *per se* in water; b – UV-Visible absorption peak intensity of SA *per se* at 297.5 nm in water; c – fluorescence peak intensity at 412 nm of SA *per se* in ethanol (70 wt.%); d – fluorescence spectra of pristine SA (1), Fe_3O_4-rGO-SA (2) and Fe_3O_4-SA (3) in ethanol (70 wt.%).

Figure 7. The UV-Visible absorbance and fluorescence of pristine SA to determine concentration of complexed drug molecules in Fe_3O_4-rGO-SA and Fe_3O_4-SA nanoparticles

6.4 Electronic properties of Fe_3O_4-rGO-SA nanoparticles in the Fenton process

The catalytic efficiency of Fe_3O_4-rGO-SA nanoparticles to diminish ·OH radical formation was examined in the electro-Fenton process (Appendix 5). The formation of ·OH radicals in aqueous solution of pristine SA is associated with the characteristic current peak at ~18.51 mA (~0.48 V) due to oxidation and a small broad peak at ~-9.86 mA (~0.18 V) by reduction (Figure 8).

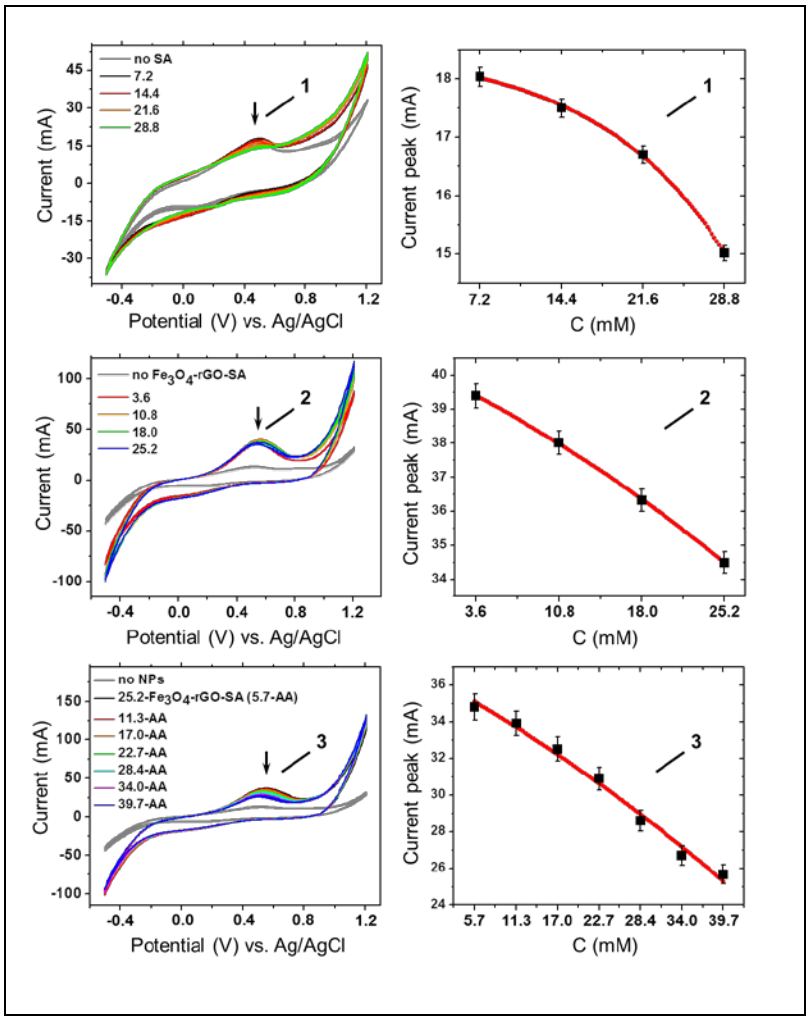

Figure 8. Cyclic voltammograms of the relative response of current (mA) in aqueous solutions of pristine SA (CV-1), Fe_3O_4-rGO-SA (CV-2) and Fe_3O_4-rGO-SA-AA (CV-3) after ascorbic acid (AA) addition (5.7 mM-39.7 mM) and their corresponding current peak values (mA) of ·OH formation during the electro-Fenton process

At increased SA concentration from 7.2 mM to 28.8 mM the oxidation peak disappeared at a reaction rate ~1.6 [27] and two reduction peaks were developed at ~-9.52 mA (~0.21 V) and ~-4.29 mA (~0.64 V), which indicated site-specific drug location [46], caused by iron binding ability and formation of SA-Fe(III) complex [47] (Figure 8, CV-1). The salicylate-iron complex has superoxide-dismutase (SOD) activity, which involves the reduction of Fe(III) complex to Fe(II), generating $^{\cdot}OH$ [7]. SA decreases the flux of hydroxyl radicals through chelation, which causes a redox deactivation mechanism of iron Fenton reaction centers in the reaction $Fe(II)+H_2O_2 \rightarrow Fe(III)+{}^{\cdot}OH+ OH^-$ [5]. SA enables bringing about the catalytic dismutation of the superoxide radical ($O_2^{\cdot -}$), resulting in its removal depending on iron and the salicylate:iron molar ratio (in our work from 7.2 to 28.8) (Figure 9).

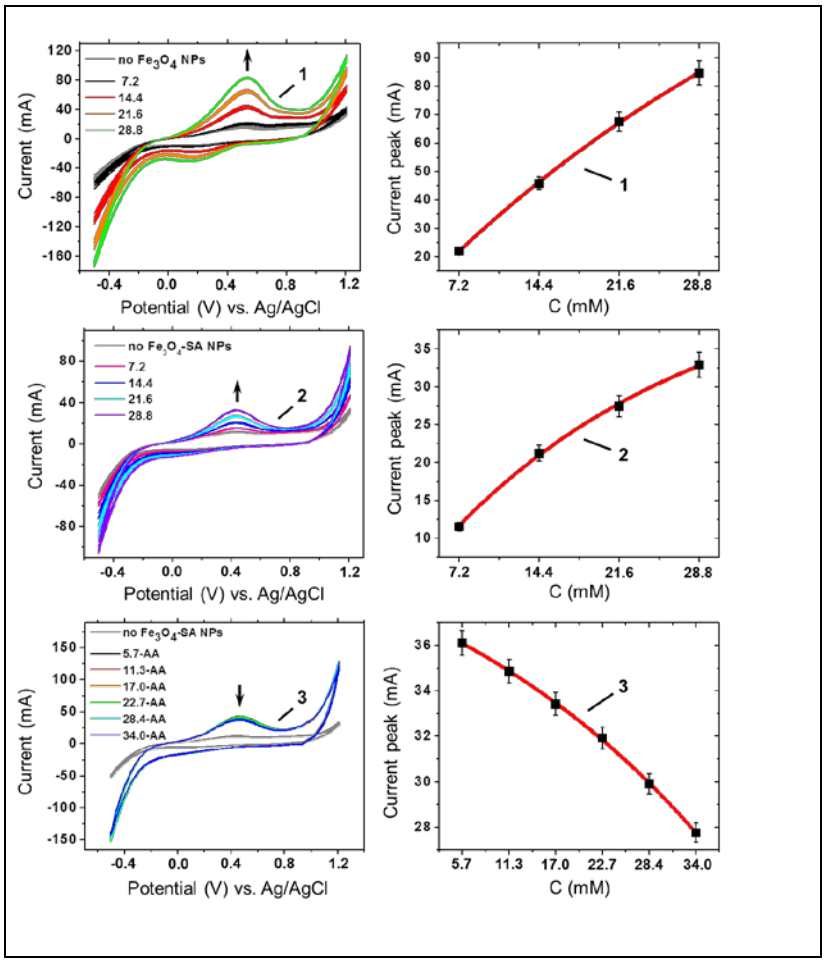

Figure 9. Cyclic voltammograms of the relative response of current (mA) in aqueous solutions of bare Fe_3O_4 (CV-1), Fe_3O_4-SA (CV-2) and Fe_3O_4-SA-AA (CV-3) after ascorbic acid (AA) addition (5.7 mM-34.0 mM) and their corresponding current peak values (mA) of $^{\cdot}OH$ formation during the electro-Fenton process

In contrast to free SA molecules, the iron-salicylate complex does not have the thermodynamic driving force to act as an effective Fenton reagent necessary for the production of damaging oxygen-containing radicals. It was proved that salicylate (in contrast to SA) acts by redox deactivation of iron, not by hydroxyl radical scavenging.

The decrease of the current ·OH peak is recorded in CV of Fe_3O_4-rGO-SA nanoparticles at concentration from 3.6 mM to 25.2 mM at a higher reaction rate ~7.1 than of pristine SA (Figure 8, CV-2). This reaction rate is increased by tenfold (~17.1), when aqueous solution of Fe_3O_4-rGO-SA nanoparticles (25.2 mM) was stepwise added by ascorbic acid (AA) at the concentration from 5.7 mM to 39.7 mM (Figure 8, CV-3). For comparison, Fe_3O_4-SA nanoparticles (25.2 mM) in AA aqueous solution decrease the ·OH peak at a reaction rate ~6.7 [27] (Figure 9).

The enhanced catalytic activity of Fe_3O_4-rGO-SA nanoparticles can be caused by higher concentration of electronically active complexed SA ligands (~8.04 μM) than in Fe_3O_4-SA (~3.52 μM) that can reduce iron and activate AA against OH generation. In addition, the formation of Fe(III)-bis-salicylato-diaquo complexes is more pronounced in Fe_3O_4-SA than in Fe_3O_4-rGO-SA nanoparticles, meaning that ferric complexes are not reduced by $O_2^{\cdot -}$ ions acting as a precursor to H_2O_2 in superoxide dismutation, thereby promoting the Fenton reaction.

Those nanoparticles that have ferrous-SA complexes and adsorbed AA molecules contribute to the ·OH radical damage, in contrast to Fe_3O_4 and Fe_3O_4-SA nanoparticles (7.2-28.8 mM), which promote the ·OH growth at reaction rates ~6.3 and ~3.2 (Figure 9). As a result, rGO may strongly diminish ·OH radicals at the contact with AA and ascorbate free radical ($AscH^{\bullet -}$), which reduce Fe(III) complex to Fe(II) maintaining generation of soluble Fe(II) in the iron oxide system [48]. In addition, AA can directly react with ·OH, superoxide and $^1O_2$ via the ascorbate-glutathione pathway, mitigating oxidative stress [49].

To understand the antioxidant activity of Fe_3O_4-rGO-SA nanoparticles, the oxygen evolution reaction at the anode, resulting in H^+ formation is theoretically modelled (Figure 10, Appendix 5). Two opposite mechanisms of H^+ ions production by Fe_3O_4-SA (2) or Fe_3O_4-rGO-SA (3) nanoparticles (21.55-24.36x10^{-3}M) are observed in AA aqueous solutions (Figure 10b). The molar C_{H+} is increased by pristine SA (~13.0-19.0x10^{-3}M) or Fe_3O_4-SA (14.0-16.0x10^{-3}M), but it is decreased by Fe_3O_4-rGO-SA (9.9-7.8x10^{-3}M), demonstrating that AA may act as an electronic molecular switch of the antioxidant activity of two different mechanisms in a concentration dependent manner. AA molecules adsorbed on the surface of Fe_3O_4-rGO-SA interact with iron-SA complexes and cause a decreased generation of H^+ and diminishing of hydroxyl radicals in Fenton, thereby enhancing protective antioxidant mechanism of ascorbate: ascorbate+$2H^+$+$O_2{\bullet}^-$→$2H_2O_2$+dehydroascorbate, excluding oxidation of ascorbate at pH=5.0 [50].

To understand the electrokinetic activity of nanoparticles in diminishing of hydroxyl radicals, ξ-potential values of Fe_3O_4-SA and Fe_3O_4-rGO-SA were determined in comparison with bare Fe_3O_4 and Fe_3O_4-rGO [27] (Figure 11). ξ-potential values of bare nanoparticles change in the following order: -38.8±3.0 mV (Fe_3O_4) and -29.7±2.3 mV (Fe_3O_4-rGO). The surface charge of Fe_3O_4-SA becomes more positive from ξ=-10.2±0.8 mV, when SA was added during ultrasonic treatment of preformed Fe_3O_4, to ξ=12.2±0.9 mV, when SA was added during the *in situ* synthesis of nanoparticles, and ξ=29.4±1.5 mV at 15.9 μg/ml concentration of nanoparticles (Figure 11a and Table 3).

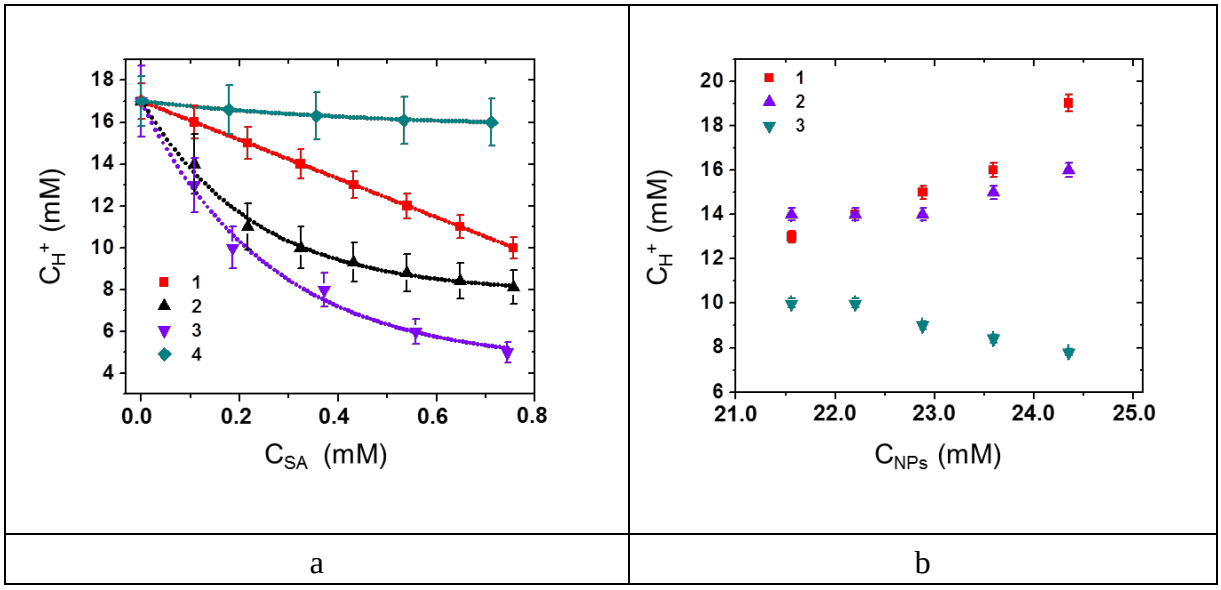

a b

a – amount of H^+ formation in SA molecules (1), bare Fe_3O_4 (2), Fe_3O_4-SA (3) and Fe_3O_4-rGO-SA (4) nanoparticles in dependence on concentration of SA; b – on concentration of SA molecules (1), Fe_3O_4-SA (2) and Fe_3O_4-rGO-SA (3) nanoparticles.

Figure 10. Theoretical modeling of the oxygen evolution reaction at the anode, resulting in H^+ formation on complexed SA molecules in Fe_3O_4-rGO-SA and Fe_3O_4-SA nanoparticles

In contrast, the surface charge of iron-SA complexes in *in situ* synthesized Fe_3O_4-rGO-SA change from ξ=-5.7±2.6 mV to 12.1±1.0 mV as the concentration of nanoparticles nonlinearly increased from 6.3 μg/ml to 250 μg/ml (Figure 11b and Table 4). Therefore, more acidic environment is formed in colloidal Fe_3O_4-rGO-SA than in Fe_3O_4-SA aqueous solution, which can change the adsorption of AA molecules on nanoparticles and switch between redox deactivation of iron (more acidic) or antioxidation (more basic) mechanisms.

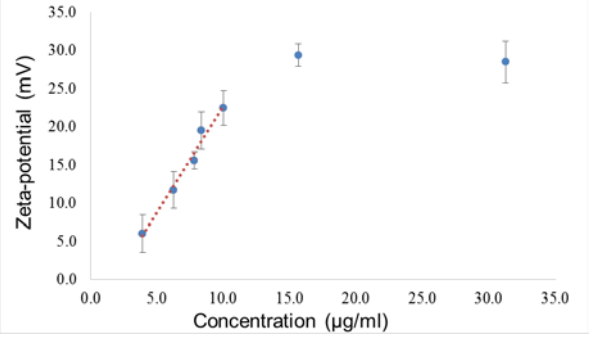

a

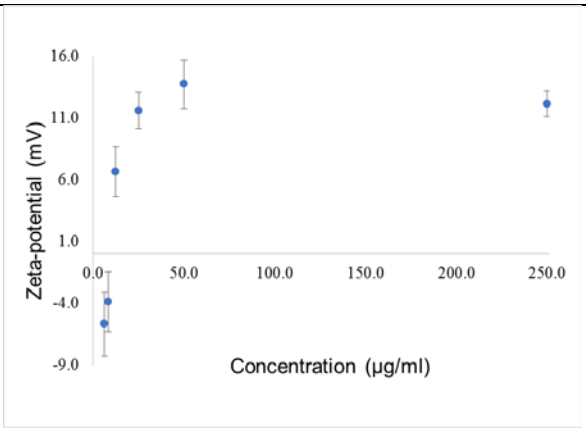

b

a – Concentration dependent Zeta potential (mV) plots of Fe_3O_4-SA; b – Fe_3O_4-rGO-SA.

Figure 11. The surface charge of aqueous solutions of Fe_3O_4-SA and Fe_3O_4-rGO-SA in dependence on concentrations of nanoparticles

Table 3

Concentration dependent Zeta potential values of *in situ* ultrasonically synthesized Fe_3O_4-SA nanoparticles in aqueous solutions

	ξ-potetial values of Fe_3O_4-SA						
C, μg/mL	3.9	6.3	7.8	8.3	10.0	15.6	31.3
<ξ>, mV	6.0	11.7	15.6	19.5	22.5	29.4	28.5
SD	2.45	2.45	1.10	2.45	2.28	1.47	2.70

Table 4

Concentration dependent Zeta potential values of *in situ* ultrasonically synthesized Fe_3O_4-rGO-SA nanoparticles in aqueous solutions

	ξ-potential values of Fe_3O_4-rGO-SA					
C, μg/mL	6.3	8.3	12.5	25.0	50.0	250.0
<ξ>, mV	-5.7	-3.9	6.6	11.6	13.7	12.1
SD	2.60	2.42	2.04	1.48	1.97	1.03

SD – standard deviation values

6.5 Modeling of electric surface potential cross section of Fe_3O_4-rGO-SA

Therefore, the next question to answer is, why does electronic AA donor accelerate the diminishing reaction of ·OH radicals at the contact with complexed SA in iron oxide system of rGO (Appendix 5).

To assess the charge carrier density with such surfaces, the computation based on 3D modelling of the electric surface potential cross section distribution (U) was performed on Fe_3O_4-rGO-SA in comparison with Fe_3O_4 and Fe_3O_4-SA nanoparticles (Figure 12).

Analysis of the 3D U distribution modeling shows that peak magnitudes appear only in the cross section regions of nanoparticles. The derived current J density peak magnitudes are the highest, if the average diameter of nanoparticles approaches the distance of 1 nm: $3.52x10^6$A m^{-2} of Fe_3O_4, $7.45x10^6$A m^{-2} of Fe_3O_4-SA and $7.97x10^4$A m^{-2} being two orders of magnitude lower in Fe_3O_4-rGO-SA, which is determined by the rGO physical properties.

The computed J values nonlinearly decrease with increased average size of nanoparticles up to 100 nm at reaction rates: by fitting to a polynomial function of the 9^{th} order on Fe_3O_4, ~87 and ~$3x10^4$ by fitting to the exponential decay function on Fe_3O_4-SA and Fe_3O_4-rGO-SA [27].

The J magnitudes decrease on Fe_3O_4-rGO-SA in a small range from $795.65x10^2$ to $795.22x10^2$A m^{-2} in contrast to Fe_3O_4-SA (from $7.99x10^6$ to $5.55x10^6$A m^{-2}), demonstrating the important role of rGO and complexed SA in enhanced charge transfer catalysis.

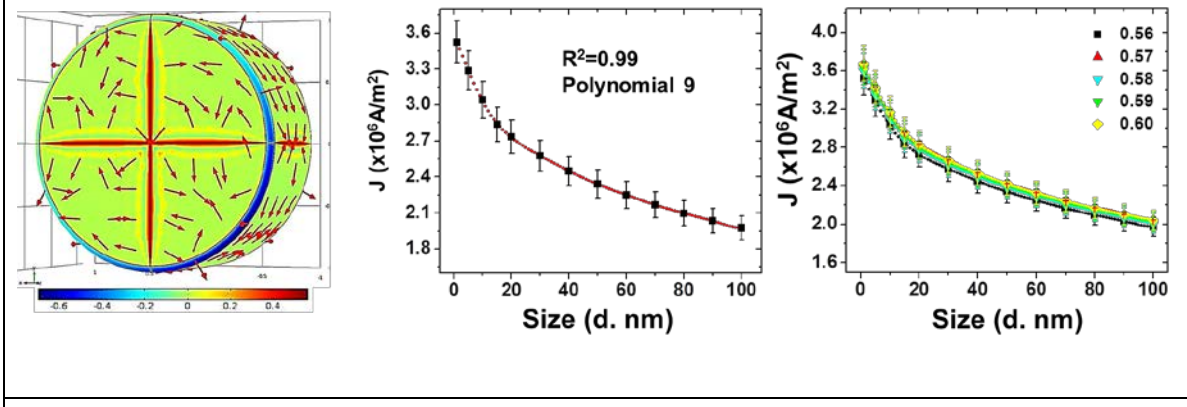

a

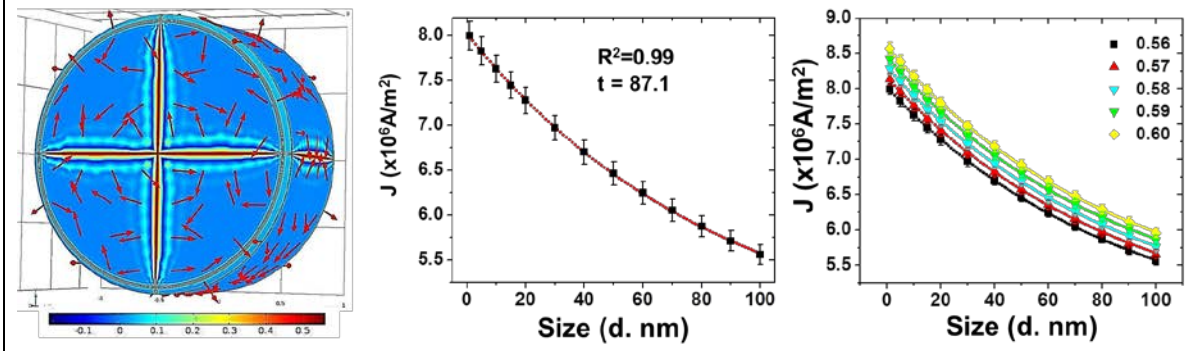

b

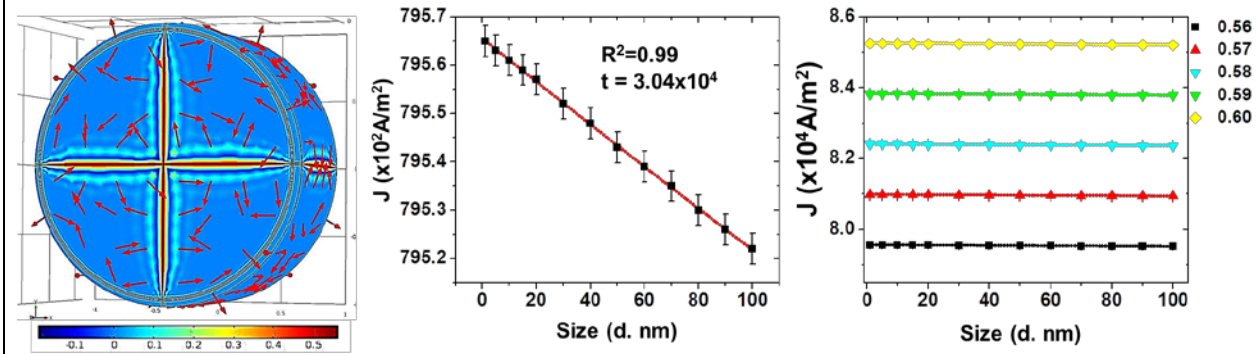

c

a – bare Fe_3O_4 ~30 nm; b – Fe_3O_4-SA ~15 nm; c – Fe_3O_4-rGO-SA ~10 nm.

Figure 12. The 3D plots of the computed electric surface potential distribution on bare Fe_3O_4, Fe_3O_4-SA and Fe_3O_4-rGO-SA nanoparticles

6.6 Intracellular accumulation and cytotoxicity of Fe_3O_4-rGO-SA nanoparticles

As it has been shown that ·OH and H^+ production can be controlled by Fe_3O_4-rGO-SA, it appears promising to advance this method for the growth inhibition study of HeLa, HepG2 and HT29 cancer cells with internalized nanoparticles (Figure 13). Most of cells exhibit bright fluorescence signals over their entire surface structure, proving successful intracellular accumulation of nanoparticles (Table 5).

Very few non-fluorescent parts inside cells can be detected arising from intracellular vesicular structures (Figure 13a). There are clear changes of the morphology of cells caused by their interaction with digested nanoparticles with respect to control live cells (without nanoparticles). These morphological changes are distinctly seen in HepG2 cells in comparison with morphology of non-fluorescent nanoparticles (Figure 13b). Therefore one may conclude that this effect can be caused by the toxicity of the dye itself. Overall, the dye color distribution in images is relatively uniform in all three lines, despite the fact that HT29 cells grow in dense clusters with surrounded mucous-like membrane (Figure 13c). In our experiments the initial number of HT29 cells was insufficient to form multiple dense clusters during the incubation period.

After 24 h of incubation in HeLa cells fluorescence images revealed a clear difference between internalized Fe_3O_4-SA and Fe_3O_4-rGO-SA NPs (Figure 13a). In particular, ~47 % of HeLa cells with intracellularly accumulated Fe_3O_4-rGO-SA and only ~22 % with Fe_3O_4-SA exhibited the brightest fluorescence over the entire surface, demonstrating that these nanoparticles degraded inside cells and left only dye molecules. In contrast to HeLa cells, almost all of HepG2 cells with intracellularly accumulated Fe_3O_4-rGO-SA showed the brightest fluorescence as individual bright dots in cytosol and nucleus and as a solid bright spot over the entire surface (Figure 13b).

For comparison, no individual bright dots were observed in bright fluorescent HepG2 cells with Fe_3O_4-SA. The mean number of fluorescent cells with the brightness over the entire surface was ~38 % with Fe_3O_4-rGO-SA and ~23 % with Fe_3O_4-SA. The presence of individual fluorescent dots that are homogenously distributed in cytosol and nucleus of HepG2 cells indicated that Fe_3O_4-rGO-SA are not fully digested in intracellular compartments after 24 h of incubation in most of these cells. This is in contrast to Fe_3O_4-SA, which are fully digested by HepG2 cells, leaving dye molecules inside cells. No significant differences in intracellularly digested Fe_3O_4-rGO-SA or Fe_3O_4-SA were observed in HT29 cells (Figure 13c). Nanoparticles with complexed SA molecules were more strongly accumulated inside cells than bare nanoparticles according to the data shown in Table 5. At the same time, nanoparticles with rGO showed an advantage in comparison with iron oxide nanoparticles.

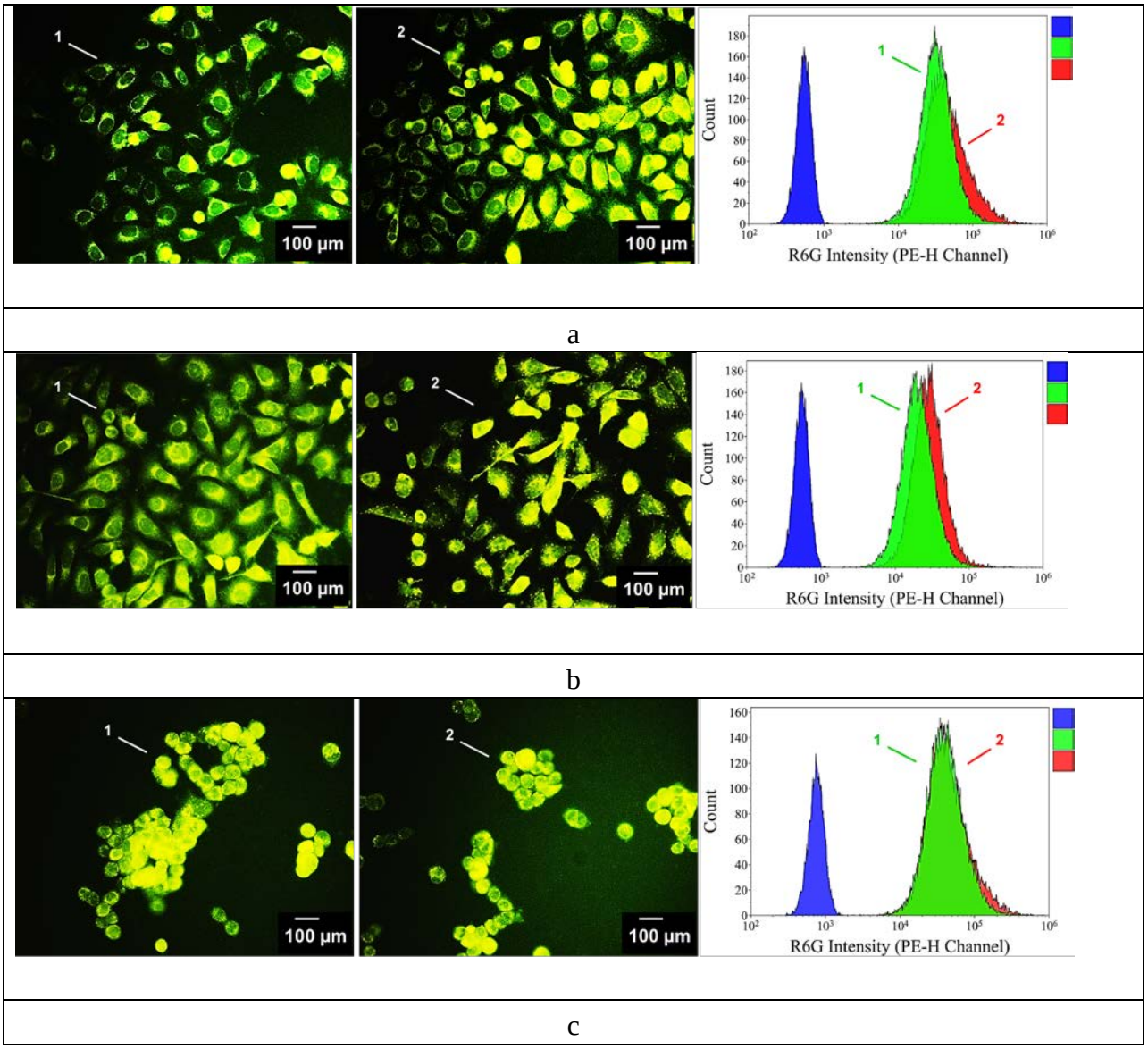

a – Fe_3O_4-SA (1) and Fe_3O_4-rGO-SA (2) intracellularly internalized nanoparticles in HeLa; b – in HepG2; c – in HT29 after 24 h of incubation.

Figure 13. Representative fluorescence microscopy images and statistical histograms of fluorescence signals obtained from flow cytometry measurements of HeLa, HepG2 and HT29 cancer cells with internalized Fe_3O_4-SA and Fe_3O_4-rGO-SA nanoparticles (blue histogram corresponds to cells untreated with nanoparticles)

Analysis of fluorescence microscopy images shows that Fe_3O_4-rGO-SA are stronger internalized, which can be explained by enhanced interaction of rGO with biological membrane

and its interference with cell signaling processes observed in intracellular studies of various graphene oxide-magnetite-drug nanoparticles [19].

Table 5

The values of the median fluorescence intensity (MFI, $x10^4$) obtained from the flow cytometry measurements of three cancer cell lines: HeLa, HepG2 and HT29 with uptaken Fe_3O_4-SA or Fe_3O_4-rGO-SA NPs in comparison with bare Fe_3O_4 and Fe_3O_4-rGO NPs

	Fe_3O_4-SA	**Fe_3O_4-rGO-SA**	**Fe_3O_4**	**Fe_3O_4-rGO**
HeLa	2.92 ± 0.05	4.18 ± 0.46	1.77 ± 0.31	3.57 ± 0.29
HepG2	2.12 ± 0.31	2.75 ± 0.27	1.41 ± 0.14	2.14 ± 0.25
HT29	3.88 ± 0.18	4.04 ± 0.28	2.93 ± 0.24	3.31 ± 0.19

Longer retention period of drug within cells was ascribed to the effect of graphene-based nanocarriers, resulting in higher intracellular concentration of this drug. Another evidence of greater interaction of graphene-based nanoparticles with biological membrane was derived from the confocal microscopy studies: graphene-based nanocarriers comparatively required longer time to gain access in the HeLa cells which is a strong indication of its improved interaction with the membrane lipid layer. In the study of nuclear apoptosis of HepG2 cells with stronger internalized Fe_3O_4-rGO-based drug nanoparticles, condensed and disintegrated nuclei and chromatin were observed from the apoptotic nuclei at the membrane boundaries [51]. The study on interaction of GO with mammalian HT-29 cells reveals that GO promotes cell attachment and proliferation [52]. The complex based on drug-GO-Fe_3O_4 structure advantageously reduced the viability of HT29 cells in comparison with bare drug-GO and free drug [53].

In HeLa line, Fe_3O_4-rGO-SA nanoparticles reproducibly decrease the number of cells by ~14 % without adsorbed AA molecules, which is in contrast to Fe_3O_4-rGO-SA-AA in titration procedure (Figure 14a).

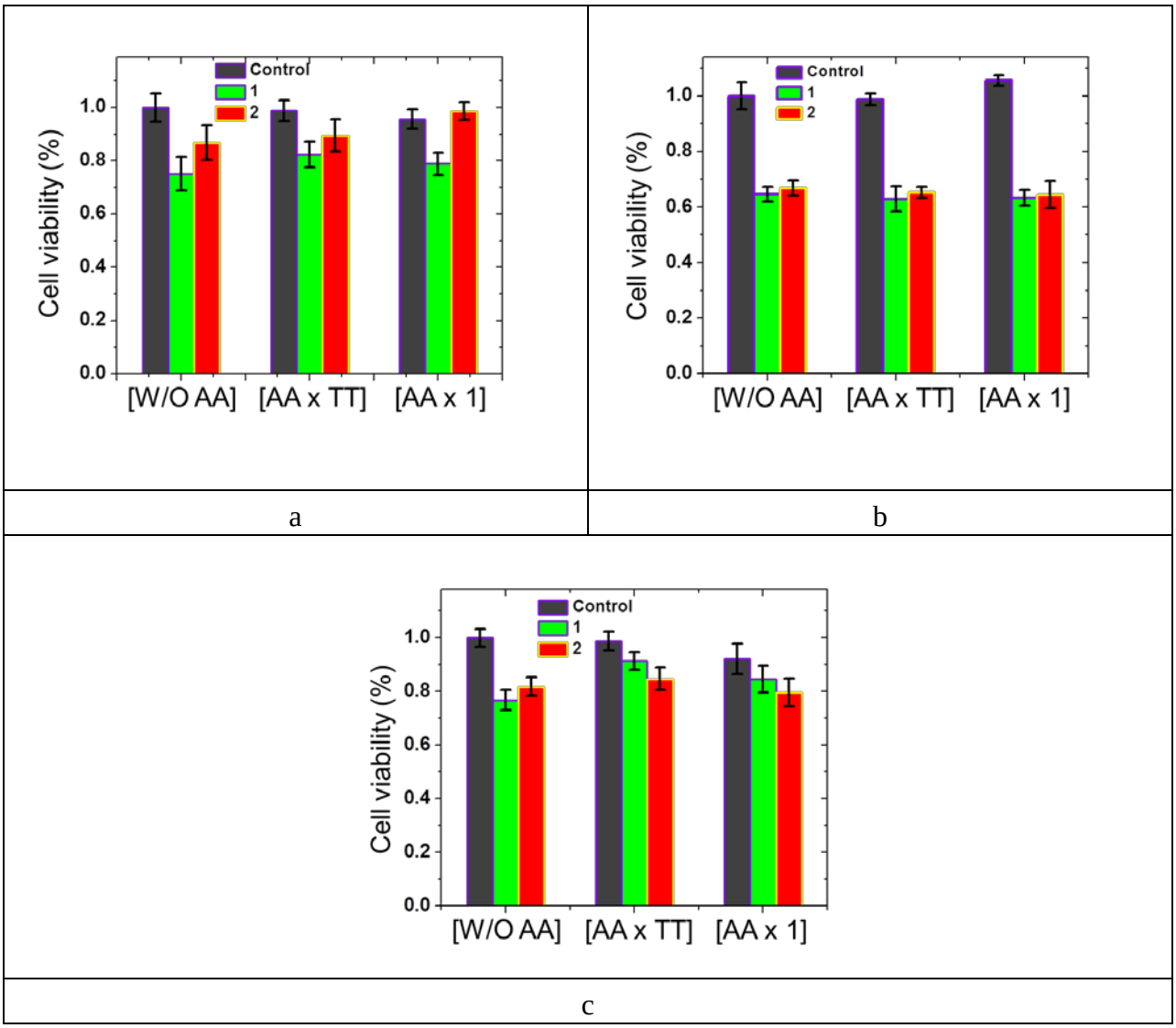

a – in HeLa cells; b – in HepG2; c – in HT29 after 24 h of incubation with nanoparticles.

Figure 14. Statistical diagrams of HeLa, HepG2 and HT29 cancer cells viability with internalized Fe_3O_4-SA and Fe_3O_4-rGO-SA nanoparticles in comparison with untreated cells (control) at conditions of without ascorbic acid (W/O AA), in ascorbic acid aqueous solution (15 μg/mL) via titration (AA x TT) and at once method (AA x 1)

This observation suggests that redox deactivation of iron occurs and not enhanced antioxidation can be a dominant mechanism of *in vitro* growth inhibition by synthesized nanoparticles. In contrast to HeLa and HT29 cells, stronger cytotoxicity effects ~67 % were determined in HepG2 with Fe_3O_4-rGO-SA in AA independent manner, suggesting that the mechanism of redox deactivation of iron at increased H^+ more contributes to the growth

inhibition of cancer cells through the decreased formation of hydroxyl radicals (Figure 14b). In all cells, control experiments of pristine AA titration or SA did not reveal any statistically relevant changes. Slight decrease of the cell viability (~0.92±0.06%) was detected, when AA was added at once, indicating the intracellular induction of reduction processes. In the absence of AA, the overall cytotoxic effects were stronger with intracellularly internalized Fe_3O_4 than Fe_3O_4-rGO, which can be caused by higher amount of hydroxyl radical production [27].

In HT29 cells the cytotoxicity of Fe_3O_4-SA without AA addition (~65%) was comparable to Fe_3O_4-rGO-SA (~63%), demonstrating the important role of site specific Fe^{2+}- and Fe^{3+}-salicylate complexes in generation of damaging oxygen-containing radicals (*e.g.* malignant neoplasm H_2O_2 and super oxide O_2^- ions) that are released as byproducts of normal respiratory cellular function, causing oxidative tissue damage (Figure 14c). However, the cytotoxicity of Fe_3O_4-rGO-SA was enhanced in comparison with Fe_3O_4-SA, when AA was added during titration, and this effect was more pronounced at once addition. The addition of AA in HT29 cancer cells caused switchable growth inhibition by Fe_3O_4-rGO-SA (~85%, ~80%) with respect to Fe_3O_4-SA (~91%, ~85%), demonstrating that enhanced antioxidation with the decreased H^+ generation can be the prevailing mechanism of antiproliferative activity of NP *in vitro*.

In summary, the developed a single step ultrasonic method (20 kHz) can be indeed applied for *in situ* complexation of pristine SA molecules during the growth of Fe_3O_4-rGO nanoplatform (~10 nm). Results of FTIR spectroscopy analysis revealed that SA ligands can be selectively complexed with Fe(III)/Fe(II) binding sites as integral parts of synthesized Fe_3O_4-rGO-SA nanoparticles with precisely defined electronic molecular structure. Fe_3O_4-rGO-SA can act as redox deactivators of iron centers and increase H^+ generation, resulting in efficient diminishing of ·OH radicals. This property of Fe_3O_4-rGO-SA nanoparticles is tenfold stronger in comparison with pristine SA molecules, when ascorbic acid molecules are adsorbed on NP's surface, resulting in enhanced antioxidation and decreased formation of H^+ ions.

Overall, ascorbic acid molecules can act as antioxidant molecular switches of H^+ production by Fe_3O_4-rGO-SA due to the four orders of magnitude larger electric surface potential on their surface, where rGO plays an important role in enhanced charge transfer catalysis. Most significantly, Fe_3O_4-rGO-SA are nontoxic to erythrocytes, human peripheral blood mononuclear cells and can surpassingly inhibit the growth of three cancer cell lines: HeLa, HepG2 and HT29 in comparison to pristine SA. This method can be successfully expanded to many other NSAIDs to better understand the intracellular drug-enzyme, drug-metal and drug-cancer intracellular interactions, which can be particularly useful in treatment of diabetes, rheumatism, liver and oncological diseases.

*****

The presented results allow us to draw the following conclusions:

1. Ultrasound-assisted complexation of pristine SA with Fe_3O_4-rGO nanoplatform results in formation of Fe_3O_4-rGO-SA nanoparticles of small size ~10.20 nm and a uniform 3D space spherical structure.
2. Fe_3O_4-rGO-SA nanoparticles become more hydrophilic due to smaller size and pH=5 of colloidal solution, in contrast to pristine free SA and Fe_3O_4-SA nanoparticles.
3. Ultrasonic complexation of SA with Fe_3O_4-rGO nanoplatform occurs through phenolic ring and hydroxyl group and involves the more pronounced intramolecular hydrogen bonding in salicylate, in contrast to nanoparticles without rGO.
4. Surface oxygen functional groups of rGO contribute to the specific ultrasonic reduction of Fe(II) at the contact with SA ligands and allow formation of the thermodynamically stable metallocomplex in nanoparticles.
5. Longer retention period of SA within live cancer cells can be ascribed to the effect of rGO at the contact with Fe_3O_4, resulting in higher intracellular concentration of nanoparticles.
6. The redox deactivation of iron can occur and not enhanced antioxidation can be a dominant mechanism of *in vitro* apoptosis caused by synthesized Fe_3O_4-rGO-SA nanoparticles.
7. In contrast to HeLa and HT29 cells, stronger cytotoxicity effects ~67 % were determined in HepG2 with Fe_3O_4-rGO-SA in ascorbic acid independent manner, suggesting that the mechanism of redox deactivation of iron at increased H^+ more contributes to the apoptosis through the scavenging of hydroxyl radicals.
8. The addition of ascorbic acid in HT29 cancer cells can cause switchable growth inhibition by Fe_3O_4-rGO-SA (~85%, ~80%) with respect to Fe_3O_4-SA (~91%, ~85%), demonstrating that enhanced antioxidation with the decreased H^+ generation can be the prevailing mechanism of antiproliferative activity of nanoparticles *in vitro*.

Appendix 1

A1.1 Calibration of ultrasonic intensity by calorimetry

Ultrasonic power developed by a homemade horn-type ultrasonic dispergator N.4-20 (Cavitation Inc., Belarus) was calibrated by using a method of calorimetry [11]. This dispergator was technically constructed in such a way that the relative magnitude of amplitude was related to the units of current in μA. For calibration we used mainly 25 μA (lower relative amplitude), 50 μA (medium relative amplitude), 75 μA (high relative amplitude) and 100 μA (maximum relative amplitude) as well as several intermediate magnitudes (30 μA and 40 μA). Calculated values are listed in the Table 1 and the calibration curve is shown below.

μA	**Slope**	**Wh_1**	**Wh_2**	**W_{us}**
25	0.042	8.79018	8.50663	8.23222
30	0.053	11.09237	11.9869	12.9536
40	0.056	11.72024	13.2325	14.94
50	0.067	14.02243	16.1032	18.4927
75	0.1005	21.03364	24.1548	27.7391
100	0.134	28.04486	32.2064	36.9854

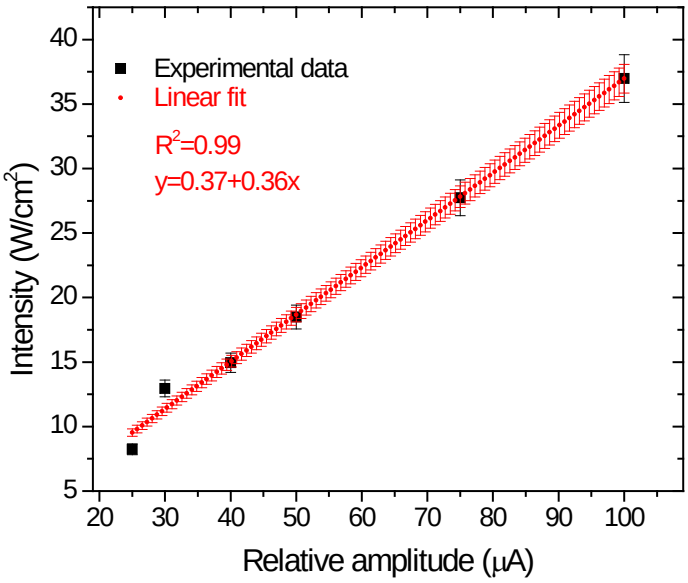

A1.2 Materials

Graphite was purchased from Imerys (France) and has dispersity 9.3-47.2 μm, crystallite size 67.7 nm, elemental composition C (94.96±2.00 at%), O (4.03±0.80 at%), Ti (0.11±0.01 at%), Ca (1.07 ± 0.10 at%), Mn (0.02 ± 0.01 at%). Sunflower oil (refined, deodorized) was obtained from the Energy Group Inc. (Belarus). $Na_2S{\cdot}9{\cdot}H_2O$ (98%), $CuCl_2{\cdot}2{\cdot}H_2O$ (99%), isopropanol (99%), H_3PO_4 (85 wt.%), $KMnO_4$ (98%), H_2SO_4 (95 wt.%), H_2O_2 (60 wt.%), HCl (35 wt.%), HNO_3 (40 wt.%), C_2H_5OH (96%), tetraethyl orthosilicate (TEOS) and polyvinyl alcohol (PVA) were obtained from Belreahim JSC (Belarus). Silver nitrate ($AgNO_3$, analytical grade, 99.8%) and sodium borohydride ($NaBH_4$, 98%) were obtained from Sigma-Aldrich Inc. (Germany). Ketorolac was purchased from Dr. Reddy's Inc. (India). For experiments 10 tablets of ketorolac were grinded in a mortar until a fine powder was obtained (more details in supporting information). This powder was dissolved in 3 mL of ethanol at a critical concentration of dissolution being 7 g/L. Deionized water (DI, pH=5.5) with specific conductivity 5 μS/cm was used. For experiments $CuCl_2{\cdot}2{\cdot}H_2O$ (powder of turquoise color) was dried at T=150°C in the oven for 20 min until it changed its color into brown followed by its grinding in a mortar bowl. $Na_2S{\cdot}9{\cdot}H_2O$ was thermally treated at T=150°C for 8 h in order to form anhydrous Na_2S.

A1.3 Synthesis of pristine graphene oxide

For the graphene oxide (GO) preparation graphite (from Imerys, m=1.16 g) was mixed with concentrated $15x10^{-3}$ L of H_3PO_4 (85 wt.%) acid and mechanically stirred until a homogeneous state was obtained. Then 6.3 g of $KMnO_4$ was added into this mixture at a weight ratio to graphite as 6:1. To obtain a homogeneous colloidal system this mixture was stirred and cooled down to 0°C. Then this mixture was stepwise added by $100x10^{-3}$ L of H_2SO_4 (95 wt.%) followed by thermal treatment at 55±5°C for 12 h in a thermostat to form GO through the oxidation process of graphite. This suspension was diluted by $290x10^{-3}$ L of iced water at a volume ratio of ice to water as 1:4. Then it was added by $1x10^{-3}$ L of 60 wt.% H_2O_2 in order to stop the oxidation process of carbon material. Obtained GO was separated by centrifugation at 4.293xg for 15 min. The sediment was added by the mixture containing $145x10^{-3}$ L H_2O, $72x10^{-3}$ L HCl (35 wt.%) and $145x10^{-3}$ L C_2H_5OH (96 wt.%) in order to remove impurities such as MnO_2 and possible metallic impurities including phosphate compounds. This mixture was washed with water by centrifugation at 4.293xg during 30 min until it obtained pH=5.5. The sediment, which is a purified GO, was dried at 100°C until a powder was obtained. The final GO powder acquired size distribution of 0.5±0.1 μm. The yield resulted in 146-152%, which is above 100% due to the presence of oxygen groups in the structure of GO nanosheets. The critical concentration of final powder was about 15-20 mg/mL and this mixture could be stored for 4-6 months. It is presumed that the GO powder mixture does not contain non-oxidized graphite flakes. Concentration of

inorganic impurities in a GO material in relation to the initial material of graphite was ≤ 1 at.% in mass: Cl is ≤ 0.18 at.%, K ≤ 0.04 at.%, Mn ≤ 0.04 at.%, Ca ≤ 0.05 at.% and P ≤ 0.07 at.%. The presence of residual S is about 1.31 at.% results from sulfuric acid during the oxidation process of graphite material.

Before the synthesis the powder of synthesized GO was dispersed in DI water (pH=5.5) by sonication at ultrasonic intensity 18 W/cm^2 for 30 min at a volume ratio of powder to water as 1:1 under ambient air in the ice bath. The GO suspension appeared with a dark brown-black color without visible sediment.

A1.4 Synthesis of CuS/Cu_2O/CuO-GO nanoplatform at the air/water interface

Before the synthesis a powder of synthesized GO was dispersed in DI water (pH=5.5) by sonication (18 W/cm^2 for 30 min) in the use of a homemade horn-type ultrasonic dispergator N.4-20 operating in a continuous mode at 20 kHz frequency with the 400 W maximal output power (Cavitation Inc. Belarus) under ambient air in the ice-cooled water bath at a volume ratio of powder to water as 1:1. For the synthesis we took 1 mL of 1 mol·L^{-1} Na_2S aqueous solution which was added into the sonicated GO suspension. The mixture of Na_2S and GO was sonicated in a sealed beaker thermostated for 1 h at lower ultrasonic intensity 8 W/cm^2 at T=60°C. After the ultrasonic treatment this mixture was cooled down to room temperature and the powder was precipitated by centrifugation at 4.293xg for 30 min. The treated mixture was decanted and the precipitant was added by 5 mL of aqueous solution of 25x10^{-3} mol·L^{-1} $CuCl_2$. This solution was sonicated at 18 W/cm^2 for 2 h in a sealed beaker thermostated and placed into an ice-cooled water bath. After that it was added by 1 mL of 1mol·L^{-1} Na_2S aqueous solution and sonicated again (18 W/cm^2 for 1 h). As the next step, this colloidal solution (pH=12) was precipitated by centrifugation (4.293xg) for 30 min and the supernatant was carefully removed. The precipitant was dispersed in DI water (pH = 5.5) and washed by repeated centrifugation until the final pH value of the colloidal mixture reached 5.5. This suspension was dried in the oven at 100°C and the fine black powder was obtained.

A1.5 Synthesis of CuS/Cu_2O/CuO-GO nanoplatform at the oil-SiO_2/water interface

Aqueous solution of PVA (5 wt.%, pH=6) was prepared under stirring for several hours at 50°C in a sealed glass vessel for complete dissolution followed by cooling down to room temperature. It was filtered through a red line cellulose membrane (pore size 8-12 nm) before being used. 30 mL of aqueous PVA (5 wt.%) solution was sonicated at 18 W/cm^2 for 30 min under air in the ice-cooled water bath in order to form a precursor emulsion solution. 5.5 mL of sonicated aqueous PVA solution was added by 5.5 mL of aqueous suspension containing CuS/Cu_2O/CuO-GO. Three types of aqueous mixtures were prepared: A) at pH = 6 (untreated); B) at pH=2 by acidifying with aqueous 1 mol·L^{-1} HCl and C) at pH=12 by addition of aqueous KOH (44 wt.%). The organic solution, consisting of 3.5 mL of TEOS and 3.5 mL of sunflower

oil, was added into the each aqueous mixture resulting in the formation of a two separate phases with the 18 mL of total volume. Ultrasonic resonator's horn was placed at the interface of these two phases and the solution was sonicated at 27 W/cm^2 for 3 min under air. During sonication the solution was cooled by ice-water and the temperature during sonication maintained below 28°C. The final solution containing prepared microspheres was stored at room temperature, aged for full three days, separated from unreacted residues by using the separation flask and washed with DI water for further characterization. For comparison, microspheres consisting of oil without TEOS were also sonochemically prepared according to the above described method. In this case, the organic solution of oil phase (no TEOS) was 7 mL.

Appendix 2

TGA of GO samples were conducted under O_2 or N_2 atmosphere during thermal treatment at 600°C at a rate 10°/min by using STA 449 C Jupiter (Erich Netzsch GmbH & Co., Holding KG, D-95100 Selb, Germany). For calibration Al_2O_3 was taken as a standard with known enthalpy and energy.

A2.1 Sonochemical synthesis of Cu/Fe-GO nanoplatforms

Powder of synthesized GO was dispersed in DI water (pH=5.5) by sonication (18 W/cm^2 for 30 min) at a volume ratio of powder suspension (0.6 g/L) to water as 1:1 under ambient air in the ice bath. As the next step 5 mL of 1 M Na_2S aqueous solution was added into the sonicated GO suspension. The colloidal solution of {Na_2S and GO} was sonicated in a sealed thermostatic round-bottomed cylindrical container (T=60±1°C) for 1 h at 8 W/cm2 ultrasonic intensity. When sonication was finished, this mixture was cooled down to room temperature and the powder was precipitated by centrifugation at 4.293 g for 30 min. The supernatant was removed and the precipitant was added by 5 mL of aqueous solution of 10 mM $CuCl_2$ and 5 mL of aqueous solution of 10 mM $FeCl_3$ and this mixture was sonicated at 18 W/cm^2 for 2 h in a sealed thermostatic container in the ice bath. Then 5 mL of 1 M Na_2S aqueous solution was added into the sonicated mixture and ultrasonically treated (18 W/cm^2 for 1 h) in the ice bath. After that the colloidal dispersion (pH=12) was centrifuged at 4.293 g for 30 min followed by decantation. The precipitant was dispersed in DI water (pH=5.5) and washed by centrifugation three times until the final pH value of the colloidal dispersion reached 5.5. This suspension was dried in the oven at ~100°C and the fine black powder was obtained.

Control experiments were carried out without $CuCl_2$ by taking 10 mL of aqueous solution of 10 mM $FeCl_3$, and without $FeCl_3$ at different concentration of aqueous solution of $CuCl_2$ (5 mM, 10 mM and 25 mM) at 0.5 M or 1 M Na_2S at a constant volume ratio of Na_2S:$CuCl_2$ as 1:2. The obtained nanomaterials were designated as Cu-GO (without Fe) and Fe-GO (without Cu).

A2.2 Ultrasonic complexation of ketorolac with Cu-GO, Cu/Fe-GO or Fe/GO

2mg of Cu/Fe-GO nanoplatforms were added by 3 mL of freshly prepared solution of ketorolac (at 7 g/L of a critical concentration of dissolution in ethanol) and sonicated in 3 mL of DI water (pH=5.5) at 8 W/cm^2 for 3 min. Then the mixture was centrifuged at 4.293xg for 15 min in order to remove the unreacted chemical residuals.

A2.3 Preparation of ketorolac in Cu-GO, Cu/Fe-GO and Fe-GO for Raman study

For Raman measurements the ketorolac loaded GO-based nanomaterials were modified with silver as the following. After centrifugation cycles the precipitant of nanomaterials was

added by 3 mL of freshly prepared ice-cold aqueous solution of 7 mM $NaBH_4$ and the colloidal suspension was sonicated in the ice bath. During first minutes of sonication 1 mL of fresh 1 mM $AgNO_3$ aqueous solution was dropwise added into this colloidal dispersion and ultrasonic treatment was immediately stopped. This dispersion was added by 3 mL of ketorolac solution followed by 3 min of sonication, removed from the ultrasonic reaction vessel and left for one hour at room temperature in a dark place. Additional ultrasonic treatment was performed of colloidal GO dispersions containing methylene blue dye instead of ketorolac.

A2.4 Ketorolac disintegration study in Cu/Fe-GO nanoparticles

1 mL of colloidal suspension containing nanoparticles loaded with ketorolac were incubated in 1 mL of DI water adjusted to one of the following pH values: 1, 5 and 8. Samples were withdrawn after 7 h, washed by repeated centrifugation at 4.293xg for 30 min in order to remove the unreacted chemical residuals and diluted with DI water. Drops of these aqueous dispersions were placed on glass or Al_2O_3 substrates and left for 8 h of drying at room temperature. The presence of intercalated ketorolac was examined by its prominent characteristic Raman peak at 1328 cm^{-1}.

Appendix 3

A3.1 Materials

Pristine diclofenac sodium was purchased from Holden Medical B.V. (The Netherlands). For experiments 10 tablets of diclofenac were grinded to fine powder. The aqueous solution of diclofenac was prepared by dissolving a powder of this drug in deionized water (pH=5.5) under continuous stirring at a critical concentration of dissolution at room temperature according to literature [50]. For experiments diclofenac aqueous solutions was filtered through a cellulose membrane filter (red line, the pore size 8-12 nm).

A3.2 Synthesis of CuO nanoparticles

The hydrothermal method was used to form CuO nanoparticles through the precipitation reaction between $Cu(CH_3COO)_2 \cdot H_2O$, NaOH and NH_4OH. Morphology, size and surface charge of CuO colloids were controlled at different molar and volume ratios of these three reagents.

a) Formation of negatively charged CuO nanoparticles

25 mL of aqueous solution of $Cu(CH_3COO)_2 \cdot H_2O$ (125 mM) and 25 mL of NaOH (500 mM) were dissolved in 15 mL liquid NH_4OH. This mixture was thermally treated on a heating plate under continuous mechanical stirring. At T=80±1°C DI water was dropwise added into the reaction mixture at a total volume of 65 mL maintaining continuous agitation until the dark sediment with brown color was obtained. Soon after the sediment was formed, the reaction mixture was cooled down to room temperature. Then the sediment was triply rinsed with DI water in the use of centrifugation cycles at a rotation frequency 11 000 $/min^{-1}$. Final product was obtained after 1 h of thermal treatment in an air saturated camera at T=400±1°C until the complete formation of pure CuO crystalline phase.

b) Formation of positively charged CuO colloids with different morphology

- «needle spheres»: 25 mL of aqueous solution of $Cu(CH_3COO)_2 \cdot H_2O$ (25 mM) and 18 mL of NaOH (100 mM) were dissolved in 15 mL of liquid NH_4OH. This mixture was thermally treated at conditions of the synthesis (a) until the formation of dark green-color sediment. After the formation of this sediment the reaction mixture was cooled down and the thermal treatment was repeated.
- «leaf spheres»: 1,82 g of $Cu(CH_3COO)_2 \cdot H_2O$ (0.2 M) and 0,40 g of NaOH (0.2 M) were dissolved in 50 mL of liquid NH_4OH. This mixture was thermally treated on a heating plate under continuous mechanical stirring. From the moment the solution reaches a temperature of the order ~80°C 7 mL of DI water was dropwise added every 10 min during 2.5 h of reaction maintaining continuous agitation until dark brown sediment appeared on the bottom of the vessel. Then the reaction mixture was cooled down to room temperature. The obtained sediment

was purified by three centrifugation cycles with DI water and one with isopropanol for 15 min. The final powder product was obtained after drying at T=150±1°C in the oven for 5 h.

- «lamellar spheres»: 1,82 g of $Cu(CH_3COO)_2 \cdot H_2O$ (0.2 M) and 0,80 g of NaOH (0.2 M) were dissolved in 50 mL of liquid NH_4OH and the synthesis was conducted at the conditions of «leaf spheres» formation.

A3.3 Sonochemical formation of graphene oxide-coated CuO nanoparticles

At first, copper oxide nucleation centers were formed via the co-precipitation chemical reaction in a solution containing 50 mL of liquid NH_4OH, 1.82 g of 0.2 M $Cu(CH_3COO)_2$ H_2O and 0.80 g of 0.4 M NaOH. This solution was heated under vigorous stirring until the temperature has reached ~80°C. Since that moment 7 mL of deionized water (DI, pH=5.5) was dropwise added into this heated solution under continuous stirring every 10 min during the total duration of 150 min followed by the formation of dark brown sediment on the bottom of the vessel. Then the obtained colloidal solution was cooled down to room temperature, triply rinsed with deionized water and once with isopropanol by using centrifugation (8.117xg). At second, the aqueous solution of GO, which has been previously sonicated in solution containing 10 mL of DI water and 10 mL of isopropanol, was added to this sediment (6.8 mg). Sonication (20 kHz, 18 $W \cdot cm^{-2}$) of this aqueous solution with GO was assisted with the mechanical stirring for 30 min in the open air. Then the final product was triply rinsed with DI water and once with isopropanol by using centrifugation (8.117xg) for 20 min, then dried at ~100°C.

The control experiment was performed by applying ultrasound (20 kHz, 18 $W \cdot cm^{-2}$) to the colloidal mixture of GO and preformed CuO powder (synthesized without GO and dried at ~400°C in the air) during 15 min under continuous stirring. Then this colloidal solution was stored for 12 h at room temperature. Finally the product was triply rinsed with DI water and once with isopropanol by using centrifugation (8.117xg) for 20 min and dried at ~100°C.

25 mL of aqueous solution of 125 mM $Cu(CH_3COO)_2$ H_2O and 25 mL of 500 mM NaOH were dissolved in 15 mL of liquid NH_4OH and heated under vigorous stirring to T=80±1°C. During heating this solution was dropwise added by 65 mL of DI water (pH=5.5) until the dark green-brown sediment appeared on the bottom of the vessel. Afterwards the solution was cooled down to the room temperature and the sediment was triply rinsed with DI water (pH=5.5) and once with isopropanol by centrifugation (8.117xg). In the next place, 2.5 mg of preformed GO was added to the sediment and sonicated under vigorous stirring for 30 min at 18 $W \cdot cm^{-2}$. In another procedure, 25 mL of aqueous solution of 0.2 M $Cu(CH_3COO)_2$ H2O and 25 mL of 0.2 M NaOH were dissolved in 50 mL of liquid NH_4OH and heated under vigorous stirring until T=80±1°C. Then this solution was dropwise added by 6.8 mg of GO and 100 mL of DI water during 190 min of continuous stirring with sonication (at 18 $W \cdot cm^{-2}$). The sediment was formed

by centrifugation (8.117xg) and triply rinsed with DI water and once with isopropanol followed by drying at ~100°C.

A3.4 Ultrasonic functionalization of pristine diclofenac with CuO-GO

30 mg of sonochemically formed GO-coated CuO nanoparticles was added by 30 mg of diclofenac in 11 mL of DI water (pH=5.5) and treated by ultrasound for 3 min (20 kHz, 18 $W \cdot cm^{-2}$) under air in a vessel placed in the ice bath. After that the colloidal suspension was triply rinsed with DI water by centrifugation (8.117xg) for a total duration of 45 min and dried at ~100°C to obtain a powder. Several control experiments were accomplished by ultrasound (3 min, 20 kHz, 18 $W \cdot cm^{-2}$): 1) the mixture (60 mg) of GO and sodium diclofenac *per se* at a mass ratio 1:1, and 2) the mixture (60 mg) of preformed CuO nanoparticles and sodium diclofenac *per se* at a mass ratio 1:1; 3) aqueous solution of sodium diclofenac *per se* (30 mg in 11 mL of DI water) of 1, 3, 5, 10 and 15 min length in order to find out the effect of ultrasound on the chemical structure of a drug. After experiments solutions were triply rinsed with DI water by centrifugation (8.117xg) and dried at ~100°C.

A3.5 pH stability study of diclofenac-CuO-GO nanoparticles

30 mg of diclofenac-CuO-GO nanoparticles were added by 3 mL of aqueous solution at pH=1, 5 or 8 and stored at room temperature. The aqueous solution at pH=1 was obtained by the addition of 1N HCl and at pH=8 – by the addition of KOH 44 wt.% aqueous solution. Samples were withdrawn after 7 h, triply rinsed by centrifugation (8.117xg) for 15 min in order to remove the unreacted chemical residuals. The obtained sediment was dispersed by deionized water (3.5 mL) and studied by UV-Vis absorption spectroscopy by using quartz cuvette SUPRASIL Hellma Analytics 111-QS (Z600725) with a pathlength of 10 mm. The presence of diclofenac was examined by its characteristic UV-Vis absorption peaks at 277-280 nm.

A3.6 Determination of crystallite thickness of CuO-GO nanoplatform

The crystallite thickness S of CuO-GO nanoplatform was determined by the Scherrer's equation (1) applied to one of the prominent X-ray powder diffraction reflexes in patterns obtained by an EMPYREAN diffractometer (PANalytical, The Netherlands) using Cu-Kα radiation (Ni-filter) at 296 K.

$$S = \frac{K \cdot \lambda}{B \cdot \cos\theta_B}, \qquad (1)$$

where K – the constant dependent on the crystallite shape (0.89); λ – the wavelength of the X-Ray radiation (Cu K_α = 1.54 Å); B – the Full Width at Half Maximum (FWHM or integral breadth) that equals to $((\theta_{High}-\theta_{Low})*\pi)/180$; θ_B – the Bragg angle.

Appendix 4

A4.1 Materials.

Pharmaceutics “Bioflor” containing live E. coli M-17 was purchased from Ferane Inc. (Republic of Belarus). A Saline solution (0.9 % NaCl) was obtained from OJSC Nesvizh Plant of Medical Preparations (Republic of Belarus). Pristine NSAID – acetylsalicylic acid (ASA, 4.21 wt.%) was purchased from Belmedpreparaty RUE (Minsk, Republic of Belarus). Fine powder of ASA was produced by grinding of 10 tablets with an agate mortar and a pestle. The aqueous solution of ASA was prepared by dissolving a powder of this drug in DI water (pH 5.5) under continuous stirring at a critical concentration of dissolution at room temperature according to literature. For experiments, NSAID aqueous solutions were filtered through a cellulose membrane filter (red line, the pore size 8-12 nm).

A4.2 Sonochemical formation of ZnO and ZnO-GO nanoparticles

Formation of ZnO nanoparticles: in a vessel of 30 mL DI water 0.05 M $ZnSO_4$ was mixed with 30 mL of 0.125 M NaOH DI aqueous solution in a single addition under mechanical stirring and was heated at T=90±1 °C in for 30 min. Soon after, it was sonicated (20 kHz, 18 W/cm^2) for 15 min in an air atmosphere and cooled down to room temperature. Then, the colloidal solution was triply rinsed with DI water (pH=5.5) at 6.7xg for 45 min and air-dried at T=120±1 °C to obtain a powder.

Formation of ZnO-GO nanoparticles: prior to the synthesis, 27.5 mg of GO was exfoliated in 30 mL of DI water (pH=5.5) by using ultrasound (10 W/cm^2) for 30 min in an ice-cooled vessel. The exfoliated GO was triply rinsed with DI water by centrifugation at 7.3xg for 45 min and added by 2 mL of DI water (pH=5.5) followed by 3 min of sonication to obtain a homogeneous colloidal solution. A mixture of 0.05 M $ZnSO_4$ and 0.125 M NaOH in 60 mL of DI water was thermally treated at T=90±1 °C under continuous mechanical stirring for 30 min. Then it was added by 2 mL of exfoliated GO colloidal solution and sonicated for 15 min in an air atmosphere. Soon after this colloidal solution was cooled down to room temperature and triply rinsed with DI water (pH=5.5) by centrifugation at 6.7xg for 45 min and air-dried at T=100±1°C to obtain a powder.

A4.3 Ultrasonic formation of ASA-ZnO and ASA-ZnO-GO nanoparticles

Ultrasonic functionalization of pristine ASA with ZnO nanoparticles: in a sealed vessel 30 mg of sonochemically synthesized ZnO nanoparticles were added by 30 mL of DI water (pH=5.5) and mechanically stirred. After 15 min it was added by 30 mg of ASA (in a powder form) and sonicated for 3 min at 18 W/cm^2 in an air atmosphere. Then, this colloidal solution was rinsed five times with DI water (pH=5.5) by centrifugation at 4.2xg for 75 min and air-dried

at T=100±1°C to obtain a powder. Control experiment of free ASA sample was performed by dissolving pristine ASA powder (1 mg/mL) in DI water (pH=5.5) under mechanical stirring and heating (T=35±1°C) for 10 min in a sealed vessel followed by five times rinsing with DI water (pH=5.5) by centrifugation at 4.2xg for 75 min and air-drying at T=100±1°C to obtain a powder.

Ultrasonic functionalization of pristine ASA with ZnO-GO nanoparticles: in a sealed vessel ZnO-GO nanoparticles (1 mg/mL) were added by DI water (pH=5.5) and mechanically stirred for 15 min. Soon after it was added by 30 mg of ASA (in a powder form) and sonicated for 3 min at 18 W/cm^2 and in an air atmosphere. Then, this colloidal solution was rinsed five times with DI water (pH=5.5) by centrifugation at 6.7xg for 75 min and air-dried at T=100±1°C to obtain a powder.

A4.4 Escherichia coli strain M-17 bacteria assessment in aqueous solutions of free ASA, ASA-ZnO and ASA-ZnO-GO nanoparticles as test substances

A pharmaceutics "Bioflor", being approved in 2010 by Ministry of Health of the Republic of Belarus, was used for preparation of E. coli M-17 inoculums. "Bioflor" contains E. coli M-17 as active substance in the amount of not less than 100x10^8 live cells at the moment of preparation and not less than 100x10^7 live cells at the end of the expiration date. In addition, "Bioflor" also contains ingredients such as 0.7 g NaCl (State Pharmacopoeia II volume 2, p. 740), not more than 100 ml DI water (State Pharmacopoeia II volume 2, p. 309) and 0.8 g the mixture of vegetable extract (soy, dill, beet, peppermint, garlic, parsley, cabbage) and propolis (standard organization-OS-029). A suspension of "Bioflor" was diluted to 10^6 colony forming units (CFU/mL) with saline (0.9wt.% NaCl) solution and used as inoculum.

Fresh aqueous colloidal suspensions were prepared in order to avoid the undesired agglomeration. Overall, 50 μL of each test substance was added to the corresponding tubes with 1 mL of bacterial inoculums, which corresponded to the concentration of ASA 3.34 μmol/L in free ASA, 0.02 μmol/L in ASA-ZnO and 2.68 μmol/L in ASA-ZnO-GO NPs. A positive control without antibacterial samples was included to evaluate the viability of the bacteria. Also, the same saline (with no microorganism but containing the same amount of antibacterial agents) was prepared and considered as a blank control. Then, all tubes were shaken followed by incubation at T=37±1°C for 30 min. Experiments were performed in duplicates. The E. coli M-17 growth inhibition was assessed by the colony counting method, i.e. 100 μL aliquots from each tube were sampled and plated on nutrient Endo agar and incubated at T=37±1°C for 20 h. Then, the colonies were counted and their surface areas were calculated by using the optical phase contrast microscope. The number of colonies and their surface area (μm^2) were expressed as the mean SE (standard error) and RSE (relative standard error, %), SD (standard deviation) and RSD (relative standard deviation, %).

Appendix 5

A5.1 Synthesis of Fe_3O_4-rGO-SA nanoparticles

Prior to the synthesis, 100 mg of GO was triply exfoliated in 20 mL of the aqueous solution consisting of DI water at pH=5.5 and isopropanol at a volume ratio of 3:1 by using ultrasound at 10 W cm^{-2} intensity (horn-type ultrasonic disperser N.4-20, 20 kHz, Cavitation Inc. Belarus) for 5 min in an ice-cooled vessel. The exfoliated GO was triply rinsed with DI water by centrifugation at 7.3xg for 15 min and added by 10 mL of DI water (pH=5.5) followed by 3 min of sonication to obtain a homogeneous colloidal solution. An aqueous mixture of 362 mM $FeCl_3$ and 170 mM $FeCl_2$ was mechanically stirred in an Ar atmosphere for 15 min, and then heated at T=80±1 °C for 15 min. Next, the pre-treated GO (10 mL) colloidal solution was sonicated for 5 min in an air atmosphere. Soon after, this colloidal solution was dropwise added by 5 mL of 44% KOH, while mechanical stirring and heating continued. Next, 6 mL of 44% KOH was dropwise added into the mixture until the black color appeared and the heating at T=80±1 °C continued for 30 min in an Ar atmosphere. Next, 29.1 mM SA aqueous solution was added, and the mixture was sonicated at the ultrasonic intensity of 18 W cm^{-2} followed by stirring for 5 min in Ar atmosphere. After synthesis, the colloidal solution obtained the dark black-brown color (pH=5.0). Then this colloidal solution was cooled down to room temperature and triply rinsed with DI water (pH=5.5) by centrifugation at 6.7xg for 15 min and air-dried at 100 °C to obtain a final powder. The formed solid product responded to external magnet. Then, 100 mg of this solid product was mixed with 29.1 mM SA aqueous mixture consisting of DI water and isopropanol at a volume ratio as 1:1, and ultrasonically treated (18 W cm^{-2}) for 5 min in an air atmosphere. The final product was triply rinsed with DI water by centrifugation (at 6.7xg) for 15 min, filtered through a cellulose membrane filter (violet line, the pore size < 1-2 μm) and air-dried at ~100°C. Control nanoparticles were prepared by using similar procedure without GO or SA.

A5.2 Theoretical modelling of the current density and potential distribution of nanoparticles

The current density pattern was calculated by using a Comsol Multiphysics software tool. In this calculation the fundamental equation of the current conduction or charge conservation (eq.2) on the surface of nanoparticles is computed.

$$\Delta \cdot (-\sigma \Delta V) = 0, \quad (2)$$

where σ is the electrical conductivity (S/m) and V is the electric potential (V).

In this model the used electrical conductivity of Fe_3O_4 nanoparticles with about 30 nm average diameter was $1x10^4$ S/m, of Fe_3O_4-SA nanoparticles with ~15 nm diameter was $3x10^4$ S/m and of Fe_3O_4-rGO-SA was $3x10^2$ S/m. The values of electric potential V are considered from the electrochemical measurements of CV curves with the peak magnitudes

corresponding to •OH evolution. The potential distribution is computed across the surface of nanoparticles varying their average diameter with the added current field flow as an arrow plot. The local magnitude of the electric current density (A/m^2) was computed by using the current conduction equation 3 (a coefficient form boundary PDE interface) with the diffusion coefficient

$$c = \sigma \cdot d, \quad (3)$$

where *d* is the electrochemical shell thickness (nm).

Due to the symmetry of the nanosphere only one cross section along *yz* plane was modelled. In the model the used initial time derivative of the potential $\delta V/\delta t = 0.01$ V/s, the conservative flux convection coefficient α (S/m) with x = 1, y =1 and z =1, convection coefficient β (S/m) with x = 1, y =1 and z =1 and the conservative flux source γ (A/m) with x = 1, y =1 and z =1. The study equation 4 is the following

$$e_a \frac{\partial^2 V}{\partial t^2} + d_a \frac{\partial V}{\partial t} + \Delta \cdot (-c\Delta \cdot V - \alpha V + \gamma) + \beta \cdot \Delta V + \alpha V = f, \quad (4)$$

where e_a is the mass coefficient (S^5A^2/m^4 kg, set to zero), da is the damping coefficient (F/m^2, set to 1) and *f* is the source term (A/m^2).

A5.3 Theoretical modelling of the H^+ production in NPs (3 electrode surface system)

This modelling was based on the fundamental computation of the electrochemical treatment of tumors with implication that the diseased tissue is treated with the direct current through the use of the metallic electrodes inserted inside the cellular environment. We assume that when tissue is electrolyzed, two competing reactions take place at the anode: oxygen evolution and chlorine production. The oxygen evolution reaction also produces H^+ ions, which lower the pH value close to the anode according to the following reactions:

$2Cl^- = Cl_2 + 2e^-$ at the cathode (5)

$2H_2O = 4H^+ + O_2 + 4e^-$ at the anode (6)

In this model we apply the Nernst-Planck equations interface in the use of Comsol Multiphysics software tool to compute the concentration of H^+ ions developed close to the electrode surface at the contact with nanoparticles. We calculate the amount of H^+ ions at different concentration of complexed SA molecules in NPs in aqueous electrolyte solution of KCl before and after addition of ascorbic acid. At the electrode surface the fluxes of H^+ and Cl^- ions are included in the electrochemical reactions, while K^+ ionic species are considered inert in this model. In the model the following equation 7 is used for molar fluxes at the boundary for the reacting species

$$N_i \cdot n = \frac{\nu_{ij} J_j}{n_j \cdot F}, \quad (7)$$

where N_i is the flux, ν_{ij} is the stoichiometric coefficient for the ionic species *i* in reaction *j* and n_j is the number of electrons in reaction *j*.

The current density for the oxygen evolution reaction is the following equation 8:

$$j_I = j_{I,0}\left\{ e^{\frac{-F(V+E_{eq,I0})}{2RT}} - (P_{O_2})^{1/4} C_{H^+} e^{\frac{F(V+E_{eq,I})}{2RT}} \right\}, \quad (8)$$

where $j_{I,0}$ is the exchange current density (A/m^2) and $E_{eq,I}$ is the standard electrode potential (V). The fluxes of H^+ ions at the electrode surface (N_H) are computed according to the equation 8, using the input values $n_I = 1$ and $\nu_{H,I} = 1$:

$$N_H \cdot n = \frac{j_I}{F}, \quad (9)$$

where *n* is the number of electrons and j_I is the exchange current density (A/m^2) in the reaction of oxygen evolution, F is the Faraday's constant (c/mol).

In the model the used diffusion coefficient of H^+ was $D_H = 9.31 \cdot 10^{-9}$ m^2/s and of Cl^- was $D_{Cl} = 2.03 \cdot 10^{-9}$ m^2/s, the initial concentration of KCl $C_{KCl} = 4.76$ mol/L and of H^+ $C_H = 1 \cdot 10^{-7}$ mol/L. The primary anodic peak was assumed the value for the ·OH production and the equilibrium potential reaction for oxygen evolution being 1.2 V. The proton concentration was computed in the domain at different time steps from 0 to 3600 s, considering that at high current densities, the concentration of produced protons is increased and it forms a front moving inwards in the domain with lower current density.

A5.4 Estimation of concentration of complexed SA molecules in Fe_3O_4-SA

The total average density of magnetite nanoparticles is 2.70×10^{22} L^{-1} and of SA molecules is 5.78×10^{22} L^{-1}, considering the molecular weight of Fe_3O_4 ~231.53 g/mol and SA ~138.12 g/mol, and $N_A = 6.02 \times 10^{23}$ mol^{-1}. Assuming covalent radius of iron atom ~$126 \cdot 10^{-12}$ m and average nanoparticle diameter ~$15 \cdot 10^{-9}$ m, the volume of a single nanoparticle is ~1.77×10^{-24} m^3 and of an iron atom is 8.38×10^{-30} m^3, so that one single magnetite nanoparticle consists of 2.11×10^7 iron atoms. Considering a covalent radius of oxygen atom (triple bond) ~53×10^{-12} m, the volume of a single oxygen atom is 6.23×10^{-31} m^3, so that the same single magnetite nanoparticle consists of 2.81×10^8 oxygen atoms. The Fe_3O_4 nanoparticle density is 1.03×10^{14} L^{-1} and when it is divided by the SA molecule density 1.33×10^3 L^{-1}, we obtain about 7.78×10^{10} complexed SA molecules in Fe_3O_4-SA nanoparticle.

A5.5 Electrochemical measurements of nanoparticles in the electro-Fenton process

In an experiment, 1 mM $FeCl_2$ (used as a catalyst, pH=5.5) in DI water and 20 mM Na_2HPO_4 (used as a phosphate-buffered solution, pH=9) in DI water were mixed at a volume ratio of 1:1. This mixture was added by 2 mM H_2O_2 (50 wt.%, pH=5.5) at a volume ratio of 1:1:1 or 1:1:2 to perform the electro-Fenton process in a final volume of 20 mL in a glass vessel equipped with a three electrode system containing two custom graphite paper sheets with the geometrical size 43x17 mm and one Ag/AgCl electrode. A saturated stock 4.76 M KCl aqueous solution was used as a supported electrolyte. Electrochemical measurements (cyclic voltammetry) were performed with the Metrohm Autolab potentiostat/galvanostat instrument operating with the Nova 1.11 software allowing data acquisition and their sophisticated analysis. The series of electrochemical experiments were performed in freshly prepared 29.1 mM SA aqueous solutions composed of the mixture of DI water and isopropanol at a volume ratio of 1:1, and prepared nanoparticles: unmodified Fe_3O_4, Fe_3O_4-SA and Fe_3O_4-rGO-SA at initial concentration of 5 mg/mL before and after addition of ascorbic acid aqueous solution (1 mg/mL) to study the Fenton reaction in the total amount of 18 mL during the electrochemical process of 10 scans at a scan rate 0.1 v/s in the applied voltage range from -0.5 V to +1.2 V.

References (Introduction)

1. Randive, N., Langford, R.M. Ed. Evers, A.S., Maze, M., Kharasch, E.D. Anesthetic Pharmacology // 2nd edition, CambridgeUniversity Press. 2011. Section 3. Chapter 34. P. 548–562.
2. Needs, C.J., Brooks, P.M. Clinical Pharmacokinetics of the Salicylates // Clin. Pharmacokinet. 1985. Vol. 10. P. 164–177.
3. Rainsford, K.D. Aspirin and Related Drugs // 1st edition, Taylor & Francis Group 2004 P. 800.
4. Gouda, A.A., Kotb El-Sayed, M.I., Amin, A.S., El Sheikh, R. Spectrophotometric And Spectrofluorometric Methods for the Determination of Nonsteroidal Anti-Inflammatory Drugs: A Review // Arabian J. Chem. 2013. Vol. 6. P. 145–163.
5. Vane, J.R. Inhibition of Prostaglandin Synthesis as a Mechanism of Action for the Aspirin-Like Drugs // Nature 1971. Vol. 231. P. 232–235.
6. Picot, D., Loll, P.J., Garavito, R.M. The X-ray Crystal Structure of the Membrane Protein Prostaglandin H2 Synthase-1 // Nature 1994. Vol. 67. P. 43–49.
7. Khan, Y.S., Gutiérrez-de-Terán, H., Åqvist, J. Molecular Mechanisms in the Selectivity of Nonsteroidal Anti-Inflammatory Drugs // Biochem. 2018. Vol. 57. P. 1236−1248.
8. Kolasa, T., Brooks, C.D.W., Rodriques, K.E., Summers, J.B., Dellaria, J.F., Hulkower, K.I., Bouska, J., Bell, R.L., Carter, G.W. Nonsteroidal Anti-Inflammatory Drugs as Scaffolds for the Design of 5-Lipoxygenase Inhibitors // J. Med. Chem. 1997. Vol. 40. P. 819−824.
9. Kurumbail, R.G., Kiefer, J.R., Marnett, L.J. Cyclooxygenase Enzymes: Catalysis And Inhibition // Curr. Opin. Struct. Biol. 2001. Vol. 11. P. 752–760.
10. Meade, E.A., Smith, W.L., DeWitt, D.L. Differential Inhibition of Prostaglandin Endoperoxide Synthase (Cyclooxygenase) Isozymes by Aspirin and Other Non-steroidal Anti-inflammatory Drugs // J Biol. Chem. 1993. Vol. 68. P. 6610–6614.
11. Engelhardt, G., Homma, D., Schlegel, K., Schnitzler, C., Utzmann, R. Anti-inflammatory, Analgesic, Antipyretic and Related Properties of Meloxicam, a New Nonsteroidal Anti-inflammatory Agent With Favourable Gastrointestinal Tolerance // Inflamm. Res. 1995. Vol. 44. P. 423–433.
12. Soslow, R.A., Dannenberg, A.J., Rush, D., Woerner, B.M., Khan, K.N., Masferrer, J., Koki, A.T. COX-2 is Expressed in Human Pulmonary, Colonic, and Mammary Tumors // Cancer 2000. Vol. 89. P. 2637−2645.

13. Sano, H., Kawahito, Y., Wilder, R. L., Hashiramoto, A., Mukai, S., Asai, K., Kimura, S., Kato, H., Kondo, M., and Hla, T. Expression of Cyclooxygenase-1 and −2 in Human Colorectal Cancer // Cancer Res. 1995, Vol. 55. P. 3785−3789.
14. Shagroni, T., Ramirez Cazares, A., Kim, J.A., Furst, D.E. Nonsteroidal Anti-inflammatory Drugs, Disease-Modifying Antirheumatic Drugs, Nonopioid Analgesics, & Drugs Used in Gout // Basic and Clinical Pharmacology. Katzung, B.G., Trevo, A.J., editors. 13 edition, New York: McGraw-Hill Education; 2015. P. 618.
15. Gunaydin, C., Bilge, S.S. Effects of Nonsteroidal Anti-Inflammatory Drugs at the Molecular Level // Eurasian J Med. 2018. Vol. 50. P. 116−121.
16. Bindu, S., Mazumder, S., Bandyopadhyay, U. Nonsteroidal Anti-inflammatory Drugs (NSAIDs) and Organ Damage: A Current Perspective // Biochem. Pharmacol. 2020. Vol. 180. P. 114147−114168.
17. Mazumder, S., De, R., Sarkar, S., Siddiqui, A.A., Saha, S.J., Banerjee, C., Iqbal, M.S., Nag, S., Debsharma, S., Bandyopadhyay, U. Selective Scavenging of Intra-Mitochondrial Superoxide Corrects Diclofenac-Induced Mitochondrial Dysfunction and Gastric Injury: A Novel Gastroprotective Mechanism Independent of Gastric Acid Suppression // Biochem. Pharmacol. 2016. Vol. 121. P. 33–51.
18. Matsui, H., Shimokawa, O., Kaneko, T., Nagano, Y., Rai, K., Hyodo, I. The Pathophysiology of Nonsteroidal Anti-Inflammatory Drug (NSAID)-Induced Mucosal Injuries in Stomach And Small Intestine // J Clin. Biochem. Nutr. 2011. Vol. 48. P. 107–111.
19. Mazumder, S., R. De, Sarkar, S., Siddiqui, A.A., Saha, S.J., Banerjee, C., Iqbal, M.S., Nag, S., Debsharma, S., Bandyopadhyay, U. Selective Scavenging of Intra-Mitochondrial Superoxide Corrects Diclofenac-Induced Mitochondrial Dysfunction And Gastric Injury: A Novel Gastroprotective Mechanism Independent of Gastric Acid Suppression // Biochem. Pharmacol. 2016. Vol. 121. P. 33–51.
20. Nadatani, Y., Watanabe, T., Suda, W., Nakata, A., Matsumoto, Y. Gastric Acid Inhibitor Aggravates Indomethacin-Induced Small Intestinal Injury via Reducing *Lactobacillus johnsoni* // Sci. Rep. 2019. Vol. 9. P. 17490.
21. Basu S. Theorized Mechanism of Non-Steroidal Anti-Inflammatory Drugs against Alzheimer's disease Onset and Progression // J Young Invist. 2001. Vol. 3. P. 1–2.
22. Franz, K.J., Metzler-Nolte, N. Introduction: Metals In Medicine // Chem. Rev. 2019. Vol. 119. P. 727−729.
23. Janoš, P., Spinello, A., Magistrato, A. All-Atom Simulations to Studying Metallodrugs/Target Interactions // Cur. Opin. Chem. Biol. 2021. Vol. 61. P. 1−8.
24. Boros, E., Dyson, P.J., Gasser, G. Classification of Metal-Based Drugs According to Their Mechanisms of Action // Chem. 2020. Vol. 6. P. 1−20.

25. Weder, J.E., Dillon, C.T., Hambley, T.W., Kennedy, B.J., Lay, P.A., Biffin, J.R., Regtop, H.L., Davies, N.M. Copper Complexes of Nonsteroidal Anti-Inflammatory Drugs: an Opportunity Yet to be Realized // Coord. Chem. Rev. 2002. Vol. 232. P. 95−126.
26. Vega-Villa, K.R., Takemoto, J.K, Yáñez, J.A., Remsberg, C.M., Forrest, M.L., Davies, N.M. Clinical Toxicities of Nanocarrier Systems // Adv. Drug Deliv. Rev. 2008. Vol. 60 P. 929−938.
27. Davies, N.M. Toxicity of Nonsteroidal Anti-Inflammatory Drugs in the Large Intestine // Dis. Colon Rectum. 1995. Vol. 38. P. 1311−1321.
28. Dillon, C.T., Hambley, T.W., Kennedy, B.J., Lay, P.A., Zhou, Q., Davies, N.M., Biffin, J.R., Regtop, H.L. Gastrointestinal Toxicity, Anti-Inflammatory Activity, And Superoxide Dismutase Activity of Copper And Zinc Complexes of the Anti-Inflammatory Drug Indomethacin // Chem. Res. Toxicol. 2003. Vol. 16. P. 28−37.
29. IVS Annual; MIMS Publishing, Crows Nest, NSW, Sydney, 1997, p. 145 & 276.
30. J.R. Biffin, Safe Administration of Copper Indomethacin to Dogs, Personal Communication (2000).
31. Vrontaki, E., Simcic, M., Grdadolnik, S.G., Afantitis, A., Melagraki, G., Hadjikakou, S.K., Mavromoustakos, T. Comparative Binding Effects of Aspirin at LOX with Cu-Complex // J. Chem. Inf. Model 2012. Vol. 52. P. 3293–3301.
32. Banti, C.N., Papatriantafyllopoulou, C., Manoli, M., Tasiopoulos, A.J., Hadjikakou, S.K. Nimesulide Silver Metallodrugs, Containing the Mitochondriotropic, Triaryl Derivatives of Pnictogen; Anticancer Activity Against Human Breast Cancer Cells // Inorg. Chem. 2016. Vol. 55.P. 8681–8696.
33. Stathopoulou, M.-E.K., Banti, C.N., Kourkoumelis, N., Hatzidimitriou, A., Hadjikakou, S.K. Silver Complex of Salicylic Acid And Its Hydrogel-Cream In Wound Healing Chemotherapy // J. Inorg. Biochem. 2018. Vol. 181. P. 41–55.
34. Hathaway, B.J. Comprehensive Coordination Chemistry. The Synthesis, Reaction, Properties & Application of Coordination Compounds // Pergamon Press, Oxford, 1987. Vol. 5. P. 634.
35. Rosenstein, E.D., Caldwell, J.R. Trace Elements in the Treatment of Rheumatic Conditions // Rheum. Dis. Clin. North Am. 1999. Vol. 25. P. 929–935.
36. Schubert, J. Chelation in Medicine // Sci. Am. 1966. Vol. 214. P. 40–51.
37. Sorenson, J.R.J. Handbook of Metal/Ligand Interactions in Biological fluids // 1st edition, Marcel Decker, New York, 1995. Vol. 2. P. 1318.
38. Bertrand, V., Guessous, F., Le Roy, A., Viossat, B., Fessi, H., El Abbouyi, A., Giroud, J., Roch-Arveiller, M. Copper-Indomethacinate Associated with Zwitterionic Phospholipids Prevents Enteropathy in Rats (Effect on Inducible NO Synthase) // Digest. Dis. Sci. 1999. Vol. 44. P. 991–999.
39. Tarushi, A., Kastanias, P., Raptopoulou, C.P., Psycharis, V., Kessissoglou, D.P., Papadopoulos, A.N., Psomas, G. Zinc Complexes of Flufenamic Acid: Characterization and Biological Evaluation // J Inorg. Biochem. 2016. Vol. 163. P. 332–345.

40. Tarushi, A., Raptopoulou, C.P., Psycharis, V., Kontos, C.K., Kessissoglou, D.P., Scorilas, A., Tangoulis, V., Psomas, G. Copper(II) Inverse-[9-Metallacrown-3] Compounds Accommodating Nitrato or Diclofenac Ligands: Structure, Magnetism, and Biological Activity // Eur. J. Inorg. Chem. 2016. Vol. 216. P. 219–231.
41. Cini, R. Anti-Inflammatory Compounds as Ligands in Metal Complexes as Revealed in X-Ray Structural Studies // Comments Inorg. Chem. 2000. Vol. 22. P. 151–186.

References (Chapter 1)

1. Pelaz, B., Alexiou, C., Alvarez-Puebla, R.A., Alves, F., Andrews, A.M., et. al. Diverse Applications of Nanomedicine // ACS Nano 2017. Vol. 11. P. 2313–2381.
2. Sanchez-Iglesias, A., Claes, N., Soles, D.M., Taboada, J.M., Bals, S., Liz-Marzan, L.M., Grzelczak, M. Reversible Clustering of Gold Nanoparticles under Confinement // Angew. Chem. Int. Ed. 2018. Vol. 57. P. 3183–3186.
3. Sreejith, S., Ma, X., Zhao, Y., Graphene Oxide Wrapping on Squaraine-Loaded Mesoporous Silica Nanoparticles for Bioimaging // J. Am. Chem. Soc. 2012 Vol. 134. P. 17346-17349.
4. Grinberg, O., Shimanovich, U., Gedanken, A. Encapsulating Bioactive Materials in Sonochemically Produced Micro- and Nano-spheres // J Mater. Chem. B 2013. Vol. 1. P. 595–605.
5. Shi, J., Zhou, X., Liu, Y., Su, Q., Zhang, J., Du, G. Sonochemical Synthesis of CuS/reduced Graphene Oxide Nanocomposites with Enhanced Absorption and Photocatalytic Performance // J. Mater. Res. 2014. Vol. 126. P. 220–223.
6. Deng, Y., Handoko, A.D., Du, Y., Xi, S., Yeo, B.S. In Situ Raman Spectroscopy of Copper and Copper Oxide Surfaces during Electrochemical Oxygen Evolution Reaction: Identification of CuIII Oxides as Catalytically Active Species // ACS Catalysis 2016. Vol. 6. P. 2473–2481.
7. Karikalan, N., Karthik, R., Chen, S.-M., Karuppiah, C., Elangovan, A. Sonochemical Synthesis of Sulfur Doped Reduced Graphene Oxide Supported CuS Nanoparticles for the Non-Enzymatic Glucose Sensor Applications // Sci. Rep. 2017. Vol. 7. P. 1–10.
8. Sardari, B., Özcan, M. Real-Time and Tunable Substrate for Surface Enhanced Raman Spectroscopy by Synthesis of Copper Oxide Nanoparticles via Electrolysis // Sci. Rep. 2017. Vol. 7. P. 1–11.
9. Reina, G., Gonzalez-Domınguez, J.M., Criado, A., Vazquez, E., Bianco, A., Prato, M. Promises, Facts and Challenges for Graphene in Biomedical Applications // Chem. Soc. Rev. 2017. Vol. 46. P. 4400–4416.
10. Marcano, D.C., Kosynkin, D.V., Berlin, J.M., Sinitskii, A., Sun, Z., Slesarev, A., Alemany, L.B., Lu, W., Tour, J.M. Improved Synthesis of Graphene Oxide // ACS Nano Vol. 4. P. 4806–4814.
11. Margulis, M.A., Margulis, I.M. Calorimetric Method for Measurement of Acoustic Power Absorbed in a Volume of a Liquid // Ultrason. Sonochem. 2003. Vol. 10. P. 343–345.
12. Tucureanu, V., Matei, A., Avram, A.M. FTIR Spectroscopy for Carbon Family Study // Crit. Rev. Anal. Chem. 2016. Vol. 46. P. 502–520.

13. Ferrari, A.C., Robertson, J. Origin of the 1150 cm^{-1} Raman Mode in Nanocrystalline Diamond // Phys. Rev. B 2001. Vol. 63. P. 121405.
14. Kudin, K.N., Ozbas, B., Schniepp, H.C., Prud'homme, R.K., Aksay, I.A., Car, R. Raman Spectra of Graphite Oxide and Functionalized Graphene Sheets // Nano Lett. 2008. Vol.8. P. 36-41.
15. Ferrari, A.C., Robertson, J. Interpretation of Raman Spectra of Disordered and Amorphous Carbon // Phys. Rev. B 2000. Vol. 61. P. 14095.
16. Wu, J.-B., Lin, M.-L., Cong, X., Liu, H.-N., Tan, P.-H. Raman Spectroscopy of Graphene-based Materials and Its Applications in Related Devices // Chem. Soc. Rev. 2018. Vol. 47. P. 1822-1873.
17. Piscanec, S., Lazzeri, M., Mauri, F., Ferrari, A., Robertson, J. Kohn Anomalies and Electron-Phonon Interactions in Graphite // Phys. Rev. Lett. 2004. Vol. 93. P. 185503.
18. Feng, H., Cheng, R., Zhao, X., Duan, X., Li, J. A Low-Temperature Method to Produce Highly Reduced Graphene Oxide // Nat. Commun. 2013. Vol. 4. P. 1539.
19. Shen, J., Hu, Y., Shi, M., Lu, X., Qin, C., Li, C., Ye, M. Fast and Facile Preparation of Graphene Oxide and Reduced Graphene Oxide Nanoplatelets // Chem. Mater. 2009. Vol. 21. P. 3514–3520.
20. Fayos, J. Possible 3D Carbon Structures as Progressive Intermediates in Graphite to Diamond Phase Transition // J of Solid State Chem. 1999. Vol. 148. P. 278-285.
21. Saxena, S., Tyson, T.A., Shukla, S., Negusse, E., Chen, H., Bai, J. Investigation of Structural and Electronic Properties of Graphene Oxide // Appl. Phys. Lett. 2011. Vol. 99. P. 013104-1-2.
22. Krishnamoorthy, K., Veerapandian, M., Yun, K., Kim, S.-J. The Chemical and Structural Analysis of Graphene Oxide with different Degrees of Oxidation // Carbon 2013. Vol. 53. P. 38–49.
23. Kukesh, J.S., Pauling, L. The Problem of the Graphite Structure // American Mineralogist 1950. Vol. 35. P. 125-125.
24. Lai, Q., Zhu, S., Luo, X., Zou, M., Huang, S. Ultraviolet-Visible Spectroscopy of Graphene Oxides // AIP Advances 2012. Vol. 2. P. 032146.
25. Nakamoto, K. Infrared and Raman Spectra of Inorganic and Coordination Compounds // 4^{th} Edition. John Wiley and Sons Inc. 1986.
26. Acik, M., Lee, G., Mattevi, C., Chhowalla, M., Cho, K., Chabal, Y.J. Unusual Infrared-Absorption Mechanism in Thermally Reduced Graphene Oxide // Nat. Mater. 2010. Vol. 9. P. 840-845.

27. Khandelwal, M., Kumar, A. One-Step Chemically Controlled Wet Synthesis of Graphene Nanoribbons from Graphene Oxide for High Performance Supercapacitor Applications // J. Mater. Chem. A 2015. Vol. 3.P. 22975-22988.
28. Deacon, G.B., Phillips, R.J. Relationships Between the Carbon-Oxygen Stretching Frequencies of Carboxylato Complexes and the Type of Carboxylate Coordination // Coord. Chem. Rev. 1980. Vol. 33. P. 227-250.
29. Choi, E.-Y., Han, T.H., Hong, J., Kim, J.E., Lee, S.H., Kim, H.W., Kim, S.O. Noncovalent Functionalization of Graphene with End-Functional Polymers // J. Mater. Chem. 2010. Vol. 20. P. 1907-1912.
30. Rodrigues, A.F., Newman, L., Lozano, N., Mukherjee, S.P., Fadeel, B., Bussy, C., Kostarelos, K. A Blueprint for the Synthesis and Characterization of Thin Graphene Oxide with Controlled Lateral Dimensions for Biomedicine // 2D Mater. 2018. Vol. 5. P. 035020.
31. Alam, S.N., Sharma, N., Kumar, L. Synthesis of Graphene Oxide (GO) by Modified Hummers Method and Its Thermal Reduction to Obtain Reduced Graphene Oxide (rGO) // Graphene 2017. Vol. 6. P. 1-18.
32. Henson, M.J., Mukherjee, P., Root, D.E., Stack, T.D.P., Solomon, E.I. Spectroscopic and Electronic Structural Studies of the $Cu(III)_2$ Bis-í-oxo Core and Its Relation to the Side-On Peroxo-Bridged Dimer // J. Am. Chem. Soc. 1999. Vol. 121. P. 10332–10345.
33. Hagemann, H., Bill, H., Sadowski, W., Walker, E., Francois, M. Raman Spectra of Single Crystal CuO // Solid State Commun. 1990. Vol. 73. P. 447–451.
34. Hsu, S.-W., Bryks, W., Tao, A.R. Effects of Carrier Density and Shape on the Localized Surface Plasmon Resonances of $Cu_{2-x}S$ Nanodisks // Chem. Mater. 2012. Vol. 24. P. 3765–3771.
35. Yang, Y., Xu, D., Wu, Q., Diao, P. Cu_2O/CuO Bilayered Composite as a High-Efficiency Photocathode for Photoelectrochemical Hydrogen Evolution Reaction // Sci. Rep. 2016. Vol. 6. P. 35158-1-13.
36. Lai, Q., Zhu, S., Luo, X., Zou, M., Huang, S. UV-Vis Spectroscopy of Graphene Oxides // AIP Advances 2012. Vol. 2. P. 032146.
37. Ross, P.K., Solomon, E.I. An Electronic Structural Comparison of Copper-Peroxide Complexes of Relevance to Hemocyanin and Tyrosinase Active Sites // J. Am. Chem. Soc. 1991. Vol. 113. P. 3246-3259.
38. Blanco, E., Esquivias, L., Litran, R., Pinaro, M., Ramirez-del-Solar, M., de la Rosa-Fox, N. Sonogels and Derived Materials // Appl. Organomet. Chem. 1999. Vol. 13. P. 399–418.
39. Shimanovich, U., Eliaz, D., Aizer, A., Vayman, I., Micheli, S., Shav-Tal, Y., Gedanken, A. Sonochemical Synthesis of DNA Nanospheres // ChemBioChem. 2011. Vol. 12. P. 1678–1681.

40. Suslick, K.S., Grinstaff, M.W. Protein Microencapsulation of Nonaqueous Liquids / J. Am. Chem. Soc. 1990. Vol. 112. P. 7809–7811.
41. Bertoluzza, A., Fagnano, C., Morelli, M.A., Gottardi, V., Guglielmi, M. Raman and Infrared Spectra on Silica Gel Evolving toward Glass // J. Non-Cryst. Solids 1982. Vol. 48. P. 117–128.
42. Muika, B., Lendl, B., Molina-Dıaz, A., Ayora-Canada, M.J. Direct Monitoring of Lipid Oxidation in Edible Oils by Fourier Transform Raman Spectroscopy // Chem. Phys. Lipids 2005. Vol. 134. P. 173–182.
43. Kundu, A., Layek, R.K., Kuila, A., Nandi, A.K. Highly Fluorescent Graphene Oxide-Poly(vinyl alcohol) Hybrid: An Effective Material for Specific Au^{3+} Ion Sensors // ACS Appl. Mater. Interfaces 2012. Vol. 4. P. 5576–5582.
44. Galande, C., Mohite, A.D., Naumov, A.V., Gao, W., Ci, L., Ajayan, A., Gao, H., Srivastava, A., Weisman, R.B., Ajayan, P.M. Quasi-Molecular Fluorescence from Graphene Oxide // Sci. Rep. 2011. Vol. 1. N. 85. P. 1–5.
45. Radziuk, D., Mikhnavets, L., Tkach, A., Tabulina, L., Labunov, V. Sonochemically Assembled Photoluminescent Copper-Modified Graphene Oxide Microspheres // Langmuir 2018. Vol. 34. P. 8599–8610.

References (Chapter 2)

1. Hassan, H.M.A., Abdelsayed, V., Khder, A.E.R.S., AbouZeid, K.M., Terner, J., El-Shall, M.S., Al-Resayes, S.I., El-Azhary, A.A. Microwave Synthesis of Graphene Sheets Supporting Metal Nanocrystals in Aqueous and Organic Media // J. Mater. Chem. 2009. Vol. 19. P. 3832–3837.
2. Wu, S., Yin, Z., He, Q., Lu, G., Zhou, X., Zhang, H. Electrochemical Deposition of Cl-Doped n-type Cu_2O on Reduced Graphene Oxide Electrodes // J. Mater. Chem. 2010. Vol. 21. P. 3467–3470.
3. Yang, X., Zhang, X., Ma, Y., Huang, Y., Wang, Y., Chen, Y. Superparamagnetic Graphene Oxide–Fe_3O_4 Nanoparticles Hybrid for Controlled Targeted Drug Carriers // J. Mater. Chem. 2009. Vol. 19. P. 2710–2714.
4. Huang, X., Qi, X., Boey, F., Zhang, H. Graphene-Based Composites // Chem. Soc. Rev. 2012. Vol. 41. P. 666–686.
5. Suslick, K.S. Sonochemistry // Science 1990. Vol. 247. P. 1439-1445.
6. Suslick, K.S., Hammerton, D.A., Cline, R.E. Sonochemical Hot Spot // J. Am. Chem. Soc. 1986. Vol. 108. P. 5641-5642.
7. Weissler, A. Formation of Hydrogen Peroxide by Ultrasonic Waves: Free Radicals // J. Am. Chem. Soc. 1959. Vol. 81. P. 1077-1081.
8. Suslick, K.S., Grinstaff, M.W. Protein Microencapsulation of Nonaqueous Liquids // J. Am. Chem. Soc. 1990. Vol. 112. P. 7807-7809.
9. Lippitt, B., McCord, J.M., Fridovich, I. The Sonochemical Reduction of Cytochrome C and Its Inhibition by Superoxide Dismutase // J. Biol. Chem. 1972. Vol. 247. P. 4688-4690.
10. Shimanovich, U., Gedanken, A. Nanotechnology Solutions to Restore Antibiotic Activity // J. Mater. Chem. B 2016. Vol. 4. P. 824-833.
11. Petreska, G.S., Salsamendi, M., Arzac, A., Leal, G.P., Alegret, N., Gilev, J.B., Tomovska, R. Covalent-Bonded Reduced Graphene Oxide–Fluorescein Complex as a Substrate for Extrinsic SERS Measurements // ACS Omega 2017. Vol. 2. P. 4123-4131.
12. Alizadeh, A., Abdi, G., Khodaei, M.M., Ashokkumar, M., Amirian, J. Graphene Oxide/Fe_3O_4/SO_3H Nanohybrid: a New Adsorbent for Adsorption and Reduction of Cr (VI) from Aqueous Solutions // RSC Advances 2017. Vol. 7. P. 14876-14887.
13. Vinodgopal, K., Neppolian, B., Lightcap, I.V., Grieser, F., Ashokkumar, M., Kamat, P.V. Sonolytic Design of Graphene − Au Nanocomposites. Simultaneous and Sequential Reduction of Graphene Oxide and Au (III) // J. Phys. Chem. Lett. 2010. Vol. 1. P. 1987-1993.

14. Neppolian, B., Wang, C., Ashokkumar, M. Sonochemically Synthesized Mono and Bimetallic Au–Ag Reduced Graphene Oxide Based Nanocomposites with Enhanced Catalytic Activity // Ultrason. Sonochem. 2014. Vol. 21. P. 1948-1953.
15. Marzuillo, P., Calligaris, L., Amoroso, S., Barbi, E. Narrative Review Shows that the Short-Term Use of Ketorolac is Safe and Effective in the Management of Moderate-to-Severe Pain in Children // Acta Paediatr. 2018. Vol. 107. P. 560-567.
16. Samal, S.K., Routray, S., Veeramachaneni, G.K., Dash, R., Botlagunta, M. Ketorolac Salt is a Newly Discovered DDX3 Inhibitor to Treat Oral Cancer // Sci. Rep. 2015. Vol. 5. P. 9982-9982.
17. Flores-Murrieta, F.J., Granados-Soto, V. Pharmacologic Properties of Ketorolac Tromethamine: A Potent Analgesic Drug // CNS Drug Rev. 1996. Vol. 2. P. 75-90.
18. Forget, P., Berliere, M., van Maanen, A., Duhoux, F.P., Machiels, J.P., Coulie, P.G., Bouche, G., De Kock, M. Cancer Surgery Induces Inflammation, Immunosuppression and Neo-Angiogenesis, but is It Influenced by Analgesics? Med. Hypotheses 2013. Vol. 81. P. 707-712.
19. Gonzalez, E.L.M., Patrignani, P., Tacconelli, S., Garcia Rodriguez, L.A. Variability Among Nonsteroidal Anti-inflammatory Drugs in Risk of Upper Gastrointestinal Bleeding // Arthritis Rheum. 2010. Vol. 62. P. 1592-1601.
20. Wongrakpanich, S., Wongrakpanich, A., Melhado, K., Rangaswami, J., A Comprehensive Review of Non-Steroidal Anti-Inflammatory Drug Use in The Elderly // Aging Dis. 2018. Vol. 9. P. 143-150.
21. Banti, C.N., Hadjikakou, S.K. Non-steroidal Anti-inflammatory Drugs (NSAIDs) in Metal Complexes and Their Effect at the Cellular Level // Eur. J. Inorg. Chem. 2016. Vol. 2016. P. 3048-3071.
22. Pelaz, B., Alexiou, C., Alvarez-Puebla, R.A., Alves, F., Andrews, A.M. et.al., Diverse Applications of Nanomedicine // ACS Nano 2017. Vol. 11. P. 2313−2381.
23. Cini, R. Anti-Inflammatory Compounds as Ligands in Metal Complexes as Revealed in X-Ray Structural Studies Comments // Inorg. Chem. 2000. Vol. 22. P. 151-186.
24. Weder, J.E., Dillon, C.T., Hambley, T.W., Kennedy, B.J., Lay, P.A., Biffin, J.R., Regtop, H.L., Davies, N.M. Copper Complexes of Non-steroidal Anti-inflammatory Drugs: an Opportunity Yet to be Realized // Coord.Chem.Rev. 2002. Vol. 232. P. 95–126.
25. Krstić, N.S., Nikolić, R.S., Stanković, M.N., Nikolić, N.G., Dorđević, D.M. Coordination Compounds of M(II) Biometal Ions with Acid- Type Anti-inflammatory Drugs as Ligands – A Review // Trop. J. Pharm. Res. 2015. Vol. 14. P. 337-349.
26. Puranik, R., Bao, S., Bonin, A.M., Kaur, R., Weder, J.E., Casbolt, L., Hambley, T.W., Lay, P.A., Barter, P.J., Rye, K.A. A Novel Class of Copper (II)-and Zinc (II)-Bound Non-steroidal

Anti-inflammatory Drugs that Inhibits Acute Inflammation in Vivo // Cell Biosci. 2016. Vol. 6. P. 9.

27. Siddiqi, Z.A., Kumar, S., Khalid, M., Shahid, M. Synthesis and Spectral Investigations of Mononuclear [N6], [N8] and Dinuclear [N10] Complexes of Polyamide Macrocycles: ^{57}Fe Mössbauer parameters of Fe(III) complexes // Spectrochim. Acta Part A 2009. Vol. 72. P. 616–620.
28. Lawal, A., Obaleye, J.A. Synthesis, Characterization and Antibacterial Activity of Aspirin and Paracetamolmetal Complexes // Biokemistri 2007. Vol. 19. P. 9–15.
29. Mahmoud, W.H., Mohamed, G.G., El-Dessouky, M.M.I. Coordination Modes of Bidentate Lornoxicam Drug with Some Transition Metal Ions. Synthesis, Characterization and In Vitro Antimicrobial and Antibreastic Cancer Activity Studies // Spectrochim. Acta Part A 2014. Vol. 122. P. 598–608.
30. Badri, W., Miladi, K., Nazari, Q.A., Greige-Gerges, H., Fessi, H., Elaissari, A. Encapsulation of NSAIDs for Inflammation Management: Overview, Progress, Challenges and Prospects // Internat. J of Pharmaceut. 2016. Vol. 515. P. 757-773.
31. Timin, A.S., Gould, D.J., Sukhorukov, G.B. Multi-Layer Microcapsules: Fresh Insights and New Applications // Expert Opin. Drug Deliv. 2017. Vol. 14. P. 583-587.
32. Senapati, S., Mahanta, A.K., Kumar, S., Maiti, P. Controlled Drug Delivery Vehicles for Cancer Treatment and Their Performance // Signal Transduct. Target Ther. 2018. Vol. 3. P. 7.
33. McCallion, C., Burthem, J., Rees-Unwin, K., Golovanov, A., Pluen, A. Graphene in Therapeutics Delivery: Problems, Solutions and Future Opportunities // Eur. J. Pharm. Biopharm. 2016. Vol. 104. P. 235-250.
34. Tran, S., DeGiovanni, P.J., Piel, B., Rai, P. Cancer Nanomedicine: a Review of Recent Success in Drug Delivery // Clin. Transl. Med. 2017. Vol. 6. P. 44.
35. Reina, G., Gonzalez-Dominguez, J.M., Criado, A., Vazquez, E., Bianco, A., Prato, M. Promises, Facts and Challenges for Graphene in Biomedical Applications // Chem. Soc. Rev. 2017. Vol. 46. P. 4400-4416.
36. del Mercato, L.L., Guerra, F., Lazzari, G., Nobile, C., Bucci, C., Rinaldi, R. Biocompatible Multilayer Capsules Engineered with a Graphene Oxide Derivative: Synthesis, Characterization and Cellular Uptake // Nanoscale 2016. Vol. 8. P. 7501-7512.
37. Gui, R., Jin, H., Wang, Z., Zhang, F., Xia, J., Yang, M., Bi, S., Xia, Y. Room-Temperature Phosphorescence Logic Gates Developed from Nucleic Acid Functionalized Carbon Dots and Graphene Oxide // Nanoscale 2015. Vol. 7. P. 8289-8293.

38. Rasoulzadeh, M., Namazi, H. Carboxymethyl Cellulose/Graphene Oxide Bio-Nanocomposite Hydrogel Beads as Anticancer Drug Carrier Agent // Carbohydr. Polym. 2017. Vol. 168. P. 320-326.
39. Deng, L., Li, Q., Al-Rehili, S., Omar, H., Almalik, A., Alshamsan, A., Zhang, J., Khashab, N.M. Hybrid Iron Oxide–Graphene Oxide–Polysaccharides Microcapsule: a Micro-Matryoshka for On-Demand Drug Release and Antitumor Therapy In Vivo // ACS Appl. Mater. Interfaces 2016. Vol. 8. P. 6859-6868.
40. Bianco, A. Graphene: Safe or Toxic? The Two Faces of the Medal // Angew. Chem. Int. Ed. 2013. Vol. 52. P. 4986-4997.
41. Ou, L., Song, B., Liang, H., Liu, J., Feng, X., Deng, B., Sun, T., Shao, L. Toxicity of Graphene-Family Nanoparticles: a General Review of the Origins and Mechanisms // Part. Fibre Toxicol. 2016. Vol. 13. P. 57.
42. Sasidharan, A., Panchakarla, L.S., Sadanandan, A.R., Ashokan, A., Chandran, P., Girish, C.M., Menon, D., Nair, S.V., Rao, C.N., Koyakutty, M. Hemocompatibility and Macrophage Response of Pristine and Functionalized Graphene // Small 2012. Vol. 8. P. 1251-1263.
43. R. Kurapati, J. Russier, M. A. Squillaci, E. Treossi, C. Menard-Moyon, A. E. Del Rio-Castillo, E. Vazquez, P. Samori, V. Palermo, A. Bianco, Dispersibility-Dependent Biodegradation of Graphene Oxide by Myeloperoxidase // Small 2015. Vol. 11. P. 3985-3994.
44. Yang, K., Feng, L., Liu, Z. Stimuli Responsive Drug Delivery Systems Based on Nano-Graphene for Cancer Therapy //Adv. Drug Deliv. Rev. 2016. Vol. 105. P. 228-241.
45. Haubner, K., Murawski, J., Olk, P., Eng, L.M., Ziegler, C., Adolphi, B., Jaehne, E. The Route to Functional Graphene Oxide // ChemPhysChem 2010. Vol. 11. P. 2131-2139.
46. Wang, Y., Polavarapu, L., Liz-Marzán, L.M. Reduced Graphene Oxide-Supported Gold Nanostars for Improved SERS Sensing and Drug Delivery // ACS Appl. Mater. Interfaces 2014. Vol. 6. P. 21798-21805.
47. Shi, J., Wang, L., Zhang, J., Ma, R., Gao, J., Liu, Y., Zhang, C., Zhang, Z. A Tumor-Targeting Near-Infrared Laser-Triggered Drug Delivery System Based on GO@Ag Nanoparticles for Chemo-Photothermal Therapy and X-ray Imaging // Biomaterials 2014. Vol. 35. P. 5847-5861.
48. Ortega-Amaya, R., Matsumoto, Y., Espinoza-Rivas, A.M., Perez-Guzman, M.A., Ortega-Lopez, M. Development of Highly Faceted Reduced Graphene Oxide-Coated Copper Oxide and Copper Nanoparticles on a Copper Foil Surface // Beilstein J. Nanotechnol. 2016. Vol. 7. P. 1010-1017.
49. Tripathi, S.K., Goyal, R., Gupta, K.C., Kumar, P. Functionalized Graphene Oxide Mediated Nucleic Acid Delivery // Carbon 2013. Vol. 51. P. 224-235.

50. Zhang, L., Wang, Z., Lu, Z., Shen, H., Huang, J., Zhao, Q., Liu, M., He, N., Zhang, Z. PEGylated Reduced Graphene Oxide as a Superior ssRNA Delivery System // J Mater. Chem. B 2013. Vol. 1. P. 749-755.
51. Liu, X., Ma, D., Tang, H., Tan, L., Xie, Q., Zhang, Y., Ma, M., Yao, S. Polyamidoamine Dendrimer and Oleic Acid-Functionalized Graphene as Biocompatible and Efficient Gene Delivery Vectors // ACS Appl. Mater. Interfaces 2014. Vol. 6. P. 8173-8183.
52. Karthikeyan, B., Udayabhaskar, R., Hariharan, S. Tuning Optical and Three Photon Absorption Properties in Graphene Oxide-Polyvinyl Alcohol Free Standing Films // Appl. Phys. Lett. 2016. Vol. 109. P. 021904.
53. Cheng, R., Xue, Y. Carbon Nanomaterials for Biomedical Applications. M. Zhang, R. R. Naik, L. Dai, (Eds.), 2016, XI 576, p. 232 ISBN: 978-3-319-22860-0.
54. Ma, J., Liu, C., Li, R., Wang, J. Properties and Structural Characterization of Oxide Starch/Chitosan/Graphene Oxide Biodegradable Nanocomposites // J Appl. Polym. Sci. 2012. Vol. 123. P. 2933-2944.
55. Kumar, S., Kumar, A. Chemically Derived Luminescent Graphene Oxide Nanosheets and Its Sunlight Driven Photocatalytic Activity Against Methylene Blue Dye // Opt. Mater. 2016. Vol. 62. P. 320-327.
56. Sreejith, S., Ma, X., Zhao, Y. Graphene Oxide Wrapping on Squaraine-Loaded Mesoporous Silica Nanoparticles for Bioimaging // J. Am. Chem. Soc. 2012. Vol. 134. P. 17346-17349.
57. Jaque, D., Maestro, L.M., del Rosal, B., Haro-Gonzalez, P., Benayas, A., Plaza, J.L., Rodríguez, E.M., Solé, J.G. Nanoparticles for Photothermal Therapies // Nanoscale 2014. Vol. 6. P. 9494-9530.
58. Srivastava, S., Awasthi, R., Tripathi, D., Rai, M.K., Agarwal, V., Agrawal, V., Gajbhiye, N.S., Gupta, R.K. Magnetic-Nanoparticle-Doped Carbogenic Nanocomposite: an Effective Magnetic Resonance/Fluorescence Multimodal Imaging Probe // Small 2012. Vol. 8. P. 1099-1109.
59. Shi, X., Gong, H., Li, Y., Wang, C., Cheng, L., Liu, Z. Graphene-Based Magnetic Plasmonic Nanocomposite for Dual Bioimaging and Photothermal Therapy // Biomaterials 2013. Vol. 34. P. 4786-4793.
60. Chen, Y., Tan, C., Zhang, H., Wang, L. Two-Dimensional Graphene Analogues for Biomedical Applications // Chem. Soc. Rev. 2015. Vol. 44. P. 2681-2701.
61. Mendes, R.G., Bachmatiuk, A., Büchner, B., Cuniberti, G., Rümmeli, M.H. Carbon Nanostructures as Multi-Functional Drug Delivery Platforms // J Mater. Chem. B 2013. Vol. 1. P. 401-428.
62. Liu, J., Cui, L., Losic, D. Graphene and Graphene Oxide as New Nanocarriers for Drug Delivery Applications // Acta Biomater. 2013. Vol. 9. P. 9243-9257.

63. Ali-Boucetta, H., Bitounis, D., Raveendran-Nair, R., Servant, A., Van den Bossche, J., Kostarelos, K. Purified Graphene Oxide Dispersions Lack in Vitro Cytotoxicity and in Vivo Pathogenicity // Adv. Healthc. Mater. 2013. Vol. 2. P. 433-441.
64. Mallakpour, S., Abdolmaleki, A., Borandeh, S. Covalently Functionalized Graphene Sheets with Biocompatible Natural Amino Acids // Appl. Surf. Sci. 2014. Vol. 307. P. 533-542.
65. Ossonon, B.D., Belanger, D. Synthesis and Characterization of Sulfophenyl-Functionalized Reduced Graphene Oxide Sheets // RSC Adv. 2017. Vol. 7. P. 27224-27234.
66. Schniepp, H.C., Li, J.-L., McAllister, M.J., Sai, H., Herrera-Alonso, M., Adamson, D.H., Prud'homme, R.K., Car, R., Saville, D.A., Aksay, I.A. Functionalized Single Graphene Sheets Derived from Splitting Graphite Oxide // J Phys. Chem. B 2006. Vol. 110. P. 8535-8539.
67. Radziuk, D., Skirtach, A., Geßner, A., Kumke, M.U., Zhang, W., Möhwald, H., Shchukin, D. Ultrasonic Approach for Formation of Erbium Oxide Nanoparticles with Variable Geometries // Langmuir 2011. Vol. 27. P. 14472-14480.
68. Lee, Y., Hanif, S., Theato, P., Zentel, R., Lim, J., Char, K. Facile Synthesis of Fluorescent Polymer Nanoparticles by Covalent Modification–Nanoprecipitation of Amine-Reactive Ester Polymers // Macromol. Rapid Commun. 2015. Vol. 36. P. 1089-1095.
69. Lavina, B., Dera, P., Kim, E., Meng, Y., Downs, R.T., Weck, P.F., Sutton, S.R., Zhao, Y. Discovery of the Recoverable High-Pressure Iron Oxide Fe_4O_5 // PNAS 2011. Vol. 108. P. 17281-17285.
70. Zhao, C., Chou, S.-L., Wang, Y., Zhou, C., Liu, H.-K., Dou, S.-X. A Facile Route to Synthesize Transition Metal Oxide/Reduced Graphene Oxide Composites and Their Lithium Storage Performance // RSC Adv. 2013. Vol. 3. P. 16597-16603.
71. Lassoued, A., Dkhil, B., Gadri, A., Ammar, S. Control of the Shape and Size of Iron Oxide (α-Fe_2O_3) Nanoparticles Synthesized through the Chemical Precipitation Method // Res. Phys. 2017. Vol. 7. P. 3007-3015.
72. Kumar, R.V., Koltypin, Y., Xu, X.N., Yeshurun, Y., Gedanken, A., Felner, I. Fabrication of Magnetite Nanorods by Ultrasound Irradiation // Appl. Phys. 2001. Vol. 89. P. 6324-6328.
73. Machala, L., Tuček, J., Zbořil, R. Polymorphous Transformations of Nanometric Iron (III) Oxide: a Review // Chem. Mater. 2011. Vol. 23. P. 3255-3272.
74. Gasgnier, M., Beaury, L., Derouet, J. Ultrasound Effects on Metallic (Fe and Cr); iron sesquioxides (α-, γ-Fe_2O_3); Calcite; Copper, Lead and Manganese Oxides as Powders // Ultrason. Sonochem. 2000. Vol. 7. P. 25-33.
75. Vijayakumar, R., Koltypin, Y., Felner, I., Gedanken, A. Sonochemical Synthesis and Characterization of Pure Nanometer-sized Fe_3O_4 Particles // Mater. Sci. Engineer. A 2000. Vol. 286. P. 101-105.

76. Brázda, P., Kohout, J., Bezdička, P., Kmječ, T. α-Fe_2O_3 versus β-Fe_2O_3: Controlling the Phase of the Transformation Product of ε-Fe_2O_3 in the Fe_2O_3/SiO_2 System // Cryst. Growth Des. 2014. Vol. 14. P. 1039-1046.
77. Suslick, K.S., Choe, S.-B., Cichowlas, A.A., Grinstaff, M.W. Sonochemical Synthesis of Amorphous Iron // Nature 1991. Vol. 353. P. 414.
78. David, B., Schneeweiss, O., Pizúrová, N., Šantavá, Kudrle, V., Synek, P., Jašek, O. Atmospheric-Pressure Microwave Torch Discharge Generated γ-Fe_2O_3 Nanopowder // Phys. Procedia 2013. Vol. 44. P. 206-212.
79. Yang, D., Velamakanni, A., Bozoklu, G., Park, S., Stoller, M., Piner, R.D., Stankovich, S., Jung, I., Field, D.A., Ventrice, C.A., Ruoff, R.S. Chemical Analysis of Graphene Oxide Films after Heat and Chemical Treatments by X-ray Photoelectron and Micro-Raman spectroscopy // Carbon 2009. Vol. 47. P. 145-152.
80. Barth, G., Linder, R., Bryson, C. Advances in Charge Neutralization for XPS Measurements of Nonconducting Materials // Surf. Interface Anal. 1988. Vol. 11. P. 307-311.
81. Wang, Y.-Q., Zhang, F.-Q., Sherwood, P.M.A. X-ray Photoelectron Spectroscopic Study of Carbon Fiber Surfaces. 23. Interfacial Interactions between Polyvinyl Alcohol and Carbon Fibers Electrochemically Oxidized in Nitric Acid Solution // Chem. Mater. 1999. Vol. 11. P. 2573-2583.
82. Xu, H., Suslick, K.S. Sonochemical Preparation of Functionalized Graphenes // J. Am. Chem. Soc. 2011. Vol. 133. P. 9148-9151.
83. Gao, D., Yang, G., Li, J., Zhang, J., Zhang, J., Xue, D. Room-Temperature Ferromagnetism of Flowerlike CuO Nanostructures // J. Phys. Chem. C 2010. Vol. 114. P. 18347-18351.
84. Moulder, J.F., Chastain, J. Handbook of X-ray Photoelectron Spectroscopy. A Reference Book of Standard Spectra for Identification and Interpretation of XPS Data. Ed. by J. Chastain, Perkin-Elmer Corporation, Minesota, USA, 1992, ISBN: 0-9627026-2-5.
85. Suslick, K.S. Mechanochemistry and Sonochemistry: Concluding Remarks // Faraday Discuss. 2014. Vol. 170. P. 411-422.
86. Virot, M., Chave, T., Nikitenko, S.I., Shchukin, D.G., Zemb, T., Möhwald, H. Acoustic Cavitation at the Water − Glass Interface // J. Phys. Chem. C 2010. Vol. 114. P. 13083-13091.
87. Frost, D.C., Ishitani, A., McDowell, C.A. X-ray Photoelectron Spectroscopy of Copper Compounds // Mol. Phys. 1972. Vol. 24. P. 861-877.
88. Yin, L., Adler, I., Tsang, T., Matienzo, L.J., Grim, S.O. Paramagnetism and Shake-up Satellites in X-ray Photoelectron Spectra // Chem. Phys. Lett. 1974. Vol. 24. P. 81-84.
89. Ebbing, D.D., Gammon, S.D. General Chemistry. 9th Edition, Edrs.: Heinle, K.; Galvin, A.; Cava, A. Houghton Mifflin Company, Boston, MA, USA, 2007, ISBN: 0-618-93469-3.

90. Brett, C.M.A., Brett, A.M.O. Electrochemistry: Principles, Methods, and Applications. Oxford University Press Inc. New York, USA, 1993, ISBN: 0-19-855388-9.
91. Poulston, S., Parlett, P.M., Stone, P., Bowker, M. Surface Oxidation and Reduction of CuO and Cu_2O Studied Using XPS and XAES // Surf. Interface Anal. 1996. Vol. 24. P. 811-820.
92. Tobin, J.P., Hirschwald, W., Cunningham, J. XPS and XAES Studies of Transient Enhancement of Cu1 at CuO Surfaces During Vacuum Outgassing // Appl. Surf. Sci. 1983. Vol. 16. P. 441-452.
93. Ramanarayanan, T.A., Alonzo, J. Oxidation of Copper and Reduction of Cu_2O in an Environmental Scanning Electron Microscope at 800°C // Oxid. Met. 1985. Vol. 24. P. 17-27.
94. Adamson, A.W. Advanced Inorganic Chemistry. By F. A. Cotton and G. Wilkinson. // Inorg. Chem. 1963. Vol. 2. P. 665-665.
95. Didenko, Y.T., McNamara, W.B., Suslick, K.S. Hot Spot Conditions during Cavitation in Water // J. Am. Chem. Soc. 1999. Vol. 121. P. 5817-5818.
96. Buckley, A.N., Woods, R. The Surface Oxidation of Pyrite // Appl. Surf. Sci. 1987. Vol. 27. P. 437-452.
97. Karthe, S., Szargan, R., Suoninen, E. Oxidation of Pyrite Surfaces: A Photoelectron Spectroscopic Study // Appl. Surf. Sci. 1993. Vol. 72. P. 157-170.
98. McIntyre, N.S., Zetaruk, D.G. X-ray Photoelectron Spectroscopic Studies of Iron Oxides // Anal. Chem. 1977. Vol. 49. P. 1521-1529.
99. Schwertmann, U., Friedl, J., Stanjek, H. From Fe (III) ions to Ferrihydrite and then to Hematite // J. Colloid Interface Sci. 1999. Vol. 209. P. 215-223.
100. Todd, E.C., Sherman, D., Purton, J. Surface Oxidation of Pyrite under Ambient Atmospheric and Aqueous (pH=2 to 10) Conditions: Electronic Structure and Mineralogy from X-ray Absorption Spectroscopy // Geochim. et Cosmochim. Acta 2003. Vol. 67. P. 881-893.
101. Pilloni, M., Kumar, V.B., Ennas, G., Porat, Z., Scano, A., Cabras, V., Gedanken, A. Formation of Metallic Silver and Copper in Non-Aqueous Media by Ultrasonic Radiation // Ultrason. Sonochem. 2018. Vol. 47. P. 108-113.
102. Bertens, C.J.F. Zhang, S., Erckens, R.J. van den Biggelaar, F.J.H.M., Berendschot, T.T.J.M., Webers, C.A.B., Nuijts, R.M.M.A., Gijs, M. Confocal Raman Spectroscopy: Evaluation of a Non-Invasive Technique for the Detection of Topically Applied Ketorolac Tromethamine in Vitro and in Vivo // Int. J Pharm. 2019. Vol. 570. P. 118641.
103. Amul, B., Muthu, S., Raja, M., Sevvanthi, S. Molecular Structure, Spectroscopic (FT-IR, FT-Raman, NMR, UV-VIS), Chemical Reactivity and Biological Examinations of Ketorolac // J Mol. Struct. 2020. Vol. 1210. P. 128040.

104. Xiao, G.-N., Man, S.-Q. Surface-Enhanced Raman Scattering of Methylene Blue Adsorbed on Cap-Shaped Silver Nanoparticles // Chem. Phys. Lett. 2007. Vol. 447. P. 305-309.
105. Beasley, D.E., Koltz, A.M., Lambert, J.E., Fierer, N., Dunn R.R. The Evolution of Stomach Acidity and Its Relevance to the Human Microbiome // PLOS ONE 2015. Vol. 10. P. e0134116-1-12.
106. Johnson, D.E., Ostrowski, P., Jaumouillé, V., Grinstein, S. The Position of Lysosomes within the Cell Determines Their Luminal pH // J. Cell Biol. 2016. Vol. 212. P. 677-692.
107. Kanbara, A., Miura, Y., Hyogo, H., Chayama, K., Seyama, I. Effect of Urine pH Changed by Dietary Intervention on Uric Acid Clearance Mechanism of pH-Dependent Excretion of Urinary Uric Acid // Nutr J. 2012. Vol. 11. P. 39.
108. Quigley, E.M., Turnberg, L.A. pH of the Microclimate Lining Human Gastric and Duodenal Mucosa in Vivo: Studies in Control Subjects and in Duodenal Ulcer Patients // Gastroenterology 1987. Vol. 92. P. 1876-1884.
109. Sky-Peck, H.H., Thuvasethakul, P. Human Pancreatic Alpha-Amylase. II. Effects of pH, Substrate and Ions on the Activity of the Enzyme // Ann. Clin. Lab. Sci. 1977. Vol. 7. P. 310-317.

References (Chapter 3)

1. Sallmann, A.R. The History of Diclofenac // Am. J Med. 1986. Vol. 80. P. 29-33.
2. Levina, E.O., Penkov, N.V., Rodionova, N.N., Tarasov, S.A., Barykina, D.V., Vener, M.V. Hydration of the Carboxylate Group in Anti-Inflammatory Drugs: ATR-IR and Computational Studies of Aqueous Solution of Sodium Diclofenac // ACS Omega 2018. Vol. 3. P. 302-313.
3. Bjarnason, I., Scarpignato, C., Holmgren, E., Olszewski, M., Rainsford, K.D., Lanas, A. Mechanisms of Damage to the Gastrointestinal Tract from Nonsteroidal Anti-Inflammatory Drugs // Gastroenterology 2018. Vol. 154. P. 500-514.
4. García-Rayado, G., Navarro, M., Lanas, A. NSAID Induced Gastrointestinal Damage and Designing GI-Sparing NSAIDs // Expert. Rev. Clin. Pharmacol. 2018. Vol. 11. P. 1031-1043.
5. Schmidt, M., Sørensen, H.T., Pedersen, L. Diclofenac Use and Cardiovascular Risks: Series of Nationwide Cohort Studies // BMJ 2018. Vol. 362. P. k3426.
6. Bende, G., Biswal, S., Bhad, P., Chen, Y., Salunke, A., Winter, S., Wagner, R., Sunkara, G. Relative Bioavailability of Diclofenac Potassium from Softgel Capsule Versus Powder for Oral Solution and Immediate-Release Tablet Formulation // Clin. Pharm. Drug Dev. 2016. Vol. 5. P. 76-82.
7. Francio, V.T., Davani, S., Towery, C., Brown, T.L. Oral Versus Topical Diclofenac Sodium in the Treatment of Osteoarthritis // J Pain Palliat. Care Pharmacother. 2017. Vol. 31. P. 113-120.
8. Elwerfalli, A.M., Ghanchi, Z., Rashid, F., Alany, R.G., ElShaer, A. New Generation of Orally Disintegrating Tablets for Sustained Drug Release: a Propitious Outlook // Curr. Drug Deliv. 2015. Vol. 12. P. 652-667.
9. Leung, C.-H., Lin, S., Zhong, H.-J., Ma, D.-L. Metal Complexes as Potential Modulators of Inflammatory and Autoimmune Responses // Chem. Sci. 2015. Vol. 6. P. 871-884.
10. Lo, K. K.-W. (Ed.); Inorganic and Organometallic Transition Metal Complexes with Biological Molecules and Living Cells; Academic Press, Hong Kong, 2017. P 406.
11. Banti, C.N., Papatriantafyllopoulou, C., Tasiopoulos, A.J., Hadjikakou, S.K. New Metalo-Therapeutics of NSAIDs Against Human Breast Cancer Cells // Eur. J Med Chem. 2018. Vol. 143. P. 1687-1701.
12. Sun, Y., Heidary, D.K., Zhang, Z., Richards, C.I., Glazer, E.C. Bacterial Cytological Profiling Reveals the Mechanism of Action of Anticancer Metal Complexes // Mol. Pharmaceutics 2018. Vol. 15. P. 3404-3416.

13. Simunkova, M., Lauro, P., Jomova, K., Hudecova, L., Danko, M., Alwasel, S., Alhazza, I.M., Rajcaniova, S., Kozovska, Z., Kucerova, L., Moncol, J., Svorc, L., Valko, M. Redox-Cycling and Intercalating Properties of Novel Mixed Copper(II) Complexes with Nonsteroidal Anti-Inflammatory Drugs Tolfenamic, Mefenamic and Flufenamic Acids and Phenanthroline Functionality: Structure, SOD-mimetic Activity, Interaction with Albumin, DNA Damage Study and Anticancer Activity // J. Inorg. Biochem. 2019. Vol. 194. P. 97-113.
14. Hussain, A., AlAjmi, M.F., Rehman, Md.T., Amir, S., Husain, F.M., Alsalme, A., Siddiqui, M.A., AlKhedhairy, A.A., Khan, R.A. Copper(II) Complexes as Potential Anticancer and Nonsteroidal Anti-Inflammatory Agents: In Vitro and in Vivo Studies // Sci. Rep. 2019. Vol. 9. P. 5237.
15. Krstić, N.S., Nikolić, R.S., Stanković, M.N., Nikolić, N.G., Dorđević, D.M. Coordination Compounds of M(II) Biometal Ions with Acid-Type Anti-Inflammatory Drugs as Ligands - a Review // Trop. J. Pharm. Res. 2015. Vol. 14. P. 337-349.
16. Lu, C., Laws, K., Eskandari, A., Suntharalingam, K. A Reactive Oxygen Species-Generating, Cyclooxygenase-2 Inhibiting, Cancer Stem Cell-Potent Tetranuclear Copper(II) Cluster // Dalton Trans. 2017. Vol. 46. P. 12785-12789.
17. Bennett, J.S. Novel Platelet Inhibitors // Annu. Rev. Med. 2001. Vol. 52. P. 161-184.
18. Berry, D.J., Steed, J.W. Pharmaceutical Cocrystals, Salts and Multicomponent Systems; Intermolecular Interactions and Property Based Design // Adv. Drug Delivery Rev. 2017. Vol. 117. P. 3-24.
19. García-Rayado, G., Navarro, M., Lanas, A. NSAID Induced Gastrointestinal Damage and Designing GI-Sparing NSAIDs // Expert. Rev. Clin. Pharmacol. 2018. Vol. 11. P. 1031-1043.
20. Lipinski, C.A., Lombardo, F., Dominy, B.W., Feeney, P.J. Experimental and Computational Approaches to Estimate Solubility and Permeability in Drug Discovery and Development Settings // Adv. Drug Delivery Rev. 2001. Vol. 46. P. 3-26.
21. Zhao, S., Caruso, F., Dähne, L., Decher, G., De Geest, B.G., Fan, J., Feliu, N., Gogotsi, Y., Hammond, P.T., et.al. The Future of Layer-by-Layer Assembly: a Tribute to ACS Nano Associate Editor Helmuth Möhwald // ACS Nano 2019. Vol. 13. P. 6151-6169.
22. Martín, C., Kostarelos, K., Prato, M., Bianco, A. Biocompatibility and Biodegradability of 2D Materials: Graphene and Beyond // Chem. Commun. 2019. Vol. 55. P. 5540-5546.
23. Guarnieri, D., Sánchez-Moreno, P., Del Rio Castillo, A.E., Bonaccorso, F., Gatto, F., Bardi, G., Martín, C., Vázquez, E., Catelani, T., Sabella, S., Pompa, P.P. Biotransformation and Biological Interaction of Graphene and Graphene Oxide During Simulated Oral Ingestion // Small 2018. Vol. 14. P. e1800227.

24. Sengupta, I., Bhattacharya, P., Talukdar, M., Neogi, S., Pal, S.K., Chakraborty, S. Bactericidal Effect of Graphene Oxide and Reduced Graphene Oxide: Influence of Shape of Bacteria // Colloids Interface Sci. Commun. 2019. Vol. 28. P. 60-68.
25. Fadeel, B., Bussy, C., Merino, S., Vázquez, E., Flahaut, E., Mouchet, F., Evariste, L., Gauthier, L., Koivisto, A.J., Vogel, U., Martin, C., Delogu, L.G., Bürki-Thurnherr, T., Wick, P., Beloin-Saint-Pierre, D., Hischier, R., Pelin, M., Carniel, F.C., Tretiach, M., Cesca, F., Benfenati, F., Scaini, D., Ballerini, L., Kostarelos, K. Prato, M., Bianco, A. Safety Assessment of Graphene-Based Materials: Focus on Human Health and the Environment // ACS Nano 2018. Vol. 12. P. 10582-10620.
26. Nishino, F., Jeem, M., Zhang, L., Okamoto, K., Okabe, S., Watanabe, S. Formation of CuO Nano-Flowered Surfaces via Submerged Photo-Synthesis of Crystallites and Their Antimicrobial Activity // Sci. Rep. 2017. Vol. 7. P. 1063.
27. Boltaev, G.S., Ganeev, R.A., Krishnendu, P.S., Zhang, K., Guo, C. Nonlinear Optical Characterization of Copper Oxide Nanoellipsoids // Sci. Rep. 2019. Vol. 9. P. 11414.
28. Deng, Z., Ma, Z., Li, Y., Li, Y., Chen, L., Yang, X., Wang, H.-E., Su, B.-L. Boosting Lithium-Ion Storage Capability in CuO Nanosheets via Synergistic Engineering of Defects and Pores // Front. Chem. 2018. Vol. 6. P. 1-9.
29. Naatz, H., Lin, S., Li, R., Jiang, W., Ji, Z., Chang, C.H., Köser, J., Thöming, J., Xia, T., Nel, A.E., Mädler, L., Pokhrel, S. Safe-by-Design CuO Nanoparticles via Fe-doping, Cu-O bond Length Variation, and Biological Assessment in Cells and Zebrafish Embryos // ACS Nano 2017. Vol. 11. P. 501-515.
30. Hajipour, P., Bahrami, A., Eslami, A., Hosseini-Abari, A., Ranjbar, H.H. Chemical Bath Synthesis of CuO-GO-Ag Nanocomposites with Enhanced Antibacterial Properties // J Alloys Comp. 2020. Vol. 821. P. 153456-1-7.
31. Kumar, S.R.K., Mamatha, G.P., Muralidhara, H.B., Anantha, M.S., Yallappa, S.; Hungund, B. S.; Kumar, K. Y. Highly Efficient Multipurpose Graphene Oxide Embedded with Copper Oxide Nanohybrid for Electrochemical Sensors and Biomedical Applications // J Sci. Adv. Mater. Devices 2017. Vol. 2. P. 493-500.
32. Radziuk, D., Mikhnavets, L., Vorokhta, M., Matolín, V., Tabulina, L., Labunov, V. Sonochemical Formation of Copper/Iron-Modified Graphene Oxide Nanocomposites for Ketorolac Delivery // Chem. Eur. J 2019. Vol. 25. P. 6233-6245.
33. Gunawan, C., Teoh, W.Y., Marquis, C.P., Amal, R. Cytotoxic Origin of Copper(II) Oxide Nanoparticles: Comparative Studies with Micron-Sized Particles, Leachate, and Metal Salts // ACS Nano 2011. Vol. 9. P. 7214 – 7225.

34. Grigore, M.E., Biscu, E.R., Holban, A.M., Gestal, M.C., Grumezescu, A.M. Methods of Synthesis, Properties and Biomedical Applications of CuO Nanoparticles // Pharm. 2016. Vol. 9. P. 1-14.
35. Applerot, G., Lellouche, J., Lipovsky, A., Nitzan, Y., Lubart, R., Gedanken, A., Banin, E. Understanding the Antibacterial Mechanism of CuO Nanoparticles: Revealing the Route of Induced Oxidative Stress // Small 2012. Vol. 8. P. 3326–3337.
36. Kayani, Z.N., Umer, M., Riaz, S., Naseem, S. Characterization of Copper Oxide Nanoparticles Fabricated by the Sol–Gel Method // J. Electron. Mater. 2015. Vol. 44. P. 3704–3709.
37. Katwal, R., Kaur, H., Sharma, G., Naushad, M., Pathania, D. Electrochemical Synthesized Copper Oxide Nanoparticles for Enhanced Photocatalytic and Antimicrobial Activity // J. Ind. Eng. Chem. 2015. Vol. 31. P. 173–184.
38. Khashan, K.S., Sulaiman, G.M., Abdulameer, F.A. Synthesis and Antibacterial Activity of CuO Nanoparticles Suspension Induced by Laser Ablation in Liquid // Arab. J. Sci. Eng. 2016. Vol. 41. P. 301–310.
39. Ananth, A., Dharaneedharan, S., Heo, M.-S., Mok, Y.S. Copper Oxide Nanomaterials: Synthesis, Characterization and Structure-Specific Antibacterial Performance // Chem. Eng. J. 2015. Vol. 262. P. 179–188.
40. Vidyasagar, C., Naik, Y.A., Venkatesha, T., Viswanatha, R. Solid-State Synthesis and Effect of Temperature on Optical Properties of CuO Nanoparticles // Nano-Micro Lett. 2012. Vol. 4. P. 73–77.
41. Kayani, Z.N., Umer, M., Riaz, S., Naseem, S. Characterization of Copper Oxide Nanoparticles Fabricated by the Sol–Gel Method // J. Electron. Mater. 2015. Vol. 44. P. 3704–3709.
42. Zhu, J., Yang, D., Yin, Z., Yan, Q., Zhang, H. Graphene and Graphene-Based Materials for Energy Storage Applications // Small 2014. Vol. 10. P. 3480–3498.
43. Zhang, K., Suh, J.M., Lee, T.H., Cha, J.H., Choi, J.-W., Jang, H.W., Rajender S. Varma, R.S., Shokouhimehr, M. Copper Oxide–Graphene Oxide Nanocomposite: Efficient Catalyst for Hydrogenation of Nitroaromatics in Water // Nano Converg. 2019. Vol. 6. P. 1-7.
44. Sarkar, C., Dolui, S.K. Synthesis of Copper Oxide/Reduced Graphene Oxide Nanocomposite and Its Enhanced Catalytic Activity towards Reduction of 4-Nitrophenol // RSC Adv. 2015. Vol. 5. P. 60763.
45. Gupta, A., Jamatia, R., Patil, R.A., Ma, Y.-R., Pal, A.K. Copper Oxide/Reduced Graphene Oxide Nanocomposite-Catalyzed Synthesis of Flavanones and Flavanones with Triazole Hybrid Molecules in One Pot: A Green and Sustainable Approach // ACS Omega 2018. Vol. 3. P. 7288−7299.

46. Suslick, K.S. Sonochemistry // Science 1990. Vol. 247. P. 1439-1445.
47. Suslick, K.S., Eddingsaas, N.C., Flannigan, D.J., Hopkins, S.D., Xu, H. The Chemical History of a Bubble // Acc. Chem. Res. 2018. Vol. 51. P. 2169-2178.
48. Nagvenkar, A.P., Perelshtein, I., Piunno, Y., Mantecca, P., Gedanken, A. Sonochemical One-Step Synthesis of Polymer-Capped Metal Oxide Nanocolloids: Antibacterial Activity and Cytotoxicity // ACS Omega 2019. Vol. 4. P. 13631-13639.
49. Maruthapandi, M., Nagvenkar, A.P., Perelshtein, I., Gedanken, A. Carbon-Dot Initiated Synthesis of Polypyrrole and Polypyrrole@CuO Micro/Nanoparticles with Enhanced Antibacterial Activity // ACS Appl. Polym. Mater. 2019. Vol. 15. P. 1181-1186.
50. Fini, A., Fazio, G., Feroci, G. Solubility and Solubilization Properties of Nonsteroidal Anti-Inflammatory Drugs // Int. J. Pharm. 1995. Vol. 126. P. 95-102.
51. El-Trass, A., ElShamy, H., El-Mehasseb, I., El-Kemary, M. CuO Nanoparticles: Synthesis, Characterization, Optical Properties and Interaction with Amino Acids // Appl. Surf. Sci. 2012. Vol. 258. P. 2997-3001.
52. Li, D., Muller, M.B., Gilje, S., Kaner, R.B., Wallace, G.G. Processable Aqueous Dispersions of Graphene Nanosheets // Nat. Nanotechnol. 2008. Vol. 3. P. 101-105.
53. Pegau, W.S.;, Zaneveld, J.R.V. Temperature Dependent Absorption of Water in the Red and near Infrared Portions of the Spectrum // Limnol. Oceanogr. 1993. Vol. 38. P. 188-192.
54. Jia, W., Reitz, E., Sun, H., Li, B., Zhang, H., Lei, Y. From $Cu_2(OH)_3Cl$ to Nanostructured Sisal-like $Cu(OH)_2$ and CuO: Synthesis and Characterization // J. Appl. Phys. 2009. Vol. 105. P. 064917-1-6.
55. Xu, H., Suslick, K.S. Sonochemical Preparation of Functionalized Graphenes // J. Am. Chem. Soc. 2011. Vol. 133. P. 9148-9151.
56. Kumar, R.V., Diamant, Y., Gedanken, A. Sonochemical Synthesis and Characterization of Nanometer-Size Transition Metal Oxides from Metal Acetates // Chem. Mater. 2000. Vol. 12. P. 2301-2305.
57. Luche, J.-L. A Few Questions on the Sonochemistry of Solutions // Ultrason. Sonochem. 1997. Vol. 4. P. 211-215.
58. Palomo, M.E., Ballesteros, M.P., Frutos, P. Analysis of Diclofenac Sodium and Derivatives // J Pharm. Biomed. Anal. 1999. Vol. 21. P. 83-94.
59. Cid-Cerón, M.M., Guzmán-Hernández, D.S., Ramírez-Silva, M.T., Galano, A., Romero-Romo, M., Palomar-Pardavé, M. New Insights on the Kinetics and Mechanism of the Electrochemical Oxidation of Diclofenac in Neutral Aqueous Medium // Electrochim. Acta 2016. Vol. 199. P. 92-98.

60. Matin, A.A., Farajzadeh, M.A., Jouyban, A. A Simple Spectrophotometric Method for Determination of Sodium Diclofenac in Pharmaceutical Formulations // Farmaco 2005. Vol. 60. P. 855-858.
61. Chen, X.Y., Cui, H., Liu, P., Yang, G.W. Shape-Induced Ultraviolet Absorption of CuO Shuttle-like Nanoparticles // Appl. Phys. Lett. 2007. Vol. 90. P. 183118.

References (Chapter 4)

1. Ornelas, A., Zacharias-Millward, N., Menter, D.G., Davis, J.S., Lichtenberger, L., Hawke, D., Hawk, E., Vilar, E., Bhattacharya, P., Millward, S. Beyond COX-1: the Effects of Aspirin on Platelet Biology and Potential Mechanisms of Chemoprevention // Cancer Metastasis Rev. 2017. Vol. 36. P. 289–303.
2. Choudhary, A., Kamer, K.J., Raines, R.T. An n→π* Interaction in Aspirin: Implications for Structure and Reactivity // J Org. Chem. 2011. Vol. 76. P. 7933–7937.
3. Fersht, A.R., Kirby, A.J. Hydrolysis of Aspirin. Intramolecular General Base Catalysis of Ester Hydrolysis // JACS 1967. Vol. 89. P. 4857–4863.
4. St. Pierre, T., Jencks, W.P. Intramolecular Catalysis in the Reactions of Nucleophilic Reagents with Aspirin // JACS 1968. Vol. 90. P. 3817–3827.
5. Hua, H., Zhang, H., Kong, Q., Wang, J., Jiang, Y. Complex Roles of the Old Drug Aspirin in Cancer Chemoprevention and Therapy // Med. Res. Rev. 2019. Vol. 39. P. 114–145.
6. Ornelas, A., Zacharias-Millward, N., Davis, J.S., Lichtenberger, L., Hawke, D., Hawk, E., Vilar, E., Bhattacharya, P., Millward, S. Beyond COX-1: the Effects of Aspirin on Platelet Biology and Potential Mechanisms of Chemoprevention // Cancer Metastasis Rev. 2017. Vol. 36. P. 289–303.
7. Leung, C.-H., Lin, S., Zhong, H.-J., Ma, D.-L. Metal Complexes as Potential Modulators of Inflammatory and Autoimmune Responses // Chem. Sci. 2015. Vol. 6. P. 871–884.
8. Krstić, N.S., Nikolić, R.S., Stanković, M.N., Nikolić, N.G., Dorđević, D.M. Coordination Compounds of M(II) Biometal Ions with Acid-Type Anti-Inflammatory Drugs as Ligands - a Review // Trop. J. Pharm. Res. 2015. Vol. 14. P. 337–349.
9. Martín, C., Kostarelos, K., Prato, M., Bianco, A. Biocompatibility and Biodegradability of 2D Materials: Graphene and Beyond // Chem. Commun. 2019. Vol. 55. P. 5540–5546.
10. Guarnieri, D., Sánchez-Moreno, P., Del Rio Castillo, A.E., Bonaccorso, F., Gatto, F., Bardi, G., Martín, C., Vázquez, E., Catelani, T., Sabella, S., Pompa, P.P. Biotransformation and Biological Interaction of Graphene and Graphene Oxide During Simulated Oral Ingestion // Small 2018. Vol. 14. P. e1800227.
11. Fadeel, B., Bussy, C., Merino, S., Vázquez, E., Flahaut, E., Mouchet, F., Evariste, L., Gauthier, L., Koivisto, A.J., Vogel, U., Martin, C., Delogu, L.G., Bürki-Thurnherr, T., Wick, P., Beloin-Saint-Pierre, D., Hischier, R., Pelin, M., Carniel, F.C., Tretiach, M., Cesca, F., Benfenati, F., Scaini, D., Ballerini, L., Kostarelos, K., Prato, M., Bianco, A. Safety Assessment of Graphene-Based Materials: Focus on Human Health and the Environment // ACS Nano 2018. Vol. 12. P. 10582–10620.

12. Rana, S., Jonnalagadda, S.B., CuO/Graphene Oxide Nanocomposite as Highly Active and Durable Catalyst for Selective Oxidation of Cyclohexane // ChemistrySelect 2017. Vol. 2. P. 2277–2281.
13. Kumar, S.R.K., Mamatha, G.P., Muralidhara, H.B., Anantha, M.S., Yallappa, S., Hungund, B.S., Kumar, K.Y. Highly Efficient Multipurpose Graphene Oxide Embedded with Copper Oxide Nanohybrid for Electrochemical Sensors and Biomedical Applications // J Sci. Adv. Mater. Devices 2017. Vol. 2. P. 493–500.
14. Biswas, K., Mohanta, Y.K., Mishra, A.K., Al-Sehemi, A.G., Pannipara, M., Sett, A., Bratovcic, A., De, D., Panda, B.P., Avula, S.K., Mohanta, T.K., Al-Harrasi, A., Wet Chemical Development of CuO/GO Nanocomposites: Its Augmented Antimicrobial, Antioxidant, and Anticancerous Activity // J Mater. Sci. Mater. Med. 2021. Vol. 32. P. 151.
15. Ji, M., Li, H., Guo, H., Xie, A., Wang, S., Huang, F., Li, S., Shen, Y., He, J. A Novel Porous Aspirin-Loaded $(GO/CTS\text{-}HA)_n$ Nanocomposite Films: Synthesis and Multifunction for Bone Tissue Engineering // Carbohydr. Polym. 2016. Vol. 153. P. 124–132.
16. Liu, S., Wu, X., Hu, J., Wu, Z., Zheng, Y. Preparation and Characterization of a Novel Polylactic Acid/Hydroxyapatite/Graphene Oxide/Aspirin Drug-Loaded Biomimetic Composite Scaffold // New J. Chem. 2021. Vol. 45. P. 10788–10797.
17. Debbichi, L., Marco de Lucas, M.C., Pierson, J.F., Krüger, P. Vibrational Properties of CuO and Cu_4O_3 from First-Principles Calculations, and Raman and Infrared Spectroscopy // J. Phys. Chem. C 2012. Vol. 116. P. 10232–10237.
18. Speier, G., Tyeklár, Z. Formation of Carboxylate Copper Oxygen Complexes in the Reaction of Metallic Copper with 1,2-dicarbonyls and Dioxygen // Transition Met. Chem. 1992. Vol. 17. P. 348–351.
19. Nyquist, R.A.; Kagel, R.O. Infrared Spectra of Inorganic Compounds; Academic Press: New York and London, 1971. P. 220.
20. Kliche, G., Popovic, Z.V. Far-Infrared Spectroscopic Investigations on CuO // Phys. Rev. B 1990. Vol. 42. P. 10060–10066.
21. Rainsford, K.D. (Ed.); Aspirin and Related Drugs; CRC Press, Boca Raton, USA, 2004. P. 800.
22. Iwunze, M.O. Absorptiometric Determination of Acetylsalicylic Acid in Aqueous Ethanolic Solution // J Anal. Lett. 2008. Vol. 41. P. 2944–2953.
23. Kitamura, K., Majima, R. Determination of Salicylic Acid in Aspirin Powder by Second Derivative Ultraviolet Spectrometry // J Anal. Chem. 1983. Vol. 55. P. 54–56.

References (Chapter 5)

1. Alfonso, L., Ai, G., Spitale, R.C., Bhat, G.J. Molecular Targets of Aspirin and Cancer Prevention // Br. J. Cancer. 2014. Vol. 111. P. 1–7.
2. Hawkins, D., Pinckard, R.N., Farr, R.S. Acetylation of Human Serum Albumin by Acetylsalicylic Acid // Science 1968. Vol. 160. P. 780–781.
3. Bjornsson, T., Schneider, D., Berger, H. Aspirin Acetylates Fibrinogen and Enhances Fibrinolysis. Fibrinolytic Effect is Independent of Changes in Plasminogen Activator Levels // J Pharmacol. Exp. Ther. 1989. Vol. 250. P. 154–161.
4. Pinckard, R.N., Hawkins, D., Farr, R.S. In Vitro Acetylation of Plasma Proteins, Enzymes and DNA by Aspirin // Nature 1968. Vol. 219. P. 68–69.
5. Rainsford, K., Schweitzer, A., Brdne, K. Distribution of the Acetyl Compared with the Salicyl Moiety of Acetylsalicylic Acid: Acetylation of Macromolecules in Organs wherein Side-Effects are Manifest // Biochem. Pharmacol. 1983 Vol. 32. P. 1301–1308.
6. Marangos, M., Nightingale, C., Quintiliano, R., Nicolau, D. Influence of Aspirin on the Treatment of Experimental *Enterococcus faecalis* and methicillin resistant *Staphylococcus aureus endocarditis* // J. Infect. Dis. Pharmacother. 1997. Vol. 2 P. 47–53.
7. Hockertz, S., Heckenberger, R. Treatment of an Acute Bacterial Infection with a Combination of Acetylsalicylic Acid/Ibuprofen and Interon Gamma // Arzneimittelforschung 1996. Vol. 46. P. 1012–1015.
8. Obsuka, S., Ohta, M., Masuda, K., Arakawa, Y., Kaneda, T., Kato, N. Lidocaine Hydrochloride and Acetylsalicylate Kill Bacteria by Disrupting the Bacterial Membrane Potential in Different Ways // Microbiol. Immunol. 1994. Vol. 38. P. 429–434.
9. Bartzatt, R., Cirillo, S.L.G., Cirillo, J.D. Antibacterial Activity of Dipeptide Constructs of Acetylsalicylic Acid and Nicotinic Acid // Drug Delivery 2007. Vol. 14. P. 105–109.
10. Caselli, M., Pazzi, P., LaCorte, R., Aleotti, A., Trevisani, L., Stabellini, G. Campylobacter-Like Organisms, Nonsteroidal Anti-Inflammatory Drugs and Gastric Lesions in Patients with Rheumatoid Arthritis // Digestion 1989. Vol. 44. P. 101–104.
11. Wang, W.H., Wong, W.M., Dailidiene, D., Berg, D.E., Gu, Q., Lai, K.C., Lam, S.K., Wong, B.C. Aspirin Inhibits the Growth of Helicobacter pylori and Enhances Its Susceptibility to Antimicrobial Agents // Gut 2003. Vol. 52. P. 490–495.
12. Domenico, P., Schwartz, S., Cunha, B.A. Reduction of Capsular Polysaccharide Production in Klebsiella Pneumoniae by Sodium Salicylate // Infect. Immun. 1989. Vol. 57. P. 3778–3782.

13. Farber, B.F., Wolff, A.G. The Use of Nonsteroidal Anti-Inflammatory Drugs to Prevent Adherence of Staphylococcus Epidermidis to Medical Polymers // J Infect. Dis. 1992. Vol. 166. P. 861– 865.
14. Farber, B.F., Wolff, A.G. The Use of Salicylic Acid to Prevent the Adherence of Escherichia coli to Silastic Catheters // J Urol. 1993. Vol. 149. P. 667–670.
15. Zimmermann, P., Curtis, N., Antimicrobial Effects of Antipyretics // Antimicrob. Agents Chemother. 2017. Vol. 61. P. e02268-16.
16. Hong, N.-H., Sekhon, S.S., Ahn, J.-Y., Le, T.-H., Min, J., Kim, Y.-H. Stress Response in E. coli Exposed to Different Pharmaceuticals // Toxicol. Environ. Health Sci. 2014. Vol. 6. P. 106–112.
17. Jian, Z., Tang, L., Yi, X., Liu, B., Zhang, Q., Zhu, G., Wang, G., Gao, T., Li, C. Aspirin Induces Nrf2-mediated Transcriptional Activation of Haem Oxygenase-1 in Protection of Human Melanocytes from H_2O_2-induced Oxidative Stress // J Cell Mol. Med. 2016. Vol. 20. P. 1307–1318.
18. Chen, H., Fang, Q., Tu, Q., Liu, C., Yin, J., Yin, Y., Xia, L., Bian, X., Zhang, Y. Identification of a Contact-dependent Growth Inhibition System in the Probiotic Escherichia coli Nissle 1917 // FEMS Microbiol. Lett. 2018. Vol. 365. P. 11.
19. Cha, S.-H., Hong, J., McGuffie, M., Yeom, B., VanEpps, J.S., Kotov, N.A. Shape-Dependent Biomimetic Inhibition of Enzyme by Nanoparticles and Their Antibacterial Activity // ACS Nano 2015. Vol. 9. P. 9097–9105.
20. Hu, C., Wang, L.-L., Lin, Y.-Q., Liang, H.-M., Zhou, S.-Y., Zheng, F., Feng, X.-L., Rui, Y.-Y., Shao, L.-Q. Nanoparticles for the Treatment of Oral Biofilms: Current State, Mechanisms, Influencing Factors, and Prospects // Adv. Healthcare Mater. 2019. Vol. 1901301.
21. U.S. Food and Drug Administration, Code of Federal Regulations, Title 21, Volume 3, 21CFR182.8991 (revised as of April 1, 2019).
22. Wang, Y.-W., Cao, A., Jiang, Y., Zhang, X., Liu, J.-H., Liu, Y., Wang, H. Superior Antibacterial Activity of Zinc Oxide/Graphene Oxide Composites Originating from High Zinc Concentration Localized around Bacteria // ACS Appl. Mater. Interfaces 2014. Vol. 6. P. 2791–2798.
23. Martín, C., Kostarelos, K., Prato, M., Bianco, A. Biocompatibility and Biodegradability of 2D Materials: Graphene and Beyond // Chem. Commun. 2019. Vol. 55. P. 5540–5546.
24. Yadav, R.S., Pandey, A.C. Needle-like ZnO Nanostructure Synthesized by Organic-Free Hydrothermal Process // Phys. E 2008. Vol. 40. P. 660–663.

25. Zare, M., Namratha, K., Byrappa, K., Surendra, D.M., Yallappa, S., Hungund, B. Surfactant Assisted Solvothermal Synthesis of ZnO Nanoparticles and Study of Their Antimicrobial and Antioxidant Properties // J Mater. Sci. Technol. 2018. Vol. 34. P. 1035–1043.
26. Widiyastuti, W., Wang, W.-N., Purwanto, A., Lenggoro, I.W., Okuyama, K. A Pulse Combustion-Spray Pyrolysis Process for the Preparation of Nano- and Submicrometer-Sized Oxide Particles // J. Am. Ceram. Soc. 2007. Vol. 90. P. 3779–3785.
27. Saloga, P.E.J., Thünemann, A.F. Microwave-Assisted Synthesis of Ultrasmall Zinc Oxide Nanoparticles // Langmuir 2019. Vol. 35. P. 12469–12482.
28. Hinman, J.J., Suslick, K.S. Nanostructured Materials Synthesis Using Ultrasound // Top Curr. Chem. (Z) 2017. Vol. 375. P. 59–94.
29. Zhong, L., Liu, H., Samal, M., Yun, K. Synthesis of ZnO Nanoparticles-decorated Spindle-shaped Graphene Oxide for Application in Synergistic Antibacterial Activity // J Photochem. Photobiol. B 2018. Vol. 183. P. 293–301.
30. Mitra, P., Dutta, D., Das, S., Basu, T., Pramanik, A., Patra, A. Antibacterial and Photocatalytic Properties of ZnO-9-Aminoacridine Hydrochloride Hydrate Drug Nanoconjugates // ACS Omega 2018. Vol. 3. P. 7962–7970.
31. Zhao, W., Wei, J.-S., Zhang, P., Chen, J., Kong, J.-L., Sun, L.-H., Xiong, H.-M., Möhwald, H. Self-Assembled ZnO Nanoparticle Capsules for Carrying and Delivering Isotretinoin to Cancer Cells // ACS Appl. Mater. Interfaces 2017. Vol. 9. P. 18474–18481.
32. Sadhukhan, P., Kundu, M., Rana, S., Kumar, R., Das, J., Sil, P.C. Microwave Induced Synthesis of ZnO Nanorods and Their Efficacy as a Drug Carrier with Profound Anticancer and Antibacterial Properties // Toxicol. Rep. 2019. Vol. 6. P. 176–185.
33. Mocanu, A., Isopencu, G., Busuioc, C., Popa, O.-M., Dietrich, P., Socaciu-Siebert, L. Bacterial Cellulose Films with ZnO Nanoparticles and Propolis Extracts: Synergistic Antimicrobial Effect // Sci. Rep. 2019. Vol. 9. P. 17687.
34. Laurenti, M., Lamberti, A., Genchi, G.G., Roppolo, I., Canavese, G., Vitale-Brovarone, C., Ciofani, G., Cauda, V. Graphene Oxide Finely Tunes the Bioactivity and Drug Delivery of Mesoporous ZnO Scaffolds // ACS Appl. Mater. Interfaces 2019. Vol. 11. P. 449–456.
35. Alipour, N., Namazi, H., Chelating ZnO-dopamine on the Surface of Graphene Oxide and its Application as pH-responsive and Antibacterial Nanohybrid Delivery Agent for Doxorubicin // Mater Sci. Eng. C Mater. Biol. Appl. 2020. Vol. 108. P. 110459.
36. Moezzi, A., Cortie, M., McDonagh, A. Aqueous Pathways for the Formation of zinc Oxide Nanoparticles // Dalton Trans. 2011. Vol. 40. P. 4871–4878.
37. Rice, S.B., Chan, C., Brown, S.C., Eschbach, P., Han, L., Ensor, D.S., Stefaniak, A.B., Bonevich, J., Vladár, E.A., Walker, A.R.H., Zheng, J., Starnes, C., Stromberg, A., Ye, J.,

Grulke, E.A. Particle Size Distributions by Transmission Electron Microscopy: an Interlaboratory Comparison Case Study // Metrologia 2013. Vol. 50. P. 663–678.

38. Tkach, A., Burko, A., Bandarenka, H., Khrustaleva, T., Zhigulin, D., Tabulina, L., Labunov, V., Veltruská, K., Matolín, V., Radziuk D. Potent E. coli M-17 Growth Inhibition by Ultrasonically Complexed Acetylsalicylic Acid-ZnO-Graphene Oxide Nanoparticles // ACS Appl. Nano Mater. 2021. Vol. 4. P. 778–792.
39. Govender, K., Boyle, D.S., Kenway, P.B., O'Brien, P. Understanding the Factors that Govern the Deposition and Morphology of Thin Films of ZnO from Aqueous Solution // J Mater. Chem. 2004. Vol. 14. P. 2575–2591.
40. Eda, G., Lin, Y.-Y., Mattevi, C., Yamaguchi, H., Chen, H.-A., Chen, I.-S., Chen, C.-W., Chhowalla, M. Blue Photoluminescence from Chemically Derived Graphene Oxide // Adv. Mater. 2010. Vol. 22. P. 505–509.
41. Neogi, A., Karna, S., Shah, R., Phillipose, U., Perez, J., Shimada, R., Wang, Z.M. Surface Plasmon Enhancement of Broadband Photoluminescence Emission from Graphene Oxide // Nanoscale 2014. Vol. 6. P. 11310–11315.
42. Spanhel, L. Colloidal ZnO Nanostructures and Functional Coatings: A Survey // J Sol-Gel Sci. Techn. 2006. Vol. 39. P. 7–24.
43. Wood, A., Giersig, M., Hilgendorff, M., Vilas-Campos, A., Liz-Marzán, L.M., Mulvaney, P. Size Effects in ZnO: the Cluster to Quantum Dot Transition // Aust. J Chem. 2003. Vol. 56. P. 1051–1057.
44. Ludi, B., Niederberger, M. Zinc Oxide Nanoparticles: Chemical Mechanisms and Classical and Non-classical Crystallization // Dalton Trans. 2013. Vol. 42. P. 12554–12568.
45. Pesika, N.S., Stebe, K.J., Searson, PC. Determination of the Particle Size Distribution of Quantum Nanocrystals from Absorbance Spectra // Adv. Matter. 2003. Vol. 15, P. 1289–1291.
46. Ferrari, A.C. Raman Spectroscopy of Graphene and Graphite: Disorder, Electron-phonon Coupling, Doping and Nonadiabatic Effects // Solid State Commun. 2007. Vol. 143. P. 47–57.
47. Šćepanović, M., Grujić-Brojčin, M., Vojisavljević, K., Bernik, S., Srećković, T. Raman Study of Structural Disorder in ZnO Nanopowders // J. Raman Spectrosc. 2010. Vol. 41. P. 914–921.
48. Sahoo, S. Sharma, G.L., Katiyar, R.S. Raman Spectroscopy to Probe Residual Stress in ZnO Nanowire // J. Raman Spectrosc. 2012. Vol. 43. P. 72–75.
49. Arguello, C.A., Rousseau, D.L., Porto, S.P.S. First-Order Raman Effect in Wurtzite-Type Crystals // Phys. Rev. 1969. Vol. 181. P. 1351–1363.

50. Cuscó, R., Alarcón-Lladó, E., Ibáñez, J., Artús, L., Jiménez, J., Wang, B., Callahan, M.J. Temperature dependence of Raman scattering in ZnO // Phys. Rev. B 2007. Vol. 75. P. 165202.
51. Nakamoto, K. Infrared and Raman Spectra of Inorganic and Coordination Compounds. 4th Ed. John Wiley & Sons. 1984. P. 484.
52. Moulder, J.F., Chastain, J. Handbook of X-ray Photoelectron Spectroscopy. A Reference Book of Standard Spectra for Identification and Interpretation of XPS Data. Ed. by J. Chastain, Perkin-Elmer Corporation, Minesota, USA. 1992. ISBN: 0-9627026-2-5.
53. Yang, D., Velamakannia, A., Bozoklu, G., Park, S., Stoller, M., Piner, R.D., Stankovich, S., Jung, I., Field, D.A., Ventrice Jr, C.A., Ruoff, R.S. Chemical Analysis of Graphene Oxide Films after Heat and Chemical Treatments by X-ray Photoelectron and Micro-Raman Spectroscopy // Carbon 2009. Vol. 47. P. 145–152.
54. Stankovich, S., Dikin, D.A., Piner, R.D., Kohlhaas, K.,A., Kleinhammes, A., Jia, Y., Wu, Y., Nguyen, S.T., Ruoff, R.S. Synthesis of Graphene-based Nanosheets via Chemical Reduction of Exfoliated Graphite Oxide // Carbon 2007. Vol. 45. P. 15585–1565.
55. Al-Gaashani, R., Najjar, A., Zakaria, Y., Mansoura, S., Atieh, M.A. XPS and Structural Studies of High Quality Graphene Oxide and Reduced Graphene Oxide Prepared by Different Chemical Oxidation Methods // Ceram. Int. 2019. Vol. 45. P. 14439–14448.
56. Johra, F.T., Lee, J.-W., Jung, W.-G. Facile and Safe Graphene Preparation on Solution based Platform // J Ind. Eng. Chem. 2014. Vol. 20. P. 28832887.
57. Alshammari, A.S., Chi, L., Chen, X., Bagabas, A., Kramer, D., Alromaeh, A., Jiang, Z. Visible-light Photocatalysis on C-doped ZnO Derived from Polymer-assisted Pyrolysis // RSC Adv. 2015. Vol. 5. P. 27690–27698.
58. Araújo, M.P., Soares, O.S.G.P., Fernandes, A.J.S., Pereira, M.F.R., Freire, C. Tuning the Surface Chemistry of Graphene Flakes: New Strategies for Selective Oxidation // RSC Adv. 2017. Vol. 7. P. 14290–14301.
59. Ganguly, A., Sharma, S., Papakonstantinou, P., Hamilton, J. Probing the Thermal Deoxygenation of Graphene Oxide Using High-resolution in Situ X-ray-based Spectroscopies // J. Phys. Chem. C 2011. Vol. 115. P. 17009–17019.
60. López-Díaz, D., Holgado, M., García-Fierro, J.L., Velázquez, M.M. Evolution of the Raman Spectrum with the Chemical Composition of Graphene Oxide // J. Phys. Chem. C 2017. Vol. 121. P. 20489–20497.
61. Barreca, D., Gasparotto, A., Maccato, C., Maragno, C., Tondello, E. ZnO Nanoplatelets Obtained by Chemical Vapor Deposition, Studied by XPS // Surf. Sci. Spectra 2007. Vol. 14. P. 19–26.

62. Ballerini, G., Ogle, K., Barthes-Labrousse, M.-G. The Acid–Base Properties of the Surface of Native Zinc Oxide Layers: an XPS Study of Adsorption of 1, 2-diaminoethane // Appl. Surf. Sci. 2007. Vol. 253. P. 6860–6867.
63. Zhang, Y., Muhammed, M. Critical Evaluation of Thermodynamics of Complex Formation of Metal Ions in Aqueous Solutions: VI. Hydrolysis and Hydroxo-Complexes of Zn^{2+} at 298.15 K // Hydrometallurgy 2001. Vol. 60. P. 215–236.
64. El-Shahawy, A.S. Spectroscopic Structural Studies of Salicylic Acid, Salicylamide and Aspirin // Spectrochim. Acta Part A. 1988. Vol. 44A. P. 903–907.
65. Gunasekaran, S., Devi, K.M. UV-Vis Spectroscopic Investigation on Hydrolysis of Starch and Starch-drug Interaction // Asian J Chem. 2007. Vol. 19. P. 3363–3374.
66. Larentzos, J.P., Greathouse, J.A., Cygan, R.T. An ab Initio and Classical Molecular Dynamics Investigation of the Structural and Vibrational Properties of Talc and Pyrophyllite // J. Phys. Chem. C 2007. Vol. 111. P. 12752–12759.
67. Schrank, S., Kann, B., Windbergs, M., Glasser, B.J., Zimmer, A., Khinast, J., Roblegg, E. Microstructure of Calcium Stearate Matrix Pellets: a Function of the Drying Process // J Pharm. Sci. 2013. Vol. 102. P. 3987–3997.
68. Tarakeshwar, P., Manogaran, S. Ground State Vibrations of Citric Acid and the Citrate Trianion - an Ab Initio Study // Spectrochim. Acta Part A 1994. Vol. 50. P. 2321–2343.
69. Björnström, J., Martinelli, A., Johnson, J.R.T., Matic, A. Panas, I. Signatures of a Drying $SiO_2 \cdot (H_2O)_x$ Gel from Raman Spectroscopy and Quantum Chemistry // Chem. Phys. Lett. 2003. Vol. 380. P. 165–172.
70. Kontoyannis, C.G., Orkouf, M. Quantitative Non-destructive Determination of Salicylic Acid Acetate in Aspirin Tablets by Raman Spectroscopy // Talanta 1994. Vol. 41. P. 1981–1984.
71. Namazi, H., Hasani, M., Yadollahi, M. Antibacterial Oxidized Starch/ZnO Nanocomposite Hydrogel: Synthesis and Evaluation of Its Swelling Behaviours in Various pHs and Salt Solutions // Int. J Biol. Macromol. 2019. Vol. 126. P. 578–584.
72. Ma, J., Zhu, W., Tian, Y., Wang, Z. Preparation of Zinc Oxide-Starch Nanocomposite and Its Application on Coating // Nanoscale Res. Lett. 2016. Vol. 11. P. 200.
73. Tso, C., Zhung, C., Shih, Y., Tseng, Y.-M., Wu, S., Doong, R. Stability of Metal Oxide Nanoparticles in Aqueous Solutions // Water Sci. Technol. 2010. Vol. 61. P. 127–133.
74. Escherich, T. The Intestinal Bacteria of the Neonate and Breast-fed Infant 1884 // Rev Infect Dis. 1988. Vol. 10. P. 1220–1225.
75. Salat, M., Petkova, P., Hoyo, J., Perelshtein, I., Gedanken, A., Tzanov, T. Sonochemical Coating of Textiles with Hybrid ZnO/Chitosan Antimicrobial Nanoparticles // Carbohydr. Polym. 2018. Vol. 189. P. 198–203.

76. Aldsworth, T.G., Sharman, R.L. Bacterial Suicide through Stress // Cell. Mol. Life Sci. 1999. Vol. 56. P. 378–383.
77. Yamamoto, O., Hotta, M., Sawai, J., Sasamoto, T., Kojima, H. Influence of Powder Characteristic of ZnO on Antibacterial Activity // J. Ceram. Soc. Japan 1998. Vol. 106. P. 1007–1011.
78. Wang, Y.-W., Cao, A., Jiang, Y., Zhang, X., Liu, J.-H., Liu, Y., Wang, H. Superior Antibacterial Activity of Zinc Oxide/Graphene Oxide Composites Originating from High Zinc Concentration Localized around Bacteria // ACS Appl. Mater. Inter. 2014. Vol. 6. P. 2791–2798.
79. Hu, Y.-L., Lu, Y., Zhou, G.-J., Xia, X.-H. A Simple Electrochemical Method for the Determination of Hydroxyl Free Radicals without Separation Process // Talanta 2008. Vol. 74. P. 760–765.

References (Chapter 6)

1. Rena, G., Sakamoto, K. Salicylic Acid: Old and New Implications for the Treatment of Type 2 Diabetes? // Diabetol. Int. 2014. Vol. 5. P. 212-218.
2. Bashir, A.I.J., Kankipati, C.S., Jones, S., Newman, R.M., Safrany, S.T., Perry, C.J., Nicholl, I.D. A Novel Mechanism for the Anticancer Activity of Aspirin and Salicylates // Int. J. Oncol. 2019. Vol. 54. P. 1256-1270.
3. Nyúl, E., Kuzma, M., Mayer, M., Lakatos, S., Almási, A., Perjési, P. HPLC study on Fenton-reaction initiated oxidation of salicylic acid. Biological relevance of the reaction in intestinal biotransformation of salicylic acid // Free Radic. Res. 2018. Vol. 52. P. 1-261.
4. Van Jaarsveld, H., Kuyl, J.M., van Zyl, G.F., Barnard, H.C. Salicylate in the Perfusate During Ischemia/Reperfusion Prevented Mitochondrial Injury // Commun. Mol. Pathol. Pharmacol. 1994. Vol. 86. P. 287-295.
5. Cheng, I.F., Zhao, C.P., Amolins, A., Galazka, M., Doneski, L. A Hypothesis for the in Vivo Antioxidant Action of Salicyclic Acid // BioMetals 1996. Vol. 9. P. 285-290.
6. Shi, X., Ding, M., Dong, Z., Chen, F., Ye, J., Wang, S., Leonard, S.S., Castranova, V., Vallyathan, V. Antioxidant Properties of Aspirin: Characterization of the Ability of Aspirin to Inhibit Silica-Induced Lipid Peroxidation, DNA Damage, NF-kappaB Activation, and TNF-alpha Production // Mol. Cell Biochem. 1999. Vol. 199. P. 93-102.
7. Jay, D., Jay, E.G., Medina, M.A. Superoxide Dismutase Activity of the Salicylate-Iron Complex // Arch. Med. Res. 1999. Vol. 30. P. 93-96.
8. Janoš, P., Spinello, A., Magistrato, A. All-Atom Simulations to Studying Metallodrugs/Target Interactions // Curr. Opin. Chem. Biol. 2021. Vol. 61. P. 1-8.
9. Stathopoulou, M.-E.K., Banti, C.N., Kourkoumelis, N., Hatzidimitriou, A.G., Kalampounias, A.G., Hadjikakou, S.K. Silver Complex of Salicylic Acid and Its Hydrogel-Cream in Wound Healing Chemotherapy // J Inorg. Biochem. 2018. Vol. 181. P. 41-55.
10. Banti, C.N., Papatriantafyllopoulou, C., Tasiopoulos, A.J., Hadjikakou, S.K. New Metalo-Therapeutics of NSAIDs Against Human Breast Cancer Cells // Eur. J Med. Chem. 2018. Vol. 143. P. 1687-1701.
11. Wu, X.-W., Zheng, Y., Wang, F.-X., Cao, J.-J., Zhang, H., Zhang, D.-Y., Tan, C.-P., Ji, L.-N., Mao, Z.-W. Anticancer IrIII–Aspirin Conjugates for Enhanced Metabolic Immuno-Modulation and Mitochondrial Lifetime Imaging // Chem. Eur. J. 2019. Vol. 25. P. 7012-7022.

12. Deng, J., Gou, Y., Chen, W., Fu, X., Deng, H. The Cu/Ligand Stoichiometry Effect on the Coordination Behavior of Aroyl Hydrazone with Copper(II): Structure, Anticancer Activity and Anticancer Mechanism // Bioorg. Med. Chem. 2016. Vol. 24. P. 2190-2198.
13. Giardina, C., Inan, M.S. Nonsteroidal Anti-Inflammatory Drugs, Short-Chain Fatty Acids, and Reactive Oxygen Metabolism in Human Colorectal Cancer Cells // Biochim. Biophys. Acta 1998. Vol. 1401. P. 277-288.
14. Giardina, C., Boulares, H., Inan, M.S. NSAIDs and Butyrate Sensitize a Human Colorectal Cancer Cell Line to TNF-α and Fas Ligation: the Role of Reactive Oxygen Species // Biochim. Biophys. Acta 1999. Vol. 1448. P. 425-438.
15. Lewandowski, W., Kalinowska, M., Lewandowska, H. The Influence of Metals on the Electronic System of Biologically Important Ligands. Spectroscopic Study of Benzoates, Salicylates, Nicotinates and Isoorotates // J Inorg. Biochem. 2005. Vol. 99. P. 1407-1423.
16. Englinger, B., Pirker, C., Heffeter, P., Terenzi, A., Kowol, C.R., Keppler, B.K., Berger, W. Metal Drugs and the Anticancer Immune Response // Chem. Rev. 2019. Vol. 119. P. 1519-1624.
17. Arami, H., Khandhar, A., Liggitt, D., Krishnan, K.M. In Vivo Delivery, Pharmacokinetics, Biodistribution and Toxicity of Iron Oxide Nanoparticles // Chem. Soc. Rev. 2015. Vol. 44. P. 8576-8607.
18. Zanganeh, S., Hutter, G., Spitler, R., Lenkov, O., Mahmoudi, M., Shaw, A., Pajarinen, J.S., Nejadnik, H., Goodman, S., Moseley, M., Coussens, L.M., Daldrup-Link, H.E. Iron Oxide Nanoparticles Inhibit Tumor Growth by Inducing Pro-inflammatory Macrophage Polarization in Tumor Tissues // Nat. Nanotechnol. 2016. Vol. 11. P. 986-994.
19. Nandi, S., Kale, N.R., Takale, V., Chate, G.C., Bhave, M., Banerjee, S.S., Khandare, J.J. Cell Deformation and Acquired Drug Resistance: Elucidating the Major Influence of Drug-Nanocarrier Delivery Systems // J. Mater. Chem. B 2020. Vol. 8. P. 1852-1862.
20. Li, D., Deng, M., Yu, Z., Liu, W., Zhou, G., Li, W., Wang, X., Yang, D., Zhang, W. Biocompatible and Stable GO-coated Fe_3O_4 Nanocomposite: a Robust Drug Delivery Carrier for Simultaneous Tumor MR Imaging and Targeted Therapy // ACS Biomater. Sci. Eng. 2018. Vol. 4. P. 2143-2154.
21. Zeiger, B.W., Suslick, K.S. Sonofragmentation of Molecular Crystals // J. Am. Chem. Soc. 2011. Vol. 133. P. 14530-14533.
22. Kim, H.N., Suslick, K.S. Sonofragmentation of Ionic Crystals // Chem. Eur. J. 2017. Vol. 23. P. 2778-2782.
23. Suslick, K.S., Schubert, P.F., Goodale, J.W. Sonochemistry and Sonocatalysis of Iron Carbonyls // J. Am. Chem. Soc. 1981. Vol. 103. P. 7342-7344.

24. Suslick, K.S., Fang, M., Hyeon, T. Sonochemical Synthesis of Iron Colloids // J. Am. Chem. Soc. 1996. Vol. 118. P. 11960-11961.
25. Bang, J.H., Suslick, K.S. Sonochemical Synthesis of Nanosized Hollow Hematite // J. Am. Chem. Soc. 2007. Vol. 129. P. 2242-2243.
26. Xu, H.X., Suslick, K.S. Sonochemical Preparation of Functionalized Graphenes // J. Am. Chem. Soc. 2011. Vol. 133. P. 9148-9151.
27. Mikhnavets, L., Abashkin, V., Khamitsevich, H., Shcharbin, D., Burko, A., Krekoten, N., Radziuk, D. Ultrasonic Formation of Fe_3O_4 Reduced Graphene Oxide−Salicylic Acid Nanoparticles with Switchable Antioxidant Function // ACS Biomater. Sci. Eng. 2022. Vol. 8. P. 1181-1192.
28. Fukuoka, E., Makita, M., Yamamura, S. Evaluation of Crystallite Orientation in Tablets by X-Ray Diffraction Methods // Chem. Pharm. Bull. 1987. Vol. 35. P. 1564-1570.
29. Nakamoto, K. Infrared and Raman Spectra of Inorganic and Coordination Compounds. 4th Ed. John Wiley & Sons. 1984. P. 264.
30. Khadikar, P.V., Ali, S.M., Heda, B.D. Kinetics of Thermal Dehydration of Some Bis-Salicylato-Diaquo Complexes of Transition Metal Ions // J Therm. Anal. 1985. Vol. 30. P. 167-176.
31. Cornell, R.M., Schwertmann, U. The Iron oxides: Structure, Properties, Reactions, Occurences and Uses, 2nd edition. Wiley-VCH. Verlag GmbH & Co. KGaA, Weinheim, Germany. 2003. P. 1-199.
32. Mackay, A.L. Some Aspects of the Topochemistry of Iron Oxides and Hydroxides. In: de Boer J.H. (ed.) Reactivity of solids. Proc. 4th Int. Symp. Reactivity of Solids, Amsterdam, 1961. P. 571-583.
33. Dutta, S.K., Ghosh, M., Biswas, P., Flörke, U., Saal, C., Haase, W., Nag, K. Formation of Oxo-Bridged Tetrairon(III) Complexes Mediated by Oxygen Activation. Structure, Spectroscopy, Magnetism and Electrochemistry // New J. Chem. 2007. Vol. 31. P. 93-101.
34. Wang, Z., Zhou, C., Xia, J., Via, B., Xia, Y., Zhang, F., Li, Y., Xia, L. Fabrication and Characterization of a Triple Functionalization of Graphene Oxide with Fe_3O_4, Folic Acid and Doxorubicin as Dual-Targeted Drug Nanocarrier // Colloids Surf. B: Biointerfaces 2013. Vol. 106. P. 60-65.
35. Lia, Y.-S., Church, J.S., Woodhead, A.L. Infrared and Raman Spectroscopic Studies on Iron Oxide Magnetic Nano-particles and Their Surface Modifications // J. Magn. Magn. Mater. 2012. Vol. 324. P. 1543-1550.
36. Soler, M.A.G., Qu, F. Chapter 14: Raman Spectroscopy of Iron Oxide Nanoparticles. Challa S. S. R. Kumar (ed.), Raman Spectroscopy for Nanomaterials Characterization, Springer-Verlag Berlin Heidelberg 2012. P. 379-416.

37. Hanesch, M. Raman Spectroscopy of Iron Oxides and (Oxy)hydroxides at Low Laser Power and Possible Applications in Environmental Magnetic Studies // Geophys. J. Int. 2009. Vol. 177. P. 941-948.
38. Volovšek, V., Colombo, L., Furić, K. Vibrational Spectrum and Normal Coordinate Calculations of the Salicylic Acid Molecule // J Raman Spectrosc. 1983. Vol. 14. P. 347-352.
39. Kudin, K.N., Ozbas, B., Schniepp, H.C., Prud'homme, R.K., Aksay, I.A., Car, R. Raman Spectra of Graphite Oxide and Functionalized Graphene Sheets // Nano Lett. 2008. Vol. 8. P. 36-41.
40. Ferrari, A.C., Robertson, J. Origin of the 1150 cm^{-1} Raman Mode in Nanocrystalline Diamond // Phys. Rev. B 2001. Vol. 63. P. 121405-1-4.
41. Ruiz-Medina, A., Fernández-de Córdova, M.L., Ortega-Barrales, P., Molina-Díaz, A. Flow-through UV Spectrophotometric Sensor for Determination of (Acetyl)salicylic Acid in Pharmaceutical Preparations // Int. J Pharm. 2001. Vol. 216. P. 95-104.
42. Wang, Y., Xu, P.-P., Li, X.-X., Nie, K., Tuo, M.-F., Kong, B., Chen, J. Monitoring the Hydrolyzation of Aspirin During the Dissolution Testing for Aspirin Delayed-Release Tablets with a Fiber-Optic Dissolution System // J Pharm. Anal. 2012. Vol. 2. P. 386-389.
43. Wudarska, E., Chrzescijanska, E., Kusmierek, E. Electroreduction of Salicylic Acid, Acetylsalicylic Acid and Pharmaceutical Products Containing These Compounds // Portugaliae Electrochim. Acta 2014. Vol. 32. P. 295-302.
44. Antonov, V.N., Harmon, B.N., Antropov, V.P. Electronic Structure and Magneto-optical Kerr Effect of Fe_3O_4 and Mg^{2+}- or Al^{3+}-substituted Fe_3O_4 // Phys. Rev. B 2001. Vol. 64. P. 134410.
45. Yang, J.H., Ramaraj, B., Yoon, K.R. Preparation and Characterization of Superparamagnetic Graphene Oxide Nanohybrids Anchored with Fe_3O_4 Nanoparticles // J. Alloys Compd. 2014. Vol. 583. P. 128-133.
46. Aruoma, O.I., Halliwell, B. The Iron-Binding and Hydroxyl Radical Scavenging Action of Anti-Inflammatory Drugs // Xenobiotica 1988. Vol. 18. P. 459-470.
47. Baltazar, M.T., Dinis-Oliveira, R.J., Duarte, J.A., Bastos, M.L., Carva, F. Antioxidant Properties and Associated Mechanisms of Salicylates // Curr. Med. Chem. 2011. Vol. 18. P. 3252-3264.
48. Hou, X., Huang, X., Ai, Z., Zhao, J., Zhang, L. Ascorbic Acid/Fe@Fe_2O_3: A Highly Efficient Combined Fenton Reagent to Remove Organic Contaminants // J Hazard. Mater. 2016. Vol. 310. P. 170-178.
49. Dewhirst, R.A., Fry, S.C. The Oxidation of Dehydroascorbic Acid and 2,3-diketogulonate by Distinct Reactive Oxygen Species // Biochem. J 2018. Vol. 475. P. 3451-3470.

50. Halliwell, B.; Foyer, C.H. Ascorbic Acid, Metal Ions and the Superoxide Radical // Biochem. J 1976. Vol. 155. P. 697-700.
51. Zhang, Z. Su, T., Han, Y., Yang, Z., Wei, J., Jin, L., Fan, H. A Convergent Synthetic Platform for Dual Anticancer Drugs Functionalized by Reduced Graphene Nanocomposite Delivery for Hepatocellular Cancer // Drug Deliv. 2021. Vol. 28. P. 1982-1994.
52. Ruiz, O.N., Fernando, K.A.S., Wang, B., Brown, N.A., Luo, P.G., McNamara, N.D., Vangsness, M., Sun, Y.-P., Bunker, C.E. Graphene Oxide: A Nonspecific Enhancer of Cellular Growth // ACS Nano 2011. Vol. 5. P. 8100-8107.
53. Einafshar, E., Asl, A.H., Nia, A.H., Mohammadi, M., Malekzadeh, A., Ramezani, M., New Cyclodextrin-Based Nanocarriers for Drug Delivery and Phototherapy Using an Irinotecan Metabolite // Carbohydr. Polym. 2018. Vol. 194. P. 103-110.